UNIVERSITÀ DEGLI STUDI DI TRIESTE
Dipartimento di FISICA

XXII Ciclo del Dottorato di Ricerca in

NANOTECNOLOGIE

Electronic structure, morphology and chemical reactivity of nanoclusters and low-dimensional systems: fast photoemission spectroscopy studies

(FIS/03 – Fisica della Materia)

DOTTORANDO

Paolo LACOVIG

DIRETTORE DELLA SCUOLA DI DOTTORATO

Chiar.mo Prof. Maurizio FERMEGLIA
(Università degli Studi di Trieste)

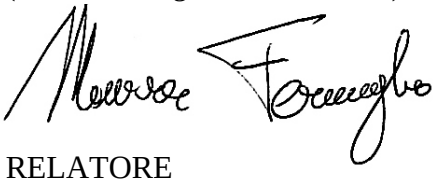

RELATORE

Dott. Alessandro BARALDI
(Università degli Studi di Trieste)

CORRELATORE

Dott. Silvano LIZZIT
(Sincrotrone Trieste S.C.p.A.)

ANNO ACCADEMICO 2008/2009

Abstract

L'obiettivo di questa tesi è l'applicazione della spettroscopia di fotoemissione allo studio di nanoparticelle supportate e di sistemi a bassa dimensionalità.

Ad una primo periodo dedicato allo sviluppo del rivelatore e del software per un nuovo analizzatore d'energia per elettroni installato presso la linea di luce SuperESCA ad Elettra, è seguita una fase durante la quale ho eseguito una serie di esperimenti mirati ad esplorare le potenzialità del nuovo apparato sperimentale.

Il primo risultato ottenuto riguarda la comprensione della relazione che intercorre tra le variazioni della reattività chimica del sistema Pd/Ru(0001) e il numero degli strati di Pd cresciuti in modo pseudomorfico sul substrato di rutenio.

La risoluzione temporale raggiunta con la nuova strumentazione ci ha permesso di studiare processi dinamici su una scala temporale fino ad ora inaccessibile per la spettroscopia di fotoemissione dai livelli di core: in particolare abbiamo studiato la crescita del grafene ad alta temperatura sulla superficie (111) dell'iridio e la reattività chimica di nanocluster di Pt supportati su MgO. Nel primo caso abbiamo messo in evidenza come la formazione del grafene proceda attraverso la nucleazione di nano-isole di carbonio che assumono una peculiare forma di cupola. Nel secondo caso siamo riusciti a seguire sia la dinamica del processo di adsorbimento di CO, sia la reazione $CO + \frac{1}{2}O_2 \rightarrow CO_2$ sulle nanoparticelle di Pt depositate su un film ultrasottile di ossido di magnesio.

Infine, abbiamo caratterizzato la morfologia di nanoparticelle di Pd, Pt, Rh e Au cresciute su diversi substrati a base di carbonio, in particolare grafite, nanotubi a parete singola e grafene. Tra i vari risultati abbiamo compreso come l'interazione metallo-substrato dipenda dalla dimensione delle nano-particelle e abbiamo evidenziato il ruolo centrale dei difetti del substrato nei processi di nucleazione e intercalazione.

Abstract

The objective of this thesis is the application of photoelectron spectroscopy for the investigation of supported nanoclusters and low-dimensional systems.

After a first stage devoted to the development of the detector and the software for the electron energy analyser installed on the SuperESCA beamline at Elettra, during the PhD project I've performed a series of experiments aimed to explore the capabilities of the new experimental apparatus.

One of the first results concerns the understanding of the relation between the modifications in the chemical reactivity the Pd/Ru(0001) system and the thickness of the pseudomorphically grown Pd overlayer.

The temporal resolution achieved with the new experimental set-up allowed us to study dynamical processes on a new time scale, in particular the graphene growth process at high temperature on the Ir(111) surface and the chemical reactivity of Pt nanoclusters supported on MgO. In the former case, we discovered that graphene formation proceeds via preliminary nucleation of dome-shaped C nano-islands. In the second case, we succeded in following both the dynamics of CO adsorption process and the $CO + \frac{1}{2}O_2 \rightarrow CO_2$ reaction on Pt nano-clusters grown on a ultra-thin film of magnesium oxide.

Finally, the morphology of Pd, Pt, Rh and Au nanoclusers grown on different carbon-based substrates (namely graphite, single-walled carbon nanotubes and graphene) has been characterized. Among the results we report the understanding of the dependence of the metal-substrate interaction on the cluster size and the role of defects in the nucleation and intercalation processes.

Contents

Chapter 1

Introduction

In his talk given on December 1959 at the annual meeting of the American Physical Society, and considered as the founding speech of *nanotechnology* [1], Richard Feynman suggested new field of studies with the target of manipulating and controlling things on a small scale". Somehow inspired by biological systems, he dreamed of small systems capable of building smaller ones and so on up to the atomic scale: in his thoughts this could have led, for instance, to the possibility of synthesizing any chemical substance just by placing single atoms in the right positions, and even of realizing mechanical *nano-surgeons* to be directly introduced inside the human body.

Actually, besides these visionary scenarios, Feynamn talked also on revealing the DNA sequence, miniaturizing the computer's circuits, arranging atoms in the desired regular patterns and tailoring the properties of materials by controlling single atomic layers in order to exploit "new kinds of forces and new kind of possibilities, new kinds of effects" that would have come out "if we could really arrange the atoms the way we want them".

Fifty years later, we can say that many efforts have been spent in this kind of studies and a long list of remarkable results have been obtained that, in turn, opened up exciting opportunities in several research fields.

From the point of view of *life sciences*, for instance, human DNA has completely been sequenced [2], leading to a deeper knowledge of the mechanisms at the basis of *life*; and, as another example, biologists have also learned how to artificially stimulate cell proliferation by using suitable nanomaterial-based scaffolds, opening the so-called "Tissue Engineering" research field that promises to replace today's conventional treatments on damaged organs [3].

Microelectronic industry succeded in developing fabrication methods that allow making electronic components as small as 30 nm. Studies on autonomous ordering and assembly of atoms and molecules on atomically well-defined surfaces promise to be a route towards even smaller functional systems [4]. Fullerenes [5] and carbon nanotubes [6] are examples of nano-sized building blocks for such systems.

A large part of the systems studied during my PhD project, and reported in this thesis, are related to one of the fields that obtained more benefits from nanotechnology, and will probably continue with this trend: catalysis.

What we want to study and why...

Probably this is not an exciting topic as *nano-robots* or *nano-surgeons* could be, but for sure heterogeneous catalysis is an important part of the technological processes for production of low-cost and high-quality raw materials, production and storage of transportation fuels and many other aspects related with our *everyday* lives. In the last decades, in particular, the expanding world population, the increasing energy demand in developing countries and the worsening of environmental problems have raised even more attention on catalysis and have determined the new challenges for this branch of studies: (i) achieve the highest selectivity for the desired product in multipath reactions, in order to avoid undisered dangerous side products; and (ii) develop and optimize processes based on renewable energy.

Many efforts have already been spent on surface chemistry studies: using model surfaces—single crystals at first—many information have been obtained on atomic and molecular structures, composition and oxidation states, and energy transfer upon adsorption, desorption and scattering of molecules from surfaces.

However, the importance of catalyst's size in catalytic processes plays a central role in heterogeneous catalysis, and has been widely exploited long before the advent of nanotechnology. The efficiency of a catalyst is directly proportional to its surface area: for this reason many of the currently used catalysts consist of one or several catalytically active component(s) in the form of very small particles (typically in the size range of 1–100 nm) deposited on the surface of a highly porous and thermally stable support material (usually an oxide) with a high surface-to-volume ratio.

The rise of nanoscience permitted the synthesis and characterization of nanoparticles with a controlled average size (or even monodispersed nanoclusters) on different supports. As summarized in fig. 1.1, transition metal nanoparticles on oxide supports, thus, became the model catalysts, after

Figure 1.1: Evolution of surface science and its link with nanotechnology. From [7].

metal single crystals had been used for decades [7].

As explained more in detail in ch. 7, devoted to the analysis of the Pt/MgO/Ag(100) model catalyst, studies on these systems evidenced how selectivity depends both on size and morphology of nanoclusters, but also on the role of the support in the adsorption of the reactants as well as on peculiar geometric and electronic properties arising at the interface between transition metal particles and oxide substrate.

Moreover, when the particle size reaches the 1 nm range, the "new kind of effects" predicted by Feynman also appear, related to the quantum nature of matter. The most famous example of this effects is the abrupt increase of the catalytic activity of Au nanoparticles deposited on titania when their mean diameter approaches the value of 3 nm (see fig. 1.2); this effect appears related to the fact that such small clusters present electronic characteristics similar to those of non-metals, while larger particles behave like metallic gold [8].

Nevertheless, catalysis is not the only research field touched by the experiments presented in this thesis.

The properties of metal interfaces (like the one studied in ch. 5) and

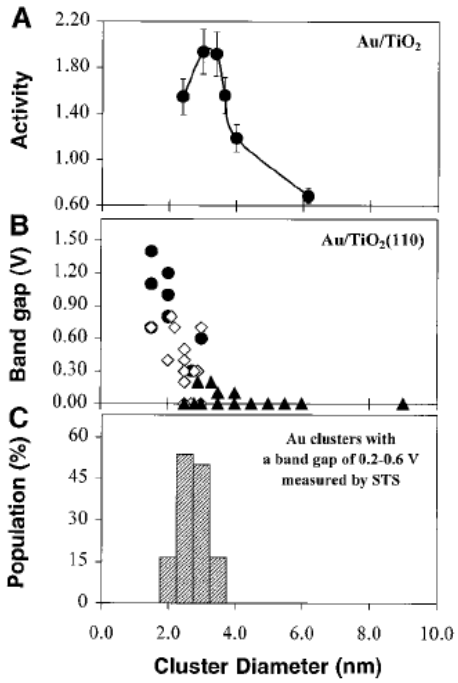

Figure 1.2: Correspondence between the strong increase in Au activity for clusters of ≈ 3 nm and the opening of a band gap at the Fermi level. (A) CO oxidation turnover frequencies at 350 K as a function of the average size of the Au clusters supported on $TiO_2(1 \times 1)$ support. (B) Cluster band gap measured by STS as a function of the Au cluster size. (C) Relative population of the Au clusters. From [8].

of oxide thin films (used as support for Pt nanoclusters studied in ch. 7) are of great interest also for the development of electronic devices: metal oxide field effect transistors (MOSFET) are, in fact, based on layered structures consisting of semiconductors, insulating thin oxide films and metal contacts [9].

Transition metal nanoclusters, then, besides being the active part of a catalyst, can be used in the development of new materials with well-defined mechanical properties. Alternatively, in the case of magnetic metals, ordered arrays of nanoparticles can be the starting point for new high density data storage techniques [10].

Finally, graphene, extensively studied in ch. 8, can be an interesting support for metal nanoparticles, but it is also an exciting material that

presents outstanding electronic and mechanical properties.

... And how we are going to do it.

The invention of the scanning tunneling mircoscope (STM) by Binnig and Rohrer in 1982 [11] is considered somehow the date of birth of nanotechnology. As a matter of fact, scanning tunneling microscopy, together with all the imaging techniques invented or developed in the following years (AFM, SEM and TEM) gave the fascinating possibility of directly *looking* at single atoms. Nowadays, atomic resolution microscopy techniques are the main investigation tools when dealing with nanostructured systems.

Nevertheless, many other experimental techniques are used to investigate these particular samples. Among them, we felt that PhotoEmission Spectroscopy (PES) could give a important contribution to the understanding of the electronic and chemical properties of nano-systems, but also of their morphology. This technique, indeed, offers several interesting opportunities for this kind of investigations:

- Core level spectra allow the identification of the atomic and molecular species present on the sample, being them in the substrate, in the deposited nanoclusters or even the reactant/product molecules on the catalyst's surface.

- The analysis of photoemission intensity, after proper calibration procedures can give quantitative information on the population of the species identified on the sample and, possibly, on its temporal evolution.

- As will be seen in the brief survey on photoemission spectroscopy presented in ch. 2, core level binding energies are very sensitive to the local environment of the emitting atom; as reported for the study of the Pd/Ru interface (ch. 5), the nucleation of Pd nanoclusters on graphite and carbon nanotubes (ch. 6), and the graphene growth on Ir(111) (ch. 8), this sensitivity, combined with theoretical calculations, allows investigations on electronic properties, structure and morphology of the sample.

- Finally, if a high photon flux is combined with a good efficiency in collecting photoelectrons, real-time measurements can be performed in order to follow the evolution of the studied system, for instance during a chemical reaction. The study of CO oxidation on the Pt nanoclusters presented in ch. 7 is an example of this kind of application.

However, it must be kept in mind that the nanostructured systems we are interested in (nanoclusters, oxide thin films, bimetallic interfaces and graphene) present a very low atomic density. This requires some shrewdness in order to effectively perform photoemission experiments on such samples.

First of all, synchrotron radiation sources must be used, since they are capable of intense photon flux. For this reason our *starting point* has been the SuperESCA beamline at Elettra (see ch. 3), specifically designed to deliver high photon flux in the range 100–1000 eV.

The second point is the efficiency of the instrumentation: even with synchrotron radiation, due to the low atomic density of the investigated systems, the expected rate of photoemitted electrons is low. For this reason the first part of my PhD project has been devoted to the development of the experimental set-up aimed to an increased efficiency. As reported in ch. 4, the improvements consisted in (i) the installation of a new electron energy analyser on the beamline experimental station, with a larger acceptance angle and thus with a higher efficiency in collecting photoelectrons, and (ii) the realization of a novel detector for the analyser. As will be seen, the implementation of this last device resulted also in an enhanced temporal resolution of real-time acquisitions that has been exploited for monitoring the CO oxidation on supported Pt nanoclusters and the graphene growth process on the Ir(111) surface.

This thesis is structured as follows. In the first chapter a brief summary of the basic principles of photoelectron spectroscopy is outlined. Then, after a description of the experimental station (ch. 3), the development of the detector for the analyser and the characteristics of the new software I wrote for managing data acquisition on the beamline are reported in ch. 4. In the remaining chapters the experiments performed with the novel experimental set-up are described. In ch. 5 we studied the chemical properties of the Pd/Ru interface by comparing the measured core level shifts of single Pd layers grown on Ru(0001) surface with those obtained from density functional theory calculations. The nucleation of Pd nanoclusters on graphite and carbon nanotubes was monitored following the evolution of the Pd $3d_{5/2}$ core level (ch. 6). We then exploited the temporal resolution of the novel experimental apparatus to follow the carbon monoxide oxidation on Pt nanoclusters deposited on a magnesium oxide thin film grown on Ag(100) surface (ch. 7). Chapter 8 is devoted to the study of several properties of graphene on the Ir(111) surface: first the graphene growth was studied, then a peculiar angular dispersion of the C $1s$ core level is reported and finally graphene was used as support for nucleation of Au, Pt and Rh nanoclusters.

Bibliography

[1] R. Feynman, *There's Plenty of Room at the Bottom*, http://www.zyvex.com/nanotech/feynman.html (1959).

[2] Human Genome Project (http://www.ornl.gov).

[3] R. Langer and J.P. Vacanti, *Tissue engineering*, Science **260** (1993), 920–926.

[4] J.V. Barth, G. Costantini, and K. Kern, *Engineering atomic and molecular nanostructures at surfaces*, Nature **437** (2005), 671–679.

[5] H.W. Kroto, J.R. Heath, S.C. O'Brien, R.F. Curl, and R.E. Smalley, C_{60}*: Buckminsterfullerene*, Nature **318** (1985), 162–163.

[6] S. Iijima, *Helical microtubules of graphitic carbon*, Nature **354** (1991), 56–58.

[7] G.A. Somorjai, Heinz Frei, and J.Y. Park, *Advancing the Frontiers in Nanocatalysis, Biointerfaces, and Renewable Energy Conversion by Innovations of Surface Techniques*, Journal of the American Chemical Society **131** (2009), 16589–16605.

[8] M. Valden, X. Lai, and D.W. Goodman, *Onset of Catalytic Activity of Gold Clusters on Titania with the Appearance of Nonmetallic Properties*, Science **281** (1998), 1647–1650.

[9] J. Millman and C.C. Halkias, *Electronic Fundamentals and Applications: For Engineers and Scientists*. McGraw-Hill Inc., US, 1976.

[10] N. Weiss, T. Crena, M. Epple, S. Rusponi, G. Baudot, S. Rohart, A. Tejeda, V. Repain, S. Rousset, P. Ohresser, F. Scheurer, P. Bencok, and H. Brune, *Uniform Magnetic Properties for an Ultrahigh-Density Lattice of Noninteracting Co Nanostructures*, Physical Review Letters **95** (2005), 157204.

[11] G. Binnig, H. Rohrer, Ch. Gerber, and E. Weibel, *Tunneling through a controllable vacuum gap*, Applied Physics Letters **40** (1982), 178–180.

Chapter 2

Fundamentals of Photoemission Spectroscopy

2.1 Introduction

The photoemission spectroscopy tecnique is based on the photoelectric effect that was explained by Albert Einstein in 1905, who for this discovery was awarded the Nobel Prize in Physics in 1921. Later on, in the 60's, Kai M. Siegbahn developed the ESCA (Electron Spectroscopy for Chemical Analysis) technique and he also won the Nobel Prize in Chemistry in 1981 "*for his contribution to the development of high-resolution electron spectroscopy*" [1]. Since then, photoelectron spectroscopy has attracted a lot of attention and was used in many fields such as heterogeneous catalysis, corrosion prevention, tribology as well as in material science and semiconductor technology.

One of the most striking properties of this technique is its *chemical sensitivity*. The photoemitted electrons have a particular binding energy which is a fingerprint of the elements present in the sample. Moreover, also different types of bonds affect electron binding energies resulting in the so called *chemical shifts* which are useful to distinguish between atoms or molecules in different chemical or structural environments. In order to form a molecule or a solid, individual atoms have to be brought together. The bond between the atoms can be formed only if this rearrangement lowers the energy of the system. This causes, in the case of molecules, the formation of atomic orbitals while, in the case of a solid, the appearance of energy bands. Since the core levels are too deep (in energy) in order to partecipate directly in the bonding, they usually retain their localized atomic character. However, even if they do not partecipate, they feel the bonding itself and

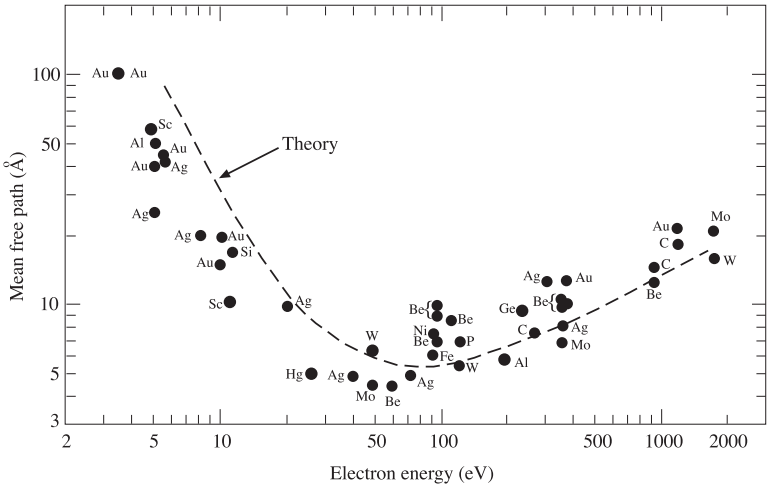

Figure 2.1: Universal curve of dependence of the inelastic mean free path on the electron kinetic energy [3].

this causes a shift in their binding energy with respect to the free atom case. By measuring these shifts it is possible to make a distinction among several chemically inequivalent atoms in a molecule or, considering a solid surface, to distinguish atoms or molecules sitting in different adsorption sites or, even more, to distinguish between surface and bulk atoms of a solid [2].

The other important property is the *surface sensitivity* of this technique. In fact, one of the main reasons to use electrons in surface science studies (in this case the photoelectrons created in the photoemission process) is the inelastic mean free path (IMFP) of the electrons in matter. This quantity is shown in fig. 2.1 as a function of the kinetic energy of the electrons, in the energy range typical of photoemission experiments. As can be noted, independently from the elemental solid considered, the mean free path curve shows a broad minimum between 50 and 100 eV kinetic energy, where it is less than 10 Å. This means that the photo-electrons that can be observed originate from the first few layers of the solid. This renders photoemission spectroscopy suitable to identify the chemical elements present on a surface and in the first substrate layers and to gain insight on the actual electronic structure of the surface itself.

The photoemission event from a solid takes place when electromagnetic radiation, i.e. the photons of a proper source, hit the solid and kick out

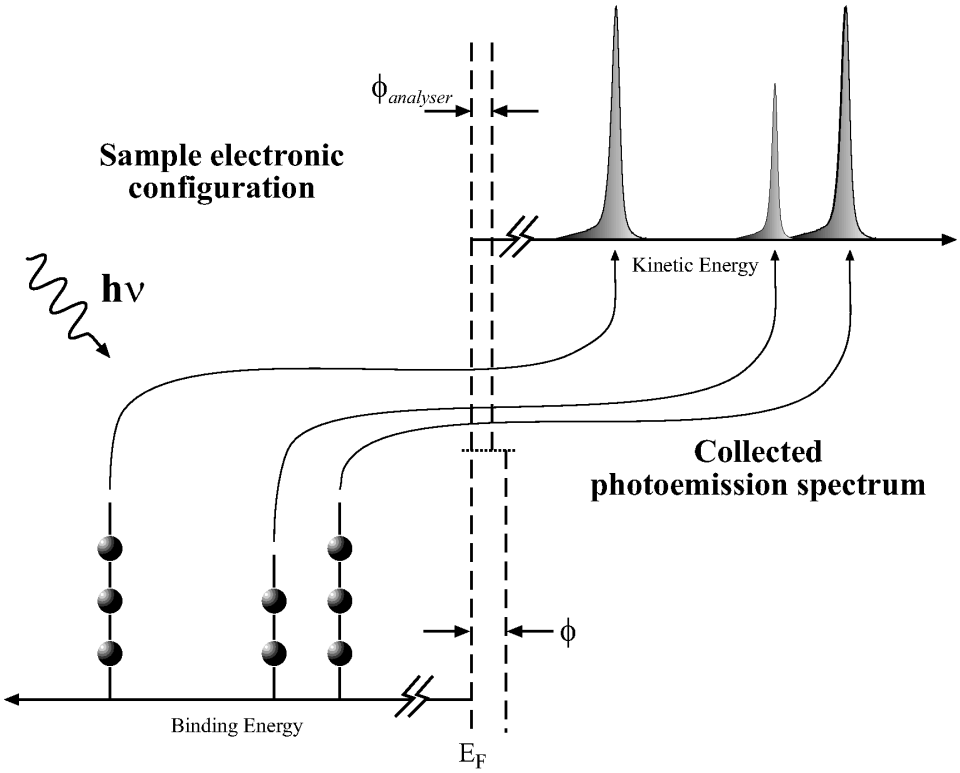

Figure 2.2: Schematic representation of the photoemission process. The small spheres on the left side indicate the occupied core levels of the sample.

electrons that are detected outside. Obviously the energy of the photons, $h\nu$, has to be high enough in order to remove the electron from a core level and let it overcome the work function ϕ of the solid. The energy distribution of the electrons detected outside reflects in a first approximation the density of states inside the solid. This is skematically shown in fig. 2.2. If we refer the binding energies, E_b^F, to the Fermi level E_F, a quantity that can be easily measured in the photoemission spectrum from a metal, than the energy with respect to the vacuum level E_b becomes:

$$E_b = E_b^F + \phi \tag{2.1}$$

The kinetic energy of the electrons in the vacuum level is given by

$$E_{kin} = h\nu - E_b^F - \phi. \tag{2.2}$$

When the photoelectrons are detected, the work function difference between the electron energy analyser and the sample needs to be taken into account:

$$E_{kin}^{meas} = E_{kin} - \phi_{analyser} = h\nu - E_b^F - \phi - (\phi_{analyser} - \phi) =$$
$$= h\nu - E_b^F - \phi_{analyser}. \tag{2.3}$$

This formula underlines how the measured binding energy depends on the analyser work function.

The trick in a photoemission experiment is therefore to use monochromatic light, i.e. electromagnetic radiation with a well defined energy, to ionize the sample and obtain, through the relations (2.2) and (2.3), once the work function ϕ is known, the binding energies of the electrons in the solid. Since these binding energies are individual for all the elements in the periodic table, and are tabulated, it is possible to detect and study in this way a well defined chemical element.

Depending on the energy of the photons used to ionize the sample, the photoemission technique can be divided into two main branches, namely UPS (Ultraviolet Photoemission Spectroscopy) and XPS (X-ray Photoemission Spectroscopy). The UPS, performed with low photon energies, deals mainly with the valence levels while in XPS the higher energy of the photons allows to ionize deeper electronic core levels. For this reason it is also called Core-Level Photoemission Spectroscopy. In the following the XPS technique will be considered.

2.2 The photoemission process

The photoemission process is the result of the transition of the electrons from initial, occupied orbitals, to free final states. In order to describe such a process, we need to consider the wave function and the energy of the system before and after the interaction with an electromagnetic radiation field with energy $h\nu$. Therefore, considering a system with N electrons, the removal of one electron from the orbital k can be sketched as follows [4]:

$$\Psi_{tot}^i(N)E_{tot}^i(N) \overset{h\nu}{\rightarrow} \Psi_{tot}^f(N,K)E_{tot}^f(N,K). \tag{2.4}$$

where $\Psi_{tot}^i(N)$ is the initial state wavefunction of the N electrons with total energy $E_{tot}^i(N)$ and $\Psi_{tot}^f(N,K)$ is the final state wavefunction of the N electrons with total energy $E_{tot}^f(N,K)$. Here K denotes not only the orbital from which the electron has been removed but also the excitation modes of the final state.

Since the energy of the system is conserved, we can write

$$E^i_{tot}(N) + h\nu = E^f_{tot}(N, K). \tag{2.5}$$

If we consider the electron in the final state as being decoupled from the remaining N-1 electrons of the system, the wave function of the final state is the sum of that of the ionic system $\Psi^f_{tot}(N-1, K)$ and that of the electron with kinetic energy E_{kin}. The energy can be expressed as

$$E^i_{tot}(N) + h\nu = E^f_{tot}(N-1, K) + E_{kin}. \tag{2.6}$$

The binding energy of the electron becomes therefore

$$E_b(K) = h\nu - E_{kin} = E^f_{tot}(N-1, K) - E^i_{tot}(N), \tag{2.7}$$

i.e. it is given by the difference between two total energies, which can be evaluated by means of theoretical calculations.

2.2.1 Photoemission cross section

The intensity of the photoemission signal is related to the photoemission cross section, defined as the probability per unit time for exciting a system from an initial state $\Psi^i(N)$ to a final state $\Psi^f(N)$ with a flux of 1 photon $\times \mathrm{cm}^{-2}\mathrm{s}^{-1}$ [4]. In order to calculate the cross section, we need to consider the Hamiltonian for a system in the presence of an external electromagnetic field. From the classical point of view, considering Maxwell's equations, a particle with charge e and velocity $\mathbf{v}$ in an electromagnetic field defined by $\mathbf{E}$ and $\mathbf{B}$ feels the Lorentz's force:

$$\mathbf{F} = e(\mathbf{E} + \frac{1}{c}\mathbf{v} \wedge \mathbf{B}). \tag{2.8}$$

The electromagnetic radiation, be defined via the scalar potential V and the vector potential $\mathbf{A}$, obeys to the following relations:

$$\mathbf{E} = -\nabla V - \frac{1}{c}\frac{\partial \mathbf{A}}{\partial t} \tag{2.9}$$

$$\mathbf{B} = \nabla \wedge \mathbf{A}. \tag{2.10}$$

The Hamiltonian of the system is therefore:

$$H = \sum_{n=1}^{3} \frac{1}{2m}\left(p_n - \frac{e}{c}A_n\right)^2 + eV + U \tag{2.11}$$

where m is the electron mass, p_n are the components of the electron momentum, and U is an external potential. The Hamiltonian operator can be written as:

$$\hat{H} = \frac{\hat{\mathbf{p}}^2}{2m} - \frac{e}{2mc}(\hat{\mathbf{p}}\hat{\mathbf{A}} + \hat{\mathbf{A}}\hat{\mathbf{p}}) + \frac{e^2}{2mc^2}\hat{\mathbf{A}}^2 + e\hat{V} + \hat{U} \tag{2.12}$$

or using the commutator $[\hat{\mathbf{p}}, \hat{\mathbf{A}}] = -i\hbar\nabla\hat{\mathbf{A}}$:

$$\hat{H} = \frac{\hat{\mathbf{p}}^2}{2m} - \frac{e}{2mc}(2\hat{\mathbf{A}}\hat{\mathbf{p}} - i\hbar\nabla\hat{\mathbf{A}}) + \frac{e^2}{2mc^2}\hat{\mathbf{A}}^2 + e\hat{V} + \hat{U}. \tag{2.13}$$

The term $e^2/2mc^2\hat{\mathbf{A}}^2$ is always *small* and can be neglected. Moreover, within the *Coulomb gauge*, the scalar potential $V = 0$. Furthermore, considering a propagating *transverse wave*, the term $\nabla\hat{\mathbf{A}} = 0$ and the Hamiltonian becomes

$$\hat{H} = \frac{\hat{\mathbf{p}}^2}{2m} + \hat{U} - \frac{e}{mc}\hat{\mathbf{A}}\hat{\mathbf{p}}. \tag{2.14}$$

The first two terms represent the Hamiltonian $\hat{\mathbf{H}}_0$ of the unperturbated system while the last term represents the perturbation Hamiltonian

$$\hat{H}' = -\frac{e}{mc}\hat{\mathbf{A}}\hat{\mathbf{p}}. \tag{2.15}$$

Since the interaction of the photons with charged particles is a time dependent process, we make use of the time dependent perturbation theory for solving this problem. The transition rate between the initial state $\Psi^i(N)$ and the final state $\Psi^f(N)$ is given by the *Fermi's golden rule* [5]:

$$\frac{d\omega'}{dt} \propto | < \Psi^f(N)|\hat{H}'(N)|\Psi^i(N) > |^2\delta(E_f - E_i - h\nu) \tag{2.16}$$

or, considering eq. (2.15),

$$\frac{d\omega'}{dt} \propto | < \Psi^f(N)| \sum_{i=1}^{N} \hat{\mathbf{A}}(\mathbf{r}_i)\hat{\mathbf{p}}_i|\Psi^i(N) > |^2\delta(E_f - E_i - h\nu). \tag{2.17}$$

The incident radiation can be described as a superposition of plane waves with angular frequency ω, photon wavevector $\mathbf{k}'$ directed along the propagation direction, $|\mathbf{k}'|=2\pi/\lambda = \omega/c$, and amplitude εA_0, with ε a unit vector parallel to the polarization:

$$\mathbf{A}(\mathbf{r}, t) = \varepsilon A_0 e^{i(\mathbf{k}'\mathbf{r} - \omega t)}. \tag{2.18}$$

From this, the square of the matrix element $M_{f\leftarrow i}$ of eq. (2.17), that defines the differential cross section $d\sigma/d\Omega$, becomes:

$$|M_{f\leftarrow i}|^2 \;=\; \hbar^2 A_0^2| < \Psi^f(N)| \sum_{i=1}^{N} e^{i\mathbf{k'}\mathbf{r}_i} \varepsilon \nabla_i |\Psi^i(N) > |^2. \tag{2.19}$$

Assuming electron kinetic energies lower than 1 keV, the wavelenght λ is much longer than typical atomic distances; for this reason the exponential can be approximated to

$$e^{i\mathbf{k'}\mathbf{r}} = 1 + i\mathbf{k'}\mathbf{r} - \frac{1}{2}(\mathbf{k'}\mathbf{r})^2 \approx 1, \tag{2.20}$$

which represents the so-called *dipole-approximation*. Eq. (2.19) assumes the form

$$|M_{f\leftarrow i}|^2 \;=\; \hbar^2 A_0^2 |\varepsilon < \Psi^f(N)| \sum_{i=1}^{N} \nabla_i |\Psi^i(N) > |^2. \tag{2.21}$$

The differential photoionization cross section is given by

$$\frac{d\sigma}{d\Omega} = C \left(\frac{1}{h\nu}\right) |\varepsilon < \Psi^f(N)| \sum_{i=1}^{N} \nabla_i |\Psi^i(N) > |^2. \tag{2.22}$$

As an example, the graph in fig. 2.3 shows how the photoemission cross section for $3d$ and $4f$ Ir core levels varies as a function of the incident photon energy. Since Ir $4f$ presents a larger cross-section, we decided to measure this latter Ir core level during the experiments on the graphene/Ir(111) system reported in ch. 8.

Sudden approximation

In order to determine the transition rate one should know the many-body wave functions of the initial and final states. The most often used approximation for further treatment of this problem is to work in a single-particle picture. In this way, the wave function of the initial/final state can be splitted into two contributions, namely a one-electron and a (N-1) electron wave function. The initial, ground state wave function is therefore

$$\Psi^i(N) = \psi_k(1)\Psi_R(N-1), \tag{2.23}$$

while the final state is

$$\Psi^f(N) = \phi_f(1)\Phi_{k,j}(N-1), \tag{2.24}$$

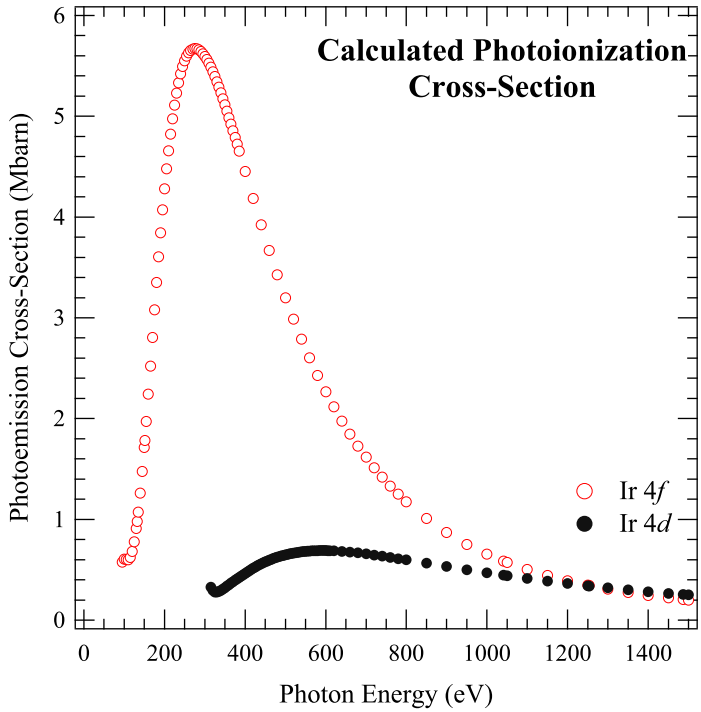

Figure 2.3: Calculated photoemission cross-section for Ir $4d$ and Ir $4f$ core levels as a function of the energy of the incident photons [6].

where $\psi_k(1)$ is the single-particle wave-function of the electron to be removed from orbital k, $\Psi_R(N-1)$ is the anti-symmetrized determinant of the $N-1$ electrons in the initial state, $\phi_f(1)$ is the wave-function of the free electron and $\Phi_{k,j}(N-1)$ are the possible states of the ionic system that has one electron missing in orbital k.

A further assumption is the so-called *sudden approximation* where the transition from the initial to the final state is considered to be fast compared to the relaxation times of the $(N-1)$ electrons [7]. The N electron matrix elements present in eq. (2.22) split up into a single and many-particle part and the differential cross section becomes

$$\frac{d\sigma}{d\Omega} \propto | < \phi_f(1)|\varepsilon\mathbf{r}|\psi_k(1) >< \Phi_{k,j}(N-1)|\Psi_R(N-1) > |^2. \qquad (2.25)$$

2.2.2 Electron Binding energy

Free atoms

Keeping in mind eq. (2.25), it is possible to discuss the binding energy position of a core-level photoemission process taking place on a free atom. If we consider $< \Phi_{k,j}(N-1)|\Psi_R(N-1) >= \delta_{k,0}$, the matrix element turns into the single-particle picture

$$\frac{d\sigma}{d\Omega} \propto | < \phi_f(1)|\varepsilon \mathbf{r}|\psi_k(1) > |^2. \tag{2.26}$$

which is the form most frequently used to perform cross sections calculations. In this case the (N-1) electrons in the ionic state do not feel the presence of the hole, they remain in the same configuration and with the same energy as in the non-ionized system i.e. they are *frozen* in their original distribution: this is the assumption of Koopmans' theorem [8]. This means that the electron binding energy, as calculated with eq. (2.7) within the Hartree-Fock theory for total energy calculations, simply equals the negative orbital energy ϵ_k

$$E_b(K) = -\epsilon_k. \tag{2.27}$$

When considering a real system, the first correction for the binding energy which has to be taken into account is the term ΔE_c due to *electron correlation effects*, which is not considered in the Hartree-Fock approximation; secondly, the effect of the presence of the hole must be included. In fact, since the remaining electrons do feel the ionization, they reorganize themselves to the new potential. This last effect is called *intra-atomic relaxation* and it depends on the kinetic energy of the emitted electron. In the case of low kinetic energy, we are in the *adiabatic* limit in which the (N-1) electron system is left fully relaxed, i.e. in the ionic state with the lowest energy. In this case the ejected electron picks up the full relaxation energy ϵ_{rel} thus increasing its kinetic energy.

The photoemission spectrum is qualitatively similar to that calculated in the frozen orbital approximation but now the binding energy of the photoelectron becomes

$$E_b(K) = -\epsilon_k + \Delta E_c - \epsilon_{rel} \tag{2.28}$$

A large ϵ_{rel} implies that the initial and final state wave functions are very different.

The adiabatic approximation is valid in the time regime of $10^{-15} - -10^{-16}$ s. On the other hand, when we consider higher photon energies, i.e. higher kinetic energies of the emitted electrons, the time scale of the

photoemission process falls in the region of 10^{-17} s and we can proceed within the sudden approximation framework. This means that the photoemission process is faster than the relaxation and the (N-1) electron system is left, with a certain probability, in an excited state. Therefore in eq. (2.25), if we project $\Psi_R(N-1)$ onto the eigenstates of the ionic system there will be overlap not only with the ground state but also with some of the excited states with j not equal to zero. This reduces the energy given to the photoelectron and shake-up or shake-off satellites appear in the spectrum with kinetic energy lower than that of the fully relaxed, adiabatic *main line*. All the structures present in a spectrum, coming from a well defined excitation, are related to the binding energy of the Koopmans' theorem through the following "sum rule"

$$-\epsilon_k = \frac{\sum_p I_p (E_b)_p}{\sum_p I_p} \tag{2.29}$$

where I_p is the intensitiy of the peak at binding energy $(E_b)_p$. This is summarized in fig. 2.4.

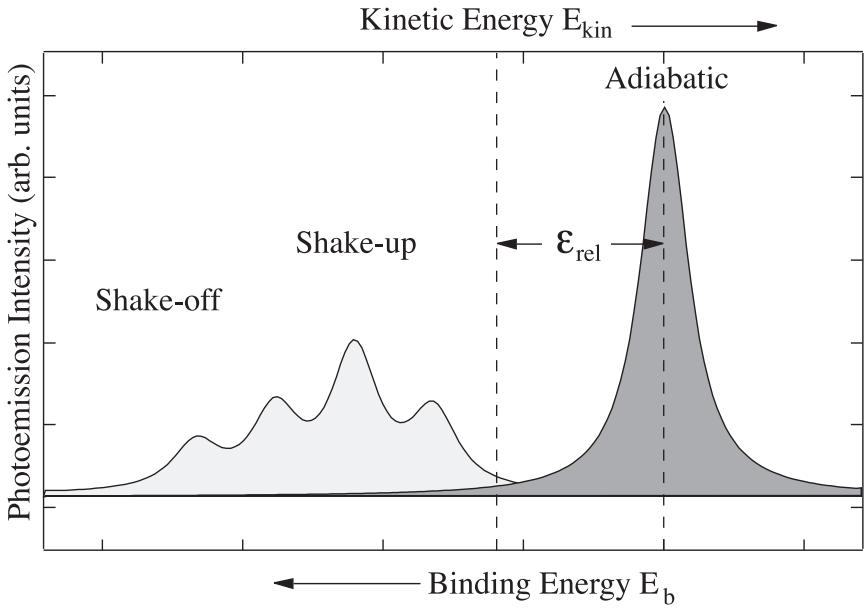

Figure 2.4: Schematic representation of an XPS spectrum. The main line is the adiabatic peak while the other, smaller components, are the shake-up and shake-off transitions. The total area under the curves corresponds to the intensity calculated in the frozen-orbital approximation.

Let's consider again eq. (2.26) and decompose the initial and final wave functions $\psi_k(1)$ and $\phi_f(1)$ into a radial and an angular part (the spin part is neglected)

$$\psi_k(1) = U_{nl}(r)Y_{lm}(\theta, \varphi), \tag{2.30}$$

$$\phi_f(1) = U_{l'}(r)Y_{l'm'}(\theta, \varphi), \tag{2.31}$$

where l, l' are the initial and final orbital quantum numbers, m, m' are the initial and final magnetic quantum numbers and n is the initial principle quantum number. The evaluation of the angular integrals in eq. (2.26) leads to the well known selection rules

$$l' = l \pm 1 \qquad m' = m, m \pm 1. \tag{2.32}$$

Therefore for a given l the final state will be a coherent sum of the two angular momentum states $l + 1$ and $l - 1$, generally called *channel up* and *channel down*. In general it is found that, for photon energies well above threshold, the channel up is the most probable. Within this framework, the actual cross section is contained in the radial integrals that are also influenced by the n and l values.

Metals

In the case of an atom in a solid metal surface, the presence of all the nuclei should be considered in eq. (2.4) but, using the Born-Oppenheimer approximation, it is possible to decouple the Hamiltonian of the nuclei from that of the N electrons. Therefore eq. (2.7) can be used again to estimate the core level binding energies.

In a metal, the valence electrons available in the conduction band are very mobile and therefore can flow to the site of the core-hole, screening in this way its positive charge. This means that the core ionized atom is a neutral atom with a core hole, meanwhile in the above described free atom case the final state is an ionic state.

In the adiabatic limit, the full energy coming from the valence electrons is transfered to the emitted electron. Thus, its kinetic energy is higher than from the atom in its free state, by an amount called *interatomic relaxation* energy, denoted here with ϵ_{rel}^{int}:

$$E_{kin} = h\nu - \epsilon_k + \epsilon_{rel} + \epsilon_{rel}^{int}. \tag{2.33}$$

In the sudden approximation we would expect to see well separated shake-up and shake-off related features in the spectrum as explained before for the free atom case. This actually does not happen for the atom in the solid because its excited states now form a continuum. In this case electron-hole pairs around the Fermi level are excited. These low energy excitations give rise to a low kinetic energy tail in the observed photoemission peak. This effect was firstly experimentally observed on many metals by Hüfner *et al.* [9, 10]. The most important conclusion of these studies was that the transition metals exibit larger asymmetry than noble metals. The reason of this is that the transition metals have higher density of states at the Fermi level which results in higher probability of electron-hole pair excitation.

2.3 Photoemission spectra analysis

2.3.1 Photoemission spectral contributions

The shape of an XPS spectrum is much more complicated than that described in the previous section. There are many contributions that one has to take into account in order to explain the spectral features and their line profile. All the losses explained up to now take place in the photoemission process itself and for this reason they are called *intrinsic losses*. There is however another possibility in a solid, i.e. to have *extrinsic losses* which can be incurred by the emitted electrons during their transport from the emitting atom to the surface. Their effect on the spectral line profile adds to that of the intrinsic losses and, unfortunately, a clear separation between these two types of losses is difficult to achieve, because the time that the photoelectron needs to reach the surface is not long compared to photoemission process itself and the two effects can interfere coherently. Therefore care has to be taken when applying the sum rule of eq. (2.29) in the case of core level photoemission from solids.

One of the processes which have to be taken into account in the case of solids is the excitation of surface or bulk *plasmons*, that are collective oscillations of the electrons in valence band. The corresponding satellites will have lower kinetic energy than the adiabatic peak (with differences that are multiples of the plasmon energy).

Another phenomenon which results in strong modification of the core level spectra line shape is the *vibrational motion* of the ions around their lattice points. This effect, actually, is more evident in the case of vibrational excitations caused by electronic transitions in molecules. In this case the removal of a core electron modifies substantially the electronic structure of

the emitting atom thus influencing also the bond equilibrium positions and the potential energy curve of the molecule. Since the photoemission process is much faster than the nuclear motion, the final state is created in the initial state geometry, i.e. the nuclei can be considered frozen, according to the Born-Oppenheimer approximation. If the difference in geometry or in the shape of the potential energy curves of the initial and final state is large, different vibrational modes will be excited in the final state with the distribution of the vibrational states being governed by the Franck-Condon principle.

This reasoning can be extended to the lattice vibration is a solid, where *phonon* excitations can occur during the photoemission process, producing either a core level shift or a line broadening, depending on the energy of the vibrationally adiabatic transition.

Another phenomenon that can induce phonon excitations is the recoil of the core ionized atom because of the emission of the photoelectron. This is due to the requirement of momentum conservation in the XPS event. It is quite obvious that the recoil energy is bigger for light atoms than for heavier elements. In any case it is always quite small, as demonstrated by the fact that its maximum value for Li is 0.1 eV and 0.01 eV for Rb using a photon energy of 1486 eV obtained with a conventional X-ray source.

2.3.2 Analysis of the photoemission line-shape

In order to extract quantitative information from a photoemission spectrum we need to make a decomposition, i.e. to perform a fit of the measured spectrum with a model line of appropriate line shape and broadening. In this section, only the shape of the main line of the photoemission spectrum will be considered. This line shape can be decomposed into several contributions, the most important being the natural lifetime and the gaussian broadening.

Life-time broadening

The dependance of E_b from the energy of the ionic system causes the broadening of the photoemission peaks because of the Heisenberg uncertainty principle

$$\Delta E \Delta t \geq \hbar/2 \tag{2.34}$$

with $\hbar = 6.6 \times 10^{-16}$ (eV·s). This gives a line width broadening of the order of $\hbar/\tau$ where τ is the lifetime of the core-hole in seconds. The core-hole decay can be either radiative and non radiative [11]. These processes involve some of the orbitals that have a lower binding energy than the excited core

level. The influence of the chemical surrounding on the decay rate is usually quite small and this turns in that the intrinsic width is essentially an atomic property.

For a typical core-hole lifetime of the of the order of 10^{-15} s the peak will have a natural width of 100–200 meV. This broadening, always present in a photoemission spectrum, is described with a Lorentzian distribution (eq. (2.35)), whose full width at half maximum (FWHM) is denoted with Γ and E_0 is the position for the maximum intensity I_0

$$I_{Lor}(E_{kin}) = I_0 \frac{\frac{\Gamma}{2\pi}}{(E_{kin} - E_0)^2 + \frac{\Gamma^2}{4}}. \tag{2.35}$$

Gaussian broadening

The Gaussian broadening of a core level photoemission peak is mainly given by three contributions, namely the experimental energy resolution, the vibrational and inhomogeneous broadening.

The contribution of the *experimental energy resolution* is due to the fact that the photon source has a finite line width determined by the monochromator, and the electron energy analyser has a certain resolving power. During the years this instrumentation has improved quite a lot and the increased energy resolution allows now to distinguish very fine structures in the spectra.

The *vibrational broadening*, in molecules or solids, is given by the excitation of low energy vibrational modes in the final state as explained in sect. 2.3.1. For solids, the extrinsic phonons produce secondary electrons while the intrinsic ones induce a phonon broadening of the photoemission peaks which can, in most cases, be described by a gaussian distribution [12].

The *inhomogeneous broadening* is due to the presence in the spectrum of unresolved chemical or structural shifted components.
These three effects are represented by a gaussian distribution with FWHM, σ,

$$I_{Gaus}(E_{kin}) = I_0 \exp\left(- \frac{(E_{kin} - E_0)^2}{2\sigma^2} \right). \tag{2.36}$$

Doniach-Ŝunjić line-shape

Summarizing the arguments exposed so far, it can be said that, in the case of a metal, the shape of the peak is the convolution of a Lorentzian lifetime broadening, of a Gaussian broadening plus an asymmetry due to the

creation of electron-hole pairs at the Fermi level. The most commonly used line shape in analyzing photoemission spectra from metals is the *D-$\hat{S}$* line shape calculated by Doniach and Ŝunjić [13]. It is obtained by making the convolution of a singularity function

$$f(E) \propto \frac{1}{(E_0 - E)^{1-\alpha}} \tag{2.37}$$

representing the core-hole excitation in metals for a constant density of states around the Fermi level at $T = 0$ K, with the Lorentzian broadening of eq. (2.35). The calculated intensity is:

$$I_{DS}(E_{kin}) = I_0 \frac{\Gamma_E(1-\alpha)}{\left((E_0 - E_{kin})^2 + \frac{\Gamma^2}{4}\right)^{\frac{(1-\alpha)}{2}}} \xi(E_{kin}), \tag{2.38}$$

with

$$\xi(E_{kin}) = cos\left[\frac{1}{2}\pi\alpha + (1-\alpha)tan^{-1}\left(2\frac{(E_0 - E_{kin}}{\Gamma}\right)\right] \tag{2.39}$$

where Γ_E is the so-called Γ *function* defined as

$$\Gamma_E(x) = \int_0^\infty t^{x-1}e^{-t}dt, \tag{2.40}$$

α the asymmetry parameter and Γ the FWHM of the lifetime broadening.

The $T = 0$ K approximation implies that there are no electron-hole pair excitations in the neutral ground state. At finite temperature the core-level should exibit additional broadening due to thermal excitations of the conduction electrons. However, this effect is quite small with respect to the phonon or lifetime broadening and is well approximated with an additional gaussian broadening.

2.4 Core-level shifts

In this section, the origin of chemical and surface core level shifts will be briefly reviewed. These changes of the core levels' binding energy play a fundamental role in photoemission data analysis. In particular the comparison of experimentally measured shifts with the values obtained from theoretical calculations can lead to valuable results. Among the experiments described in the present thesis, this approach has been successfully exploited in particular for the surface core level shift analysis on the Pd/Ru(0001) system

presented in ch. 5, for the study on palladium nucleation on graphite and carbon nanotubes reported in ch. 6 and for the investigations on the graphene/Ir(111) system outlined in ch. 8.

2.4.1 Chemical shifts

So far we have considered the effects on the core level line shape due to different kinds of excitations taking place in the photoemission process. Another important aspect that has to be taken into account in photoemission is that the core levels of an atom are affected by the kind of chemical bond the atom is involved. This means that the measured core level binding energy depends also on the chemical surroundings of the emitting atom. The binding energy difference of a certain core level in two atoms of the same element but with different chemical surroundings is called *chemical shift*.

The demonstration that the high resolution core level photoelectron spectroscopy technique is a sensitive probe of the chemical environment of the emitting atom was given by Siegbahn and co-workers studying the oxidation of copper [14]. They found that the $1s$ core level of copper was shifted towards higher binding energy by 4.4 eV on going from metallic copper to copper oxide. This is because the exact peak position of the core level lines is determined by the oxidation level of the emitting atom and the electric field generated by adjacent atoms [15]. In general, when the emitting atom is bound with a more electronegative ligand, i.e. it undergoes a withdrawal of electrons, it is more difficult to excite its core level electrons that for this reason appear at higher binding energy in the spectra. This is a quite general behaviour that can be observed on many metal atoms where changes in the oxidation state of the metal are usually accompanied by binding energy shifts towards higher binding energies.

The chemical shifts span an energy range from a few meV to several eV, thus enabling an identification of binding partners and a distinction of single or double covalent bonds. An example of the chemical shift is shown in fig. 2.5 for the ethyl-trifluoroacetate $C_4F_3O_2H_5$ molecule for which the C $1s$ photoemission signal shows four well separated components.

In order to understand the origin of the chemical shift, let's consider again eq. (2.7) for the calculation of the binding energy of a core electron. The chemical shift is given by:

$$\begin{aligned} \Delta E_b &= E^f_{tot,A}(N-1) - E^i_{tot,A}(N) - E^f_{tot,B}(N-1) - E^i_{tot,B}(N) = \\ &= \Delta^f_{A,B} - \Delta^i_{A,B}. \end{aligned} \tag{2.41}$$

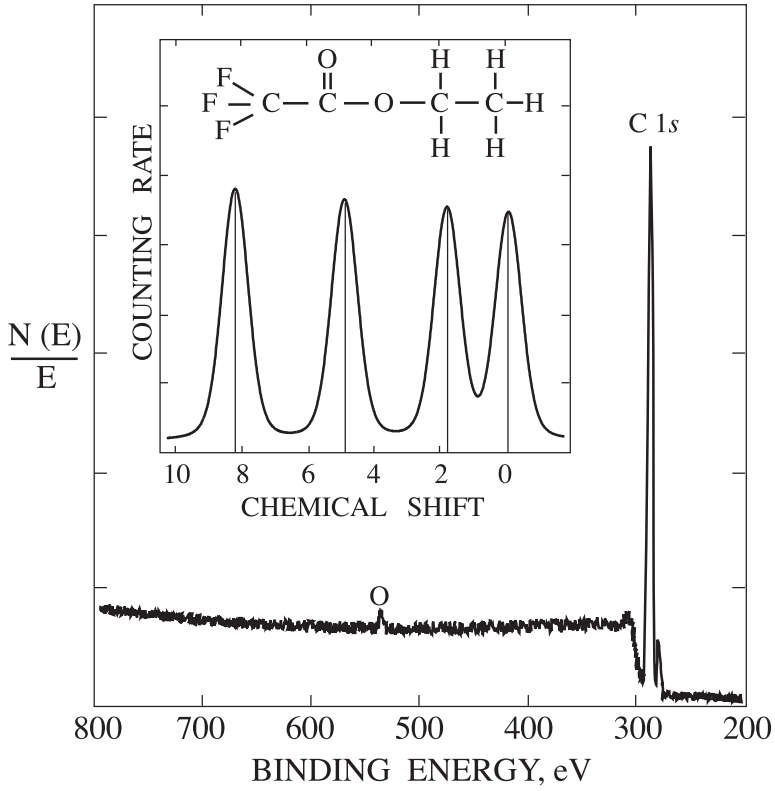

Figure 2.5: Photoemission spectra from $C_4F_3O_2H_5$ molecule. The $C1s$ peak shows four different components related to the carbon atoms bound to different ligands.

where A and B denote the system A and system B respectively and $\Delta_{A,B}$ the total energy difference between the two systems. From eq. (2.41) it is clear that the chemical shift is not just an initial state effect but, to achieve a complete description of such shifts, one has to take into account also final state contributions.

2.4.2 Surface Core Level Shifts

A special type of binding energy shift is the one arising between the bulk and the surface atoms of a solid. This shift, named *surface core level shift* (SCLS), is caused by the structural environment modification of the atoms at the surface with respect to the bulk. The SCLSs are usually small compared to the chemical shifts occuring in compounds, since the electronic

modifications are not as strong, and therefore the detection of these shifts is possible only by means of the high energy resolution photoelectron spectroscopy measurements.

The first experimental evidence of such a shift, explained in terms of SCLS, was obtained by Citrin and co-workers in 1978 measuring the Au $4f_{7/2}$ core level of a polycristalline Au surface [16]. After that experiment a number of measurements on other systems have been performed trying to understand the origin of SCLSs and to predict their magnitude on the basis of theoretical calculations. Moreover, such experiments have pointed out that SCLSs appear not only in the case of clean surfaces but also on adsorbate covered ones. In fact, in presence of an adsorbate, the atoms at the surface change their chemical surrounding and this changes also the SCLS.

It is possible to give a qualitative explanation for the SCLSs of the transition metals within a framework outlined in ref. [17] which considers only initial state effects. In order to do this, we need to understand how the shifts of the core levels are related to those of the valence d levels. In this model, by approximating the d orbitals by a spherical shell with radius R and containing N_d electrons, the Hartree potential energy inside the sphere is given by

$$V = e^2 \frac{N_d}{R}. \tag{2.42}$$

Any change in N_d is reflected in the potential through the eq. (2.42): this potential change is felt by the core levels, which are inside the sphere, and their energy shifts accordingly. Moreover, in the tight binding theory framework, a change in the potential of the surface atoms is reflected in a shift of the same amount of the valence band centroid.

With all these information we can now make a qualitative picture of the SCLS whose schematic representation is shown in fig. 2.6 for a d band less and more than half full respectively [18]. Here the d band of a transition metal is approximated with a symmetric distribution around a central value. The difference between surface and bulk atoms is that the former have a narrower distribution of the band due to their lower coordination. Therefore a charge rearrangement is needed in order to mantain a common Fermi level between the bulk and surface atoms, i.e. electrons will flow from the bulk to the surface in the case of a band more than half full and the opposit happens in the case of a band less than half full. This gives rise to an electrostatic potential difference $\delta\epsilon_d$ that shifts rigidly both the valence band centroid and the deep core levels of the surface atoms. This shift is towards higher (lower) binding energies for a d band less (more) than half full.

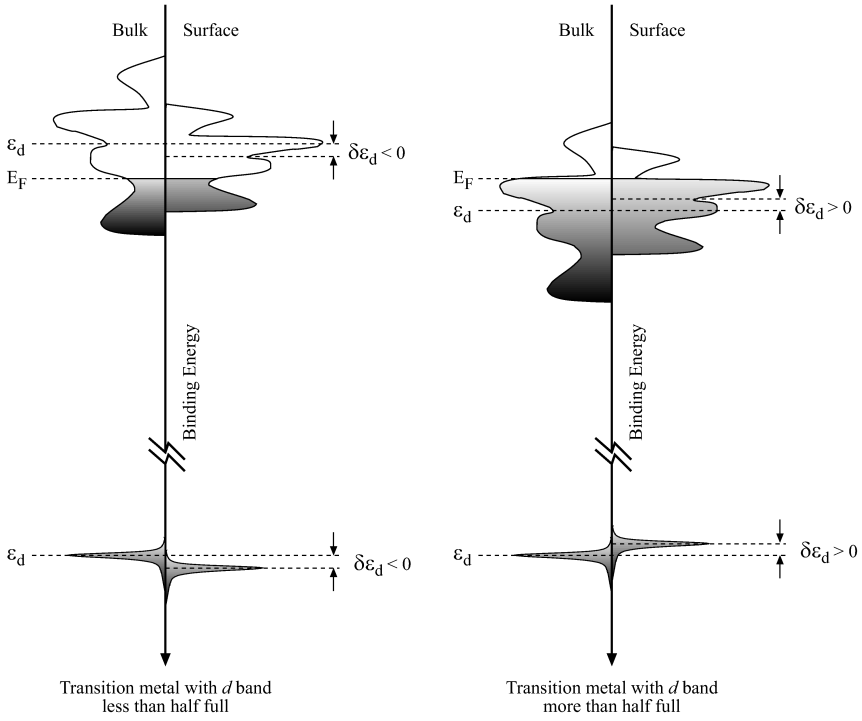

Figure 2.6: Schematic representation of the SCLS for transition metals caused by the *d*-band narrowing and the consequent electrostatic shift. On the left the *d*-band is less than half full while on the right it is more than half full.

From all the above considerations it comes out that the SCLSs of a transition metal series should go hand in hand with the occupation number of the valence *d* band. Moreover, the more the band narrows, the stronger should be the SCLS.

The explanation exposed so far is named *microscopic approach* and considers the SCLSs just within the initial state approximation and does not take into account the contribution of final state effects due to the screening of the core-hole, which can be quite large. The first theoretical approach that was used in this sense is the so-called *thermodynamic approach* [19, 20]. The basic assumption is that the core ionized state is an electronically completely screened final state where the conduction electrons have attained a fully relaxed configuration in presence of the core-hole. Moreover, a further approximation is made, the so called *equivalent core approximation* (ECA) to describe the system with the core-hole. Within this approximation the

core electrons are assumed to be located entirely inside the valence electron spatial distribution. In this way it is reasonable to assume that the removal of a core electron is felt by the valence electrons as a change in the nuclear charge from Z to Z+1. Therefore the properties of the core ionized atom are the same as the next element in the periodic table [21]. With these assumptions, the SCLS results from the difference between the total energy of a Z metal with a Z+1 impurity at the surface and the energy of a Z metal with a Z+1 impurity in the bulk.

The thermodinamic approach is quite general: it can be applied to all the elements and, most important, takes into account for the screening effects.

2.5 Photoelectron diffraction

The intensity of a core level photoemission peak at a certain photon energy is proportional to the integral over the solid acceptance angle of the electron detection system, to the photoelectric cross section defined in sec 2.2.1 and to the number of emitters. In the case of photoemission from solids there are however other effects that determine such intensity like the elastic and inelastic scattering events that take place during the transport of the photoelectrons from the emitters to the vacuum. The latter cause a lowering of the photoemission signal when the emitters are found in deeper layers, due to the inelastic mean free path, while the former, called photoelectron diffraction effects, can either give a lowering or an increase of the photoemission signal that depends on the geometry around the emitter, the atomic species involved in the process, the photoelectron kinetic energy and the detection angle. A schematic picture of the photoelectron diffraction effect is shown in fig. 2.7. The photoemission process, including the elastic and inelastic scattering effects, is usually described using the *three step model* in which the photon absorption, the transport of the photoelectron from the emitter to the surface and its propagation from the surface to the detector, are treated separately.

- *Step I : Photoemission*
  The photoemission process has already been extensively treated in sect. 2.2. In this section is worth noting that the cross section depends on the angle θ_p between the polarization vector of the incident radiation and the emission direction. In order to avoid such atomic effects on the photoemission intensity, the photoelectron diffraction experimets are performed by keeping the photon incidence and electron analysis directions constant. Therefore the photoelectron diffraction

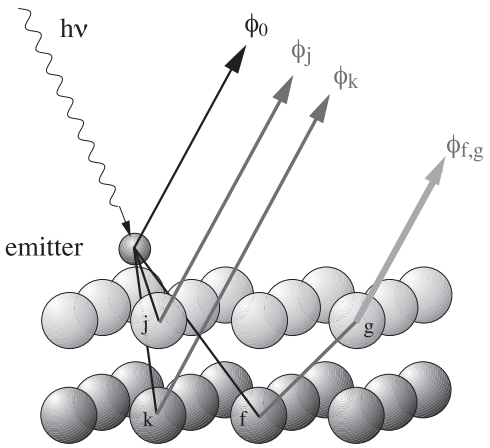

Figure 2.7: Schematic representation of the photoelectron diffraction effect. The primary wave ϕ_0 is generated by the photoemission process of the atom adsorbed on top of the surface of a crystal. The secondary waves ϕ_j, ϕ_k are the singly scattered waves by the atoms j and k of the surface and subsurface layers respectively. A double scattered wave $\phi_{f,g}$ is also shown.

pattern is obtained by rotating the sample or changing the photon energy at constant θ_p. In this way the measured intensity is just due to the interference between direct and scattered waves. By using this data collection mode the so-called *Constant Initial State* (CIS) spectra are obtained.

- *Step II : Scattering from atoms*
  After the photoemitted electron leaves the emitter, it undergoes scattering with the surrounding atoms. In the *single scattering approximation* [22] the final state wave function $\phi(\mathbf{r}, \mathbf{k})$ is a linear superposition of the direct wave $\phi_0(\mathbf{r}, \mathbf{k})$ with all the waves $\phi_j(\mathbf{r}, \mathbf{r}_j \rightarrow \mathbf{k})$ singly scattered at $\mathbf{r}_j$ and emerging in the direction $\mathbf{k}$. In a real system, on the other hand, the emitted photoelectron usually does not suffer only for one scattering event and therefore multiple scattering must be considered; the only possibility to do that is, once more, to make use of numerical calculations. In order to perform reliable multiple scattering calculations several computational approaches have been developed: usually the Green function of the total system is expanded into a series over all scattering pathways from the emitter to the detector but further approximations are needed in order to reduce the

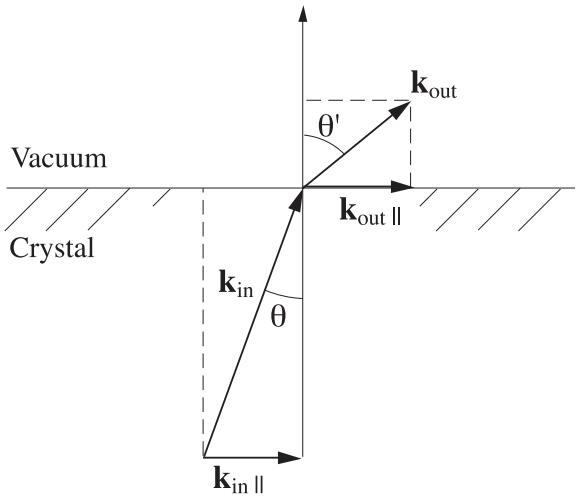

Figure 2.8: Electron refraction at the surface potential barrier.

computational time [23].

- *Step III: Surface refraction*
  The last step of the model considered is the transmission of the electron through the surface to reach the vacuum. This implies that the electron must overcome the potential barrier at the surface, that can be approximated to a sharp step whose height is the *inner potential* V_0. This lowers its kinetic energy in the vacuum by V_0. As a consequence refraction takes place at the surface barrier of the solid. The conservation of the momentum of the photoelectron parallel to the surface $\mathbf{k}_{\|}$ has to be fulfilled when the wave in the solid matches to the free electron wave in the vacuum. This defines the change in $k_{\perp}$ and therefore the change of the angle respect to the surface normal, between the electron trajectory in the solid and in vacuum. This is shown in fig. 2.8. The angle θ' is given by:

$$\sin\theta' = \sin\theta\sqrt{\frac{(E' + V_0)}{E'}}. \tag{2.43}$$

  The value of the inner potential is given roughly by the sum of the work function and the valence band width. It can assume values from 5 to 20 eV. In a scattering simulation it is usually treated as adjustable parameter.

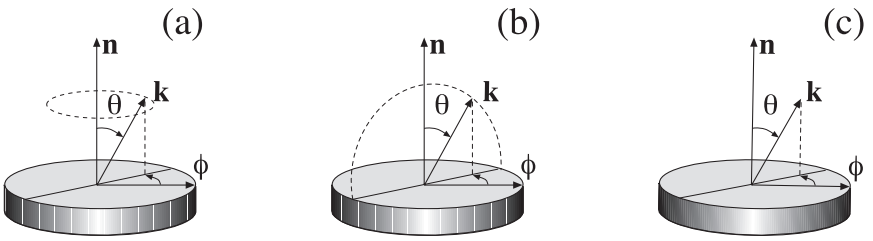

Figure 2.9: Three different modes to perform photoelectron diffraction: (a) azimuthal scan, (b) polar scan and (c) photon energy scan (varying the modulus of the **k** vector).

We can summarize the basic elements of this technique saying that (i) as the photoelectron undergoes the scattering process, it collects information on the local surroundings of the emitting atom and that (ii), from a practical point of view, in a photoelectron diffraction experiment the final diffraction intensity can be measured as a function of the azimuthal emission angle, of the polar angle or as a function of the photon energy at fixed emission angles, as shown in fig. 2.9. The collected data contain chemical and structural information on the investigated surface. Moreover, because of the inelastic effects, this technique is capable of *local* structural characterization. Furthermore, since different atoms hitted by the incident light act as time uncorrelated photoemitters and their intensities add-up incoherently, there is no need to have long range order to exploit the photoelectron diffraction technique. Finally, in order to extract the relevant information, because of the complexity of the underlying physical phenomena, the measured interference pattern has to be compared with multiple scattering calculations performed for a model structure.

A particular class of photoelectron diffraction measurements deserves attention for the immediacy of its results. Fig. 2.10 shows a typical behaviour of the so-called *scattering factor* (which determines the amplitude of the scattered wave) as a function of the emission angle. The most notable feature is the strong peak at 0° which dominates at all kinetic energies and becomes narrower at higher kinetic energies. It is the so-called *forward scattering* peak. On the contrary, at the opposite angle, 180°, in the *back scattering* geometry, the intensity is very small at 1100 eV and grows when the kinetic energy decreases. A forward scattering geometry is found when

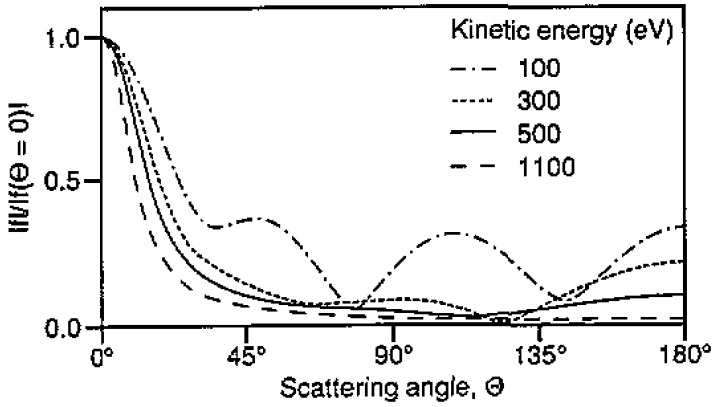

Figure 2.10: Modulus of the electron scattering factor of a copper atom as a function of the scattering angle and the electron energy [24].

an atom is sitting in line between the electron detector and the emitter [24]. In this particular direction, at sufficently high kinetic energy, the photoemission intensity increases because of the forward scattering enhancement, also called *forward focusing*. This is due not only to the strong forward scattering but also to the small scattering phase shift at high kinetic energy, otherwise the interference could also be destructive. A sketch of this effect is shown in fig. 2.11. Forward scattering photoelectron diffraction has been

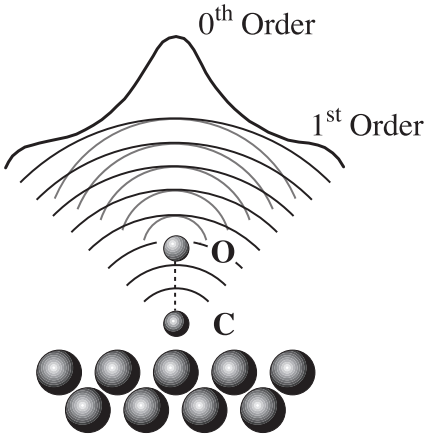

Figure 2.11: CO molecule adsorbed on a surface, in the on-top adsorption site. C is the emitter while O is the scatterer.

extensively used to determine the orientation of molecules adsorbed on surfaces by performing angular scans, either polar and azimuthal. Moreover, azimuthal scans at a grazing emission angle can give valuable informations on the symmetry of the adsorption site [24].

Bibliography

[1] K.M. Siegbahn, *Electron spectroscopy for atoms, molecules and condensed matter* in *Nobel Lectures in Physics 1981-1990* (G. Ekspong, ed.), World Scientific Publishing Company, Singapore, 1993.

[2] N. Mårtensson and A. Nilsson, *High-Resolution Core-Level Photoelectron Spectroscopy of Surfaces and Adsorbates* in *Applications of Synchrotron Radiation* (W. Eberhardt, ed.), Springer-Verlag, Berlin, Heidelberg, 1995.

[3] A. Zangwill, *Physics at surfaces*. Cambridge University Press, 1988.

[4] C.S. Fadley, *Basic Concepts of X-ray Photoelectron Spectroscopy* in *Electron Spectroscopy. Theory, Techniques, and Applications* (C.R. Brundle and A.D. Baker, eds.), vol. II, 1–156, Pergamon Press, 1978.

[5] A. Messiah, *Quantum Mechanics*, vol. II. North-Holland Publishing Company, Amsterdam, 1961.

[6] J.J. Yeh, *Atomic Calculation of Photoionization Cross-Sections and Asymmetry Parameters*. Gordon and Breach Science Publishers, Langhorne, PE (USA), 1993.

[7] R. Manne and T. Alberg, *Koopmans' theorem for inner-shell ionization*, Chemical Physics Letters **7** (1970), 282–284.

[8] T.A. Koopmans, *Über die Zuordnung von Wellenfunktionen und Eigenwerten zu den Einzelnen Elektronen Eines Atoms*, Physica **1** (1933), 104–113.

[9] S. Hüfner, G.K. Wertheim, D.N.E. Buchanan, and K.W. West, *Core line asymmetries in XPS-spectra of metals*, Physics Letters A **46** (1974), 420–421.

[10] S. Hüfner and G.K. Wertheim, *Core-line asymmetries in the x-ray-photoemission spectra of metals*, Physical Review B **11** (1975), 678–683.

[11] W. Bambynek, B. Craseman, R.W. Fink, H.U. Freund, H. Mark, C.D. Swift, R.E. Prince, and P.V. Rao, *X-ray fluorescence yields, Auger, and Coster-Kronig transition probabilities*, Reviews of Modern Physics **44** (1972), 716–813.

[12] P.H.Citrin, G.K. Wertheim, and Y. Baer, *Many-body processes in X-ray photoemission line shapes from Li, Na, Mg, and Al metals*, Physical Review B **16** (1977), 4256–4282.

[13] S. Doniach and M. Ŝunjić, *Many-electron singularity in X-ray photoemission and X-ray line spectra from metals*, Journal of Physics C: Solid State Physics **3** (1970), 285–291.

[14] E. Sokolowski, C. Nording, and K. Siegbahn, *Chemical shift effect in inner electronic levels of Cu due to oxidation*, Physical Review **110** (1958), 776.

[15] P. Bagus, F. Illas, G. Pacchioni, and F. Parmigiani, *Mechanisms responsible for chemical shifts of core-level binding energies and their relationship to chemical bonding*, Journal of Electron Spectroscopy and Related Phenomena **100** (1999), 215–236.

[16] P.H. Citrin, G.K. Wertheim, and Y. Baer, *Core-level binding energy and density of states from the surface atoms of gold*, Physical Review Letters **41** (1978), 1425–1428.

[17] C.S. Fadley, S.B.M. Hagström, M.P. Klein, and D.A. Shirley, *Chemical Effects on Core-Electron Binding Energies in Iodine and Europium*, Journal of Chemical Physics **48** (1968), 3779–3794.

[18] P.H. Citrin and G.K. Wertheim, *Photoemission from surface-atom core levels, surface densities of states, and metal-atom clusters: A unified picture*, Physical Review B **27** (1983), 3176–3200.

[19] B. Johannson and N. Mårtensson, *Core-level binding-energy shifts for the metallic elements*, Physical Review B **21** (1980), 4427–4457.

[20] A. Rosengren and B. Johansson, *Calculated transition-metal surface core-level binding-energy shifts*, Physical Review B **22** (1980), 3706–3709.

[21] A. Rosengren and B. Johansson, *Surface heat of segregation from surface core-level binding-energy shifts*, Physical Review B **23** (1981), 3852–3858.

[22] C.S. Fadley, *The Study of Surface Structures by Photoelectron Diffraction and Auger Electron Diffraction* in *Synchrotron Radiation research: Advances in Surface and Interface Science* (R.Z. Bachrach, ed.), vol. I: Techniques, Plenum Press, New York, London, 1992.

[23] Y. Chen, F.J.G. de Abajo, A. Chassé, R.X. Ynzunza, M.A. Van Hove A.P. Kaduwela, and C.S. Fadley, *Convergence and reliability of the Rehr-Albers formalism in multiple-scattering calculations of photoelectron diffraction*, Physical Review B **58** (1998), 13121–13131.

[24] D.P. Woodruff and A.M. Bradshaw, *Adsorbate structure determination on surfaces using photoelectron diffraction*, Reports on Progress in Physics **57** (1994), 1029–1080.

Chapter 3

Experimental setup

The key ingredients to perform a photoemission experiment are (i) the x-ray or ultraviolet source, which provides the electromagnetic radiation to excite the sample, and (ii) the electron energy analyser, needed to measure the kinetic energy distribution of the photoelectrons. These devices are usually in an experimental station, which usually provides also facilities for sample preparation and instrumentation for other experimental characterizations.

In this chapter a brief outline of the main features of these two fundamental elements will be given, as well as a description of the experimental ultra high vacuum (UHV) chamber where all the experiments descibed in this thesis have been performed.

3.1 The SuperESCA beamline at Elettra

The excitation sources used in photoelectron spectroscopy are of several different kinds. In core level photoemission studies, the X-rays are usually produced using conventional anode-based sources (Mg or Al K_α emission). These provide photons at fixed energy of ≈1256 and ≈1486 eV (the energy difference between the $1s$ and $2p$ levels of the two materials).

Nowadays many large facilities have been built (i.e. electron storage rings) that provide synchrotron radiation. There are many advantages in using synchrotron radiation, the most important ones being its energy tunability and high photon flux.

Synchrotron radiation is produced by the electrons that orbit in a large storage ring with a velocity close to the speed of light (see fig. 3.1 [1]). In this case the radiation is sharply peaked in the forward direction when observed form the laboratory frame, and has a broad, continuum range of photon

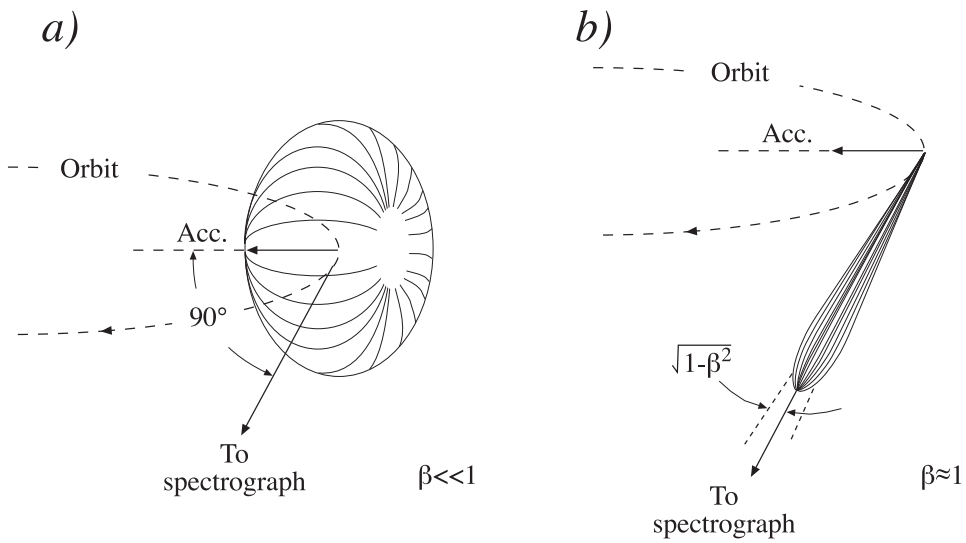

Figure 3.1: Radiation pattern for *a)* a slow electron and *b)* a relativistic electron moving in a circular path.

energies, high brilliance and high photon flux. Moreover, in the orbit plane the synchrotron radiation is plane polarized while it is elliptically polarized slightly out of this plane.

All the photoemission studies presented in this thesis have been performed on the SuperESCA beamline of the Elettra storage ring, in Trieste, Italy [2]. Elettra is a third generation synchrotron facility, where the light is produced not only by the bending magnets but also by insertion devices, called *undulators*, which are placed in the straight sections of the storage ring. These are periodic arrays of magnets which can deliver radiation in a narrower (but tunable by varying the gap between the arrays) energy range and with a higher intensity than the bending magnets.

The insertion device of the SuperESCA beamline is a 56 mm period undulator (minimum gap 19 mm), composed of three sections with 81 periods, which covers a photon energy range of 85 to 1500 eV at a ring energy of 2 GeV. When the ring is operated at 2.4 GeV the photon energy range is 120 to 2100 eV.

The beamline is sketched in fig. 3.2. The monochromator is a stigmatic

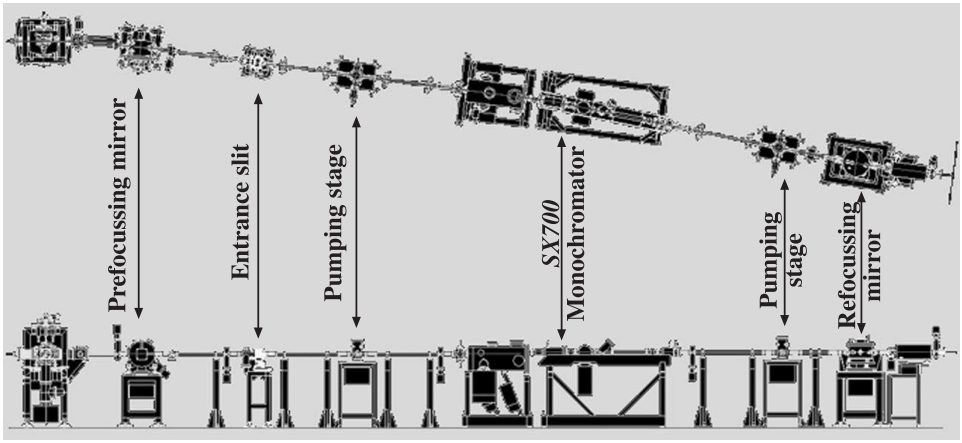

Figure 3.2: Sketch of the SuperESCA beamline. The optical elements are: a cylindrical pre-focusing mirror; a fixed focus PGM (SX700) monochromator with plane mirror, plane grating and ellipsoidal focusing mirror; an ellipsoidal re-focusing mirror. Fixed entrance and exit slits are also present. The exit slit is at the end of the monochromator.

SX700 with a horizontally pre-focusing mirror (cylindrical symmetry, magnification 8:1) and an entrance slit, and covers the photon energy range from 85 to ≈1000 eV with a single plane grating. The resolving power of the monochromator, $(E/\Delta E)$ is of the order of 10^4 at 400 eV, while it decreases to $\approx 5 \times 10^3$ at 900 eV. An ellipsoidal re-focusing mirror (magnification 2:1) focusses the monochromatized radiation in the center of the experimental chamber. The size of the spot on the sample is 100×(exit slit dimension) μm^2. The photon flux at 400 eV photon energy and resolving power 10^4, is of the order of 10^{11} photons/s.

3.1.1 Experimental station

Photoelectron specroscopy experiments, as well as all the investigation techniques using electrons, need to be performed in ultra-high vacuum for two reasons. The first "technical" reason is that these techniques are effective only if the mean free path of the electrons in the gas-phase is long enough to allow them to reach the detector, i.e. it is in the metric range. The second "experimental" reason is the need of keeping the surface of the sample clean enough to be able to study it. The effects of the contaminants coming from the ambient atmosphere are proprortional to the impact rate for a gas onte

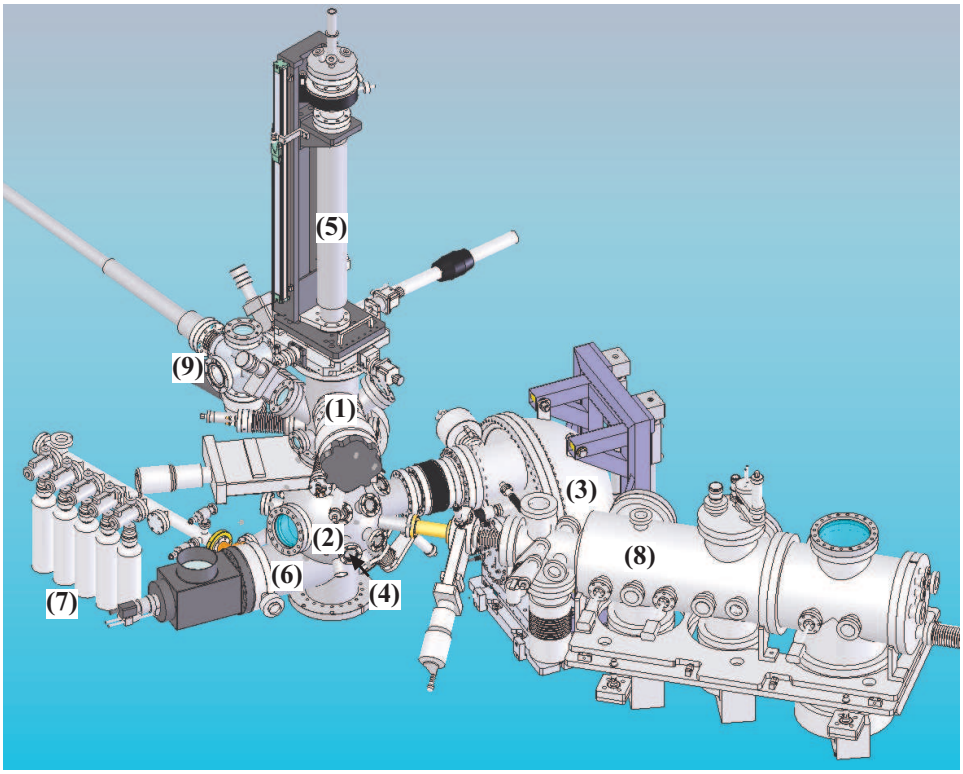

Figure 3.3: Drawing of the SuperESCA experimental chamber. (1) Preparation chamber. (2) μ-metal measurement chamber.(3) Electron energy analyser. (4) Connection to the beamline. (5) Sample manipulator. (6) Low-Energy Electron Diffraction (LEED). (7) Gas inlet system. (8) Molecular beam apparatus. (9) Sample transfer system with fast entry lock.

the surface

$$\frac{P}{\sqrt{2\pi m k_B T}}$$

where P is the pressure, m is the mass of the molecules, T is the temperature and k_B is Boltzmann's constant [3]. With a sticking probability of 1, the sample would become completely covered in a few seconds at a pressure of 10^{-6} mbar, thus preventing any kind of measurement to be performed. This is why pressures in the range of 10^{-10} mbar, or below, are needed.

The SuperESCA experimental station (sketched in fig. 3.3) consist of two UHV chambers separated by a valve. The upper chamber (1) is made

of stainless steel and is devoted to sample preparation. It is equipped with a sputter gun for sample cleaning by means of ion bombardement, and with various evaporators for layer growth or cluster deposition. A fast entry lock and a transfer system are connected to this chamber (9), allowing sample changes without breaking the vacuum. On the top of the chamber a sample manipulator is mounted (5). Two different manipulators are available, namely a 5 degrees of freedom (x, y, z, θ, ϕ) fully computer-controlled sample manipulator and a manual, 4 degrees of freedom manipulator. The first one, shown in fig. 3.3, is a modified version of the CTPO from VG Instruments and the allowed sample temperature range is 120–1500 K while the second one is an He cryostat with xyz translations and just 1 rotational axes θ but with sample temperature range of 20–2000 K. The transfer system is not usable with the low temperature manipulator.

The manipulators are used also to move the sample from the preparation chamber to the bottom one. The lower chamber (2) is made of μ-metal in order to isolate the sample environment from stray magnetic fileds which would deflect the electron trajectories. In this UHV chamber a LEED (low energy electron diffraction) instrument (6), a mass spectrometer and a gas inlet system (7) are mounted.

The supersonic molecular beam apparatus (8) offers an alternative method for exposing samples to a gas in a more controlled manner. It consists of three UHV chamber aligned with the sample and connected through a system of *collimators* (*skimmers*). The gas is introduced at high pressure by means of a *nozzle* in the first chamber and expands adiabatically in the second and third one through the skimmers' orifices; the molecular beam finally hits (with a spot diameter of about 4 mm) the sample placed in the measuring position. This apparatus allows performing experiments for which the control of the incidence angle and the energy of the incident molecules is required.

Finally, at the same level of the beamline connection (4) and at an angle of 40° respect to it, what can be considered the hearth of the experimental setup is installed: the electron energy analyser (3). The instrument is a PHOIBOS analyser, from SPECS GmbH, with a mean radius of 150 mm. It is capable of an energy resolution of about 4 meV (FWHM) and is provided with a 9-element lens system: by varying the potentials on the various elements, different lens modes can be set, allowing the user to select an acceptance angle up to ±15°, or a viewed area in the range 0.1–20 mm^2.

The analyser is equipped with a home-made delay line detector. The detector development and its integration with the commercial instrument is exactly part of this PhD project and will be described in detail in the next

chapter. For this reason, in the following section the working principle of electron energy analysers will be summarized; this will help in defining the characteristics required for the detector whose development is reported in ch. 4.

3.1.2 Electron energy analyser

Energy dispersion and resolution

Since the information obtained by photoemission spectroscopy is contained in the kinetic energy distribution of the photoemitted electrons, a device, capable of *energy filtering* the electrons emitted by the sample, is needed. The instrument mostly used in photoemission experiments is the *hemispherical analyser*.

An ideal hemispherical analyser consists of two concentric hemispherical electrodes (inner and outer hemispheres) held at proper voltages. It is possible to demonstrate that in such a system, (i) the electrons are linearly dispersed along the direction connecting the entrance and the exit slit, depending on their kinetic energy (see fig. 3.4 (a)), while (ii) electrons with the same energy are first-order focused (see fig. 3.4 (b)) [4].

When the potentials V_1 and V_2 are applied to the inner and outer hemispheres respectively, the potential and the electric field in the region between the two electrodes can be calculated by solving the Laplace equation:

$$V(r) = -\frac{V_2 - V_1}{R_2 - R_1}\frac{R_1 R_2}{r} + const \tag{3.1}$$

$$|E(r)| = \frac{V_2 - V_1}{R_2 - R_1}\frac{R_1 R_2}{r^2} \tag{3.2}$$

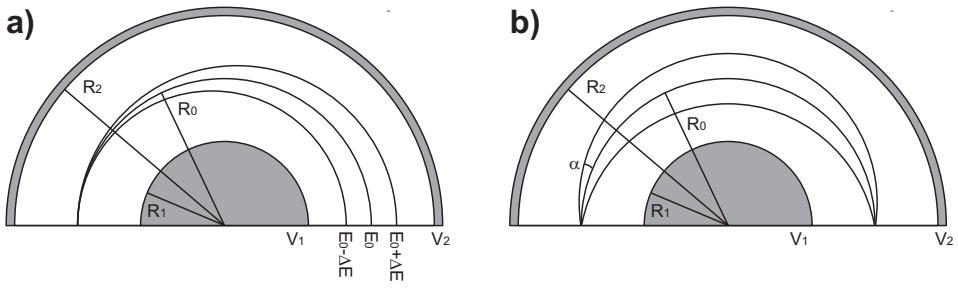

Figure 3.4: Energy dispersion properties (a) and focusing properties (b) of a hemisferical analyser.

where R_1 and R_2 are the radii of the two hemispheres. In order for the electrons with kinetic energy E_0 to follow a circular trajectory with radius $R_0 = (R_1 + R_2)/2$, the force due to the electric field ($F_E = -e|E(r)|$) must be equal to the centripetal force (F_C) along the whole path. From this consideration, after a series of mathematical steps, we obtain the following expression for the potential

$$V(r) = \frac{V_0 R_0}{r} + const, \tag{3.3}$$

where $V_0 = E_0/e$ is the energy of the electrons expressed in eV. From this equation we can calculate the potential difference between the two hemispheres, obtaining

$$V_2 - V_1 = V_0 \left(\frac{R_2}{R_1} - \frac{R_1}{R_2} \right). \tag{3.4}$$

This last equation can be used to determine the potentials to be applied to the hemispheres in order to select electrons with energy V_0, the so called *pass energy*.

Up to now only the possibility to select electrons with a given kinetic energy has been demonstrated, but nothing has been stated about the resolution of the analyser and its dispersing properties. In order to highlight these aspects we need to calculate the electron trajectories inside the instrument [5]. Solving the differential equation for the trajectory of a particle in a central force field leads to the following expression for the displacement of the radial position ($r(\pi)$) of the electrons respect to R_0 after the complete travel inside the analyser as a function of $\Delta E = E - E_0$, the difference between the electron kineetic energy and the pass energy (see fig. 3.5 as a reference):

$$r(\pi) - R_0 = -r(0) + R_0 - 2R_0 \left(\frac{1}{1 + \sin^2\alpha - \frac{\Delta E}{E_0}\left(1 - \sin^2\alpha\right)} \right). \tag{3.5}$$

Finally, considering small entrance angles and small difference with respect to the pass energy, it is possible to neglect the highest order terms and perform a series expansion; the final result is

$$r(\pi) - R_0 = -r(0) + R_0 - 2\frac{\Delta E R_0}{E_0} - 2R_0\alpha^2. \tag{3.6}$$

Equation (3.6) is quite simple and useful for understanding the main properties of the emispherical analyser.

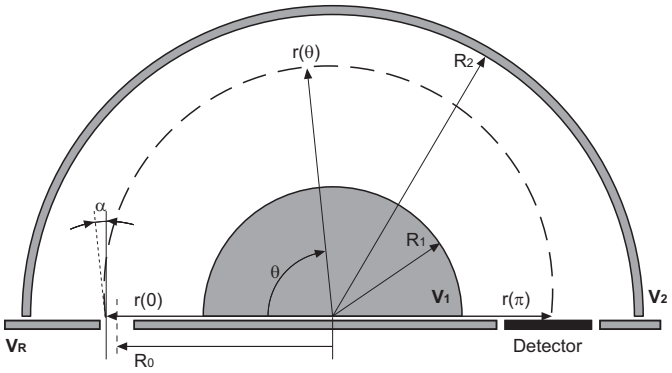

Figure 3.5: Schematic representation of the emispherical analyser.

- As stated at the beginning of this section, it is possible to see that the system focuses at first order in α, since the dependence of the final position of the electrons on α is expressed by a second-order term.
- The energy dispersion at the exit plane has a linear dependence on the kinetic energy: electrons with energy higher than pass energy are shifted towards the outer hemisphere, while the ones with lower energy are displaced towards the inner hemisphere. This will be of fundamental importance for the development of the *snapshot* acquisition mode described in sec. 4.1.6.
- Finally, considering the finite size of the entrance and exit slits of the analyser, and defining w as the average width of the two slits, eq. (3.6) can give an estimation of the resolution of the instrument [6]:

$$FWHM = E_0 \left(\frac{w}{2R_0} + \frac{\alpha^2}{4} \right) \tag{3.7}$$

  where $FWHM$ is the full width at half maximum of the energy distribution curve which could be obtained with an ideal monochromatic electron source.

From eq. (3.7), it is evident that the resolution depends linearly on the kinetic energy of the electrons passing through the analyser (i.e. on the pass energy), so that a good strategy in order to obtain *high-resolution* spectra with a *constant* resolution throughout the whole data range consists in choosing a constant pass energy and decelerating the electrons by means of a retarding potential before they enter the analyser.

Another consideration is related to the mean diameter of the analyser: better resolutions can be achieved with larger analysers and typical values for R_0 are between 100 and 200 mm. Such large devices cannot be installed in the experimental chamber very close to the sample; actually, for mechanical reasons, the analyser is usually set at several tens of centimeters from the sample. On the other hand, by combining the large distance from the sample and the small width of the entrance slit needed for high energy resolution, the small solid angle viewed by the instrument would result in a very low transmission of photoelectrons, making data acquisition a long time consuming task. These drawbacks can be overcome by using a system of electrostatic lenses in order to collect the electrons from a solid angle as large as possible, focalize them on the entrance slit of the analyser and, at the same time, decelerate them to the pass energy.

Electrostatic lenses

As a starting point to understand how electron beams (and in general charged particle beams) can be deflected and focused, it may be helpful to look at some systems which have similar behaviour in photon and particle optics. The simplest one is the plane boundary separating two regions which differ in some properties. In the case of photon optics, the important property is the refractive index. The path of a ray of light incident non-normally onto the boundary is changed on crossing the boundary itself, the directions in the two regions being related by Snell's law. The analogue in particle optics is a boundary separating two regions at different electrostatic potentials. If we consider a particle having a velocity v_1 in the first region and v_2 in the second, these velocities are related to the potentials, V_1 and

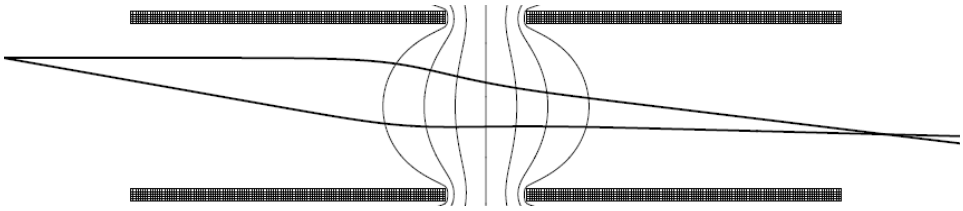

Figure 3.6: Simulation of the paths of charged particles and equipotential boundaries in a two-cylinder lens, obtained with the version 8.0 of the Simion 3D code. The paths become asymptotic to straight lines only away form the central region of the lens; however, the behaviour of this system strongly resembles that of thin lenses, usually studied in a geometric optics treaty.

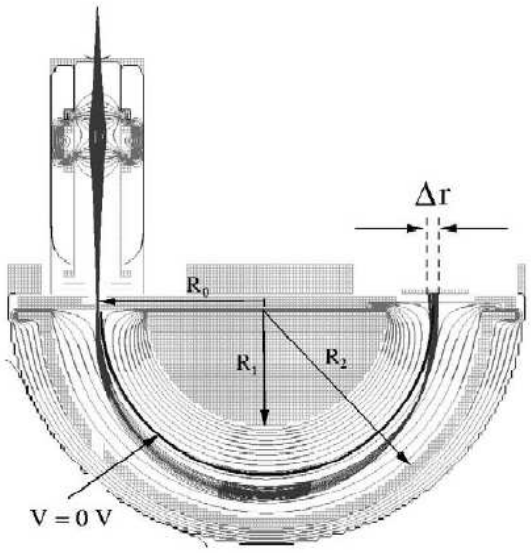

Figure 3.7: Representation of a typical assembly for an electron energy analyser. Simulated electron trajectories and equipotential lines inside the instrument are also drawn [8].

V_2 in the two regions and the conservation of the parallel component of the momentum leads to the equation

$$\frac{\sin\alpha_1}{\sin\alpha_2} = \left(\frac{V_2}{V_1}\right)^{1/2} \tag{3.8}$$

which is exactly Snell's law with $V^{1/2}$ playing the role of the refractive index, while α_1 and α_2 are the angles between the normal to the boundary and the path of the particle in the two regions [7].

That example was rather artificial, because abrupt changes in potential do not occur in free space, but we can use the previous considerations to understand the system represented in fig. 3.6. This picture illustrates an electrostatic analogue of a lens in photon optics. It consists of two coaxial cylinders separated by half their common diameter for clarity and held at potentials V_1 and V_2. No mathematical analysis should be needed to show that, deep inside each cylinder, the potentials are very close to those of the electrodes, but within a diameter or so from the centre of the system the potential changes quite rapidly as evidenced by the equipotential lines drawn in the figure. It would be possible to regard the equipotentials as

boundaries separating regions having some mean potential and to use the Snell's-like law (3.8) to follow the refraction, boundary by boundary, through the lens and deduce the charged particle path. Actually, this is not the most accurate and the most convenient way to calculate the particle trajectory: normally, a computer simulation program is used (one of the most common is Simion 3D [9]) which computes the potentials and the trajectories by means of the finite-difference method. However, the important result is that the asymptotic behaviour of the charged particle path strongly resembles that of light ray passing through a lens, as evidenced in the figure.

By combining several elements similar to the one discussed above, it is possible to implement an electrostatic lens system which can be placed close to the sample (typical distance is about 40 mm) to collect the electrons and bring them to the entrance slit of the analyser, controlling, at the same time, the solid angle or the area viewed by the instrument.

Bibliography

[1] S. Krinsky, M.L. Perlman, and R.E. Watson, *Characteristics of synchrotron radiation and of its sources* in *Handbook of Synchrotron Radiation* (E.E. Koch, ed.), vol. 1a, 67–172, North-Holland Publishing Company, 1983.

[2] A. Abrami, M. Barnaba, L. Battistello, A. Bianco, B. Brena, G. Cautero, Q.H. Chen, D. Cocco, G. Comelli, S. Contrino, F. DeBona, S. Di Fonzo, C. Fava, P. Finetti, P. Furlan, A. Galimberti, A. Gambitta, D. Giuressi, R. Godnig, W. Jark, S. Lizzit, F. Mazzolini, P. Melpignano, L. Olivi, G. Paolucci, R. Pugliese, S.R. Qian, R. Rosei, G. Sandrin, A. Savoia, R. Sergo, G. Sostero, R. Tommasini, M. Tudor, D. Vivoda, F.-Q. Wei, and F. Zanini, *Super ESCA: First beamline operating at ELETTRA*, Review of Scientific Instruments **66** (1995), 1618–1620.

[3] A. Zangwill, *Physics at surfaces*. Cambridge University Press, 1988.

[4] E.H.A. Granneman and M.J. Van Der Wiel, *Transport, dispersion and detection of electrons, ion and neutrals* in *Handbook of Synchrotron Radiation* (E.E. Koch, ed.), vol. 1a, 367–462, North-Holland Publishing Company, 1983.

[5] F. Hadjarab and J.L. Herskine, *Image properties of the hemispherical analyzer applied to multichannel energy detection*, Journal of Electron Spectroscopy and Related Phenomena **36** (1985), 227–243.

[6] D. Roy and J.D. Carette, *Design of electron spectrometers for surface analysis* in *Electron Spectroscopy for Surface Analysis* (H. Ibach, ed.), 13–58, Springer-Verlag, 1977.

[7] D.W.O. Heddle, *Electrostatic Lens Systems*. Institute of Physics Publishing, second ed., 2000.

[8] T.J.M. Zouros and E.P. Benis, *The emispherical deflector analyser revisited. I. Motion in the ideal* $1/r$ *potential, generalized entry conditions, Kepler orbits and spectrometer basic equation*, Journal of Electron Spectroscopy and Related Phenomena **125** (2002), 221–248.

[9] D.J. Manura and D.A.Dahl, *Simion Version 8.0 user manual*. Scientific Instrument Services, Inc., 2007.

Chapter 4

Instrumentation development

The class of experiments we were planning to perform at the SupeESCA beamline involved measurements on supported nanoclusters and low-dimensional systems. All these systems are characterized by a very low atomic density. As will be seen in chapters 6 and 7 and in section 8.4, in the case of supported nanoparticles we deal with a low surface density of small clusters. Low-dimensional system of interest are, for instance, oxide thin films as supports for the nanoparticles (ch. 7) or bi-metallic interfaces (as in the case of Pd-Ru interface studied in ch. 5); in both cases we work with few atomic layers and even with a single layer when graphene is the object of the experiments, as discussed in chapter 8. With these considerations in mind, low rates of emitted photoelectrons were certainly expected to drastically increase the data acquisition time. This becomes a critical problem when we are interested in following the *temporal evolution* of physical and chemical phenomena occurring on such systems. In order to make possible this kind of experiments on very diluted systems, we needed all the three elements necessary for photoemission experiments to be optimized in our experimental set-up.

- *Photon source.* It is evident that the samples we were interested in can hardly be studied using a conventional anode-based x-ray source (flux of about 10^9 photon/s dipersed over a spot of ≈ 20 mm). On the other hand, SuperESCA beamline, described in sec. 3.1, is optimized for delivering high photon flux and is capable of 10^{11} photon/s, concentrated in an area of about 100 μm. We see, then, how the synchrotron radiation produced by the Elettra storage ring is a key ingredient to

perform real-time acquisitions.

- *Electron collection and energy filtering.* As explained in ch. 3), the flux of electron through an electron energy analyser, among the other contributions, is determined by the acceptance angle of the instrument, i.e. the solid angle from which its electrostatic lens system is capable to collect the photoelectrons and focus them on the entrance slit of the hemispheres. The electron energy analyser we installed on the beamline experimental station (a PHOIBOS 150 analyser from SPECS GmbH) is capable of an acceptance angle up to $\pm 15^{\circ}$, much larger than that of the old instrument ($\approx \pm 2^{\circ}$). This ensures an electron transmission through the instrument that can be one order of magnitude larger than that of the previous set-up. The PHOIBOS analyser is is also able to provide high energy resolution measurements, being its ultimate energy resolution of about 4 meV.

- *Detection system.* In order to maximize data throughput during spectra acquisition, one would like to collect as a large fraction as possible of the electrons arriving at the exit plane of the analyser. As described in sec. 3.1.2, in fact, we can infer the kinetic energy of all these electrons accordingly to their coordinate along the dispersive direction. The ideal detector, thus, should cover the whole space between the two hemispheres. Such a wide detector would allow also fast *snapshot* acquisitions, as will be explained in detail in sec. 4.1.6. Enlarging the size of the detector, on the other hand, can greatly increase the complexity of the read-out electronic system. After careful considerations on the possible detector architectures, we decided to develop a one-dimensional delay-line detector to be installed on the new analyser.

In this chapter, after a brief outline of the possible detectors that can be mounted on an electrostatic energy analyser (sec. 4.1.1), the working principle of a delay line detector will be described in detail as well as the electronic read-out system we developed for the novel instrument (sec. 4.1.2 and 4.1.4). In sec. 4.2 the software I realized to integrate the detection system with the analyser and all the other components of the experimental station will be described. Finally, one of the first test experiments performed with the new instrumentation is presented (sec. 4.3): the measurements described are a good exemple of the possibilities offered by the new system combining real-time acquisition, high energy resolution and sensitivity to diluted systems.

4.1 The novel delay-line detector for SuperESCA analyser

4.1.1 Detectors for electron energy analysers

Channel Electron Multipliers

Let's suppose we have an electron analyser and we want to install a device at its exit slit in order to detect the electrons with the selected kinetic energy. The ideal detector should be able to reveal each single electron. To do that, a first problem needs to be solved: the charge of an electron is so small (1.602×10^{-19} Coulomb) that eletronic devices, even if equipped with up to date amplification systems, are not able do detect single electrons. For this reason, electron detection setups always include a first stage dedicated to the *charge amplification* of the incoming electrons: the so-called *electron multiplier*.

An electron multiplier is basically a device that produces at the output a cloud of some million electrons for each incoming electron, in such a way that the resulting charge is large enough to be measured [1]. The most popular devices that perform charge multiplication are Channel Electron Multipliers (CEM). CEMs are essentially small tubes fabricated with lead-doped glass with an internal diameter of ≈ 1 mm and a length-to-diameter ratio (L/D) that ranges, generally, from 40 to 100 (this last parameter, actually, plays an important role in determining the CEM amplification factor). The internal walls of the tube are coated with hydrogen-reduced lead silicate glass, the *active material* which has the property to emit a large amount of secondary electrons when primary particles impinge upon it. A thin metal electrode is deposited at the ends of the tube to provide electrical contact.

When a positive potential (2000–3000 V) is applied between the funnel-shaped input and the output aperture of the CEM, the secondary electrons generated by the primary particle can gain enough energy to create further secondary electrons upon striking the surface of the interior channel walls. The resulting electron avalanche (see fig. 4.1) follows the channel to the positively biased end where it is collected by an anode and produces an easily detectable output pulse containing up to 10^8 electrons with a duration of the order of ≈ 8 ns. The typical shape of a single-channel CEM, often addressed as Channeltron$^{\text{TM}}$, presents a spiral geometry (see CEM picture in scheme of fig 4.2) in order to increase the efficiency and to reduce the *ion feedback* effect which can originate spurious events: by hitting the channel walls, the electron cloud can desorb and ionize gas atoms that, accelerated

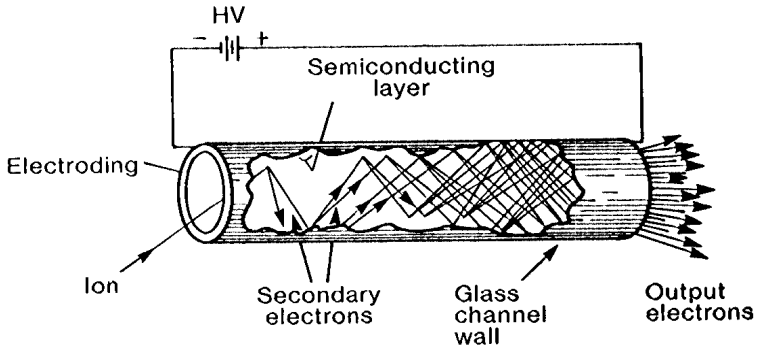

Figure 4.1: Electron avalanche creation inside a channel electron multiplier.

by the electric field back to the channel input, can strike the CEM walls originating a second electron avalanche indistinguishable from a *real* event. The spirals prevent the ions reaching the CEM entrance with enough kinetic energy to produce the secondary electron avalanche.

The acquisition chain for a Channeltron based detector is schematized in fig. 4.2. The CEM output pulse, after decoupling from the high voltage, is amplified and fed into a *discriminator*: if the pulse amplitude is higher than

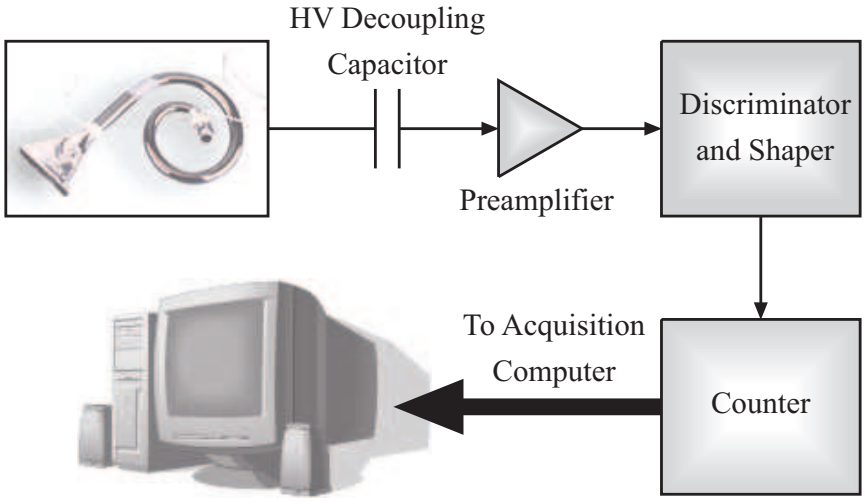

Figure 4.2: Acquisition chain for a channeltron-based detector.

the threshold, the *shaper* produces a standard digital pulse (the most common are TTL and ECL signals) that can be registered by a *counter*. Usually, this last instrument is interfaced with a computer which controls also the voltages supplied to the analyser. This configuration allows the acquisition of photoemission spectra: once the pass energy has been selected, the lens and hemisphere voltages are set to the correct values for the electrons with the first kinetic energy to reach the middle of the exit plane, pass through the exit slit and be detected by the channeltron; counts are recorded during the selected *time window* and then the whole process is repeated for the second kinetic energy and so on throughout the desired energy range. This acquisition process can take a long time before giving spectra with a reasonable signal-to-noise ratio; indeed, the procedure can be improved.

Going back to sec. 3.1.2, we can recall that when a kinetic energy E_0 is selected, besides the electrons with the correct energy, also the electrons with energies close to E_0 are focussed onto the exit plane; the relation between the position and the energy is well known (eq. (3.6)), but it is evident that, using the detection configuration described above, all these electrons are lost. The simplest solution to improve the acquisition system consists in placing more than one channeltron on the exit plane of the analyser, in this way during an energy scan the counts referring to different energies are acquired simultaneously, speeding up the acquisition time by a factor n, where n is the number of parallel channetrons installed at the end of the analyser. For mechanical reasons related to the physical dimensions of CEM, the maximum number af channeltrons that can be installed in a standard analyser is about 10. In order to further increase the number of channels, a different kind of charge multiplier is needed.

Microchannel plate based detectors

Essentially Microchannel Plates (MCPs) are thin (0.5–1 mm) silicon-lead oxide glass wafers composed of a large number ($\approx 10^5 \mathrm{cm}^{-2}$) of small CEM tubes called microchannels (typical diameter $\approx 10\ \mu$m). Similarly to CEMs, the inner channel surface of MCPs consist of a secondary emitting coating, with an underlying semiconducting layer which replenishes the emitted electrons and, at the same time, presents a resistance high enough for the accelerating electric field to be established.

The MCP working principle is the same of that of CEMs but, due to small thickness of the plates, the gain that can be obtained ($\approx 10^4$) is too low for the charge pulses to be detected. For this reason detection systems that need to work in counting mode use stacks with 2 (Chevron configuration,

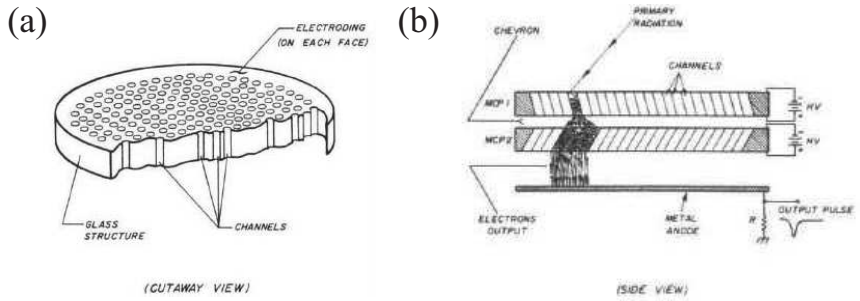

Figure 4.3: (a) Section view of a microchannel plate and (b) operation of a chevron assembly.

see fig. 4.3 (b)) or 3 (Z-stack configuration) MCPs: in this way the total gain can reach the value of 10^8 secondary electrons per each primary particle.

The microchannels form an angle with respect to the direction normal to the surface that can range between 6° and 13°. This trick, as highlighted in fig. 4.3 (b) for the Chevron configuration, reminds the spirals of the channeltrons and allows to minimize the ion feedback effect.

Because of the small size of the channels and their large density on the MCP surface, microchannel plates can be thought as a spatially *continuous* electron multiplier along its surface, which spatial resolution is ultimately limited by the pore size and spacing and can be better that 5 μm. Therefore, we can plan to use a microchannel plate system at the end of the electron analyser, separated from the analyser volume by a thin mesh that screens the emisphere region from spurious field due to MCP polarization. With this configuration the characteristics of the detection system are determined by the geometry and the architecture of the anode that collects the electron clouds behind the MCPs.

Multianode detectors In a multianode architecture the electron clouds resulting from the charge muiltiplication process are collected by anodes deposited on a ceramic support. It is important noting that with MCP based detectors, since no exit slit is placed at the analyser focusing plane, the anodes themselves act as exit slits and their size determines the resolution of the system, accordingly to eq. (3.7). Within the "Instrumentation & Detector laboratory" at Elettra, detector systems with 16, 48 and 96 channels have been developed [2] (fig 4.4).

The acquisition chain is similar to that of a single channeltron; the main

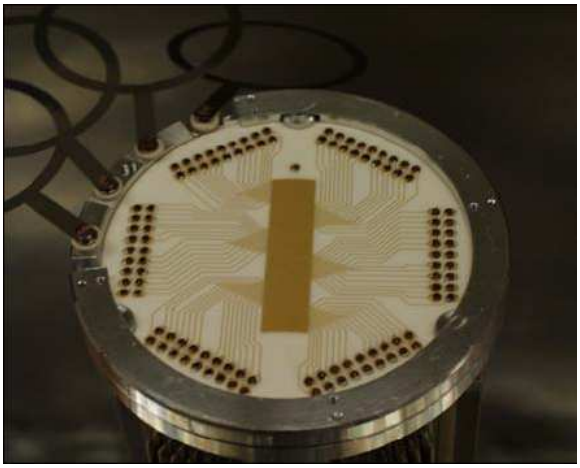

Figure 4.4: 96-channel detector. The anodes consist of a gold layer deposited on an alumina support.

difference is that, because of the large number of acquisition channels that need to be managed, printed circuit boards had to be developed which integrate up to 16 preamplifier-discriminator-shaper chains and up to 32 counters [3].

Although multianode acquisition represents a great improvement, this architecture presents some serious limits: first of all it is very difficult to manage more than 100 channels. This is not a limit of anode machining technology (in principle anodes of some tens of microns are realizable), but it depends on the difficulty of interfacing each anode in ultra high vacuum with its acquisition electronics outside the experimental chamber by means of UHV compatible electrical feedthroughs. However, upon development of special, UHV compatible electronic circuitry, part of the data acquisition chain can be moved inside the analyser chamber, so that only digital data need to be transmitted through the the vacuum/air interface. Using this approach, detectors with up to 768 channels have been inplemented [4].

Phosphor screen and CCD camera In recent years the use of bidimensional detectors in electron analysers is increasing. The main reason is that by operating the analyser lenses in the so-called *Fourier mode*, electrons leaving the sample with equal angles are focused on the same position on the analyser entrance slit, and since the information on the position along the non-dispersive direction is conserved inside the hemispheres, a bi-

dimensional detector allows the parallel acquisition of spectra corresponding to different emission angles, considerably speeding up the measurement procedure in Angular Resolved Photoemission (ARPES) experiments.

The simplest detector that can be used to acquire bi-dimensional data, consist in a phosphor screen placed immediately behind the MCPs and held at a voltage 3–4 kV higher than the last MCP face in order to accelerate the electron clouds against the phosphorus and produce the emission of visible light that can be imaged with a standard CCD camera installed outside the UHV chamber. The advantage of this detector is that almost no feedthroughs are required (only a standard viewport) and the only device that needs to be interfaced with the whole acquisition system is simply a commercial CCD camera. Moreover, the spatial resolution is good (few tens of microns), essentially limited by the MCP pore size, by the blurring of the illuminated phosphorus and by the CCD pixel dimensions. On the other hand, this is not a system which allows counting the single electrons: the information on the relative number of electron impinging on the detector is inferred from the intensity of the light emission and problems can arise at high count rates when the linearity of the response of the phosphor screen (the correlation between the number of pulses that reach the phosphor screen and the light intensity) is not guaranteed.

Resistive anode detector A class of detectors which combine the bi-dimensional information and the possibility to count the single events is based on *centroid position encoding* techniques. These detectors derive individual event positions finding the centroid of the electron clouds arising from the charge multipliers. Supposing a symmetrically shaped pulse exiting from the MCP, if it is possible to detect with good precision its centroid the spatial resolution is limited only by the microchannel diameter.

One of the most popular methods for finding the centroid consist in measuring how the total charge is divided on one or more anodes. The *resistive anode detector* [5, 6], made of a single resistive pad deposited on an insulating substrate and placed immediately after the MCPs, is the most widely used configuration that employs this technique. The charge from the MCP stage is partitioned among the four corners of the resistive pad where it is collected by amplifiers. Event positions can be determined from charge signal ratios at opposite pairs of the four contacts using the simple

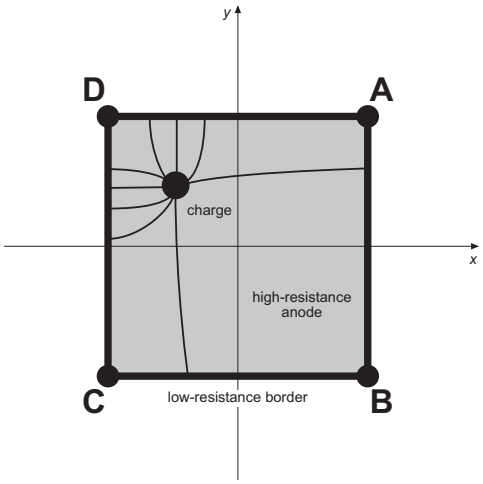

Figure 4.5: Charge dividing mechanism in a resistive anode. Reference axis are also sketched according to eq. (4.1)

approximate formulas

$$\begin{aligned} x &= \frac{(Q_A + Q_B) - (Q_C + Q_D)}{Q_A + Q_B + Q_C + Q_D} \\ y &= \frac{(Q_A + Q_D) - (Q_B + Q_C)}{Q_A + Q_B + Q_C + Q_D} \end{aligned} \tag{4.1}$$

where Q_i are the pulse amplitudes proportional to the charge collected at each corner (see fig. 4.5). In this way, with only four wires it is possible to obtain event position with a resolution that can be as good as $\approx$ 50 μm. The main drawback of the resistive anode is an intrinsic distortion of the image related to reflections of the pulses at the edges of the resistive pad; although several geometries that minimize this effect have been developed, an image completely void of deformations always requires software corrections. The second limit of this approach concerns the counting rate: in the case of the resistive anode detector, the position is determied through the accurate knowledge of the four charges at the corners: an high resolution acquisition chain can hardly manage the data with a dead-time less than 1 μs.

4.1.2 Delay-line working principle

The exit plane of the new analyser was designed with a wide aperture of 8 cm along the dispersive direction. The ideal detector for such a system has to fit the aperture and completely exploit the available field of view along the analyser dispersive direction, so that the widest possible energy range is detected. At the same time it should be able to achieve high spatial resolution, despite of its outstanding overall dimensions. Excluding multi-anode readout systems (a rough calculation for a 100 μm resolution results in about 800 channels needed!) and resistive anode setups because of the intrinsic distortion, we concentrated on the delay-line (DL) architecture.

In this read-out architecture planar delay line is employed as charge collector and encodes event position as a difference in time of arrival of the signal at the two ends of the delay line. In recent approaches the transmission line is usually fabricated in the form of a microstrip: a conductor deposited on a planar insulating substrate whose opposite face is covered by a ground plane.

The method whereby event positions are coded as time intervals is shown schematically in fig. 4.6. A pulse of charge arrives on the delay line and divides in two equal parts. Each of them propagates towards its end of the line

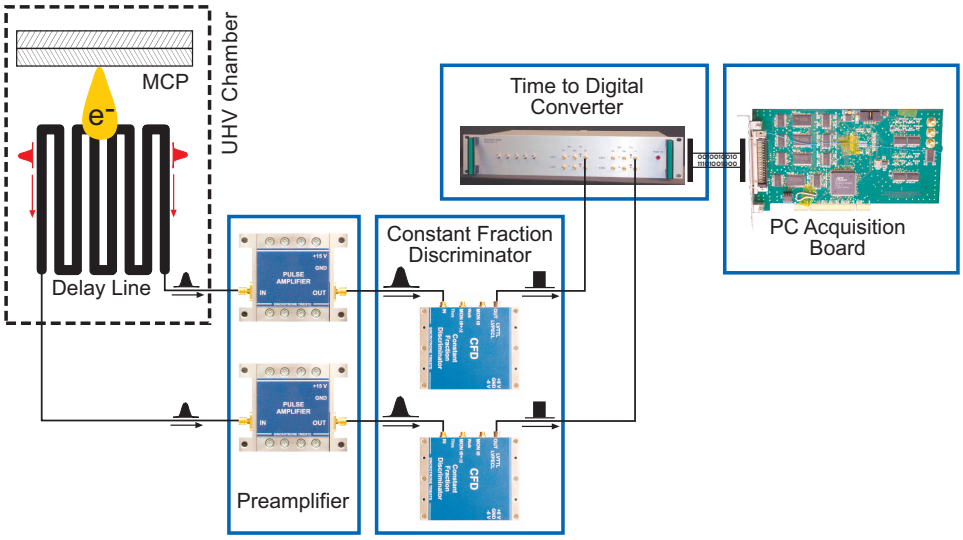

Figure 4.6: Encoding scheme for a delay-line detector. The acquisition chain with all the in-house developed devices is also shown.

where it is terminated, amplified, discriminated and finally transferred to a time interval measuring circuit. The STOP terminal has a fixed additional delay which assures that the STOP signal never precedes the START one. In such a system, the time interval registered by the timer will be

$$t = t_0 + \frac{2x}{v}, \tag{4.2}$$

where x is the event centroid location, v is the characteristic velocity of propagation of the line, and t_0 is a constant that accounts for the propagation time along the whole transmission line and the addition delay at the STOP terminal [7]. The event position is decoded from the observed time interval between START and STOP by inverting eq. (4.2):

$$x = x_0 + \frac{1}{2}vt. \tag{4.3}$$

The error in the derived location of an event δx can be expressed in terms of the system's timing error by differentiating eq. (4.3)

$$\delta x = \frac{1}{2}v\delta t. \tag{4.4}$$

Through this equation, the challenge in designing high resolution delay-line imaging systems is seen to be hinged on two factors: obtaining a low propagation velocity and achieving a small timing error. Another consideration is worth to be explained about spatial resolution: if the event charge were confined to a single meander of the transmission line, the resolution would be limited to the pitch of the meanders. To provide a real interpolation process (achieving in this way a much higher spatial resolution) several adjacent meanders must simultaneously receive charge from the event, with the contribution diminishing with distance: in this way a reliable position for the centroid can be determined. For this reason, a delay line anode is usually placed at some millimeters from the rear of MCPs in order to allow the widening of the electron cloud.

4.1.3 UHV section and high voltage decoupling

Fig. 4.7 is a photograph of the anode that has been designed for this detector. It consist of a 3.33 meters microstrip meander line deposited on a barium titanate ($BaTiO_3$) support. The total *active area* is of 90×20 mm^2 while the spacing between the strips is 570 μm. The width of the conducting strip is 260 μm so that the impedance of the transmission line is 25 Ω; the

impedance matching to 50 Ω (the standard for cables, coaxial feedthroughs and electronic devices) is obtained by means of two UHV compatible SMD (Surface Mounting Device) transformers directly connected to the ends of the transmission line. Carefulness in matching the impedance prevents pulse reflections that can cause *ghost* counts. Barium titanate has been chosen as the material for the support because of its high dielectric constant $\epsilon_r = 80$. Since the velocity of propagation of an electromagnetic signal on a microstrip is $v = c/\sqrt{\epsilon_r}$, where c is the light speed 2.9979×10^8 m/s, the use of barium titanate instead of the more common alumina (Al_2O_3, ϵ_r=9.9) allows slowing down the propagation time by a factor ≈ 3, improving in this way the spatial resolution by the same factor (see eq. (4.4)).

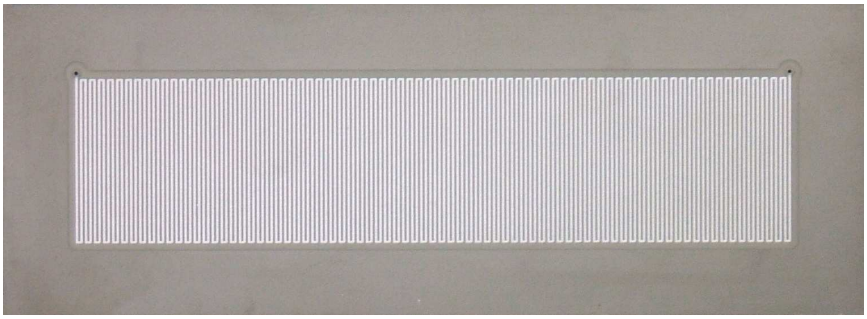

Figure 4.7: The delay-line anode realized for the SuperESCA analyser. The meander line consists in a silver-platinum alloy deposited on a barium titanate support.

The charge multiplication is provided by a couple of rectangular microchannel plates in Chevron configuration. One of the problems with charged-particle detectors is that, in order to collect the electron cloud from the MCPs, the anode is held at a high positive voltage, while all the readout electronics works at low voltage and cannot be directly connected to the anode. Usually the high voltage is decoupled from the signal by means of capacitors, but in the case of delay-line anodes the resulting distortion of the pulse shape prevents from achieving the required spatial resolution.

After a long series of tests we decided for a configuration with a thin dielectric sheet covered with a resistive layer (facing the MCPs) placed in direct contact with the anode. With this choice the resistive layer and the meander line act as the two plates of a capacitor. The resistive layer is biased with the high voltage and, actually, acts as the real anode collecting the output charge from the MCPs. When an electron cloud arrives on the resistive pad, on the underlying ground-referenced anode an *image charge* is

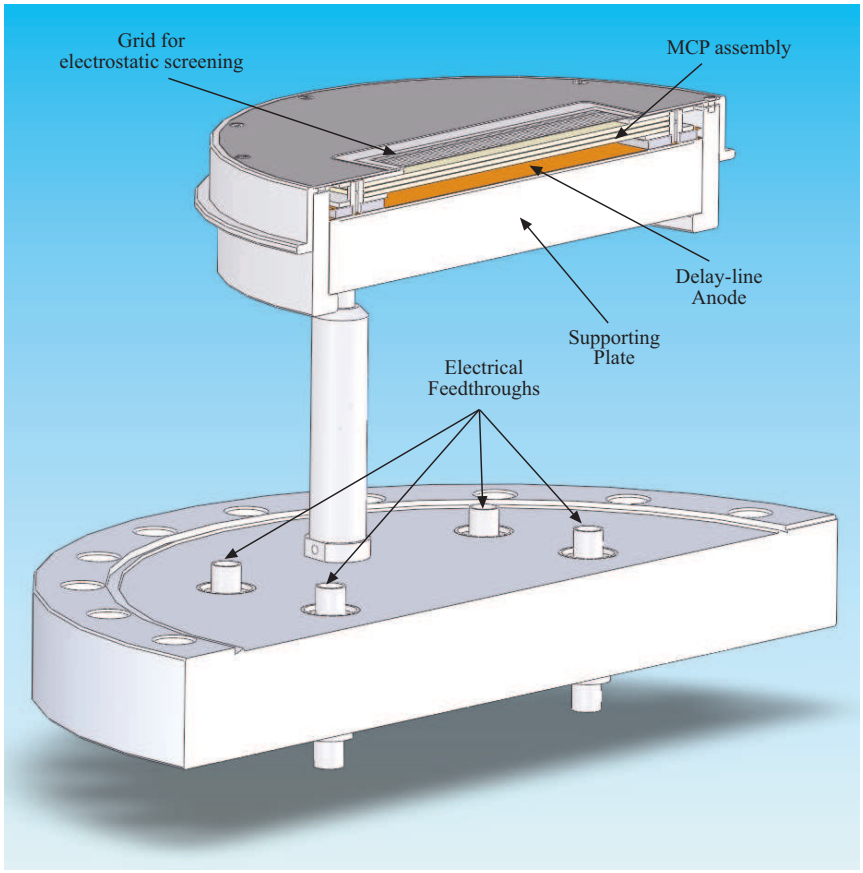

Figure 4.8: Section of the detector mechanical assembly.

generated which originates the electromagnetic pulse exploited for position encoding. Fig. 4.8 shows a sectional view of the detector assembly: the metallic mesh for electrostatic screening, the microchannel plate mounting and the delay-line anode can be distinguished.

4.1.4 Read-out electronics

Preamplifiers

The START and STOP signals from the detector are carried out from the UHV chamber by means of two SMA feedthroughs and immediately amplified by preamplifiers mounted directly on the UHV flange, reducing in this way the

possibility of noise pick-up.

The homemade preamplifiers have been designed according to the following constraints: bandwidth around 150 MHz (requested by the length of the input pulses, around 4 ns), input and output impedence of 50 Ω and good resistance to electrostatic discharges. A Monolithic Microwave Integrated Circuits (MMIC) preamplifier produced by MiniCircuits [8] has been used as active device, providing a large bandwidth (3 GHz), a nominal input and output impedence of 50 Ω and a rugged design.

Each preamplifier uses two cascaded MMICs. On the board, all components external to the amplifier, such as bias resistors, DC blocking and bypass capacitors, and the RF choke have been placed in close proximity of the MMICs, according to the rules for RF circuit design. In order to characterize the developed device, its frequency response was measured using an Agilent ENA E50701C network analyser and is reported in fig. 4.9. It may be seen that the gain is about 43 dB for frequencies between 10 and 400 MHz; the upper -3 dB cutoff frequency is 1 GHz, while the lower one is below 100 kHz.

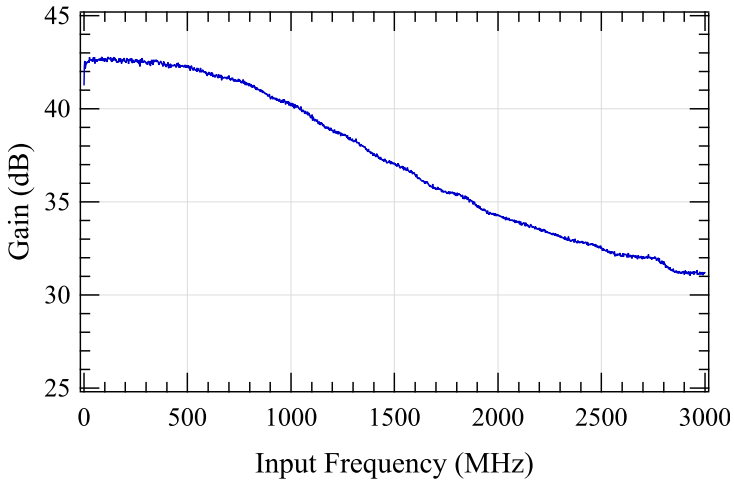

Figure 4.9: Frequency response of the two-stage MMIC-based preamplifier for frequencies between 100 kHz and 3 GHz.

Constant Fraction Discriminators

The amplitude of the pulses coming out from a MCP assembly can vary appreciably, as reported in many articles [9, 10], and their pulse height distribution shows a strong dependence on the voltage applied to the MCP setup and on the count rate of the events. Consequently, it is necessary to use constant fraction discriminators (CFDs), instead of simple threshold discriminators. CFDs are devices capable of giving a digital signal (LV-PECL in our case) at the exact moment when the anode pulse reaches the fraction of its amplitude preset by the user, independently of the absolute value of the amplitude itself; with this instrument it is possible to get measures of delay between START and STOP signals almost unaffected by peak amplitude variations.

In our detector setup the pulses width mainly depends on the distance between the MCP and the anodes and on the voltage applied between them; these parameters influence the number of detector traces involved by the electrons bunches coming from the MCP and the consequent widening of the signal [7]; a further spreading is introduced by the amplifier section, which always contains a high frequency noise filter section, so that at the end of the signal "chain" the width of the final pulse fed to CFDs is around 4 ns.

The CFDs built for this application have been designed in order to process pulses with

- approximately Gaussian shape, with a full width at half maximum (FWHM) of 4 ns,
- amplitude between 0.5 and 2 V,
- rise and fall time around 2.8 ns (so most of the frequency content is below 175 MHz,
- jitter lower than 20 ps and *walk error* lower than 40 ps [1].

This demanding specifications allow obtaining an overall spatial resolution better than 100 μm.

A threshold comparator is also used to both avoid triggering due to noise, and to generate a CFD ACTIVE signal; this signal is exploited by a logic circuitry in order to allow a *latch mode* operation, which can be used

[1] Both jitter and walk error refer to the temporal uncertainty in the digital output pulse; they are due to the noise at the input, and the variations of the input pulse amplitude, respectively.

in case of poor line mismatch, when it can be advisable to latch on the first pulse and reject the following pulse reflections. Experimental results on the CFD alone (using a Le Croy 9210/9211 pulse generator and a Le Croy 8500 Wavemaster 20 Gs/s oscilloscope) have shown, for 4 ns FWHM Gaussian pulses, a jitter lower than 17 ps for pulse amplitudes between 215 mV and 2 V.

Time to Digital Converter

The start and stop LV-ECL signals coming from the CFD are fed to the Time-to-Digital Converter (TDC). The task fulfilled by this instrument consist in measuring the time interval between START and STOP signals and giving a corresponding 16-bit number. The TDC implemented for this application follows the *digital* scheme after which the whole processing is performed by a digital VLSI that directly receives the START and STOP signals and measures the time interval exploiting chains of logical gates with known delays; further tricks are also implemented in order to improve the circuit resolution and precision.

Actually, the *analog* approach provides a time resolution which is generally better than what is possible with the totally digital counterpart, however it suffers from two important limitations: (i) the time resolution scales with the maximum time window and (ii) the relatively long time periods needed by the analog circuit limit the maximum count rate to about 1 MCount/s. On the contrary, totally digital TDCs provide a resolution which is independent on the time range, being only limited by the registry bits depth, and are generally faster than the analog ones, due to the absence of the analogue step.

According to the previously exposed considerations, the TDS system we deveolped is based on a digital TDC chip, the ACAM TDC-GPX, that can provide a time resolution of 27 ps [11]. This corresponds to a spatial resolution in our detector of about 70 μm as explained in sec. 4.1.5. The TDC chip is mounted on a 6 layer PCB, the *TDC Plugin Board*. The LV-PECL signals enter this board through differential traces; on the board, the signals are routed using impedance controlled traces, and proper 50 Ω terminations are provided as near as possible to the integrated circuit pins. The lines have been designed with the same length, so that the delay introduced is the same on all the input signals, and with careful minimization of cross-talk effects which would worsen the behaviour of the transmission lines. The TDC is managed using a 92-pin Altera Cyclone Field Programmable Gate Array (FPGA), which handles the flux of events, controls their logical consistency

(e.g., a STOP must follow a START, otherwise it is a false event) and manages the transfer of the digitalized data.

The TDC system is connected via an external SCSI II cable to a home made PCI Interface Board (BiDiMem) that is placed inside a computer. In this way the PC is able to retrieve the acquired data using a 32-bit bus and a simple handshaking based on only two lines, Read REQuest and Read ACKnowledge. Internal data transmission exploits the standard PCI bus.

4.1.5 Detector characterization

Once all the elements of the acquisition chain had been characterized individually, some bench test were performed on the complete system. After these test the performance of the detector was also characterized in UHV conditions.

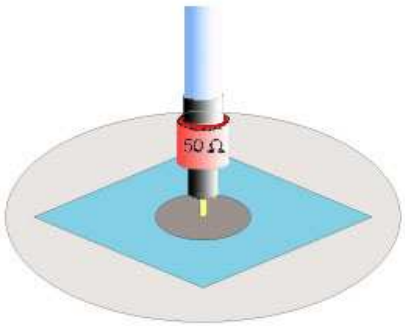

Figure 4.10: Picture of the probe used to inject pulses on the delay-line anode during bench tests.

The linearity of the system was first tested, exciting the delay line anode by means of a pulse generator capacitively coupled to it using a suitable tip (Fig. 4.10) which was moved along the detector by means of a micrometer system. Experimental results (shown in Fig. 4.11) evidence a strict linear relation between measured and effective position of the probe on the detector, with a small divergence only at the borders of the active area.

Other measurements were devoted to the determination of the short term stability of the system. Fig. 4.12 shows the relationship between the standard deviation and the position, working at the repetition rate of 1 MHz; even if the standard deviation is slightly dependent on the position and lower

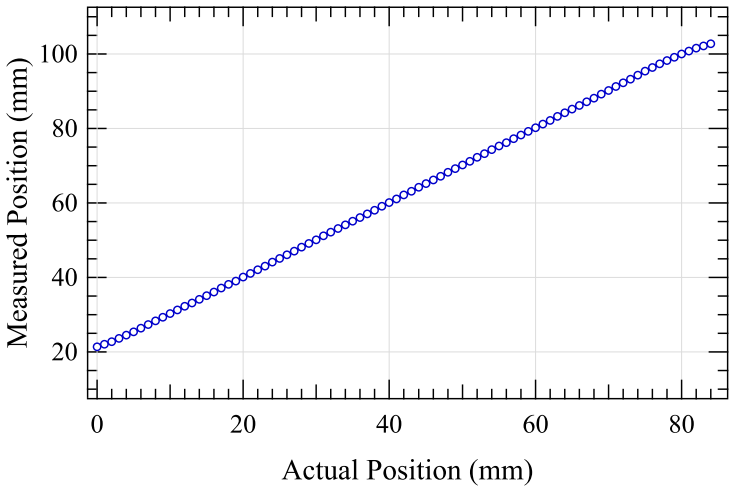

Figure 4.11: Linearity of the sensor: measured position versus real position of the excitation.

in the middle of the detector, its maximum value is better than 60 μm over the whole detector range.

The stability of the system has been validated also with long-term tests. The graph in Fig. 4.13 shows the average values measured during a period of $\approx$ 12 hours of acquisition at a rate of 1 sample per second: the long-term variations are below 10 ps.

Dark counts and spatial resolution of the detector have been investigated in UHV conditions. Dark counts analysis has been performed by polarizing the MPCs and the resistive decoupling pad as in a normal experimental condition, while not using, of course, any light or electron source to excite the MCPs. In a 20 hour test we recorded an average of 4 counts/s, uniformly distributed on the whole area of the detector. In order to extimate the spatial resolution of the system, the detector was partially covered with a steel blade and, with this configuration, the electrons provided by an electron gun were detected. The measured transition across the blade edge is shown in fig 4.14, from which an overall resolution of $\approx$ 60 μm can be deduced.

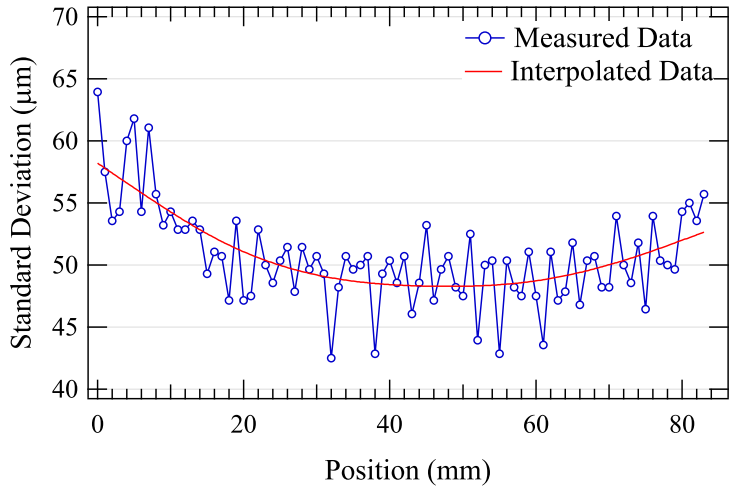

Figure 4.12: Short-term standard deviation of the measurements versus the position on the detector. Blue line with markers: measured data; red line: interpolated data.

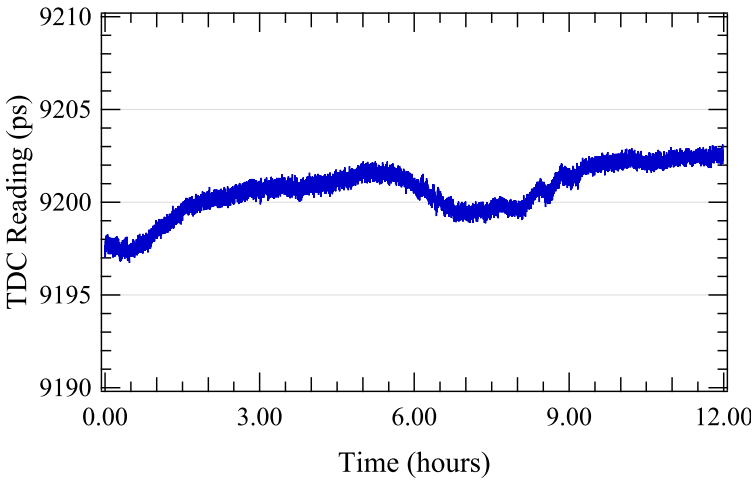

Figure 4.13: Long-term behaviour of the system.

4.1.6 Detector tests on the electron energy analyser

Once bench measurements and first UHV test were performed, the detector was ready to be installed on the PHOIBOS analyser. For data acquisition

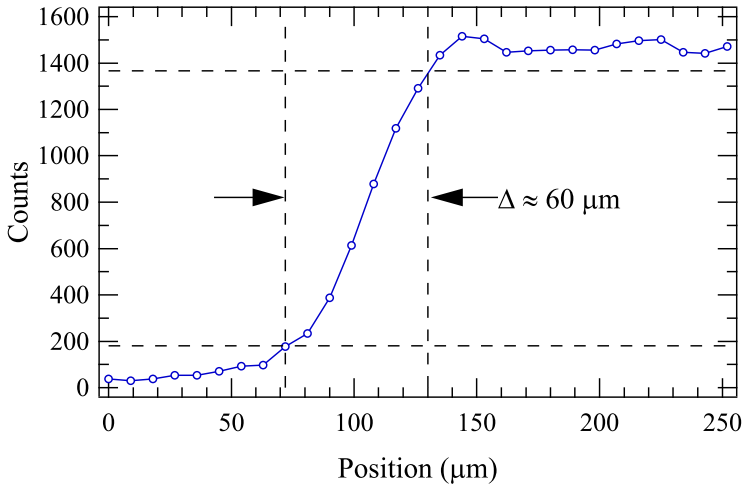

Figure 4.14: Profile of a steel blade perpendicular to the detector encoding direction; from the transition across the edge (10–90%) the resolution is deduced.

the detector was *virtually* divided via software in 1068 channels: the time interval (measured in TDC units) of the whole detector range. This results in a spatial width of the channels of 75 μm, a value that well matches the resolution of the system.

Before any reliable photoemission spectra acquisition, a preliminar calibration of the energy dispersion was needed. In fact, the theoretical relation (3.6) is derived for an ideal analyser and does not take into account trajectory distorions due to fringing fields. By measuring how the kinetic energy value of the Ag $3d_{5/2}$ photoemission peak varies as a function of the region of the detector used to acquire the spectrum, it was possible to find a value for the dispersion of 0.27 meV/channel with pass energy of 1 eV. This parameter is sufficient for every working condition, since the dispersion scales lineraly with the pass energy.

Once calibrated the energy dispersion, we were ready to acquire the first photoemission spectra; for these first tests a Ag(111) sample was used. The measurement of the Ag $3d$ spin-orbit splitting gave a value of 6.00 ± 0.02 eV, in perfect agreement with tabulated references [12], certifying the accuracy of the energy calibration. Moreover, from the evaluation of the Fermi Level broadening at 90 K, the overall resolution with pass energy 5 eV and entrance slit width of 1 mm was extimated to be 25 meV; this result confirmed that

with the new measurement system high-resolution spectra can be achieved even if the analyser parameters are not set to the extreme values of 1 eV for the pass energy and 0.2 mm for the entrance slit, i.e. high-resolution and relatively high count rates can be obtained at the same time.

All the measurements described up to now were performed in the standard scanning mode: for a given energy range, energy step and time window, the "analyzed" energy is scanned with a proper step so that at the end of the process every point of the spctrum includes the contribution of each detector channel, i.e. each channel counts electrons with that kinetic energy for a time interval equal to the selected time window. Using this procedure the time window can be reduced by a factor N with respect to a single channel acquisition (where N is the number of channels) obtaining the same statistical uncertainty. This possibility indeed speeds up the acquisition procedure, but even exploiting the high photon flux delivered by the SuperESCA beamline the fastest acquisitions take $\approx$ 10 s; this time interval between each spectrum can be a limiting factor when real-time measurements are of interest.

In order to drastically reduce the acquisition time per spectrum, the so-called *snapshot* acquisition is needed. This procedure exploits the well known relation between energy and position on the detector (cfr. eq. (3.6)); if the energy range covered by the detector is sufficiently wide and if enough channels are available for the photoemission features to be clearly resolved, it is possible to acquire a detector *image* and obtaining in this way the photoemission spectrum in one single cycle (a single *shot*) of the standard procedure described above.

From this point of view, the newly realized delay-line detector presents some advantages respect to the multianode detectors used for the first attempts of snapshot acquisition:

- The large dimension of the detector along the dispersive direction (80 mm, while for multianode detectors 45–50 mm where the standard values) allows to cover an energy range of $\approx$ 2 eV and $\approx$ 3.8 eV using pass energy 10 and 20 eV respectively. Actually, even larger ranges are available at higher pass energies ($\approx$ 18 eV at pass energy 100 eV), but the worsening of the energy resolution limits the use of these "extreme" parameters.

- The 1068 (virtual) channels of the detector allow the acquisition of spectra with well defined features; as an example, we can consider

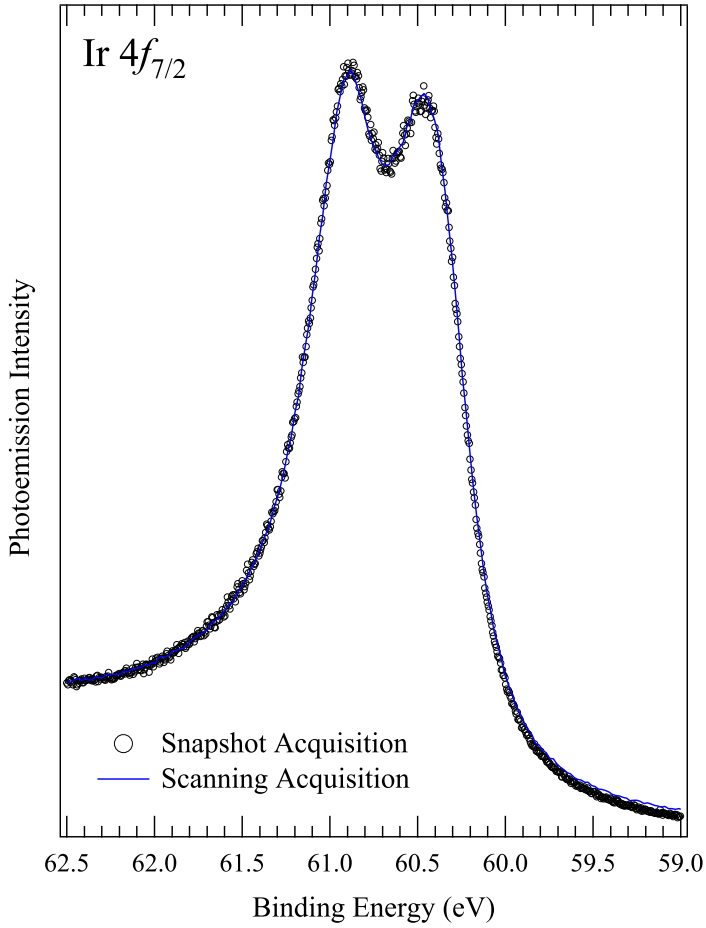

Figure 4.15: Comparison between snaphot spectrum (black open circels) and scanning mode spectrum (blue line) of the Ir $4f_{7/2}$ photoemission peak from a clean Ir(111) surface. Both spectra have been acquired with pass energy 20 eV. It's worth noting the high density of data points on the snapshot spectrum that allows accurate measurements also with this method.

that for a snapshot acquisition at pass energy 10 eV the energy step in the spectrum is 2.7 meV.

- The increase in the number of channels with respect to multianode detectors is obtained without increasing the complexity of the readout system: independently of the number of channels, in fact, only two

signals (START and STOP) need to be managed.

Probably, the most complicated problem to face in order to perform a snapshot acquisition with a multianode detector is the difference in sensitivity of each acquisition chain: it can be so dramatic that differences in measured count rates of 50% between adjacent anodes can be reached. Actually, setting properly the thresholds for one hunderd channels or so is quite a tricky job and the results are not always satisfactory. One possible solution is using a weghting function for snapshot acquisition correction, but the correcting function itself is not easily determined, the main problem being the fact that the weighting factors for adjacent channels are not correlated at all and it is difficult to minimize the error associated with each value.

In the case of a delay-line detector, on the other hand, only two thresholds need to be set (one for each CFD) and the weighting function needs to take into account only for (i) different sensitivities in different areas of the microchannel plate assembly, and (ii) for different transmission of the lens-hemisphere system in different regions of the analyser exit plane. Both these effects are expected to vary smoothly so that, by comparing a flat region of a photoemission spectrum acquired in snapshot mode with the same region measured in scanning mode, a proper weighting function can be easily built.

Fig. 4.15 highlights the accuracy of the results that can be obtained following the weighting procedure described above. The capability of acquiring accurate snapshot data leads to the possibility of obtaining spectra with a sufficiently good signal-to-noise ratio even in time windows as short as 50 ms, as will be explained in more detail in sec. 4.3. Actually, the readout electronics could perform measurements every 5 ms, but in this case, even using synchrotron radiation, the rate of photoelectrons is too low to obtain reasonable photoemission spectra.

4.2 The SuperESCA data acquisition software

Once the new instrumentation was tested and ready for operation, an appropriate control software was needed in order to make the experimental procedures as user friendly as possible. The software was required to fulfill the following tasks:

- controlling the *SPECS HSA 3500 plus* power supply system in order to set the proper voltages to the analyser lenses and hemispheres during

the acquisition process;

- managing data acquisition from the detector readout electronics and synchronizing it with the power supply operation during sweep mode measurements;

- operating the manipulator movements: in particular synchronizing the polar and azimuthal rotations of the sample with spectra acquisition is fundamental in angular resolved experiments;

- giving to the user the possibility to change the pothon energy by setting the monochromator and varying the undulator gaps;

- remotely controlling all the instruments installed on the experimental chamber, e.g. temperature controller, electrometer, pressure gauge, etc.

The software that I developed is written within the LabVIEW^{TM} (Laboratory Virtual Instrumentation Engineering Workbench) platform.

LabVIEW^{TM} is a *dataflow graphical programming language* (G language) from National Instruments [13] commonly used for data acquisition, instrument control and industrial automation. The programs and subroutines are called Virtual Instruments (VIs) and basically consist of a front panel, a block diagram and a connector pane. The *front panel* contains controls and indicators and allows an operator to input data into or to extract data from a running VI: actually it can be considered as the user interface. In the *block diagram* the *code* is implemented by means of function-nodes connected by wires through which the variables propagate following a scheme absolutely similar to a block diagram. Finally, the *connector pane* is mainly used in subroutines (subVIs) to define input and output variables. Fig. 4.16 shows an example of front panel and block diagram of a LabVIEW^{TM} subVI.

Thanks to the structure described above where front panel objects (controls and indicators) are essentially the variables processed in the block diagram, the creation of user interfaces is strictly interconnected to the development of the code and does not require an additional step for the programmer. However, the major benefit of LabVIEW^{TM} over other development environments is the extensive support for accessing instrumentation hardware. Drivers and abstraction layers for many types of instruments and buses are included or are available for inclusion. All this low-level drivers are represented as graphical nodes in the block diagram window and their use is equivalent to that of the large number of functions available in the

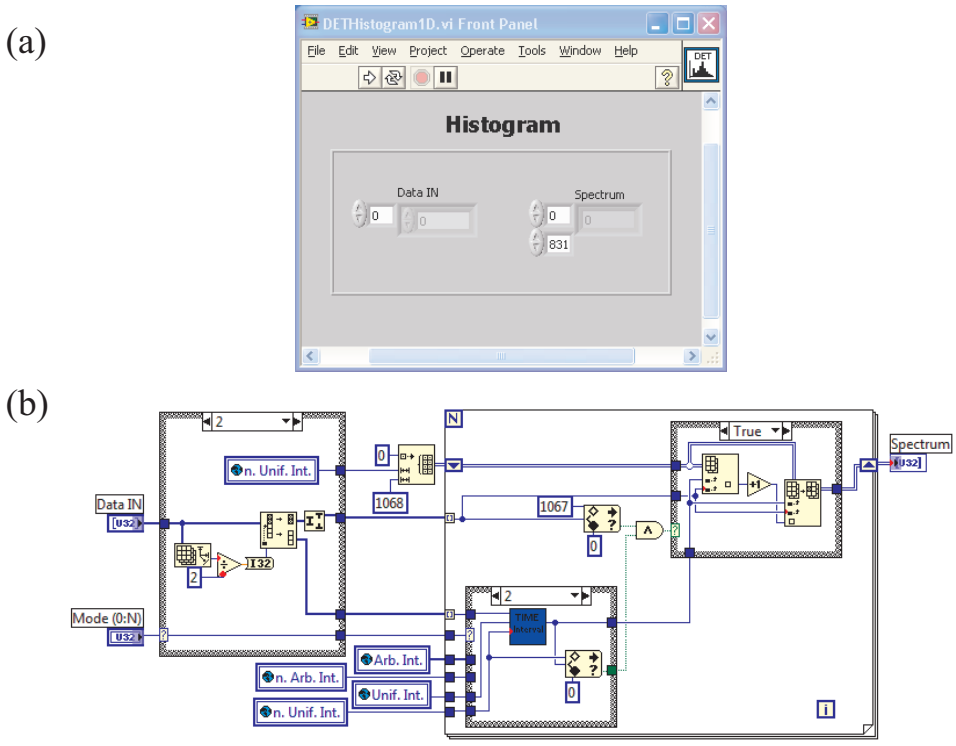

Figure 4.16: Example of the front panel (a) and the block diagram (b) of a LabVIEW^{TM} VI: the Histogram VI on the client PC.

libraries for data acquisition, signal generation, signal processing and analysis, data storage and so on. All these tools render programs written in LabVIEW^{TM} so flexible that they can be easily modified implementing new required features even during experiment performance.

4.2.1 Embedded PC–client PC architecture

The system designed for the SuperESCA beamline software is based on the use of an *embedded PC* controlled by a *client PC*. The former is dedicated to the most demanding instrumentation control processes, while the latter is the computer on which the user works during experiments. The main reason for such a choice is that detector data acquisition and processing are computationally heavy tasks and using a standard solution with a single computer would have expanded the acquisition time up to 30%. In fact, de-

tector data from the TDC consists in an array of values which correspond to the event positions on the detector: these data have to be reorganized in an histogram to obtain a "Frequency vs Position (or Energy)" plot. Within the chosen architecture, the two tasks are shared between the two computers: the embedded PC manages data communication with the detector acquisition chain and in parallel sends the acquired array to the client PC that, in turn, processes data to display the desired type of graph. Fig. 4.17 shows a schematic representation of the configuration used. The tasks executed by the two computers and the user interface of the beamline control program will be described in the next paragraphs.

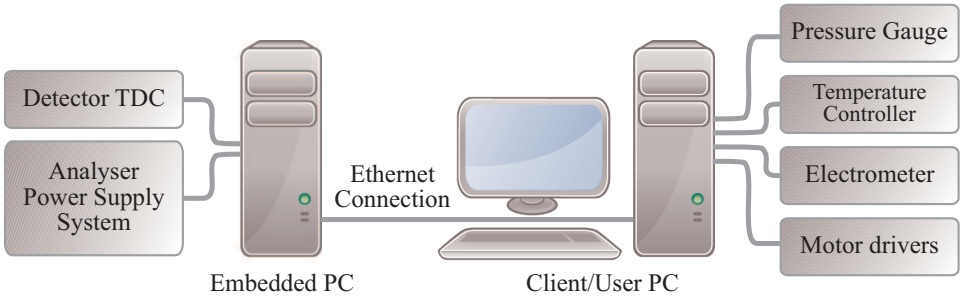

Figure 4.17: Schematic representation of the architecture used for the SuperESCA control system. The devices controlled by each of the two computers are also indicated.

4.2.2 The embedded PC

The embedded PC hosts the *BiDiMem* acquisition board which communicates with the time-to-digital converter and manages the timing to accurately define the counting time window. An ethernet connection provides also control on the SPECS HSA 3500 plus power supply system. Once the computer boot procedure has completed, a LabVIEW^{TM} VI is started automatically; this VI listens for an ethernet connection and once the connection is established, it waits for commands from the client PC.

When a "DETRead:*time*" command is received, the following procedure is executed on the embedded PC:

- the BiDiMem board is asked to acquire event positions for a 5 ms time interval;

- a subVI reads the acquired data through the native PCI bus of the computer and starts another 5 ms acquisition;

- while the new acquisition is performed, another subVI sends data to the client PC via ethernet connection.

All these operations are repeated N times, where N is the number of 5 ms units needed to cover the whole interval specified with the *time* parameter. The parallelization of the BiDiMem reading and data sending procedures allows significant time saving. On the other side of the ethernet connection, the client PC hosts a subVI that receives the position array. Once all the 5 ms cycles are completed, it sends data to a second subVI dedicated to the histogram preparation; while this latter routine processes the data, the first subVI is ready for receiving the subsequent acquisition from the embedded PC. This further task parallelization results very useful when a large number of subsequent detector readings is required as in the case of scanning mode acquisitions.

The other primary task fulfilled by the embedded PC software is to set the proper voltages on the power supply system for the analyser operation at the selected kinetic energy/pass energy combination. This is assured by means of a dll library provided by SPECS and called in a LabVIEW^{TM} subVI each time the "SetKE" command is received.

4.2.3 The User Interface on the client PC

The client computer, besides to the embedded PC, is connected with the Elettra LAN (Local Area Network) and to the BCS system (Beamline Control System) which controls monochromator and undulator gap movements. Moreover, it controls through a multiple serial-port board the manipulator moto drivers, the pressure gauge, the temperature controller and a Keithley electrometer. This latter instrument measures the photoemission current induced by the photon beam on the last focussing mirror of the beamline: since the current is proportional to the photon flux, its value can be used to normalize the intensity of spectra acquired in different moments/conditions.

In order to illustrate the most important features of the software developed for the SuperESCA beamline, the functionalities of the startup window and of the three panels relative to the mostly used acquisition procedures will be described.

The Startup window

Once this VI is launched, it opens the TCP-IP connection with the embedded PC, sets the analyser and detector voltages and initializes the serial-port communication with all the connected devices. From this panel it is possible to select the required acquisition mode and open the corresponding window.

Figure 4.18: Front panel of the Startup VI.

The Global Detector Setup window

This VI continuously reads detector data according to the analyser parameters set on the corresponding controls (kinetic/binding energy, pass energy, lens mode and time window). Besides the graph where the instantaneous spectra are shown, an indicator and a chart with the total counts and their trend have been added in order to facilitate the sample alignement procedure via maximization of the count rate at the beginning of the measurement session.

From this panel (fig. 4.19) the detector voltages can be adjusted to optimize its efficiency and response. Moreover, two cursors can be accessed on the displayed graph by means of which it is possible to define the area of the detector used for the measurements, eliminating eventual distortions at the detector edges. Finally, a control for setting the photon energy is also available.

Figure 4.19: Front panel of the Global Detector Setup VI.

The Sweep Mode window

This panel (fig. 4.20) is designed to manage the traditional sweep (also called scanning) mode acquisitions. In the lower left box, energy range, energy step, integration time and the number of sweeps to be summed are set. It is also possible to select pass energy and lens mode as well as the photon energy. All these parameters can be stored as an XPS-region, so that they can be recalled in a second moment, allowing the possibility to define a series of spectra to be acquired automatically.

On the right side of the panel there are two graphs: in the upper one the current scan is displayed, while in the lower one the sum of the previous sweeps is shown if several scans are expected to be summed.

Data are saved in Igor text format[2]. A parameter file is also stored containing data about the pressure in the experimental chamber, the temperature of the sample, the current on the mirror (so, indirectly, the photon flux) and the polar and azimuthal angles.

Several procedures, corresponding to different types of experiments, have

[2]Igor Pro is a data analysis software from WaveMetrics, Inc. [14].

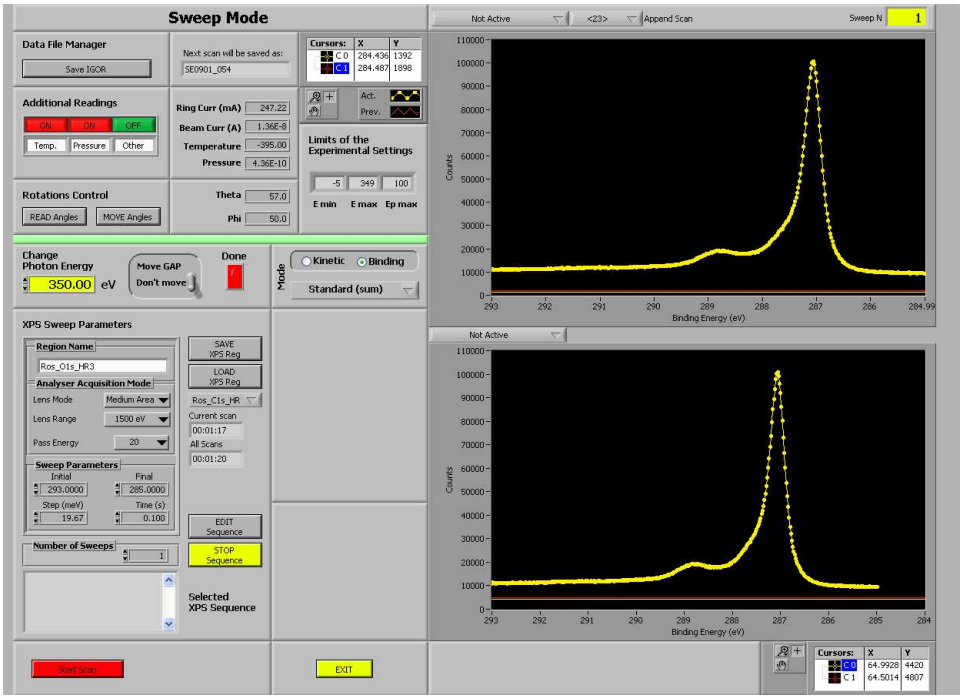

Figure 4.20: Front panel of the Sweep Mode VI as appears when the Standard Acquisition is selected.

been implemented within this VI and can be selected by means of a drop-down menu.

- *Standard (Sum).* The selected number of scans are acquired and summed. It's the most traditional way of performing photoemission experiments.

- *Time Resolved.* The selected scan is repeated and each spectra is saved separately as a column in a matrix together with a time label, so that the temporal evolution of the spectra can be reconstructed.

- *Energy Scan.* The spectrum is recurrently acquired with different photon energies. The photon energy range and the step for the acquisition series are set in a dedicated control box. As explained in sec. 2.5, this is one of the possible acquisition procedures in photoelectron diffraction experiments.

- *Polar (Theta) Scan.* When the CTPO manipulator is used, whose rotations are driven by motors controlled via software, other three modalities are available, dedicated to photoelectron diffraction experiments. When the Polar Scan is active, a series of spectra is acquired with polar emission angles varying according to the selected angular range and step.

- *Azimuthal (Phi) Scan.* Very similar to the Polar Scan, but in this case the azimuthal emission angle is varied throughout the desired angular range.

- *"Pizza".* This acquisition procedure combines polar and azimuthal scans: for each polar angle of the series, an azimuthal scan is performed. The number of points for the azimuthal scans is calculated by the software as a function of the polar angle in order to obtain

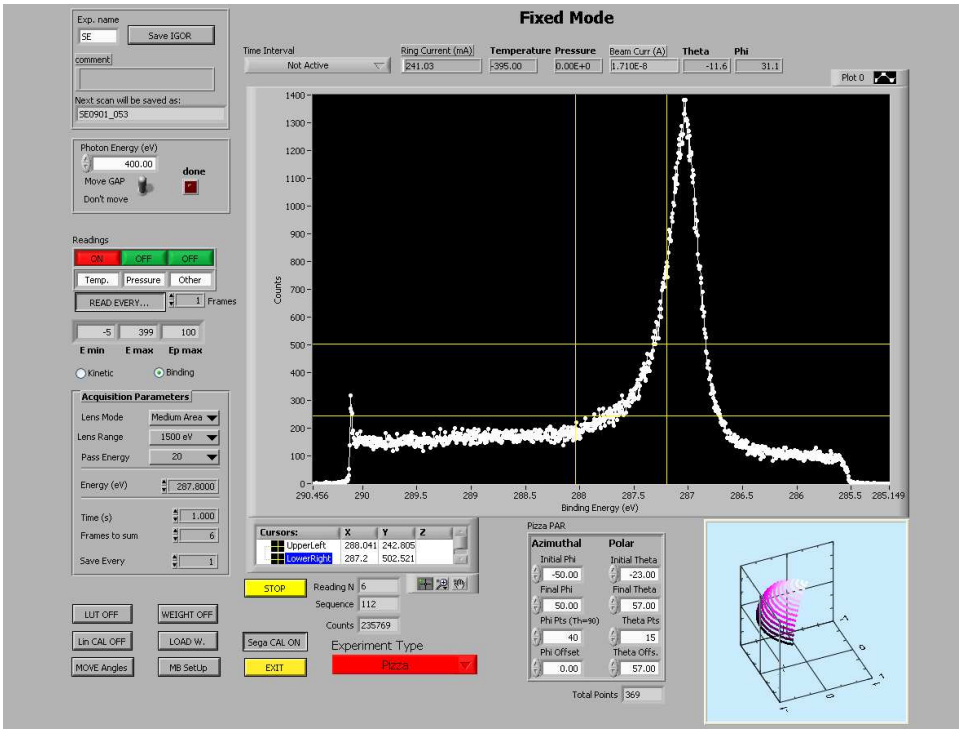

Figure 4.21: Front panel of the Fixed Mode VI when the "Pizza" acquisition is selected.

a uniform sampling over an ideal hemisphere centered on the sample surface.

The Fixed Mode window

This VI controls snapshot (also named "fixed") acquisitions. In this case only the center of the spectrum is selected by the user, because the range and the step are determined by the pass energy and the detector dimensions. The same experimental procedures described for the Sweep Mode window are available.

4.3 The first test: hydrogen oxidation reaction on Rh(111)

4.3.1 Introduction

One of the first test experiments performed with the novel experimental setup was aimed to explore the possibilities offered by the fast snapsot acquisition in following in real-time the evolution of the measured spectra. For this first experiment we chose to investigate a process which is quite important in heterogeneous catalysis: the hydrogen oxidation reaction on Rh(111). The $H_2 + \frac{1}{2}O_2 \rightarrow H_2O$ reaction is of fundamental importance for many reactions widely used in industrial processes, e.g. the partial oxidation of methane that is one of the most exploited processes for natural gas conversion into liquid products, such as methanol, via intermediate *syngas* formation (a mixture of CO and H_2). The high selectivity for H_2 formation of Rh based catalysts (if compared with Pt based ones) is related to the low rate of the competing reaction ($O + H \rightarrow OH$) [15]. The detailed knowledge of the mechanisms involved in the reaction constitutes the groundwork for the development of novel, more efficient catalysts. We decided, therefore, to use the Rh(111) surface as the symplest model for the catalyst: this choice allows focusing on the reaction steps avoiding, in this first stage, complications arising from the influence of the catalyst's morphology on the chemical process.

In the following the reactions steps are listed: essentially it proceeds via adsorption and dissociation of H_2 and O_2, subsequent formation of hydroxyl groups and water molecules and, finally, water desorption from the rhodium

surface.

$$\begin{array}{lrcl} 1. & \mathrm{H_{2,gas}} + 2* & \rightleftharpoons & \mathrm{H_{ads}} + \mathrm{H_{ads}} \\ 2. & \mathrm{O_{2,gas}} + 2* & \rightleftharpoons & \mathrm{O_{ads}} + \mathrm{O_{ads}} \\ 3. & \mathrm{O_{ads}} + \mathrm{H_{ads}} & \rightleftharpoons & \mathrm{OH_{ads}} + * \\ 4. & \mathrm{OH_{ads}} + \mathrm{H_{ads}} & \rightleftharpoons & \mathrm{H_2O_{ads}} + * \\ 5. & \mathrm{OH_{ads}} + \mathrm{OH_{ads}} & \rightleftharpoons & \mathrm{N_2O_{ads}} + \mathrm{O_{ads}} \\ 6. & \mathrm{H_2O_{ads}} & \rightleftharpoons & \mathrm{H_2O_{gas}} + * \end{array} \tag{4.5}$$

Here, *gas* and *ads* indicate the state of the atom or the molecule (in gas phase or adsorbed on the metal surface), $*$ indicates a free adsorption site.

Each reaction step is governed by the respective *reaction rate coefficient*, k_i or k_{-i} if the i-th step is considered as taking place from the right to the left.

The velocity of an adsorption process (steps 1 and 2) is proportional to the sticking coefficient S, that can be expressed as

$$k_i \propto S = S_0 \left(1 - \frac{\theta}{\theta_{max}}\right)^2 \tag{4.6}$$

where S_0 is a constant accounting for the depencence on temperature and surface morphology and $(1 - \theta/\theta_{max})$ expresses the probability of finding free adsorption sites with θ and θ_{max} being the coverage and the coverage at saturation, respectively. The quantity in brackets is powered to the number of surface sites occupied after dissociation, 2 in the case of H_2 and O_2.

The desorption probability (step 6 and the inverse reaction of steps 1 and 2) and intermediate reactions (steps 3 to 5) are described by the Arrhenius equation

$$k_i = \mathrm{A} e^{-\frac{\mathrm{E_a}}{\mathrm{k_B T}}} \tag{4.7}$$

where $\mathrm{k_B}$ is the Boltzmann's constant and A is the so-called pre-exponential factor related to the frequency of collisions between the reactants (typical values fall in the range 10^{12}–10^{13} $\mathrm{s^{-1}}$). $\mathrm{E_a}$ is the activation energy, i.e. the energy barrier that, for desorption processes, atoms or molecules need to overcome in order to reach the final state in gas phase or, in case of intermediate reactions, the barrier that separates the initial state with two isolated reactants A and B from the final state with the molecule AB.

From all these considerations follows that the reaction kinetics, and thus also the selectivity of the catalyst, depends upon the activation energies involved in the process; the detailed analysis of the activation energy for all the intermediate products of a chemical process is a fundamental step for the complete understanding of a catalytic reaction. In this experiment, our

goal was the evaluation of the activation energy for the third step in the reaction process ($O_{ads} + H_{ads} \rightleftharpoons OH_{ads} + *$) by exploiting the fast acquisitions allowed by our novel experimental set-up to follow the evolution of oxygen coverage while dosing O_2 in a background pressure of H_2. The background hydrogen pressure feeds continuously H atoms, so that as soon the first O_2 molecules dissociate on the Rh surface the reaction begins taking place and the trend in the growth of the oxygen coverage depends upon the reaction rate coefficients, until a dynamical equilibrium is reached, when the rate of O adsorption is equal to that of O leaving the surface upon formation of water molecules.

4.3.2 Experimental details

The Rh(111) crystal was cleaned by iterated cycles of Ar^+ sputtering, followed by annealing to 1300 K and oxygen treatment in a 5×10^{-8} mbar of O_2 pressure with the temperature varied periodically between 470 and 1120 K.

During spectra acquisition, the Rh crystal was kept in a constant background pressure of H_2, while O_2 was fed by means of the supersonic molecular beam apparatus described in sec. 3.1.1. By acquiring Rh $3d_{5/2}$ and O $1s$ spectra during modulation of the oxygen flux, obtained by opening a closing periodically the molecular beam shutter, it was possible to follow the evolution of the oxygen coverage.

All the photoemission spectra were acquired at normal emission, i.e. with the sample surface normal to the analyser. Rh $3d_{5/2}$ core level spectra were acquired in "Fixed Mode" with a photon energy of 380 eV. Pass energy was set to 20 eV, so that the measured binding energy range was 306.8–311.2 eV; the 3 mm entrance slit fixed the overall energy resolution of the analyser to ≈90 meV. For O $1s$ core level we used a photon energy of 650 eV, pass energy of 30 eV (binding energy range 524.4–532.6 eV) and we also opened the entrance slit up to 7 mm: this was necessary to increase the electron flux, otherwise the small value of photoemission cross-section for O $1s$ and the lower photon flux delivered by the beamline at this energy wouldn't have allowed fast acquisitions. The time window was set to 50 ms, which resulted in an overall interval of ≈75 ms between consecutive spectra, due to intrinsic dead-time of the acquisition system.

The acquisition procedure was repeated for two hydrogen background pressures (4×10^{-9} and 1×10^{-8} mbar) and in a temperature range between 470 and 590 K, where hydrogen and water molecules are expected to desorb very rapidly, since their desorption temperature is much lower (250 and

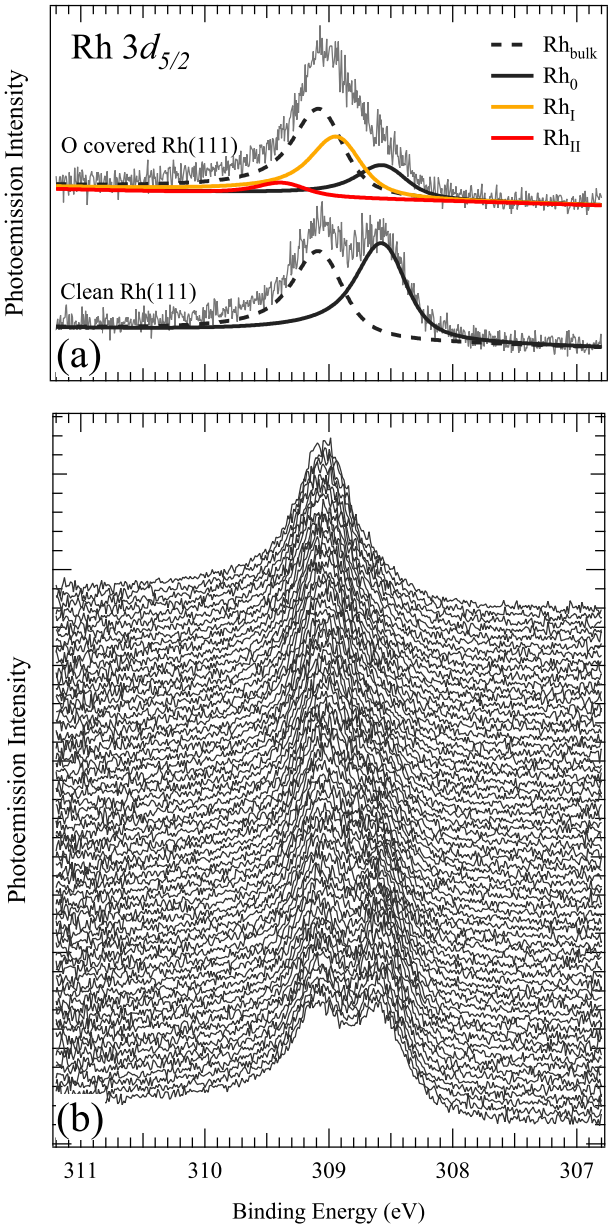

Figure 4.22: (a) Example of Rh $3d_{5/2}$ obtained in Fixed Mode with a 50 ms acquisition. (b) Selection of real-time Rh $3d_{5/2}$ spectra acquired during oxygen uptake.

160 K, respectively), while oxygen remains chemisorbed on the surface up to 1200 K.

The ON and OFF periods for the molecular beam were set to 60 and 120 s respectively for the lower hydrogen pressure, while for higher background pressure we set 120 s ON and 60 s OFF.

At the end of real-time acquisitions, high resolution Rh $3d_{5/2}$ (both of clean and O covered sample) and O $1s$ spectra were acquired both in "Fixed" and in "Sweep Mode", in order to obtain reliable line shape parameters to be used in the fits of real-time spectra.

4.3.3 Results and discussion

Panel (a) of fig. 4.22 shows an example of the good quality of the Rh $3d_{5/2}$ spectra acquired in only 50 ms counting time. The core level line shape for the clean crystal consists of two components: one due to the bulk Rh atoms at 307.15 eV and one due to the under-coordinated surface atoms that presents a surface core level shift (SCLS) of -0.50 eV.

In panel (b) it is possible to follow the evolution of the spectra during a phase of the experimental cycles with the oxygen molecular beam ON. The final spectrum presents a strong reduction of the clean surface component, while two more features appear with SCLSs of -0.14 and +0.3 eV. From previous studies [16, 17] on the ordered $p(2 \times 2)$ ($\theta = 0.25$ ML) and $p(2 \times 1)$ (maximum $\theta = 0.5$ ML) structures formed upon O adsorption on Rh(111), it is known that these two extra components are due to Rh surface atoms that are 1- and 2-fold coordinated with O atoms, respectively (see fig. 4.23). In the following these components will be indicated as Rh_I and Rh_{II}, while the clean surface feature will be addressed as Rh_0.

Fig. 4.24 shows the evolution of the intensities of the rhodium spectral components and that of the O $1s$ peak during the molecular beam ON/OFF cycles at 470 K; data acquired with the two hydrogen background pressure are displayed. The growth trends of Rh_I and O $1s$ during the periods with oxygen beam ON are evident; as can be expected, the Rh_0 intensity behaves complementarily. It is worth noting the low intensity of the Rh_{II} component, and its total absence in the measurements at 1×10^{-8} mbar of H_2, indicating that in this case the maximum O coverage is less than 0.25 ML.

The photoemission intensities could be converted in relative coverage of the corresponding atomic or molecular species. In the case of the Rh_0 component the procedure was quite straightforward: its intensity obtained for a clean surface (I_0) corresponds to a coverage of 1 ML and assuming

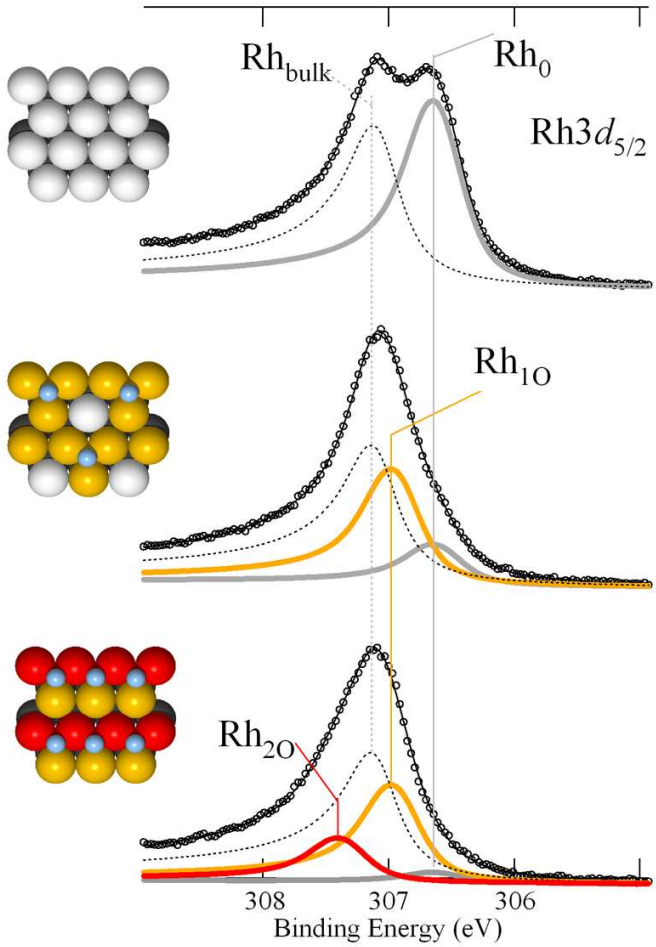

Figure 4.23: Assignment of the four spectral components that can be identified in Rh $3d_{5/2}$ core level spectra of oxygen covered Rh(111) surface.

a linear relation between the number of emitting atoms and the number of collected photoelectrons the evolution of the relative coverage can be obtained from a simple proportion $\theta_{Rh_0}(t) = I_{Rh_0}(t)/I_0$.

As far as Rh_I and Rh_{II} is concerned, we assumed that the sum of the three Rh components constantly corresponds to 1 ML coverage and the corresponding intensities have been scaled accordingly.

The normalizing procedure for the O 1s intensity was more complicated. The Rh_0 coverage was plotted as a function of the O 1s intensity; the trend

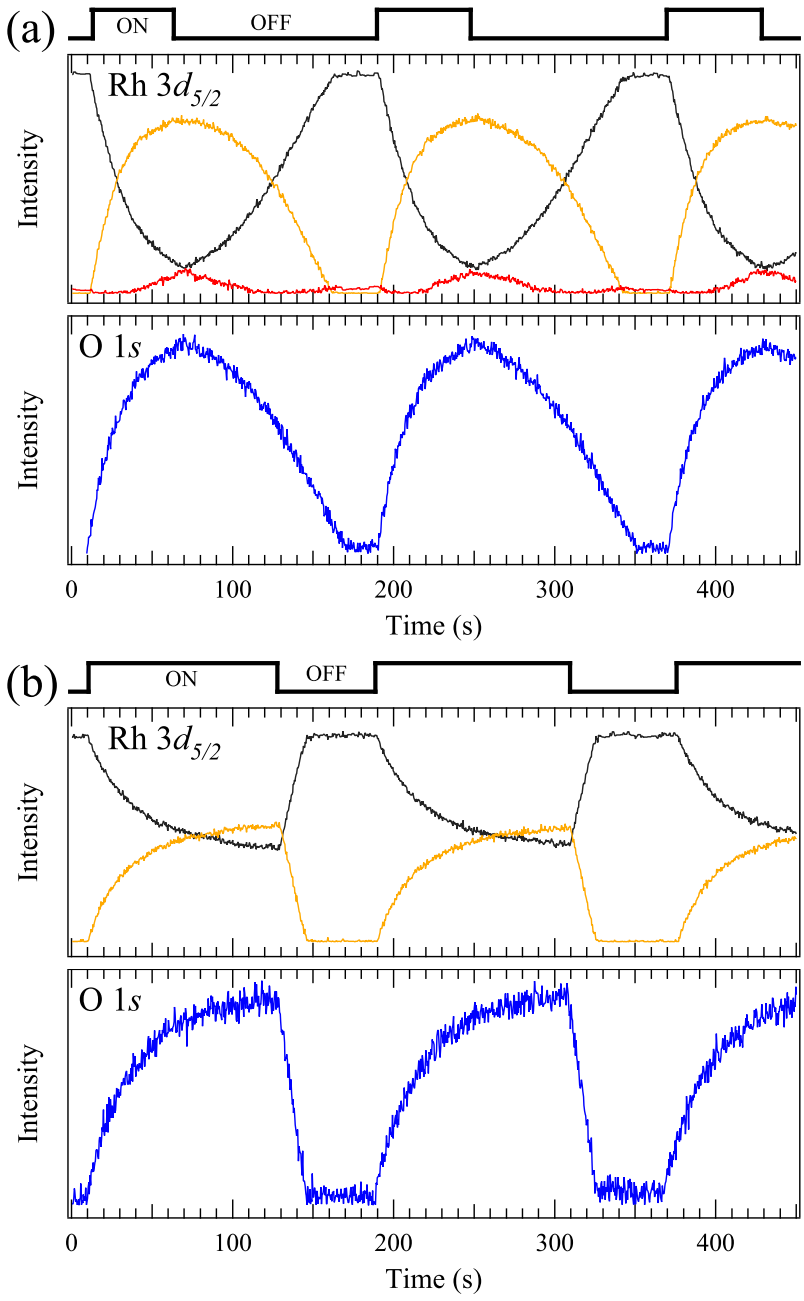

Figure 4.24: Intensity modulation of the Rh $3d_{5/2}$ spectral components and of the O $1s$ core level during oxygen flux modulation at 470 K; hydrogen pressure is 4×10^{-9} and 1×10^{-8} mbar for panel (a) and (b), respectively. The molecular beam ON and OFF periods are evidenced.

during the first seconds of the reaction have been fitted with a line. Since oxygen adsorbs in three-fold sites on Rh(111), for each adsorbed O atom, three Rh surface atoms are modified. Imposing this 3-to-1 relation on the slope that describes the the decrease of the Rh surface component related to the increasing O coverage, the intensity modulations of O 1s core level can be converted into relative coverage units. The above procedure is justified by previous uptake experiments on Rh(100) and Rh(111) crystals [18], where the uptake curves are shown to follow, at least at the beginning of oxygen exposure, a ratio determined by the geometry of the adsorption site.

In order to extrapolate the activation energy from the acquired data, we needed to describe the coverage evolution for the intermediate products starting from the reaction steps of eq. (4.5). From this analysis a set of differential equations can be inferred that express the temporal derivative of the coverage for a given species in terms of contributions of the single reaction steps.

For the adsorption and dissociation processes, the contribution to the coverage is equal to the sticking coefficient multiplied by the number of gas molecules that hit the surface in the unit time, this last quantity being expressed as $\mathrm{p}/\sqrt{2\pi \mathrm{m} \mathrm{k_B} \mathrm{T}}$ for a gas pressure p of molecules with mass m at temperature T. For intermediate reactions and desorption processes, the contribution to the coverage is given by the reaction rate coefficient multiplied by the probability for the two adsorbed species to react (i.e. the product of the coverage of the two reactants by the number of elements involved in the reaction).

In previous studies performed on the same system, several information have been collected that can be used for better defining our model:

- The constant term S_0 of the sticking coefficient for H_2 and O_2 are known with very good precision (0.3 and 0.6, respectively) [19, 20, 21], as well as the activation energy for O_2 dissociation (0.73 eV) [19, 20, 22].

- In the temperature range of our experiments the H coverage is expected to be always below 0.01 ML [20, 23].

- The maximum O coverage achievable above room temperature and in our pressure regime is 0.5 ML, when the formation of the ordered $p(2 \times 1)$ overlayer is observed [16]. For this reason, in the contribution related to oxygen adsorption the coverage needs to be normalized to 0.5 ML.

- At the temperatures of interest the water molecules desorb immediately after formation [24], so that we can omit the rate equation for H_2O coverage and also the contributions due to the dissociation of this molecule.
- The rate of OH formation is expected to be much higher than that of recombination of O atoms and O_2 desorption, so that the latter contribution can be neglected [25].
- We can also omit the contribution of the hydroxyl group dissociation, since its combination with H forming H_2O has higher probability.
- Both O and H atoms on Rh(111) surface adsorb on three-fold fcc sites (i.e. with a Rh atom of the third layer directly below the adsobed atom) [16, 23]. We need to take into account the competition between the coverage of the two species in the calculation of the free adsorption sites.

Following the rules outlined above and taking into account all the information available from previous experiments, the rate equations for O, H, and OH coverage can be expressed as follows:

$$\begin{aligned}
\frac{\mathrm{d}\theta_{\mathrm{H}}}{\mathrm{dt}} &= 2\frac{\mathrm{p}_{\mathrm{H_2}}\mathrm{S}_{0,\mathrm{H_2}}}{\mathrm{n}_0\sqrt{2\pi\mathrm{m}_{\mathrm{H_2}}\mathrm{k}_{\mathrm{B}}\mathrm{T}}}\left[1-(\theta_{\mathrm{H}}+\theta_{\mathrm{O}}+\theta_{\mathrm{OH}})\right]^2 + \\
&\quad -k_{-_1}\theta_{\mathrm{H}}^2 - k_3\theta_{\mathrm{H}}\theta_{\mathrm{O}} - k_4\theta_{\mathrm{H}}\theta_{\mathrm{OH}} \\
\frac{\mathrm{d}\theta_{\mathrm{O}}}{\mathrm{dt}} &= 2\frac{\mathrm{p}_{\mathrm{O_2}}\mathrm{S}_{0,\mathrm{O_2}}}{\mathrm{n}_0\sqrt{2\pi\mathrm{m}_{\mathrm{O_2}}\mathrm{k}_{\mathrm{B}}\mathrm{T}}}\left[1-\left(\frac{\theta_{\mathrm{H}}+\theta_{\mathrm{O}}+\theta_{\mathrm{OH}}}{0.5}\right)\right]^2 + \\
&\quad -k_3\theta_{\mathrm{H}}\theta_{\mathrm{O}} - k_5\theta_{\mathrm{OH}}^2 \\
\frac{\mathrm{d}\theta_{\mathrm{OH}}}{\mathrm{dt}} &= -k_3\theta_{\mathrm{H}}\theta_{\mathrm{O}} - k_4\theta_{\mathrm{H}}\theta_{\mathrm{OH}} - 2k_5\theta_{\mathrm{OH}}^2
\end{aligned} \tag{4.8}$$

If all the sticking and reaction rate coefficients were known, once determined properly the initial conditions, the above differential equations could be integrated numerically and the evolution of the coverage could be simulated. In this experiment, however, the rate coefficients are the object of the analysis: in this case the simulations can be used to fit the measured coverage evolution, the unknown coefficients being the fit parameters to be optimized. This procedure, of course, is much more complicated and time consuming than the fit routines used for the analysis of the photoemission spectra. As a starting point, the values found in literature for the activation

energies and the pre-exponential factors have been used, then, one at the time, all the parameters were relaxed. Results of the fitting procedure for the data collected for the two hydrogen pressures at 470 K are reported in fig. 4.25.

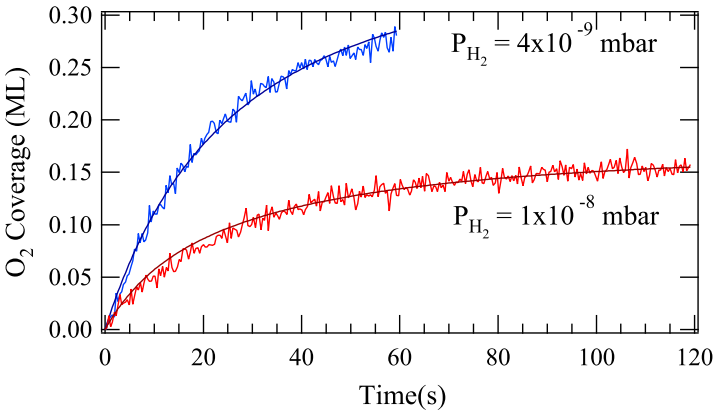

Figure 4.25: Fits of the oxygen uptake curves obtained during the measurement session at 470 K.

From these plots the first inconsistencies in the model we used to interpret the experimental data can be argued. As can be noted in the graph, the different slopes at the beginning of oxygen exposure require two different S_{0,O_2} coefficients to properly fit the uptake curves. On the other hand, being the sample temperature and the pressure of the molecular beam the same, this parameter is expected to have the same value for both experiments. The different initial growth rates appear somehow related to the different hydrogen pressures used in the experiments: in our model, on the other hand, while the OH production appears fundamental in determining the different coverage values at equilibrium (note the different equilibrium coverage in the two plots of fig. 4.25), it is not effective in limiting the O coverage immediately after opening the O_2 molecular beam. The initial behaviour of the oxygen coverage is thus not explained within our model that, for this reason, needs to be improved in order to achieve fully relieble results. In order to achieve first approximated results, however, two values for S_{0,O_2} have been allowed in the fitting procedures.

Another problem in data interpretation arises from the fact that k_{-1}

and k_3 coefficients are correlated: actually, they regulate the amount of hydrogen desorbing from the surface or involved in OH formation. For this reason the two parameters cannot be estimated within a reasonable uncertainty: keeping their ratio constant, in fact, the absolute values for the two coefficients can vary even of one order of magnitude without significant worsening of the fit results.

The last limit of the proposed model emerges form the observation of the plot relative to the low H_2 experiment in fig. 4.25 (a). The fit does not fit in the proper way the experimental data: at ≈ 0.2 ML the fit leads to an underestimation of the coverage, while above ≈ 0.25 ML the experimental values are overestimated. This effect is probably related to the phase transition between the $p(2 \times 2)$ and the $p(2 \times 1)$ structures occurring in this coverage range, slowing down the O uptake process. This transition is not taken into account in rate equations, since our simplified model is based on the assumption that sticking and reaction rate coefficients are constants. Such an assumption was required in order to obtain a soluble set of equations, but several theoretical [26] and experimental [27] studies indicate that these quantities are coverage-dependent.

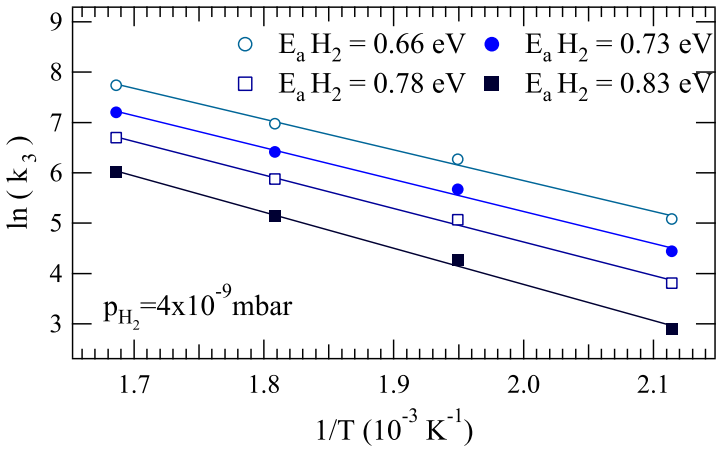

Figure 4.26: Arrhenius plots of the k_3 reaction rate constant obtained from the fitting procedure of the oxygen uptake curve. The four plots refer to different values guessed for the activation energy of hydrogen desorption (see text).

Although the proposed model evidenced some limits, we finalized our analysis extrapolating the activation energy for OH production. Since it was not possible to determine both k_{-1} and k_3 by fitting the uptake curves, we limited the k_{-1} value in a range determined by the values found in literature: the pre-exponential factor was set to 1×10^{13} s^{-1} and the activation energy for hydrogen desorption was limited in the range 0.66–0.83 eV.

Fig. 4.26 reports the Arrhenius plots obtained for the set of experiments at the lower hydrogen pressure by reporting the natural logarithm of k_3 as a function of the inverse temperature 1/T. According to Arrhenius equation, these quantities are supposed to follow a linear relation and the slope obtained from the linear regression procedure, normalized by k_B, gives the activation energy value. In the graph four sets of data are reported, corresponding to different assumptions for the activation energy of H_2 desorption. The resulting activation energy for OH formation is 0.57 ± 0.05 eV.

4.3.4 Conclusions

From a quantitative point of view, the results of this investigation on the hydrogen oxidation reaction on the Rh(111) surface cannot be considered brilliant. The value we obtained for the activation energy of the OH formation step (0.57 eV) differs significantly from the values found in literature (≈ 0.9 eV).

Such a large discrepancy can be due to incorrect choices for the rate constants we had to insert *a priori* in the equations that describe our model. As a matter of fact, if we use 10^{15} s^{-1} as the pre-exponential factor of k_{-1} (instead of 10^{13} s^{-1}) and 0.73 eV for the corresponding activation energy, we obtain a final value of 0.67 eV, i.e. an increas as large as the 17%. We can therefore conclude that the kind of analysis we attempted for this system can give reliable results only when they are obtained by means of a self-consistent algorithm, i.e. when all the unknown parameters can be inferred from the fitting procedure with the desired accuracy.

The unsatisfactory numerical result can also be ascribed to a not complete modelization of the reaction: the above considerations on (i) the $p(2 \times 2)$–$p(2 \times 1)$ phase transition and (ii) the unexplained differences in the first stages of O uptake for the two hydrogen background pressures indicate that some fundamental aspects in the reaction process have been neglected in our model.

Improvements can come only from other experimental investigations that could help in designing a new, more rigorous model for the examined chemical reaction.

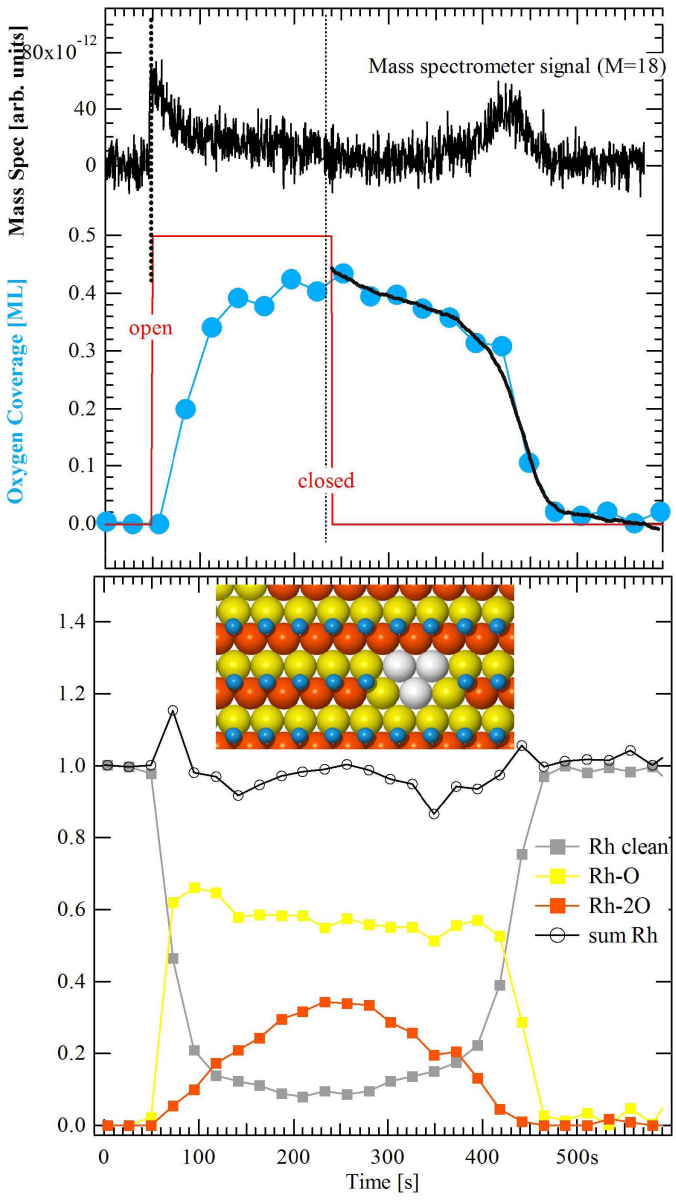

Figure 4.27: (Top panel) Evolution of oxygen coverage and water formation rate during an O molecular beam ON/OFF cycle. Oxygen coverage is detemined from the intensity of the O 1*s* core level, while water formation is monitored by means of a mass spectrometer tuned on 18 a.m.u. molecular mass. (Bottom panel) Evolution of the Rh $3d_{5/2}$ spectral components during an equivalent ON/OFF cycle. From [26].

From the instrumental point of view, this experiment highlighted how our novel apparatus is capable of unheard-of acquisition rates that allow detailed real-time measurements and dynamical analysis of chemical reactions. A comparison with the data acquired in identical experimental conditions can help understanding the importance of the technical improvements realized on the experimental apparatus. Also this experiment was performed on the SuperESCA beamline, but using the previous experimental set-up [26]. With that apparatus, actually, the SuperESCA research group produced many pioneering works on photoemission spectroscopy real-time investigations [28]. Fig. 4.27 displays the evolution of O coverage as obtained from the analysis of the spectral component intensities. In this case the acquisition time was of ≈ 20 s/spectrum: it is evident how the oxygen growth trend upon molecular beam opening is defined by only 2–3 experimental points. With the fast acquisition times achievable with the novel apparatus (acquisition time is more than two orders of magnitude shorter), the progress of O coverage is definitely better defined (compare with plots in fig. 4.24) and such a temporal resolution permits the detection of short living species under reaction conditions.

All the technical improvements of the experimental apparatus and the acquisition procedures resulted, thus, in the high electron transmission through the analyser and the high energy- and time-resolution required for experiments on the evolution of supported nanoclusters and low-dimensional systems. In the next chapters I will report on how these characteristics were fully exploited in several experimental studies.

Bibliography

[1] Burle Industries, Inc., *Channeltron electron multiplier handbook for mass spectrometry applications.*

[2] L. Gregoratti, A. Barinov, E. Benfatto, G. Cautero, C. Fava, P. Lacovig, D. Lonza, M. Kiskinova, R. Tommasini, S. Mähl, and W. Heichler, *48-Channel electron detector for photoemission spectroscopy and microscopy*, Review of Scientific Instruments **75** (2004), 64–68.

[3] L. Gori, R. Tommasini, G. Cautero, D. Giuressi, M. Barnaba, A. Accardo, S. Carrato, and G. Paolucci, *An embedded control and acquisition system for multichannel detectors*, Nuclear Instruments and Methods in Physics Research A **431** (1999), 338–346.

[4] A. Nambu, J.-M. Bussat, M. West, B.C. Sell, M. Watanabe, A.W. Kay, N. Mannella, B.A. Ludewigt, M. Press, B. Turko, G. Meddeler, G. Zizka, H. Spieler, H. van der Lippe, P. Denes, T. Ohta, Z. Hussain, and C.S. Fadley, *An ultrahigh-speed one-dimensional detector for use in synchrotron radiation spectroscopy: first photoemission results*, Journal of Electron Spectroscopy and Related Phenomena **134–140** (2004), 691–697.

[5] M. Lampton and C.W. Carlson, *Low-distotion resistive anodes for two-dimensional position-sensitive MCP systems*, Review of Scientific Instruments **50** (1979), 1093–1097.

[6] H. Wagner, A. Orthen, H.J. Besch, S. Martoiu, R.H. Menk, A.H. Walenta, and U. Werthenbach, *On image reconstruction with the two-dimensional interpolating resistive readout structure of the Virtual-Pixel detector*, Nuclear Instruments and Methods in Physics Research A **523** (2004), 287–301.

[7] M. Lampton, O. Siegmund, and R. Raffanti, *Delay line anodes for microchannel-plate spectrometers*, Review of Scientific Instruments **58** (1987), 2298–2305.

[8] Mini-Circuits (http://www.mini circuits.com).

[9] J.L. Wiza, *Microchannel plate detectors*, Nuclear Instruments and Methods **162** (1979), 587–601.

[10] L. Giudicotti, M. Bassan, R. Pasqualotto, and A. Sardella, *Simple analytical model of gain saturation in microchannel plate devices*, Review of Scientific Instruments **65** (1994), 247–258.

[11] Acam (http://www.acam usa.com).

[12] J.F. Moulder, W.F. Stickle, P.E. Sobol, and K.D. Bomben, *A reference book of standard spectra for identification and interpretation of XPS data.* Perkin-Elmer Corporation, Physical Electronic Division, Eden Praire, Minnesota, 1994.

[13] National Instruments (http://www.ni.com).

[14] Inc. (http://www.wavemetrics.com) WaveMetrics.

[15] D.A. Hickman and L.D. Schmidt, *Production of Syngas by direct catalytic oxidation of methane*, Science **259** (1993), 343–346.

[16] M.V. Ganduglia-Pirovano, M. Scheffler, A. Baraldi, S. Lizzit, G. Comelli, G. Paolucci, and R. Rosei, *Oxygen-induced Rh* $3d_{5/2}$ *surface core-level shifts on Rh(111)*, Physical Review B **63** (2001), 205415.

[17] A. Baraldi, S. Lizzit, A. Novello, G. Comelli, and R. Rosei, *Second-layer surface core-level shift on Rh(111)*, Physical Review B **67** (2003), 205404.

[18] A. Baraldi, S. Lizzit, G. Comelli, M. Kiskinova, R. Rosei, K. Honkala, and J.K. Nørskov, *Spectroscopic Link between Adsorption Site Occupation and Local Surface Chemical Reactivity*, Physical Review Letters **93** (2004), 046101.

[19] J. Klikovits, M. Schmid, J. Gustafson, A. Mikkelsen, A. Resta, E. Lundgren, J.N. Andersen, and P. Varga, *Kinetics of the Reduction of the Rh(111) Surface Oxide: Linking Spectroscopy and Atomic-Scale Information*, Journal of Physical Chemistry B **110** (2006), 9966–9975.

[20] M.L. Wagner and L.D. Schmidt, *Model catalytic oxidation reactions: oxygen with* H_2*,* NH_3*, and* N_2H_4 *on Rh(111)*, Journal of Physical Chemistry **99** (1995), 805–815.

[21] M. Beutl, J. Lesnik, and K.D. Rendulic, *Adsorption dynamics for CO, CO-clusters and* H_2 *(*D_2*) on rhodium(111)*, Surface Science **429** (1999), 71–83.

[22] S. Wilke, V. Natoli, and M.H. Cohen, *Theoretical investigation of water formation on Rh and Pt Surfaces*, Journal of Chemical Physics **112** (2000), 9986–9995.

[23] C.J. Weststrate, A. Baraldi, L. Rumiz, S. Lizzit, G. Comelli, and R. Rosei, *A surface core-level shift study of hydrogen interaction with Rh(111)*, Surface Science **566–568** (2004), 486–491.

[24] S. Yamamoto, A. Beniya, K. Mukai, Y. Yamashita, and J. Yoshinobu, *Water Adsorption on Rh(111) at 20 K: From Monomer to Bulk Amorphous Ice*, Journal of Physical Chemistry B **109** (2005), 5816–5823.

[25] A. Schaak and R. Imbihl, *Bistability and formation of low work function areas in the O_2+H_2 reaction on a Rh(111) surface*, Journal of Chemical Physics **113** (2000), 9822–9829.

[26] A. Suriano, *Quantum mechanical modeling of the chemical reactivity of metal surfaces: two case studies involving water formation and dissociation.* PhD thesis, SISSA, Internationa School for Advanced Studies, 2007.

[27] M.H. Koch, P. Jakob, and D. Menzel, *The influence of steps on the water-formation reaction on Ru(001)*, Surface Science **367** (1996), 293–306.

[28] A. Baraldi, G. Comelli, S. Lizzit, M. Kiskinova, and G. Paolucci, *Real-time X-ray photoelectron spectroscopy of surface reactions*, Surface Science Reports **49** (2003), 169–224.

Chapter 5

Surface core level shift study of Pd/Ru(0001) pseudomorphic overlayers

5.1 Introduction

The advances in surface science techniques and instrumentation, combined with first-principles calculations, provide insight into the catalytic activity from an atomistic point of view. Detailed studies on elemetary chemical processes on well-characterized single crystal surfaces (as models of the active part of catalysts) contributed substantially to the understanding of chemical processes taking place on different supports. This offers the groundwork for the rational design of novel catalysts [1, 2].

In particular, transition metal alloys appear a very interesting subject since they often present higher or more selective catalytic activity when compared to those of the single constituents. Their enhanced catalytic properties are governed by different factors: (i) the selectivity of each component in promoting different elementary reaction steps, (ii) novel electronic structural properties arising from the interaction between the two metals, and (iii) the unique surface morphology resulting from the alloying process. The possibility of varying the composition of the surface alloy by changing the base metals or the amount of the second element deposited on the transition metal *host* offers a unique opportunity for tailoring the catalyst's properties.

However, because of the strong interplay of all the above mentioned factors, understanding the origin of the observed modifications in chemical reactivity and relating them to each individual effect is a very difficult task.

Moreover, if the design of *custom* catalysts is the target, it is still necessary to develop new experimental techniques that could allow the direct determination of the chemical reactivity of the newly synthetized materials.

In this context, bi-metallic pseodomorphic overlayers represent model systems simple enough for developing a systematic understanding of the relationship between microscopic structure and catalytic activity.

A bimetallic surface alloy can be obtained by Physical Vapour Deposition (PVD) of a metal on a well ordered surface of a host metal. If the surface *segregation energy* (defined as the energy cost of transferring an impurity atom (solute) from the bulk to the surface of the host crystal) is strongly negative (≤ -0.7 eV), the solute metal prefers lying on the host surface rather than intermixing with it, and a well defined interface can be prepared [3]. In this case, after deposition on the host surface, solute atoms diffuse until they meet a defect, a step or an existing cluster, so that they start the nucleation process. The successive behaviour depends on the surface free energies of the two metals: the deposited metal can grow layer-by-layer (Frank-van der Merwe growth) or, after the completion of the first layer, it can form three-dimensional islands (Stransky-Krastanov growth). A third possibility is the formation of three-dimensional clusters without previous formation of a wetting layer (Volmer-Weber growth) [4]. The term *pseudomorphic growth* refers to a situation where the first adlayer is formed adopting the lattice parameter of the host crystal, different from the *bulk* value of the deposited metal. In general, only the first layer grows pseudomorphically, while the succesive layers assume lattice constants progressively closer to that of the crystal structure of the bulk admetal.

Hybridization of valence atomic orbitals of the two metals in the pseudomorphic system induces perturbations on its electronic configuration. All the perturbations related to the bond between the different metals are known as *ligand effect*, while the mismatch between the lattice constants of the two metals induces the so-called *strain effect*.

All these factors that influence the electronic properties of the system act, consequently, also on the surface reactivity. For this reason we need some tool to directly determine the chemical reactivity of the resulting system. Within the Density Functional Theory (DFT) framework, the *d-band model* has been developed [5, 6]: surface chemical reactivity is directly related to the energy position of the d-band centre (ϵ_d) of pure or alloyed transition metals. This model has proven to be very successful in explaining chemical trends in the interaction of atoms and simple molecules with tran-

sition metals and has clarified the role of substrate composition, structure, and local atom coordination [7]. Indeed, it has been found that a clear linear relationship holds between ϵ_d and the adsorption energy of most common atoms and molecules [8, 9, 10].

Altough ϵ_d appears a good candidate as a descriptor of a system's chemical activity, problems arise when we try to determine experimentally its value. While DFT calculations of the surface projected d-band centre are routinely accomplished, the experimental determination of the surface d-band Density Of States (DOS) of pseudomorphic overlayers (by means of Ultraviolet Photoelectron Spectroscopy) is extremely difficult because of band dispersion, overlapping contributions from species in different chemical and geometrical environment, and the presence of bulk and surface components that cannot be clearly separated.

As already explained in sec. 2.4.2, changes in the valence band centre are directly reflected in corresponding shifts of the core-level binding energies. In their pioneering investigation on supported monolayers on different metal substrates Rodriguez and Goodman [11] reported a correlation between the changes in the desorption temperature of adsorbates and relative substrate core-level shifts, indicating that core-level measurements can be a powerful tool for examining surface chemical reactivity. However, the surface core-level shifts (SCLSs) measured in photoemission experiments are affected by final state contributions (sec. 2.4) that can be significant, in particular for noble metals like Cu and Ag where the low density of states at the Fermi level results in a rather inefficient screening of the core hole. For a large number of transition metal systems (both, clean and adsorbate-covered), high resolution photoemission experiments have shown a linear relationship between SCLS changes, and the theoretically determined ϵ_d shifts, thus indicating that the screening correction magnitude is rather small compared to the overall trend of initial state shifts [12, 13, 14, 15, 16]. Because of these properties, the idea of using the changes of SCLS as an experimental descriptor of the trends in surface chemical reactivity has been put forward [17].

In the study presented in this chapter our target consisted in understanding whether the SCLS can be considered a good indicator of the chemical properties also in the case of transition metal alloys. The Pd/Ru system was chosen because it presents a number of interesting properties, making it particularly suitable for our porposes. It has already been shown that Pd overlayers grow pseudomorpically on Ru(0001) surfaces [18]. Pd has a segregation energy of ≈ -1 eV with respect to Ru [3], which prevents intermixing up to very high temperatures (and allows therefore moderate

annealing procedures).

In this chapter I will describe how with a series of photoemission experiments, paralleled by DFT calculations, we succeded in investigating the electronic structure of pseudomorphically grown Pd layers on Ru(0001) and in showing that SCLS of Ru and Pd species are directly proportional to the calculated d-band centre shifts, thus demonstrating that also for this alloy the magnitude of the screening correction does not obscure the overall trends in the initial state shifts. Also for this pseudomorphic overlayer system, therefore, core-level shifts contain relevant electronic structure information, and can be considered a reliable descriptor of surface chemical reactivity trends.

5.2 Experimental and computational details

The Ru crystal was cleaned by performing cycles of Ar^+ sputtering, annealing to 1570 K, and oxygen treatment at 5×10^{-7} mbar in the temperature range 1000–1200 K, for removing the residual carbon. A final annealing to 1500 K was done to induce oxygen desorption. After this procedure, the sample showed a sharp (1×1) LEED pattern with low background, and flat terraces about 500 Å large.

The Pd evaporator consisted in a 0.25 mm diameter high-purity Pd wire, which could be resistively heated. The evaporation filament was housed in a tantalum cylinder, with an opening of about 20 mm at the front face for directing the metal deposition onto the Ru substrate, while preventing Pd evaporation onto UHV system components. The metal source was gradually heated and then held at the evaporation temperature for a fixed amount of time. The pressure in the UHV systems was always kept below 4×10^{-10} mbar for preventing the adsorption of background impurities on the bimetallic surface.

The growth process has been characterized in a separate UHV experimental station equipped with an Omicron Spot Profile Analysis LEED. The analysis of the intensity modulation and the line-profile changes of the zero$^{\text{th}}$-order LEED spot evidenced a periodic modulation of the diffraction intensity and the absence of extra-tails that are indicative of a Frank-van der Merwe hetero-epitaxial growth. Pd deposition at 320 K with a flux of about 0.9 ML/minute (followed by subsequent annealing to 670 K), resulted in a layer-by-layer growth up to 2 ML, as previously reported [18]. Upon formation of the third layer, a slight disorder takes place and the fourth layer starts forming before the completion of the third one.

Once determined the best evaporation conditions (filament current, evaporation time, substrate temperature and postdeposition annealing temperature) for a layer-by-layer growth of Pd on Ru(0001), the sample and the evaporator were moved to the SuperESCA beamline for the high resolution photoemission measurements. The Pd and Ru $3d_{5/2}$ photoemission measurements were performed with a photon energy of 470 eV, keeping the sample at room temperature. All the spectra were measured at normal emission. The overall energy resolution (electron energy analyser and x-ray monochromator) was 40 meV for both Pd and Ru $3d_{5/2}$ core level spectra. The electron binding energies are referred to the Fermi energy position, measured under the same experimental conditions (photon energies, analyzer setup, and surface temperature). Photoemission measurements in the C $1s$, S $2p$, and O $1s$ core level regions, confirmed the absence of contaminants.

Theoretical calculations have been performed in collaboration with D. Alfé and M. Pozzo from University College London using the PWscf code [19]. For the Density Functional Theory calculations the Generalized Gradient Approximation (GGA) developed by Perdew, Burke and Ernzerhof (known as PBE) was used [20]. Surfaces have been modelled using a slab geometry with five atomic layers and a vacuum region of 12 Å. Two atomic layers were fixed to the bulk inter-atomic distance and only the topmost three atomic layers have been allowed to relax.

The position of the d-band center ϵ_d with respect to the Fermi energy $\mathrm{E_F}$ was calculated as

$$\epsilon_d = \int_{-\infty}^{E_0} \mathrm{dE(E - E_F)pd(E)}$$

where pd(E) is the projection of the electronic density of states onto atomic orbitals of type d, and $\mathrm{E_0}$ is some cutoff energy.

5.3 Results and discussion

5.3.1 Photoemission measurements

Figures 5.1 and 5.2 show series of Ru $3d_{5/2}$ and Pd $3d_{5/2}$ core level spectra, respectively, for different Pd deposition times, up to completion of three Pd layers. As previously reported [21, 22], the Ru $3d_{5/2}$ spectrum of the clean surface (before starting Pd deposition), consists of three components: a peak centered at 279.70 ± 0.02 eV binding energy, originating from Ru atoms of

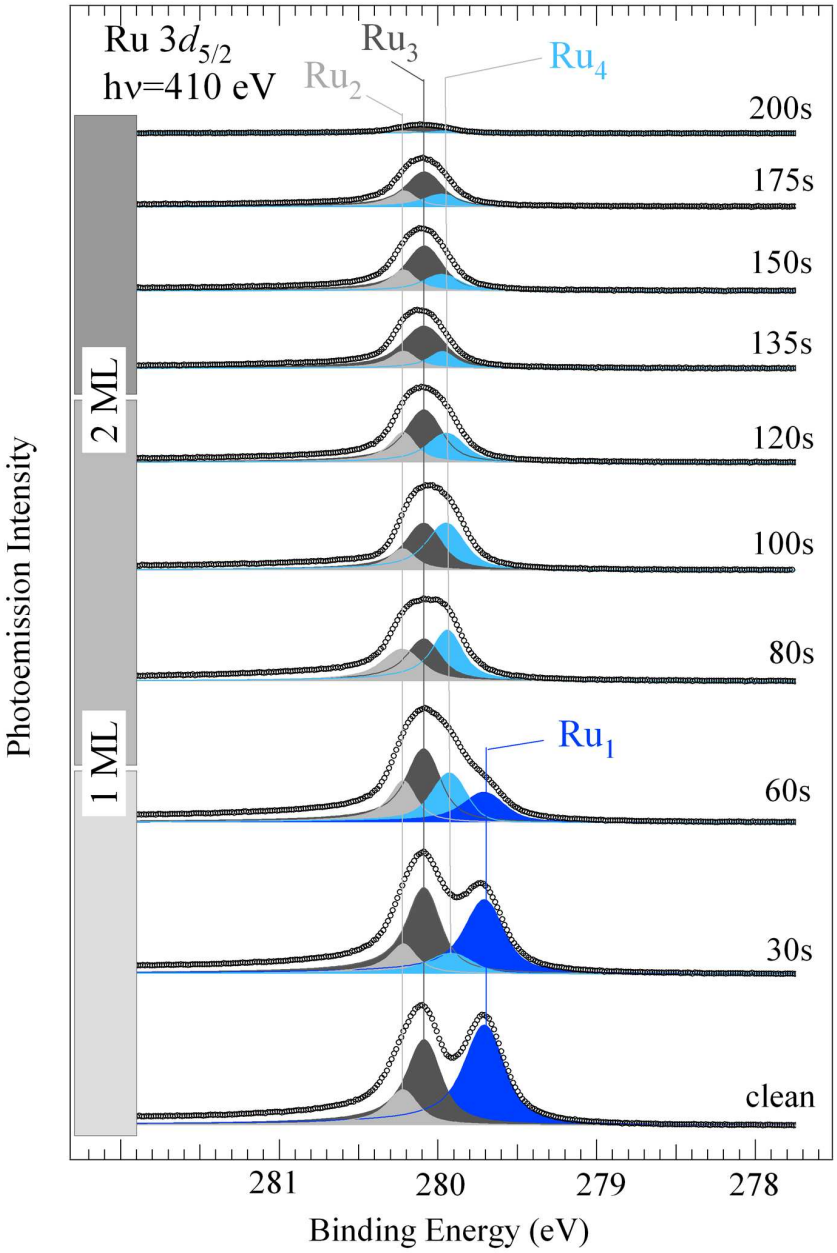

Figure 5.1: Series of high-energy resolution Ru $3d_{5/2}$ core-level spectra collected at T=300 K after different Pd deposition times. The solid lines superimposed to the experimental data (open circles) are the result of the final fits; the colored curves correspond to the different Ru components. The individual components are plotted after linear background removal.

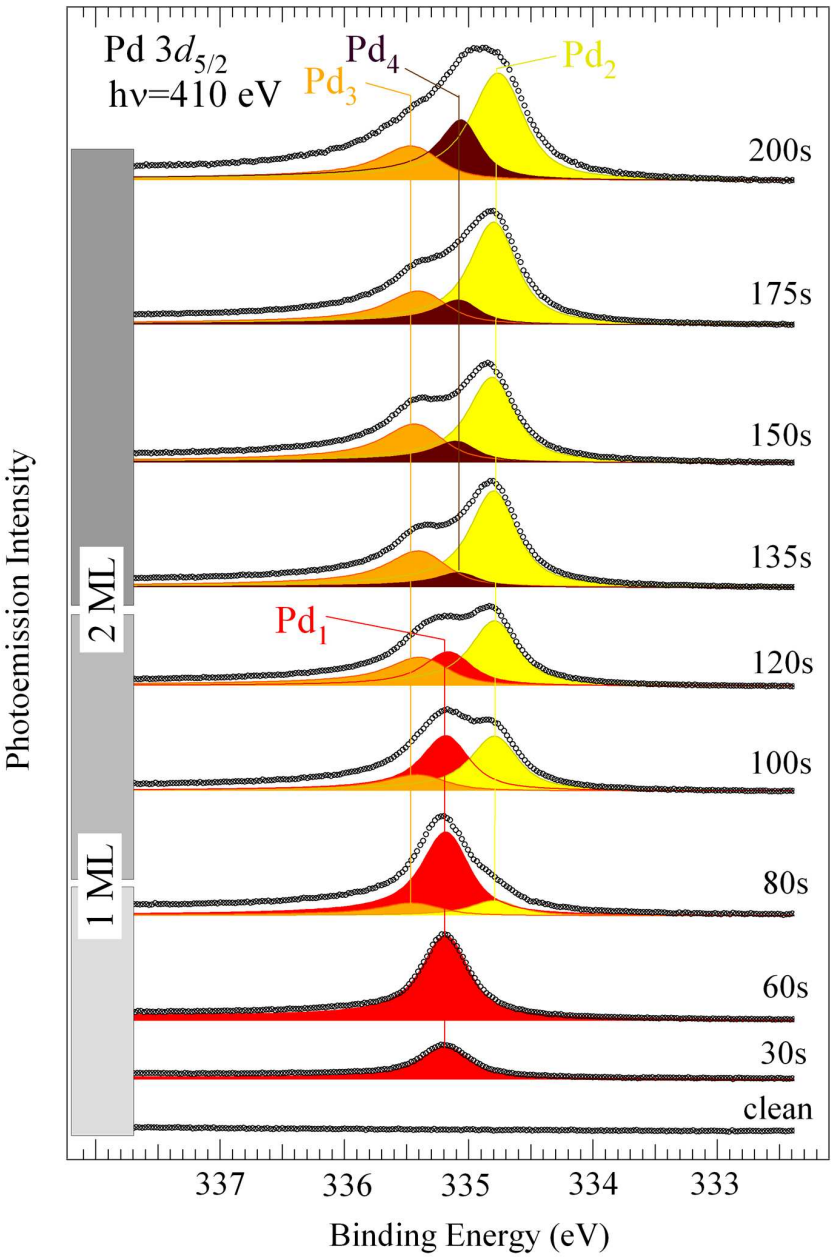

Figure 5.2: Series of high-energy resolution Pd $3d_{5/2}$ core-level spectra collected at T=300 K after different Pd deposition times. The solid lines superimposed to the experimental data (open circles) are the result of the final fits; the colored curves correspond to the different Pd components. The individual components are plotted after linear background removal.

the first layer (Ru_1, dark blue in fig. 5.1); a peak at 280.21 ± 0.02 eV, due to second layer atoms (Ru_2, light grey in fig. 5.1) and, finally, a third component at 280.08 ± 0.02 eV, due to deeper, bulk layers (Ru_3, dark grey in fig. 5.1). The best-fit parameter values were 180 ± 20 meV for the Lorentzian width, 0.08 ± 0.02 for the asymmetry parameter and 120 ± 20 meV for the Gaussian width of the bulk component, while the first- and the second-layer Gaussian widths were 170 meV and 90 meV respectively, in good agreement with previous determination.

Upon Pd deposition in the sub-monolayer range, (corresponding to exposure times of 30 s and 60 s), a single component grows in the Pd $3d_{5/2}$ spectral region, at a binding energy of 335.15 ± 0.02 eV (Pd_1, red curve in fig. 5.2).

In the corresponding Ru $3d_{5/2}$ spectra, the Ru_1 component intensity drops markedly, as expected, and a new peak (Ru_4, light blue in fig. 5.1), with a SCLS of -180 meV appears. We can assign the new spectral component to Ru atoms coordinated with Pd atoms. The progressive growth of this component in the 30 s and 60 s spectra corresponds to a decrease of the Ru_1 peak (originated by Ru *clean* surface atoms), confirming our interpretation. At the same time the signal originating from Ru bulk and Ru second layer atoms is progressively attenuated by the growing Pd overlayer.

At 80 s and 120 s Pd deposition times (corresponding, as determined by our SPA-LEED measurements, to coverages intermediate between 1 and 2 ML) the Ru_1 atoms' signal disappears, while the corresponding Pd $3d_{5/2}$ spectrum undergoes large modifications. A tail at higher binding energy and a shoulder at lower binding energy with respect the Pd_1 component appear, and the spectrum now can be successfully fitted only by using two extra components, shifted by $+220 \pm 40$ meV (Pd_3, yellow curve in fig. 5.2) and -370 ± 40 meV (Pd_2, orange curve in fig. 5.2), with respect to the first Pd component.

For a Pd deposition time of 135 s (corresponding to ≈ 2 ML coverage) the Pd_1 population has almost disappeared, and the Pd $3d_{5/2}$ spectrum can be decomposed by using only two major peaks, Pd_2 and Pd_3. A two component structure in the Pd $3d_{5/2}$ spectrum above 1 ML Pd coverage, shifted by 530 meV, was already reported by Andersen *et al.* [23], and the presence of a third component was most probably hidden by the lower experimental resolution of their measurements.

At deposition times exceeding 150 s, the Pd $3d_{5/2}$ spectrum undergoes

further modification: the spectral minimum slowly starts to be filled by a new component (Pd_4, brown curve in fig. 5.2) at 335.04 ± 0.02 eV. Although its binding energy is very similar, this new peak has a different physical origin than Pd_1. As it will be shown in the following, it arises from second layer atoms in a 3 Pd layer structure. The lowest binding energy component seems to be moderately sensitive to this further Pd thickness increase: on increasing Pd coverage from 2 to 3 ML, it appears only to shift by about 40 meV towards lower binding energy. At these Pd coverages, all the Ru $3d_{5/2}$ spectral components are still present, but with progressively decreasing intensity due to the screening effect of the above Pd layers.

5.3.2 Comparison with theoretical results and discussion

Fig. 5.3 shows a comparison of the measured Ru $3d_{5/2}$ core level shifts, with calculated d-band center shifts ϵ_d, after 30 s of Pd evaporation time. Panel (a) shows schematically the ϵ_d values (calculated with respect to the clean Ru surface ϵ_d value), while panel (b) shows the corresponding measured core level binding energies. By choosing the first layer (surface) binding energy as the origin of the shifts, the second layer's shift is 460 meV, while the third layer atoms' (representative of bulk atoms) shift is 370 meV.

As already mentioned, the Ru spectrum presents an extra component with respect to the clean surface situation (light blue, shifted by 200 meV), originating from the Ru surface atoms on which Pd atoms have adsorbed (see the layer scheme in the inset). The corresponding projected d-band center shift is 270 meV. The overall correspondence is satisfactory and confirms that the contribution of screening (always below 100 meV for the clean Ru(0001) surface [21]) does not cancel the initial state trend. Final state corrections, however, would be needed for obtaining an accurate quantitative agreement with the measured data.

In the following we discuss in particular Pd spectra, since their behavior is more closely connected to the chemical significance of our results. As already described, after 30 s of Pd deposition (corresponding to about 0.4 Pd ML), a single isolated peak appears at 335.15 eV. This feature grows linearly with Pd deposition time.

The Pd $3d_{5/2}$ SCLS for a clean Pd(111) surface has been previously measured to have a binding energy of 334.60 eV [24], so we desume that the adsorption process of Pd adatoms on a Ru(0001) surface causes a binding energy change of 550 meV for the Pd $3d_{5/2}$ core level. Since the atom

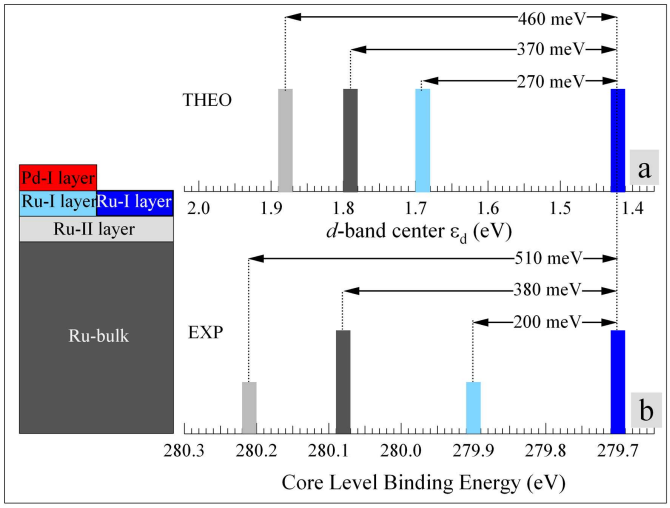

Figure 5.3: Comparison of experimental binding energy of Ru $3d_{5/2}$ core-level components and theoretical layer-projected d-band centers. (a) Shifts of the Ru d-band center with respect to the clean Ru surface. (b) Shifts of the Ru $3d_{5/2}$ core-level binding energies with respect to the core level of the clean Ru surface. The inset on the left shows schematically the physical system for which the comparison is done.

coordination number for both surfaces (Ru(0001) and Pd(111)) is the same (i.e. 9), the shift of 550 meV originates mainly from a combination of ligand and stress effects. Indeed the Ru-Ru interatomic distance is known to be slightly smaller (-1.8%) than the Pd-Pd distance.

Our DFT calculations for a clean palladium surface layer (of Pd metal), and for a Pd pseudomorphic overlayer on Ru(0001), give ϵ_d values of 1.63 eV and 2.12 eV respectively. These values are schematically compared with Pd $3d_{5/2}$ binding energy changes in figure 5.4 (a) and (b). According to the d-band model of chemical reactivity, such large energy downshift ($\Delta\epsilon_d \approx -30\%$) should correspond to a dramatic reduction of adsorbate binding energies. Indeed Behm and coworkers [25] find a reduction of -30% of deuterium adsorption energy on a single layer of palladium deposited on Ru(0001), with respect to the adsorption energy on a Pd(111) surface. Moreover Pallassana *et al.* reported a significant larger binding strength of ethylene on Pd(111) (-62 kJ/mol) when compared with a Pd monolayer on Ru(0001) (-31 kJ/mol) [26].

Panel (d) in fig. 5.4 shows the Pd $3d_{5/2}$ spectral components after 120 s

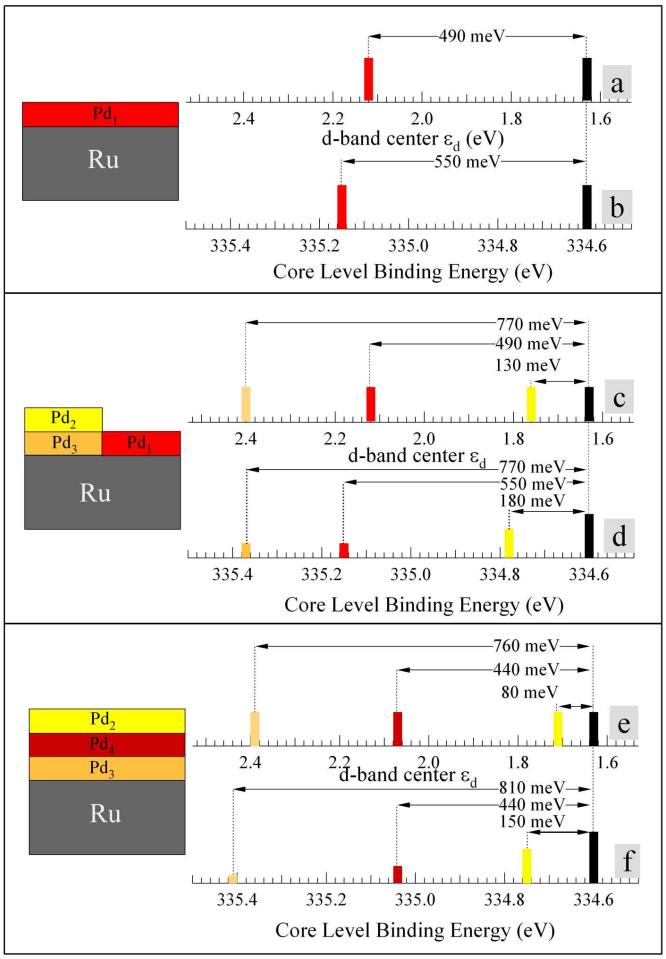

Figure 5.4: Comparison of experimental binding energy of Pd $3d_{5/2}$ core-level components and theoretical layer-projected d-band centers for Pd_n ($0 < n \leq 3$) overlayers deposited on Ru(0001): shift of the Pd d-band center and $3d_{5/2}$ core level for (a, b) 1 Pd pseudomorphic overlayer, (c, d) Pd_n layers with $1 < n \leq 2$, and (e, f) Pd_n layers with $n = 3$. The insets on the left show schematically the physical systems for which the comparisons are done. Both core-level and d-band center shifts are referred to the clean Pd(111) surface core-level and d-band center, respectively.

Pd deposition time (corresponding to a 1.8 ML coverage). In principle, after completion of 2 Pd layers, only 2 peaks should be present in our spectra (originating respectively from the outermost surface layer, and from the interface layer with the Ru substrate). The surface components of our high-resolution photoemission data reflect this situation: two major peaks are found at 770 and 180 meV with respect to the pure Pd surface peak. Actually, the spectrum at this coverage shows a third (weak) component with a 550 meV energy shift. This component is at the same energy as the Pd peak in fig. 5.4 (a) and we interpret it as originating from Pd atoms adsorbed on Ru, and not yet covered by the second Pd layer (still incomplete). According to our DFT calculations, the energy center of the d-band is found at 2.40 eV, while the surface-atoms projected ϵ_d lies at 1.76 eV. The shifts of ϵ_d with respect to a pure Pd surface layer are therefore 770 meV and 130 meV, respectively (see panel (c) in fig. 5.4). According to the d-band model, this means that the surface chemical reactivity has now substantially increased with respect to the situation of a single layer of palladium adsorbed on Ru, but it is still less than the reactivity of a pure Pd surface.

Panels (e) and (f) in fig. 5.4 depict finally the situation after 200 s of Pd deposition, when about 3 layers of Pd have been deposited. At 3 ML of Pd coverage on Ru, we expect three peaks to appear in the Pd $3d_{5/2}$ spectrum (one for each layer), and this is indeed what happens. Also the theoretical DFT results give three different ϵ_d values, at 80, 440 and 760 meV with respect to the ϵ_d of the surface Pd layer in a clean crystal.

In summary, the CL shift of the topmost Pd layer results to be 550 meV when only 1 ML is present, 180 meV when 2 layers have been deposited, and finally 150 meV when we have 3 Pd layers. The very small difference of the shifts between the 2 ML and 3 ML situation, shows that the ligand effect originating from the Ru interface does not contribute any more beyond about the third Pd atomic layer. The remaining shift therefore can only originate from the strain caused by the Pd layer maintaining the Ru lattice parameter. We conclude that the analysis of the core level binding energy shifts allows nicely separating ligand and strain effect contributions. In the case of the Pd/Ru(0001) we find that the ligand effect contribution is twice as large as the stress effect.

A compendium of our experimental and theoretical results for 1, 2 and 3 Pd layers, is shown in fig. 5.5. It can be immediately perceived that a very clear linear relationship (linear correlation coefficient 0.99 ± 0.01) between the measured surface core level binding energies, and the calculated d-band centers exists. We argue therefore that although measured binding energies are definitely affected by final state contributions intrinsic to the

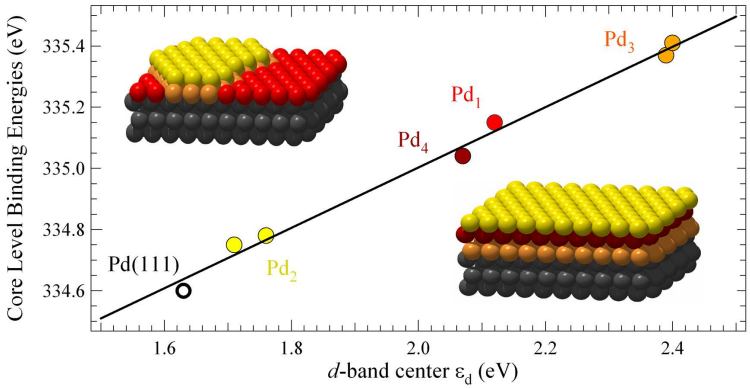

Figure 5.5: Relationship between Pd $3d_{5/2}$ core-level components, arising from Pd overlayers and corresponding DFT calculated d-band centers. The circles in the figure are color-coded according to the insets in the upper left and lower right of the figure. The relationship is strikingly linear, showing that final-state effects do not obscure the core-level shift trends, as indicators of chemical reactivity.

photoemission process, still their contribution does not obscure the overall trends in core level shifts of the Pd overlayers on Ru(0001). Our results confirm that, also for the pseudomorphic overlayers, SCLS changes are a useful experimental descriptor of the projected d-band center of the system and therefore, according to the d-band model, of transition metal alloys' chemical reactivity.

Bibliography

[1] J. Greeley, T.F. Jaramillo, J. Bonde, Ib Chorkendorff, and J.K. Nørskov, *Computational high-throughput screening of electrocatalytic materials for hydrogen evolution*, Nature Materials **5** (2006), 909–913.

[2] S. Alayoglu, A.U. Nilekar, M. Mavrikakis, and B. Eichhorn, *RuPt core-shell nanoparticles for preferential oxidation of carbon monoxide in hydrogen*, Nature Materials **7** (2008), 333–338.

[3] A.V. Ruban, H.L. Skriver, and J.K. Nørskov, *Surface segregation energies in transition-metal alloys*, Physical Review B **59** (1999), 15990–16000.

[4] J.A. Rodriguez, *Physical and chemical properties of bimetallic surfaces*, Surface Science Reports **24** (1996), 223–287.

[5] B. Hammer and J.K. Nørskov, *Electronic factors determining the reactivity of metal surfaces*, Surface Science **343** (1995), 211–220.

[6] B. Hammer and J.K. Nørskov, *Theoretical Surface Science and Catalysis—Calculations and Concepts*, Advances In Catalysis **45** (2000), 71–129.

[7] B. Hammer and J.K. Nørskov, *Electronic factors determining the reactivity of metal surfaces*, Surface Science **343** (1995), 211–220.

[8] B. Hammer, O.H. Nielsen, and J.K. Nørskov, *Structure sensitivity in adsorption: CO interaction with stepped and reconstructed Pt surfaces*, Catalysis Letters **46** (1997), 31–35.

[9] V. Pallassana, M. Neurock, L.B. Hansen, B. Hammer, and J.K. Nørskov, *Theoretical analysis of hydrogen chemisorption on Pd(111), Re(0001) and Pd_{ML}/Re(0001), Re_{ML}/Pd(111) pseudomorphic overlayers*, Physical Review B **60** (1999), 6146–6154.

[10] F. Abild-Pedersen, J. Greeley, F. Studt, J. Rossmeisl, T.R. Munter, P.G. Moses, E. Skúlason, T. Bligaard, and J.K. Nørskov, *Scaling Properties of Adsorption Energies for Hydrogen-Containing Molecules on Transition-Metal Surfaces*, Physical Review Letters **99** (2007), 016105.

[11] J.A. Rodriguez and D.W. Goodman, *The Nature of Metal-Metal Bond in Bimetallic Surfaces*, Science **257** (1992), 897–903.

[12] L. Bianchettin, A. Baraldi, S. de Gironcoli, S. Lizzit, L. Petaccia, E. Vesselli, G. Comelli, and R. Rosei, *Geometric and electronic structure of the N/Rh(100) system by core-level photoelectron spectroscopy: Experiment and theory*, Physical Review B **74** (2006), 045430.

[13] L. Bianchettin, A. Baraldi, E. Vesselli, S. de Gironcoli, S. Lizzit, L. Petaccia, G. Comelli, and R. Rosei, *Experimental and Theoretical Surface Core Level Shift Study of the S-Rh(100) Local Environment*, Journal of Physical Chemistry C **111** (2007), 4003–4013.

[14] L. Bianchettin, A. Baraldi, S. de Gironcoli, E. Vesselli, S. Lizzit, L. Petaccia, G. Comelli, and R. Rosei, *Core level shifts of undercoordinated Pt atoms*, The Journal of Chemical Physics **128** (2008), 114706.

[15] A. Baraldi, L. Bianchettin, E. Vesselli, S. de Gironcoli, S. Lizzit, L. Petaccia, G. Zampieri, G. Comelli, and R. Rosei, *Highly undercoordinated atoms at Rh surfaces: interplay of strain and coordination effects on core level shift*, New Journal of Physics **9** (2007), 143.

[16] A. Baraldi, *Structure and chemical reactivity of transition metal surfaces as probed by synchrotron radiation core level photoelectron spectroscopy*, Journal of Physics: Condensed Matter **20** (2008), 093001.

[17] A. Baraldi, S. Lizzit, G. Comelli, M. Kiskinova, R. Rosei, K. Honkala, and J.K. Nørskov, *Spectroscopic Link between Adsorption Site Occupation and Local Surface Chemical Reactivity*, Physical Review Letters **93** (2004), 046101.

[18] C. Park, *Growth of Ag, Au and Pd on Ru(0001) and CO chemisorption*, Surface Science **203** (1988), 395–411.

[19] S. Baroni, A. Dal Corso, S. de Gironcoli, and P. Giannozzi, http://www.pwsfc.org.

[20] J.P. Perdew, K. Burke, and M. Ernzerhof, *Generalized Gradient Approximation Made Simple*, Physical Review Letters **77** (1996), 3865–3868.

[21] S. Lizzit, A. Baraldi, A. Groso, K. Reuter, M.V. Ganduglia-Pirovano, C. Stampfl, M. Scheffler, M. Stichler, C. Keller, W. Wurth, and D. Menzel, *Surface core-level shifts of clean and oxygen-covered Ru(0001)*, Physical Review B **63** (2001), 205419.

[22] S. Lizzit, Y. Zhang, K.L. Kostov, L. Petaccia, A. Baraldi, D. Menzel, and K. Reuter, *O- and H-induced surface core level shifts on Ru(0001): prevalence of the additivity rule*, Journal of Physics: Condensed Matter **21** (2009), 134009.

[23] T.H. Andersen, L. Bech, Z. Li, S.V. Hoffmann, and J. Onsgaard, *Surface alloying of Pd and Cu on Ru(0001)*, Surface Science **559** (2004), 111–130.

[24] S. Surnev, M. Sock, M.G. Ramsey, F.P. Netzer, M. Wiklund, M. Borg, and J.N. Andersen, *CO adsorption on Pd(111): a high-resolution core level photoemission and electron energy loss spectroscopy study*, Surface Science **470** (2000), 171–185.

[25] H. Hartmann, T. Diemant, A. Bergbreiter, J. Bansmann, H.E. Hoster, and R.J. Behm, *Surface alloy formation, short-range order, and deuterium adsorption properties of monolayer PdRu/Ru(0001) surface alloys*, Surface Science **603** (2009), 1439–1455.

[26] V. Pallassana and M. Neurock, *Electronic Factors Governing Ethylene Hydrogenation and Dehydrogenation Activity of Pseudomorphic Pd_{ML}/Re(0001), Pd_{ML}/Ru(0001), Pd(111), and Pd_{ML}/Au(111) Surfaces*, Journal of Catalysis **191** (2000), 301–317.

Chapter 6

Nucleation of Pd nanoclusters on graphite and single walled carbon nanotubes

6.1 Introduction

The technology for depositing small amounts of atoms onto well-prepared surfaces under high vacuum has undergone significant development in the last decades, so that nowadays it is possible to routinely prepare nanostructured surfaces. Two-dimensional structures (e.g. metal thin films, like the Pd/Ru interface studied in Ch. 5) can be prepared to study their physical properties noticeably different from those of the corresponding *bulk* materials [1]. Among the possible overlayer arrangements we can annoverate also metal atomic chains: these configurations enable the study of quasi-one-dimensional metallic systems which exhibit a number of electronic and structural properties that compete and interact with each other arising novel peculiar characteristics [2].

When dealing with 3D structures, transition metal nanoclusters are of great interest for severeal reasons that lie at the boundary between basic research and technological applications [3, 4]. As an example, transition metal nanoclusters deposited on thin oxide films (as will be explained more in detail in Ch. 7) can be considered one of the best model systems to study the behaviour of real catalysts. In particular these systems allow investigations on the role of the oxide support [5] as well on the dependence

of the catalytic activity on cluster size [6, 7, 8].

Another possibility is given by ordered surperlattices of nanoclusters [9, 10]: by controlling structures at the nanometer scale new materials with novel and peculiar mechanical and optical properties can be perpared. Regular arrays of magnetic nanoparticles (e.g. of Co), moreover, open possibilities for high density magnetic devices for data storage [11].

In this context, the chemical inertness of graphite as well as the mechanical strength, the electronic properties and the high surface-to-volume ratio of carbon nanotubes make these two materials very interesting supports for transition metal clusters.

In this chapter the characterisation of Pd nanoclusters' nucleation and growth on Highly Ordered Pyrolytic Graphite (HOPG) and on Single Walled Carbon NanoTubes (SW-CNTs) by means of high resolution photoemission measurements paralleled by Density Functional Theory (DFT) calculations will be presented. These experiments aimed to a deeper understanding of the Pd atoms' nucleation mechanisms on carbon-based supports, and to the study of the thermal stability of these nanocompounds, including the process of break up at high temperature. Another interesting topic is the interaction of the support with the metal clusters, and the influence of the support's morphology on the clusters' formation. As will be shown, the use of different supports emphasized the importance of metal-support interaction and played a key role in the interpretation of experimental results. Examination of the data from the two different experiments with regard to the well known differences between the corresponding supports, provided a deeper understanding of the clusters' growth mode and their electronic properties, together with the fundamental role played by defects.

6.2 Experimental and computational details

The two substrates used in the experiments consisted in a sample of HOPG and in a commercial *bucky paper* made of SW-CNTs with average diameter of 1.3 ± 0.1 nm. They were mounted on a sample holder, composed of tantalum clips with two circular windows which exposed the deposition zones. The two samples could be resistively heated, and the temperature was determined with an uncertainty of ± 30 K from the current passing through the sample, in combination with a pyrometer and a thermocouple welded to the Ta clip.

The samples were introduced in the UHV chamber immediately after cleaving the HOPG crystal. To complete the HOPG preparation several

annealing cycles up to 1200 K were performed until a sharp C 1s core level spectrum was measured. The CNT sample was prepared with repeated annealing cycles up to 1800 K until no traces of chemical contaminants could be detected by photoemission measurements [12].

The Pd evaporator consisted in a Pd filament resistively heated. The filament was gradually heated and then held at the evaporation temperature for a fixed amount of time. During Pd deposition the pressure in the UHV system was always kept below 4×10^{-10} mbar to prevent the adsorption of background impurities.

For the photoemission measuremetns the overall energy resolution (electron energy analyser and x-ray monochromator) was 40 meV for both Pd $3d_{5/2}$ and C 1s core level spectra. The measurements were performed in the *normal emission* geometry with a photon energy of 400 eV. The electron binding energies are referred to the Fermi energy position, measured under the same experimental conditions (photon energy, analyzer setup, and surface temperature), from a Pd polycrystal mounted on the bottom of the sample holder.

We investigated different amounts of Pd deposited on the two supports at liquid nitrogen temperature (80 K), corresponding to 15, 60 and 240 s of Pd deposition time with a constant Pd filament current, constant filament-support distance and the same turn-on procedure. Immediately after Pd deposition, an overview spectrum, including the two relevant photoemission peaks was recorded in order to allow determination of the Pd deposited quantity by evaluating the intensity ratio of the two components, as will be explained in the next section. Then, the evolution of Pd $3d_{5/2}$ and C 1s spectra was followed after annealings at room temperature (300 K) and at 470, 670, 870 and 1070 K. At the end of every measurement sequence the sample was cleaned with a 5 minutes annealing at 1300 K, for removing all traces of Pd.

DFT calculations have been performed in collaboration with Prof. S. de Gironcoli from SISSA-Democritos at Trieste and his research group. The reported results have been obtained using the Quantum Espresso code [13] and the correlation functional developed by Perdew, Becke and Erznerhof (PBE) within the General Gradient Approximation (GGA) [14].

The binding energies of Pd adatoms and small clusters deposited on a graphite sheet have been obtained by computing the difference between the total energy of the omplete system and that of the two isolated configurations:

$$\mathrm{BE}_{\mathrm{adatom,cluster}} = \mathrm{E}_{\mathrm{tot}} - \mathrm{E}_{\mathrm{substrate}} - \mathrm{E}_{\mathrm{adatom,cluster}}.$$

For the evaluation of diffusion barriers and consequent estimation of cluster mobility the calculations have been performed using the Nudge Elastic Band method [15] implemented in the Quantum Espresso code.

Finally, the Pd $3d_{5/2}$ core level shifts for Pd atoms with various coordinations in small clusters (4,7 and 11-atom clusters) were calculated within the final-state approximation. This approach takes into account the possibility of a different response of the valence electrons at the surface and in the bulk to the created core hole. Indeed, it is well known that these differences can make a substantial contribution to core level shifts of clean surfaces, metallic surface alloys and small metal particles, so that considering the final-state effects is of fundamental importance in order to reliably compare theoretical calculations and experimental results.

Moreover, in order to obtain *absolute* values for the core level binding energies, in each of the studied configurations an isolated adatom was added far away from the cluster, so that for every calculation we had a common energy reference. In this way the shift of the $3d_{5/2}$ level was calculated for each atom of the three clusters considered, with respect to the that of the isolated adatom. To obtain absolute values of the electron binding energy for these shifts, a second step was needed: the collocation of the isolated adatom core level. A new simulation was performed, with a seven-layer Pd slab, with two graphene sheets deposited on the Pd surface and an isolated adatom on the graphite surface: here the binding energy shift of the adatom was computed with respect to that of a Pd bulk atom. The Pd $3d_{5/2}$ binding energy for an atom in bulk configuration is a well known quantity, determined both theoretically and experimentally, so that by this double-reference method the core level shift for each atom of the three clusters has been determined.

6.3 Results and discussion

6.3.1 Pd coverage determination

In order to evaluate the amount of Pd deposited during the three different evaporation periods, we compared the Pd $3d_{5/2}$ and the C $1s$ peak areas in spectra collected using the same photon and pass energies. We performed this evaluation for the HOPG substrate, since HOPG is a smooth and well ordered support, while the SW-CNTs are highly corrugated and disordered, and the Pd atoms might end up inside a CNT that would screen the Pd signal, invalidating the results.

In fig. 6.1 overview spectra for the three different exposure times are

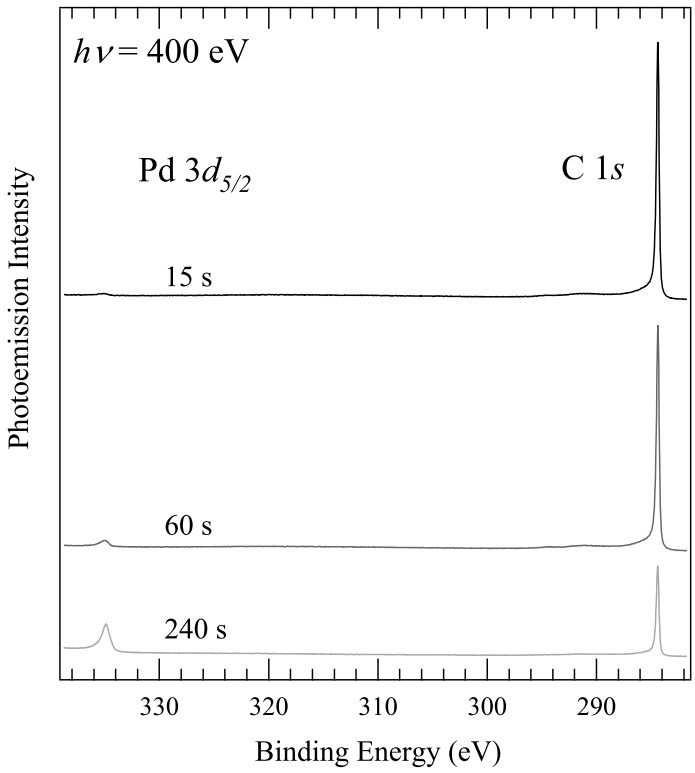

Figure 6.1: Overview spectra including C 1S and Pd $3d_{5/2}$ peaks for different Pd deposition times. For the sake of clarity spectra have been offset vertically to avoid overlap.

shown. To determine the Pd coverage the numerical values obtained for the peaks' areas were weighted with the Pd 3d and C 1s cross sections at the used photon energy: 3.52 and 0.464 MBarn respectively. The model for the coverage evaluation is based on simple assumptions on the inelastic mean free path (IMFP) of the photoelectrons from a layered structure. As shown in fig. 6.2, the outcoming photoelectrons pass through a varying number of layers of different material. For an evaluation of the signal attenuation we should consider the material-specific mean free path for the different kinetic energies and average on the number of atomic layers that photoelectrons can meet. As suggested by Høirup Hansen *et al.* [16], we supposed that cluster height does not exceed 5 atomic layers; in this way, considering a Poisson

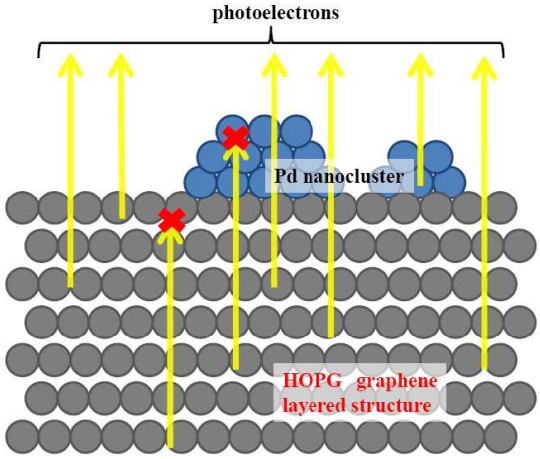

Figure 6.2: Normal emission paths for photoelectrons outcoming from a layered structure. The red crosses indicate the occurrence of the inelastic scattering events that prevent photoelectrons from reaching the sample's surface.

distribution of the cluster heights, we can approximate the thickness mean value to about 2 atomic layers. Under the hypothesis that the photoelectron signal (at the kinetic energies involved in our experiment, about 60 and 115 eV for Pd and C, respectively) is negligible after a 5-layer path, we can write down the two formulas for the evaluation of the Pd coverage:

$$\begin{aligned} I_{Pd} &= \alpha \cdot \exp\left(\frac{n \cdot c_{Pd}}{\lambda_{Pd}}\right) \\ I_C &= (1-\alpha) \cdot \sum_{n=0}^{4} \exp\left(\frac{n \cdot c_C}{\lambda_C}\right) + \alpha \cdot \exp\left(\frac{n \cdot c_{Pd}}{\lambda_{Pd}}\right) \sum_{n=0}^{2} \exp\left(\frac{n \cdot c_C}{\lambda_C}\right) \end{aligned}$$

where $I_{C,Pd}$ are the photoemission intensities weighted by cross sections, $\lambda_{C,Pd}$ the IMFPs resulting from the universal mean free path curve (showed in fig. 2.1) for the two kinetic energies involved and $c_{C,Pd}$ are the lattice constants in the direction normal to the surface. The only unknown value is the coverage α: the values for the coverage obtained from these calculations range from 0.005 to 0.09 ML (detailed results are reported in table 6.1). This is a reasonable result, though it is affected by uncertainties introduced by strong assuptions like the Poisson distribution of clusters' height and the use of the universal curve for the evaluation of the mean free paths. A confirmation of the coverage calculated from the photoemission data comes

Pd ev. time t(s)	coverage (ML) PES analysis	coverage (ML) SEM analysis
15	0.005	0.01
60	0.02	0.04
240	0.09	0.15

Table 6.1: Evaluation of the Pd coverage obtained from the analysis of photoemission intensity and SEM images.

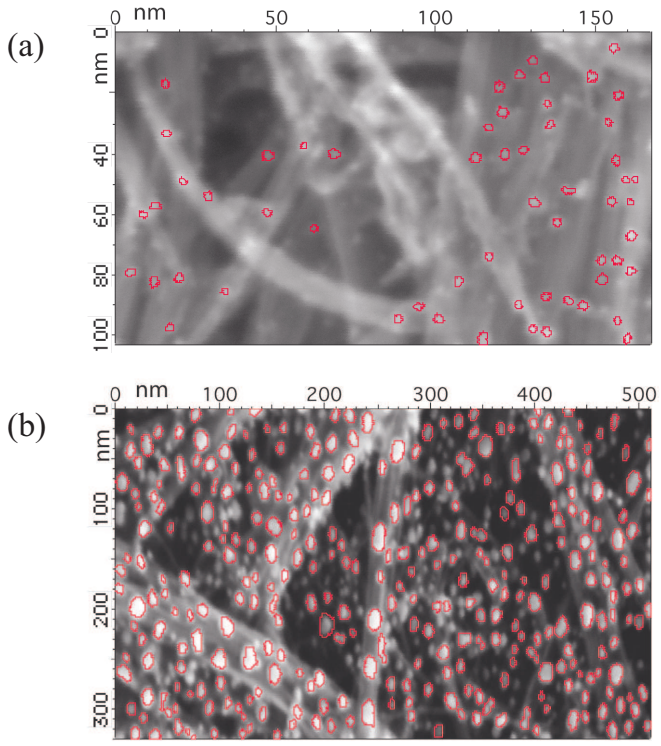

Figure 6.3: SEM images of Pd nanoclusters on CNTs for 15 s (a) and 240 s deposition time (b).

from the analysis of scanning electron microscopy (SEM) images; fig. 6.3 shows images acquired for the higher and the lower Pd coverage on the CNT

substrate. The image processing gives coverage values ranging from 0.01 to 0.15 ML corresponding to 15 s and 240 s deposition times (with an average number of Pd atoms of 200 and 10000, respectively), in rough agreement with coverages obtained from the peak intensity analysis. Nonetheless, the most important point is that also for the maximum coverage we can be sure that the support area occupied by Pd nanoclusters is less than 20%, and therefore low enough to ensure the presence of small sized clusters and low coordinated atomic species.

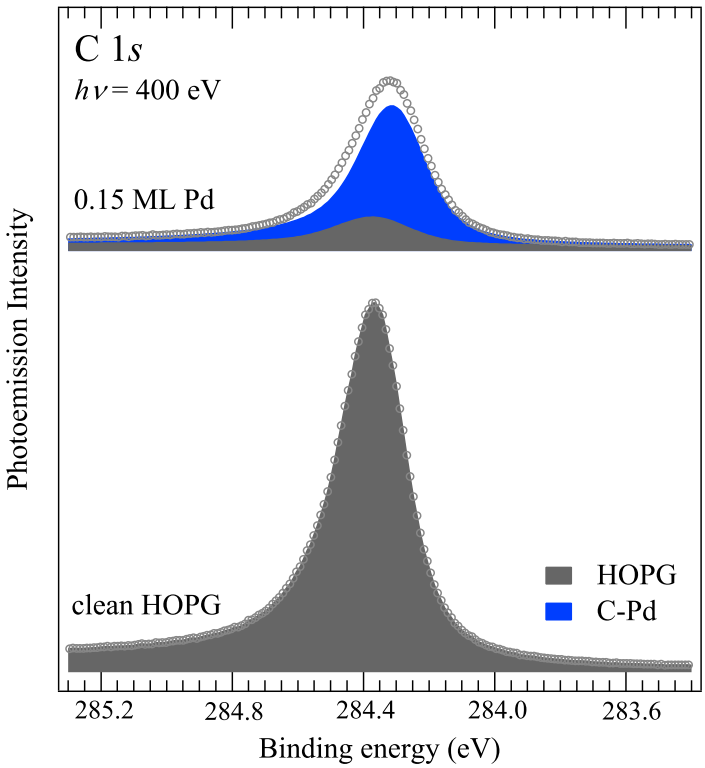

Figure 6.4: C 1*s* spectra of the clean HOPG surface and with 0.15 ML Pd coverage. The intensity of the orange peak is strongly reduced after Pd deposition and a new peak arises from C atoms interacting with Pd atoms.

6.3.2 Evolution of C $1s$ and Pd $3d_{5/2}$ core level spectra

As previously mentioned, we measured Pd $3d_{5/2}$ and C $1s$ spectra for every Pd coverage and for each annealing step. C $1s$ spectra are not particularly useful for understanding cluster structure. In fig. 6.4, an example of C $1s$ spectrum measured for the HOPG substrate is shown: when Pd atoms are deposited on clean HOPG, the sharp single-component C $1s$ spectrum is attenuated by Pd screening and is also split into two components, one arising from the bare portions of the surface, and the other, shifted by 60 meV, from the C atoms coordinated with Pd. Such a small shift between these two components suggests a weak interaction between Pd and the C atoms in the substrate.

The analysis of the Pd $3d_{5/2}$ is found to be more interesting for the understanding of the morphology evolution of the deposited clusters. In fig. 6.5 an overview of the Pd spectra is shown, for Pd deposition on CNTs and on HOPG supports. For every Pd coverage, the annealing progression goes from the deposition temperature of 80 K (black spectrum) to the highest annealing temperature of 1070 K (light grey spectrum). Before beginning with the systematic analysis and discussion of the spectra, it is worth noting some qualitative trends to determine the best approach.

In literature many works (both theoretical and experimental) can be found on Pd single crystals, and it is well known that the bulk component of the Pd $3d_{5/2}$ core level has a binding energy of 334.9 eV, whereas the Pd(111) surface component is shifted by about -0.3 eV [17, 18]. In fig. 6.5 a blue line indicates the position of bulk Pd $3d_{5/2}$ peak as a reference. With few exceptions (such as the low coverage and low temperature spectra) every spectrum seems to have one component at the *bulk* position, and almost every spectrum contains two additional components, one on each side of the bulk line. At first glance there are two main indications:

- low coverages have a larger contribution at high binding energies;
- increasing the annealing temperature two effects arise: the growth of the high binding energy contribution to the spectra, and the shift of the spectrum's intensity maximum (see the red dotted lines in fig. 6.5).

Starting with these simple observations we decided to use a three component fitting curve, with the reference peak in an energy position close to the bulk line and two additional peaks, one on each side.

In fitting these spectra we opted to preserve the spectral lineshape where possible, imposing a tight restriction on the variation of the Lorentzian width

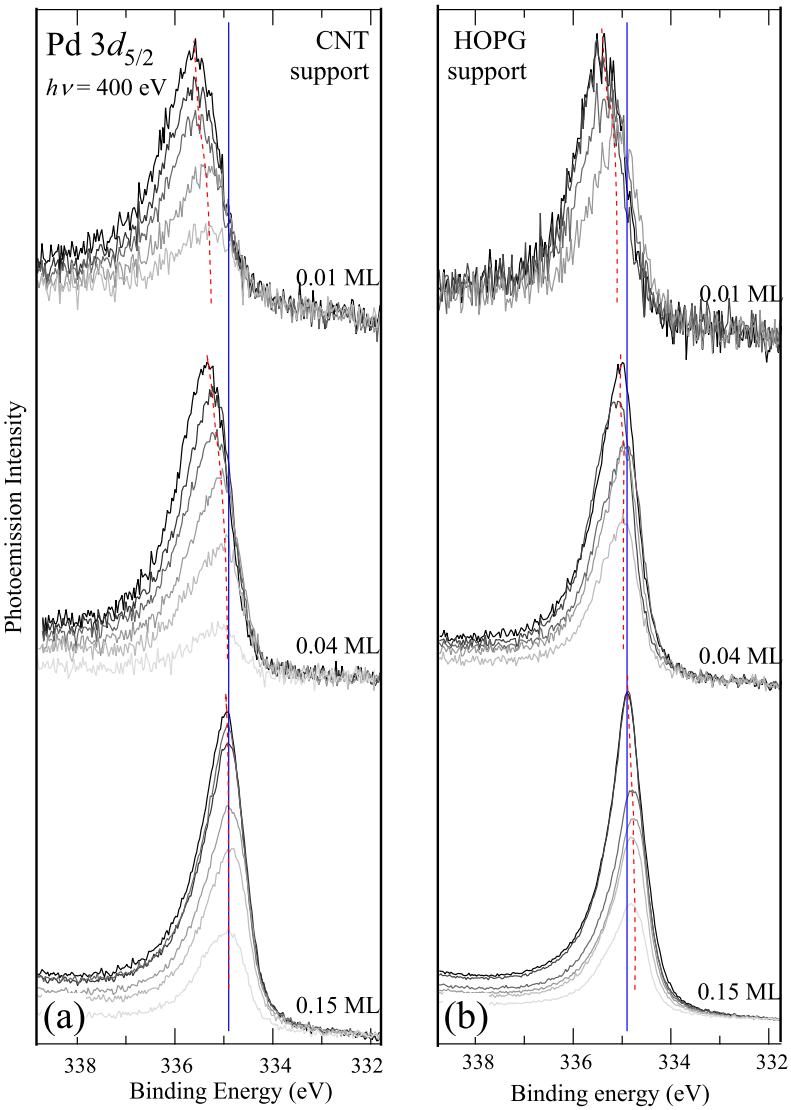

Figure 6.5: Measured Pd $3d_{5/2}$ spectra for three different amounts of Pd on carbon nanotubes (a) and HOPG (b) support. The blue line indicates the position of the bulk component [17] as a reference, while the dotted red lines follow the drifting of the intensity maximum of each spectrum. The grey scale of the plot lines indicates the temperature progression from 80 K (black) to 1070 K (light gray).

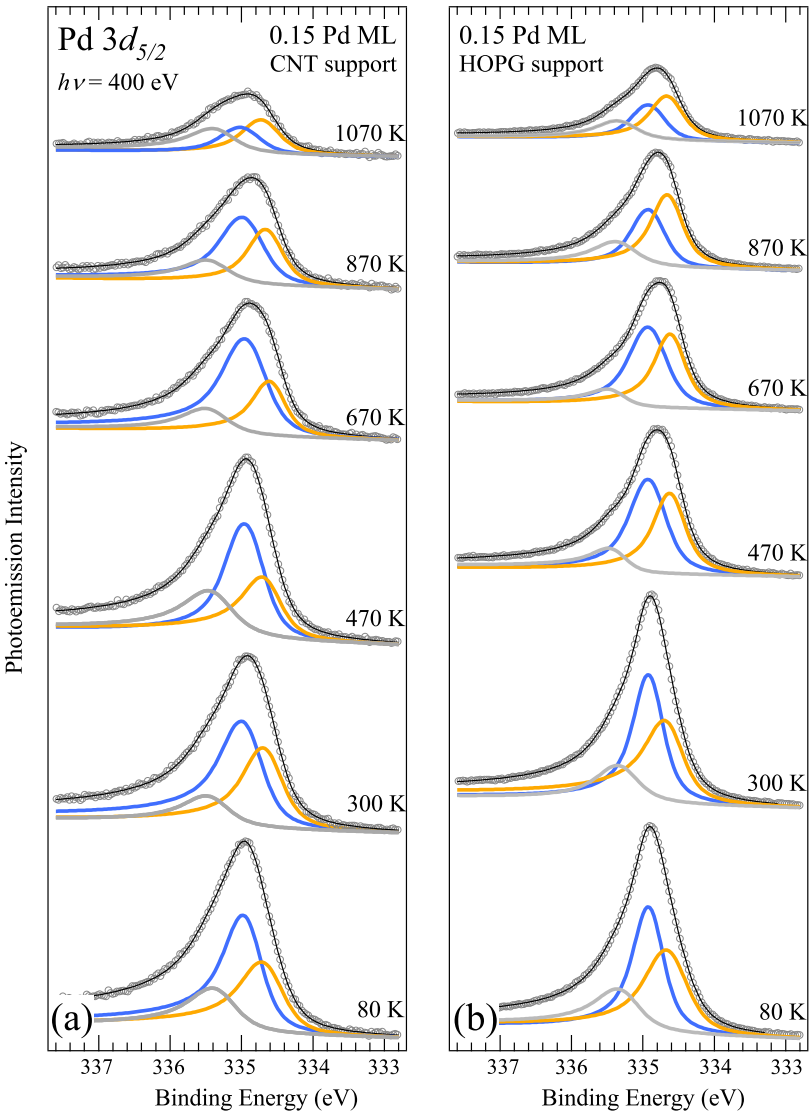

Figure 6.6: Evolution of Pd $3d_{5/2}$ spectra measured for 0.15 ML Pd coverage on CNT (a) and HOPG (b) supports upon annealing at increasing temperatures. The spectral components related to Pd atoms in bulk (blue) and surface (orange) configurations are shown, as well as the one due to interactions with defective sites on the support (grey).

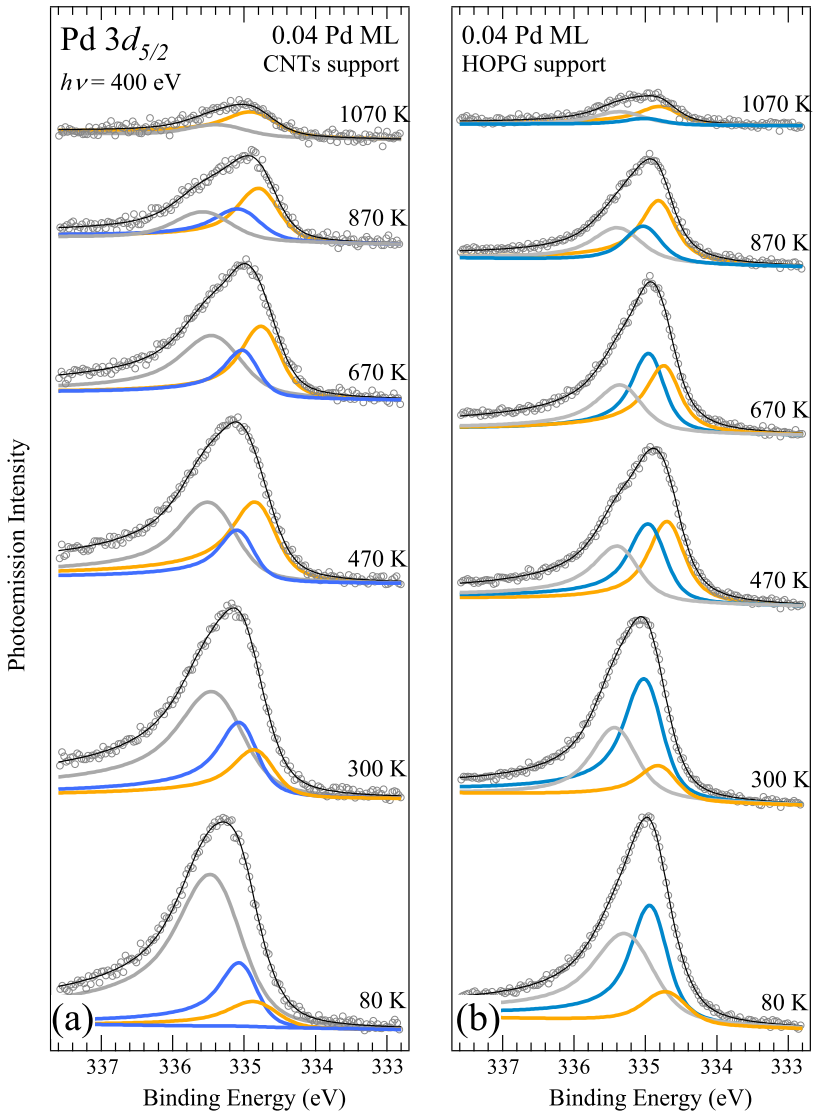

Figure 6.7: Evolution of Pd $3d_{5/2}$ spectra measured for 0.04 ML Pd coverage on CNT (a) and HOPG (b) supports upon annealing at increasing temperatures. The spectral components related to Pd atoms in bulk (blue) and surface (orange) configurations are shown, as well as the one due to interactions with defective sites on the support (grey).

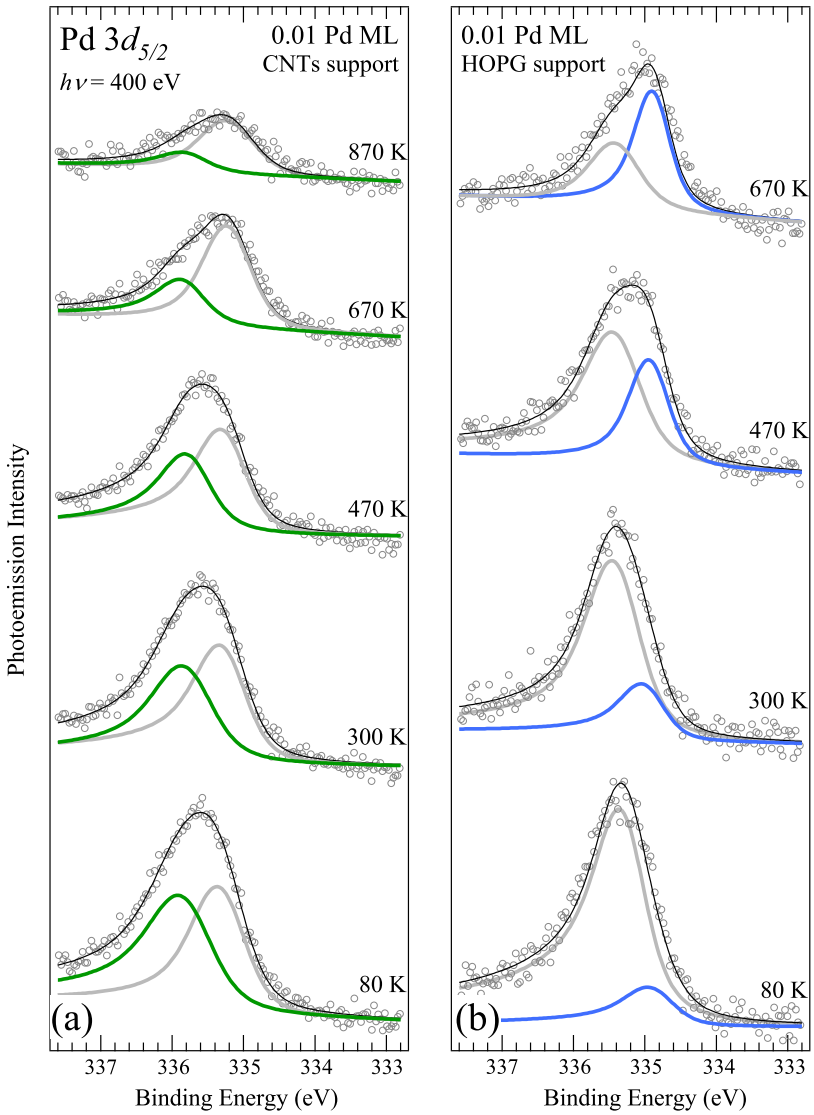

Figure 6.8: Evolution of Pd $3d_{5/2}$ spectra measured for 0.01 ML Pd coverage on CNT (a) and HOPG (b) supports upon annealing at increasing temperatures. The spectral component related to Pd atoms in bulk (blue) configuration and the one due to interactions with defective sites on the support (grey) are shown. For the CNT support an extra feature at high binding energy is also visible (green).

and asymmmetry parameter. A wider range was allowed for the Gaussian width and peak position; this was required by the large distribution of inequivalent local Pd configurations. In figures 6.6 to 6.8 the deconvoluted spectra are shown together with the components resulting from the fitting procedure.

The main trends determined from this analysis can be summarized as follows:

- *High Pd coverage*
  - the central peak (blue) is located at 334.95±0.05 eV, very close to the bulk value and the shift of the low binding energy component (yellow) with respect to the blue one is very close to the Pd(111) SCLS (-0.3 eV, [17, 18]). This appears quite reasonable: for this coverage we estimated about 10^4 atoms/cluster, and at this scale bulk and surface signals could arise and dominate over the other components;
  - with successive annealings a decrease of the Pd $3d_{5/2}$ intensity is observed; moreover, the bulk component loses intensity faster than the other components. A first possible explanation relates this behaviour to cluster evaporation: the cluster size decreases and the surface/bulk intensity ratio increases. The overall decrease (more than 10%) of the photoemission singnal, actually, appears too large to be due only to screening effects arising from cluster aggregation. However, microscopy investigations (e.g. with SEM or TEM) would be very interesting in order to definitely understand this process;
  - there are no significant differences between the HOPG and CNT spectra, because of the relatively low weight of the cluster portion that interacts with the support with respect to the overall cluster signal.
- *Intermediate Pd coverage*
  - the large intensity of the grey component at high binding energy is the main difference with respect to the high Pd coverage case;
  - the SCLS is still observed but the behaviour of bulk and surface components cannot be simply understood. At low temperatures (80 and 300 K) the bulk/surface ratio is higher than for larger clusters (the opposite of the expected trend), and above 470 K

the surface component becomes more intense than than the bulk component;

- some appreciable differences begin to arise between CNT and HOPG spectra. Whereas the HOPG spectra are still dominated by bulk and surface components, the grey component is the principal one in the CNT spectra. Furthermore, the peaks' Gaussian widths for CNT are slightly larger than for HOPG.

- *Low Pd coverage*

  - CNT and HOPG spectra are now completely different. In HOPG spectra we find only two peaks (the surface peak has vanished), with the high binding energy component dominating over the bulk. In CNT spectra both the surface and the bulk components have vanished; at the same time a new feature (green peak in fig. 6.8 (a)) is observed, shifted by 500 meV with respect to the grey one.

After this overview of experimental data, a comparison with theoretical results is required, in order to understand the chemical environment of the atoms giving rise to each component. Indeed, up to now *bulk* and *surface* are names given for simplicity and a more realistic and precise interpretation must be achieved.

6.3.3 Theoretical calculations and comparison with experimental results

A first set of DFT calculations was aimed to the evaluation of the Pd-C interaction. From this analysis it results that on graphite single Pd atoms are preferentially adsorbed in bridge sites between two carbon atoms, with a binding energy of 1.12 eV; when adsorbed on top of a C atom or in between three C atoms (hollow site), Pd is less strongly bond to the substrate (1.09 and 0.91 eV, respectively). The most significant result, however, arises when the same calculation is repeated for dimers and trimers. In this case a clear trend is observed: increasing the number of Pd atoms in the clusters, the bond between Pd and the substrate becomes weaker; the average on all the possible configurations gives a binding energy value of ≈ 0.6 eV and ≈ 0.15 eV for dimers and trimers, respectively.

The analysis of diffusion barriers for a Pd adatom on a defect free HOPG surface results in a very high mobility of Pd adatoms on defect-free HOPG:

diffusion barriers of 0.03 and 0.19 eV (for bridge-bridge and bridge-hollow-bridge hopping, respectively) allow high mobility even at liquid nitrogen temperature. Similar calculations were also performed for dimer and trimer surface diffusion, and the resulting energy barriers (0.11 and 0.14 eV) are very low also for small clusters.

DFT computations gave also hints on the mechanism for the transition from two-dimensional to three-dimensional clusters: the energy barrier for moving a Pd atom from the edge of a 4-atom planar cluster to the top of the remaining atoms (0.2 eV) is significantly lower than that for the opposite process (≈ 1 eV).

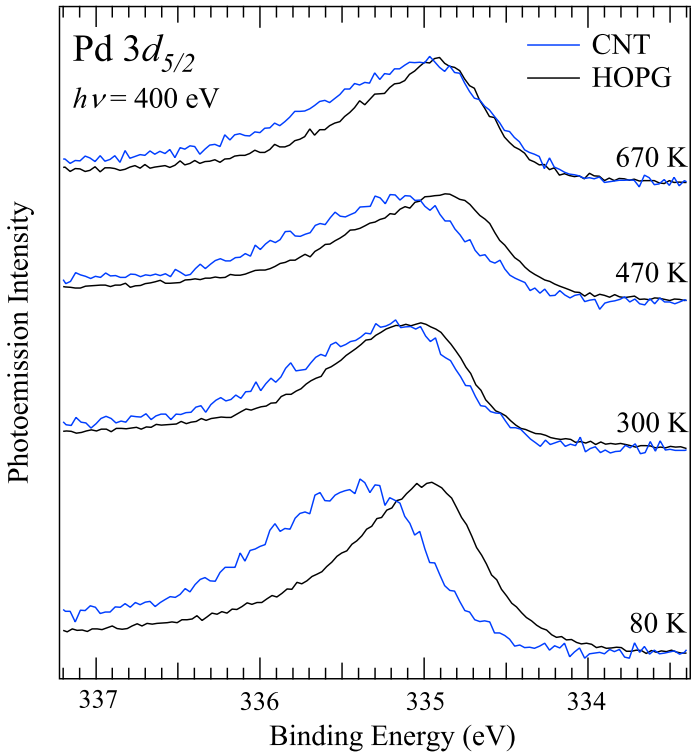

Figure 6.9: Comparison between Pd $3d_{5/2}$ spectra acquired for 0.04 ML of Pd deposited on CNT (blue) and HOPG (black). The spectral weight of the data acquired for the CNT support is always shifted towards higher BE with respect to HOPG.

Another calculation showed how for the removal of an *on top* Pd atom from a three-dimensional cluster an energy barrier of 3.06 eV needs to be overcome, while the barrier for the removal of a *side* atom is much lower (2.11 eV): this suggests that the disgregation process proceeds via the detachment of Pd atoms from the edge of the clusters, diffusion on the substrate and desorption because of the low adsorption energy.

Besides all the important information obtained from DFT calculations on the studied system, the relation between the theoretical work and the experimental findings is given by the calculation of Pd $3d_{5/2}$ binding energy shifts. The results obtained following the method described in sec. 6.2 present a problem when compared with experimental data: all the core levels calculated for the nine different atoms belonging to the three clusters have a lower binding energies than the bulk value. This means that from theoretical calculations no intensity is expected in the high binding energy region of the grey peak in figs. 6.6, 6.7 and 6.8. Actually, this result is not completely unexpected: dealing with a more-than-half filled d-band metal, lower coordinated Pd atoms (like the ones that can be found in clusters, but also in surfaces) are expected to present core level shifts towards lower binding energy (see sec. 2.4.2).

The interpretation of the high binding energy component, still elusive after this first part of the work, was achieved thanks to a subtlety in the experimental data. Focusing our attention only on 0.04 and 0.01 ML Pd coverages, we notice several key differences between CNT and HOPG spectra. In fig. 6.9 a comparison between Pd spectra of the same coverage (0.04 ML) on the two different supports is shown.

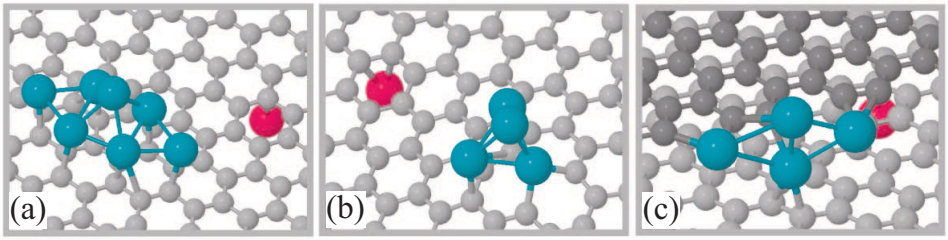

Figure 6.10: Exemples of simulated structures: (a) 7-atom cluster on a defect free HOPG surface. (b) 4-atom cluster nucleated on a carbon vacancy on the HOPG surface. (c) 4-atom cluster nucleated on a step of the HOPG surface. In each of these simulations the isolated atom (red) gives the energy reference for the binding energy shift.

For every pair of spectra, the ones measured for the CNTs are always shifted towards higher binding energy, so we may argue that the origin of the high binding energy component must be the interaction with the support. The main difference between the two supports is the presence of surface defects: the *forrest-like* SW-CNT substrate, in fact, a much higher density of defects is expected. Thus we tested the hypothesis that the high binding energy component arises from Pd atoms bound to surface defects by repeating the calculations for Pd atoms that nucleate on defective sites of the support. For simplicity two kind of defects have been studied: steps and vacancies. In fig. 6.10 some simulated structures are shown.

More than forty inequivalent Pd atoms were studied and the results

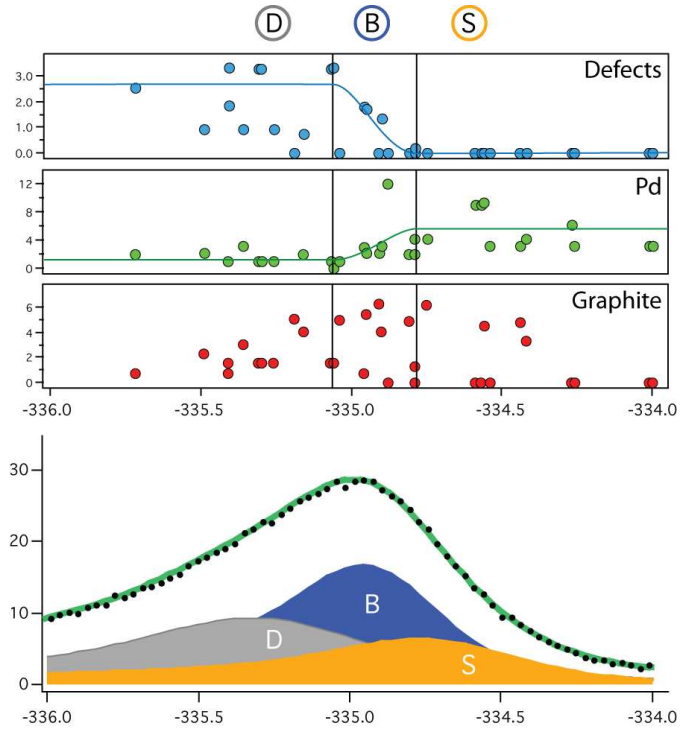

Figure 6.11: (Upper panel) Pd $3d_{5/2}$ binding energy calculated for Pd atoms in inequivalent configurations. Three groups can be identified: one at low binding energies, where palladium is not coordinated with defect, one at higher binding energies where palladium is highly coordinated with defects and a middle one, where these coordination balance each other. (Lower panel) The above defined groups perfectly match with the analysis of the experimental data.

evidenced how defective sites on the carbon support play a key role in the formation of the high binding energy component.

Fig. 6.11 shows the calculated core levels of Pd atoms in many different local configurations, and belonging to clusters nucleating in different sites. A trend for the effective coordination (a weighted sum of the different bond lenghts inside the van der Waals radius) as a function of the binding energies was found and this correlation is shown in the upper panel of the figure. Even if every core level shift arises from several contributions, the trend is unambiguous. The spectral component at low binding energy is due to Pd atoms with a high coordination with other Pd atoms region shows a higher effective coordination with Pd atoms. The opposite behaviour is observed for the high binding energy feature: the Pd coordination drops drastically and the defective sites' coordination clearly grows. The effective coordination with defect-free graphite is not as indicative as the other two quantities and has a relevant value for all the atomic species we studied. These three behaviours are easily observed in the Pd $3d_{5/2}$ of the 0.04 ML coverage (after 670 K annealing), with the different components arising from fit analysis. Previous interpretations of the high binding energy component included the effects of cluster charging during the photoemission process [19] or the effect of charge transfer from Pd to the graphitic layer [20]. Our results strongly support the latter interpretation.

6.3.4 Conclusions

The investigation on the nucleation and the thermal stability of Pd nanoclusters on graphite and CNTs reported in this chapter is a good example of the interplay between the analysis of experimental data and the results of theoretical calculations. From one hand, DFT computations provided a lot of information on the nucleation mechanism and allowed interpretation of the origin of the Pd $3d_{5/2}$ spectral components, but, on the other hand, only the analysis of the experimental data revealed the correct direction for further theoretical calculations that led to the understanding of the fundamental role of surface defects.

Thanks to this combined experimental and theoretical work, the picture obtained for the Pd nucleation process on these two supports can be summarized as follows:

- Because of their high mobility and the energy gain in cluster aggregation, Pd atoms aggregate very easily and the most stable nuclation sites are defects. Moreover, Pd does not wet the graphite's surface,

since three-dimensional configurations are more favourable compared with two-dimensional growth.

- With increasing temperature the clusters break, loosing palladium atoms mainly from the edges connected to graphite.

- At higher temperatures and for lower coverages, clusters are smaller, containing a high percentage of palladium atoms bound to defective sites. This explains the presence of the high binding energy portion of the spectra and explains the difference between small and large clusters: in large clusters palladium atoms bound to defects are present, but their relative contribution to the spectra is almost negligible. As the cluster dimensions are reduced this component becomes increasingly important, while the bulk component decreases to vanishingly small intensity.

Bibliography

[1] H. Wormeester, E. Hüger, and E. Bauer, *hcp and bcc Cu and Pd Films*, Physical Review Letters **77** (1996), 1540–1543.

[2] C. Binns, C. Norris, and M.-G. Barthes-Labroussef, *Adsorbed Metallic Chains as Approximations to Quasi-One-Dimensional Systems*, Physica Scripta **T45** (1992), 283–288.

[3] C. Binns, S.H. Baker, C. Demangeat, and J.C. Parlebas, *Growth, electronic, magnetic and spectroscopic properties of transition metals on graphite*, Surface Science Reports **34** (1999), 105–170.

[4] C. Binns, *Nanoclusters deposited on surfaces*, Surface Science Reports **44** (2001), 1–49.

[5] L.M. Molina and B. Hammer, *Active Role of Oxide Support during CO Oxidation at Au/MgO*, Physical Review Letters **90** (2003), 206102.

[6] M. Haruta, *Size- and support-dependency in the catalysis of gold*, Catalysis Today **96** (1997), 153–166.

[7] M. Valden, X. Lai, and D.W. Goodman, *Onset of Catalytic Activity of Gold Clusters on Titania with the Appearance of Nonmetallic Properties*, Science **281** (1998), 1647–1650.

[8] A. Sanchez, S. Abbet, U. Heiz, W.-D. Schneider, H. Hăkkinen, R.N. Barnett, and U. Landman, *When Gold Is Not Noble: Nanoscale Gold Catalysts*, Journal of Physical Chemistry A **103** (1999), 9573–9578.

[9] T.M. Parker, L.K. Wilson, N.G. Condon, and F.M. Leibsle, *Epitaxy controlled by self-assembled nanometer-scale structures*, Physical Review B **56** (1997), 6458–6461.

[10] C.P. Collier, T. Vossmeyer, and J.R. Heath, *Nanocrystal superlattices*, Annual Review of Physical Chemistry **49** (1998), 371–404.

[11] S. Vučković, J. Samela, K. Nordlund, and V.N. Popok, *Pinning of size-selected Co clusters on highly ordered pyrolytic graphite*, The European Physical Journal D **52** (2009), 107–110.

[12] A. Goldoni, L. Petaccia, L. Gregoratti, B. Kaulich, A. Barinov, S. Lizzit, A. Laurita, L. Sangaletti, and R. Larciprete, *Spectroscopic characterization of contaminants and interaction with gases in single-walled carbon nanotubes*, Carbon **42** (2004), 2099–2112.

[13] P. Giannozzi, S. Baroni, N. Bonini, M. Calandra, R. Car, C. Cavazzoni, D. Ceresoli, G.L. Chiarotti, M. Cococcioni, I. Dabo, A. Dal Corso, S. de Gironcoli, S. Fabris, G. Fratesi, R. Gebauer, U. Gerstmann, C. Gougoussis, A. Kokalj, M. Lazzeri, L. Martin-Samos, N. Marzari, F. Mauri, R. Mazzarello, S. Paolini, A. Pasquarello, L. Paulatto, C. Sbraccia, S. Scandolo, G. Sclauzero, A.P. Seitsonen, A. Smogunov, P. Umari, and R. M. Wentzcovitch, *QUANTUM ESPRESSO: a modular and open-source software project for quantum simulations of materials*, Journal of Physics: Condensed Matter **21** (2009), 395502.

[14] J.P. Perdew, K. Burke, and M. Ernzerhof, *Generalized Gradient Approximation Made Simple*, Physical Review Letters **77** (1996), 3865–3868.

[15] D. Bai and R. Elber, *Calculation of Point-to-Point Short-Time and Rare Trajectories with Boundary Value Formulation*, Journal of Chemical Theory and Computation **2** (2006), 484–494.

[16] K. Højrup Hansen, T. Worren, S. Stempel, E. Lægsgaard, M. Bäumer, H.-J. Freund, F. Besenbacher, and I. Stensgaard, *Palladium Nanocrystals on* Al_2O_3*: Structure and Adhesion Energy*, Physical Review Letters **83** (1999), 4120–4123.

[17] J.N. Andersen, D. Hennig, E. Lundgren, M. Methfessel, R. Nyholm, and M. Scheffler, *Surface core-level shifts of some* 4*d-metal single-crystal surfaces: Experiments and* ab initio *calculations*, Physical Review B **50** (1994), 17525–17533.

[18] F.P. Leisenberger, G. Koller, M. Sock, S. Surnev, M.G. Ramsey, F.P. Netzer, B. Klötzer, and K. Hayek, *Surface and subsurface oxygen on Pd(111)*, Surface Science **445** (2000), 380–393.

[19] G.K. Wertheim, S.B. DiCenzo, and D.N.E. Buchanan, *Noble- and transition-metal clusters: The d bands of silver and palladium*, Physical Review B **33** (1986), 5384–5390.

[20] M. Cini, M. De Crescenzi, F. Patella, N. Motta, M. Sastry, F. Rochet, R. Pasquali, A. Balzarotti, and C. Verdozzi, *Palladium clusters on graphite: Evidence of resonant hybrid states in the valence and conduction bands*, Physical Review B **41** (1990), 5685–5695.

Chapter 7

Growth and chemical reactivity of Pt nanoclusters on MgO/Ag(100)

7.1 Introduction

A typical supported catalyst (as the ones used in automotive exhausts, or for methanol synthesis and many other industrial processes) consists of a thermally stable support material with a high surface-to-volume ratio over which transition metal particles (in the range of few nanometers) are dispersed. The compositional (catalysts may contain one or more elemental species) and structural complexity of these systems is their main advantage: the change of some parameters in the catalyst preparation process offers the possibility of tuning their properties, optimizing selectivity and activity to a specific reaction. This complexity, on the other hand, is the major drawback when the detailed comprehension of the origins of the catalytic properties is the objective: the interplay of many different factors in determining the catalyst's reactivity, in fact, prevents from an atomic-level understanding of the system's behaviour.

The surface science approach to this kind of investigations consists in using simplified models instead of real catalysts as samples for experimental investigations. For more than forty years surface scientists dealt with the most simple *model catalysts*: well-defined surfaces of transition metal single crystals. This enormous work provided deep understanding of the atomic processes occurring on the surface of the so-called catalyst's *active component*.

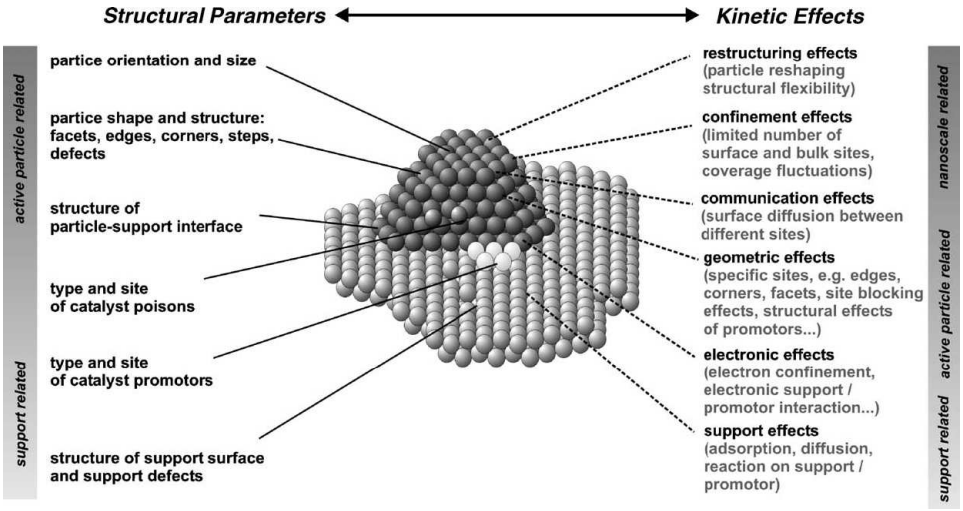

Figure 7.1: Summary of structural parameters and kinetic effects on supported metal catalysts [1].

In recent years, technical developments in sample preparation procedures as well as in experimental techniques allowed investigations on a new class of *model catalysts*: transition metal nanoclusters deposited on well-ordered oxide thin films. These systems are evidently more similar to real catalysts if compared to single crystal surfaces, but, at the same time, the possibility to control their complexity (average cluster size, number of metallic species deposited, etc.), combined with the knowledge accumulated on transition metal crystals, allows detailed studies on their chemical properties. The catalytic activity of supported metal systems appears to be determined by the interplay of several factors [1], summarized in fig. 7.1:

- In many cases, besides the *active* metal particles, also the oxide support plays a fundamental role in determining the reaction kinetics: adsorption and diffusion on the support surface may strongly influence the reaction mechanism, for instance allowing *communication effects* between small surface regions with different adsorption and reactivity characteristics.

- The limited size and the lattice distortions of metal nanoparticles, as well as their interaction with the substrate, strongly influence the electronic properties of the system.

- The high density of defects on the nanometer-sized clusters (steps, edges and corners) results in a number of sites that may exhibit specific reactivity with respect to a given reaction.

- Adsorbate induced reconstructions, a well known phenomenon on single crystal surfaces, can lead to strong changes of the particle equilibrium shape with a large potential impact on the raction kinetics.

In this chapter we will focus on Pt nanoparticles deposited on a magnesium oxide thin film grown on a Ag(111) surface, characterizing the nucleation of Pt nanoclusters and studying the oxidation process of carbon monoxide on this system. In particular we will see how high resolution photoemission measurements shed light on the nucleation mechanism and the morphology of the metal nanoparticles. Then we exploited the enhanced temporal resolution of the newly developed experimental set-up to follow the adsorption and desorption of CO on both clean and oxygen pre-covered nanoclusters with a temporal detail of 500 ms. This experiment aimed to provide a deeper understanding of the role played by the support and the clusters' size in the CO adsorption and oxidation processes.

7.2 Experimental details

The cleaning of the Ag(001) surface was achieved by repeated cycles of Ar^+ sputtering followed by annealing to 700 K. After this treatment a sharp (1×1) LEED pattern appeared and photoemission measurements revealed a contaminant-free spectrum.

The MgO thin film was grown by Mg evaporation in a 1×10^{-6} mbar oxygen pressure, with the sample temperature fixed at 500 K, according to the procedure described by Schintkel *et al.* [2], wherein the MgO/Ag(001) growth model is well described. In the first stages of the experiment a series of MgO films was prepared, corresponding to different evaporation times; for each prepared MgO film the Ag $3d_{5/2}$ core level was measured as a function of the polar emission angle θ. As will be seen in detail in sec. 7.3.1, these data allowed determining the thickness of the oxide layer and, thus, choosing the suitable thickness for Pt deposition experiments.

The Pt evaporator consists of a Pt filament resistively heated; as in the case of Pd deposition in Ch. 6, the evaporation was performed at a constant filament current with a base pressure kept below 3×10^{-10} mbar in order to avoid sample contamination. Three different depositions were performed at liquid nitrogen temperature (80 K) on the MgO/Ag(100) sample, corre-

sponding to 60, 120 and 240 s of evaporation time. The evolution of the cluster morphology was followed by measuring the Pt $4f$ core level spectra.

The reactivity of the Pt nanoclusters deposited on the MgO thin film was probed in a series of CO uptakes, performed in a temperature range between 220 and 400 K both on the clean and on the oxygen pre-covered surface. During the uptakes the C $1s$ core level was measured using the fast snapshot acquisition mode (see sec. 4.1.6): as will be reported in sec. 7.3.3 the analysis of the spectral components' intensity allowed monitoring the CO coverage with a temporal resolution of 500 ms. Carbon monoxide uptakes were performed also on the bare MgO film in order to clearly differentiate the spectral components due to CO adsorbed on Pt clusters from those due to adsorption on the MgO film: this is a first step in disentalgling the effect of the oxide support from the chemical properties of the metal clusters.

7.3 Results and discussion

7.3.1 Determination of the MgO film thickness

From the results reported in literature [2], it is known that the most favoured interface geometry between a metal oxide with a rock salt structure and the (100) surface of an fcc metal with similar lattice constant, is such that the metal atoms occupy hollow sites, whereas oxygen atoms occupy top sites in the underlying metal surface (see fig. 7.2).

STM and STS analysis reveal also that the electronic properties of a MgO/Ag(100) thin film vary with film's thickness up to 3 ML coverage, whereas beyond 3 ML the electronic structure shows no contribution from interface states, but corresponds to the electronic structure of an MgO(001) single crystal surface. This will be a useful information stating the minimum thickness of the MgO film to be prepared.

By comparing the Ag $3d_{5/2}$ spectra of the *polar scans* acquired after oxide film preparation with the peaks collected from clean silver surface, we estimated the thickness from the attenuation of the signal. The thickness (d) of the overlayer was computed for each value of θ using the equation:

$$d = \lambda_{\mathrm{MgO}}(\mathrm{E}) \cos\theta \ln\left(\frac{\mathrm{I_{clean}}}{\mathrm{I_{MgO}}}\right)$$

where $\lambda_{\mathrm{MgO}}(\mathrm{E})$ is the inelastic mean free path for the electrons inside the MgO film as a function of the kinetic energy, I_{clean} and I_{MgO} are the intensity of the Ag $3d_{5/2}$ peak for the clean and MgO covered silver surface, respectively.

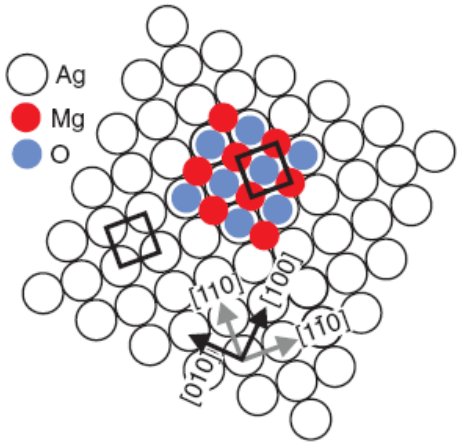

Figure 7.2: Schematic illustration of the most favourable configuration for MgO/Ag(001) growth: Mg atoms occupy hollow sites, i.e. they continue the Ag fcc lattice, while O atoms occupy on top sites. The Ag(100) surface unit cell is indicated [2].

The results are summarized in fig. 7.3. λ_{MgO} has been calculated using the TPP-2M relation [3], assuming the bulk bandgap value $E_g = 7.8$ eV, $N_v = 8$ (6 for oxygen and 2 for Mg), and the density $\rho = 3.16$ g/cm^3, obtained from the rocksalt crystal structure using the 4.2 Å lattice constant).

The results suggest some photoelectron diffraction effects (see sec. 2.5): there is clearly some systematic dependence of the calculated thickness on the polar emission angle, whereas a constant value for all θ values is expected from the TPP-2M model. Nonetheless, the average increase of the calculated thickness for polar angles in the range 40°–50° is typical for square surface lattices. Other measurements performed with higher photon energy show that the calculated thickness is always smaller at larger excitation energies, another possible consequence of the photoelectron diffraction arising from the additional symmetry of the overlayer respect to the bare silver surface. However, based on this analysis, for the Pd deposition experiments we chose the 4 minute evaporation that results in a MgO thickness in the range between 10 and 14 Å, corresponding to 5–7 atomic bilayers of MgO. In this way the oxide film is thin enough for obtaining the conductivity necessary for XPS measurments and, at the same time, its electronic properties strictly correspond to those of the single crystal surface.

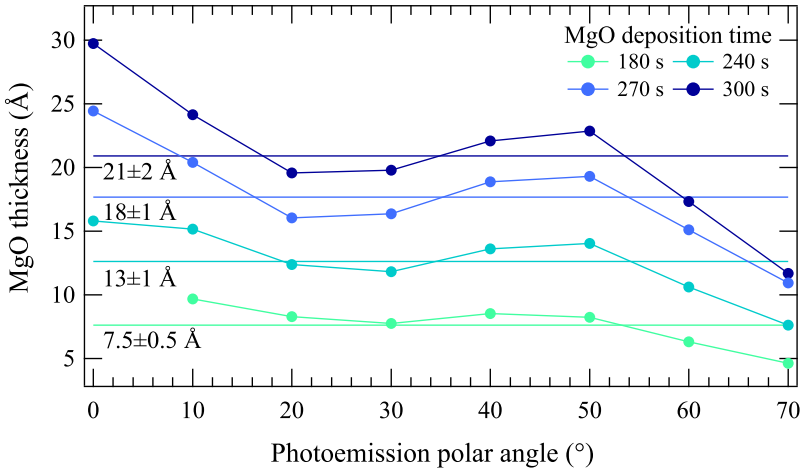

Figure 7.3: Calculation of MgO thickness from the intensity attenuation of Ag 3*d* spectra collected at hν = 550 eV. Colours refer to different deposition times.

7.3.2 Characterization of Pt nanocluster growth

Theoretical calculations of the Pt-MgO bond reveal that in the case of a defect-free MgO single crystal surface, as well as for a thin film grown on Ag(111) [4], the most stable adsorption site is on-top of the oxygen atom, with a binding energy of 2.46 eV, much higher than that for adsorption on-top of a Mg atom. The nucleation of Pt clusters is expected to take place at surface defects: from the so called F-centers, oxygen vacancies of the MgO surface, or from steps [5, 6]. Indeed, these defective sites are the most reactive sites of the MgO surface, and form stronger bonds with the adsorbed metal, as demonstrated in the case of Pd nanoclusters [7].

It is known that Pt clusters typically grow on MgO with a 3D structure, starting from a (100) base that follows the square surface lattice of the substrate. A recent theoretical work [8] suggests that the optimal aspect ratio (height/diameter) for Pt/MgO clusters is about 0.7 and that their geometry depends on the number of atoms per cluster N. For N<550, the (100) growth is the favorite one, while for larger clusters a (111) growth is expected. Cluster growth is generally determined by the interplay between surface and adhesion energy, but in the case of Pt (and also in the limit of large clusters) the difference between the two structures is quite small, as

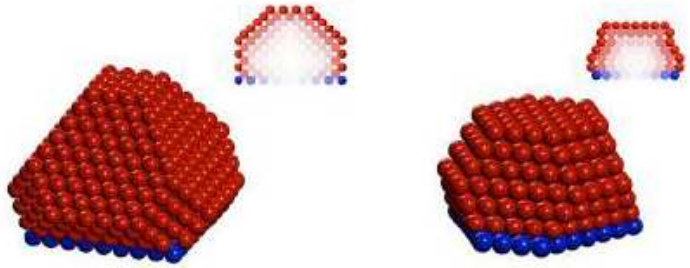

Figure 7.4: Schematic models for (100)-oriented (left) and (111)-oriented (right) cluster types grown on MgO(001). The intensity scale of the corresponding section views mimic the attenuation of the photoemission signal arising from inner atoms.

confirmed by the calculations for surface energies of Pt(111) and (100) [9].

In particular a grazing incidence X-ray scattering (GIXS) study [10] found that the (111) orientation is not observed for clusters grown below 1000 K, a temperature much higher than our hottest annealing temperature of 670 K. Models based on these results for (100) and (111) epitaxy are presented in fig. 7.4. A section through each model illustrates the attenuation of the inner atoms' contribution to photoemission spectra due to inelastic scattering. On the basis of these observations we assume that we have (100)-oriented clusters with the calculated aspect ratio.

Fig. 7.5 reports a series of Pt $4f$ spin-orbit split doublet spectra corresponding to each of the three coverages. Using a method similar to that explained in sec. 6.3.1 we found that the three Pt depositions correspond to approximately 0.03, 0.06 and 0.12 ML. Determination of the cluster size requires a microscopy study, but nonetheless it is known from previous experiments that for these coverages the clusters' size ranges from 10 to 10^4 atoms. Assuming the aspect ratio mentioned above and the (100) growth mode, we can say that our clusters' diameters range from 1 to 7 nm and the corresponding heights from 0.7 to 5 nm.

Each dataset reported in fig. 7.5 consists of 13 spectra collected at increasing annealing temperature, from 80 to 670 K. As the annealing progresses, we observe that in all the cases the doublet peaks become narrower, and shift to lower binding energies. We also observe a slight decrease in the overall intensity. Every spectrum can be tentatively fitted by the same four doublet subcomponents and a linear background, as illustrated in fig. 7.6.

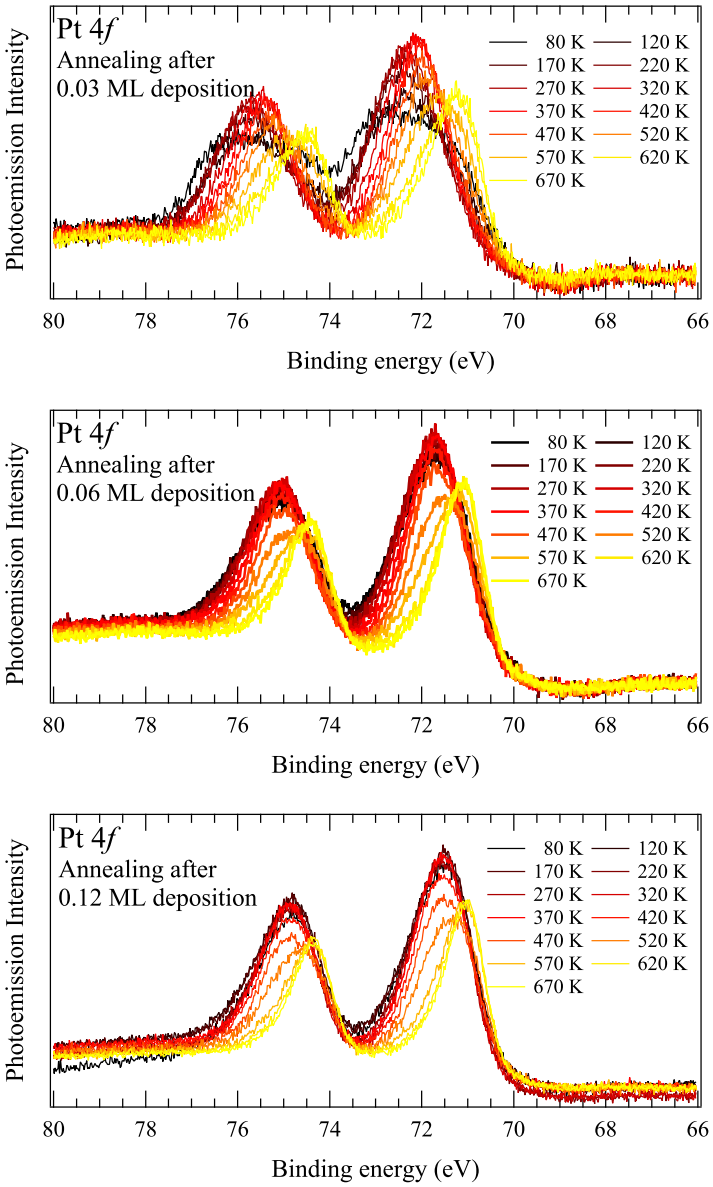

Figure 7.5: Series of Pt $4f$ core level spectra collected for the three different coverages; the color scale of the plots reflects the annealing temperature.

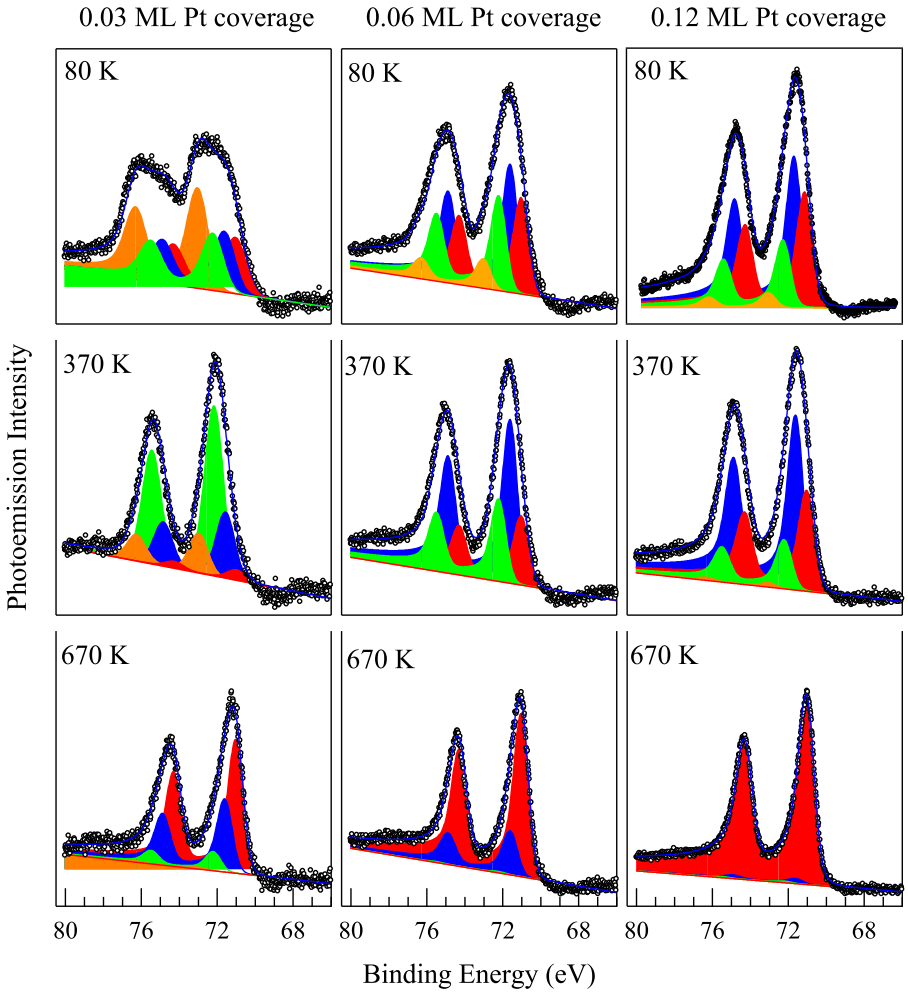

Figure 7.6: Pt $4f$ spectral components obtained from the fitting procedure for spectra acquired after annealings to different increasing temperature. For sake of clarity data for only three annealing temperatures are shown. C_0, C_1, C_2 and C_3 are respectively the red, blue, green and yellow components described in the text.

The doublets have identical lineshapes, and are split by 3.28 eV, the expected spin-orbit splitting for the $4f_{5/2}$ and $4f_{7/2}$ core levels. The branching ratio is found to be a single constant throughout the three sets of data.

The binding energies of the $4f_{7/2}$ components are reported in table 7.1,

Label	BE (eV)	CLS (eV)	Assignement
C_0 (red)	70.97	-0.59	surface/undercoordinated
C_1 (blue)	71.55	0.0	bulk/support interface
C_2 (green)	72.15	+1.19	Pt/MgO surface
C_3 (yellow)	72.96	+2.00	Pt/MgO defects

Table 7.1: Details for the Pt $4f_{7/2}$ spectral components obtained from the fitting procedure. The binding energies are referenced to the Fermi Level. Tentative assignments follow from the analysis described in the text.

together with a tentative interpretation of their origin. The shift between the red and the blue component (C_0 and C_1, respectively) is about 0.6 eV, similar to the size of the SCLS detected on Pt(100) single crystal [11]. The presence of these two spectral components confirms the formation of clusters with a certain degree of order. Unfortunately, since both types of growth lead to clusters containing (100)- and (111)-oriented surfaces, albeit with different ratios, and the difference between Pt(111) and Pt(100) SCLS is less than 0.1 eV [12], a shift too small to be resolved in our spectra because of the peak broadness due to a large distribution of non equivalent local configurations, we cannot certainly conclude that Pt clusters follow the (100) orientation. Fig. 7.7 shows the evolution of Pt $4f_{7/2}$ components, as a function of annealing temperature, plotted on the same intensity scale. For all three coverages we observe similar behaviours that reveal some details of the clusters' formation mechanism and structure.

- First af all, upon annealing the overall intensity of the Pt $4f_{7/2}$ signal decreases. This can be attributed either to the Pt atoms desorbing from the surface or, most probably, to the screening on the photoemission signal arising from inner atoms in the 3D structure.

- The intensity of C_3 component does not change with Pt coverage: this component dominates at lower coverages, but does not increase for larger amounts of Pt. If we consider that the preparation method for the MgO films did not vary between the experiments, so that one can assume that the density of F-centers is roughly constant, it seems reasonable to attribute C_3 component to Pt atoms coordinated with MgO defects. Furthermore, C_3 intensity decreases with increasing annealing temperature, a behaviour consistent with Pt atoms acting

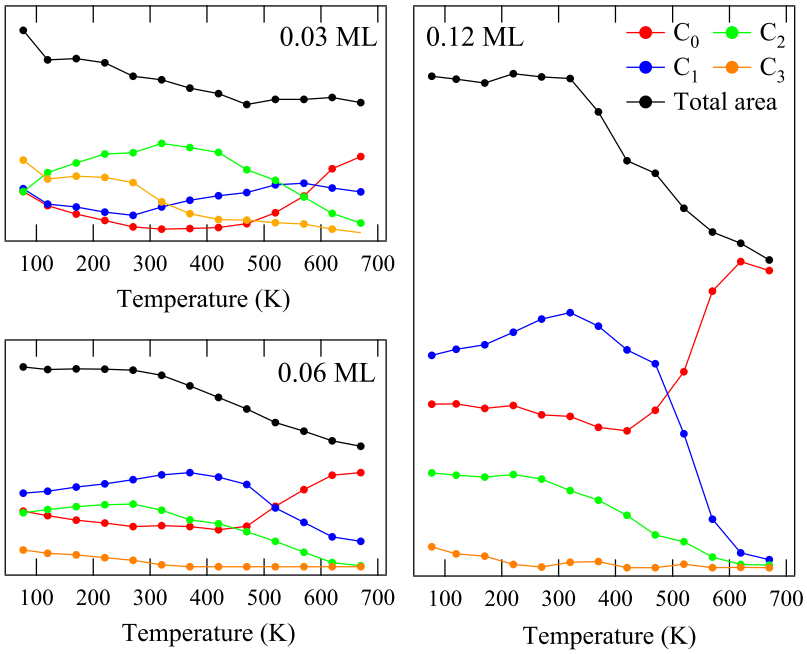

Figure 7.7: Summary of the intensity trends of Pt $4f$ spectral components as a function of annealing temperature. The black curve corresponds to the total core level intensity.

as nucleation centers and being buried and screened by clusters of increasing size.

- As suggested above, C_0 and C_1 may be interpreted as due to surface-like and the bulk-like states respectively, most probably with the surface peak comprising an overlap of the (111) and (100) contributions. In general, Pt atoms in under coordinated configurations are expected to present core level at lower binding energy with respect to bulk.

  However, at this moment the abrupt decrease of C_1 intensity, that in the case of 0.12 ML coverage goes almost to zero above 500 K, is unexplained. Thus, the preliminary assignement of this feature as due to bulk-like Pt atoms appears not fully convincing. Further investigations are needed and, in order to achieve a complete understanding of the Pt $4f$ spectra, the comparison with theoretical calculations will

be a fundamental step.

- The last component, C_2, probably arises from Pt atoms in small 2D clusters, presenting a high coordination with the MgO support and a few Pt-Pt bonds. Actually, this component vanishes at high temperatures and coverages, when formation of 3D clusters is expected.

All the experiments devoted to the characterization of chemical reactivity were performed on the three different Pt coverages after a 670 K annealing, so that the presence of well-ordered Pr nanoclusters was ensured.

7.3.3 Chemical reactivity

The final target of this experiments was the understanding of the CO oxidation mechanism on Pt supported nanoclusters by surveying the C 1*s* core level during the reaction. However, before these final measurements, several preliminary investigations were done in order to gain a sufficient understanding of the first reaction steps involving CO and O_2 molecules, i.e. CO and oxygen adsorption.

The first step in this preliminary phase of the experiment consisted in the investigation of the interaction between CO and bare MgO. The study of this process is very important for disentangling the Pt and the MgO contributions to the lineshape of C 1*s* spectra.

Another fundamental step is the understanding of the interaction between the Pt single crystal surfaces [(111) and (100)] and the two species involved in the reaction.

Of course, good understanding of the CO oxidation mechanism on Pt single crystal is also useful and completes the background for the experiment. By comparing our results with those reported in literature for Pt single crystals we could obtain information on the dependence of CO oxidation mechanism on temperature and cluster size.

CO adsorption on bare MgO

Many recent works are focused on the adsorption of CO on several kinds of MgO(001) surfaces, ranging from the single crystal to the thin films grown on Ag or Mo supports. Thermal desorption spectroscopy (TDS) investigations [13, 14] compared MgO capabilities for CO adsorption with those of intermixed metal-MgO systems. These experiments evidenced the presence of two CO species that desorb from MgO surface at 60 and 130 K. The two desorption peaks are interpreted as due to CO desorbing from regular

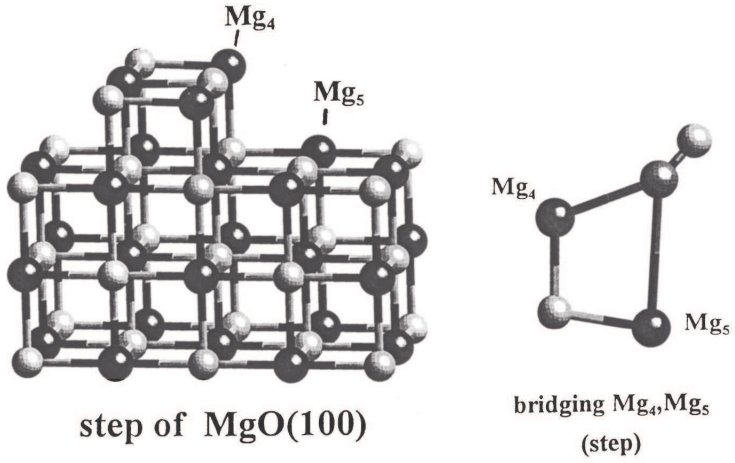

Figure 7.8: Model of a step site of a MgO(100) surface. The left part of the figure shows the adsorption configuration for a CO molecule [13].

surface sites (binding energy ≈ 0.13 eV) and from surface defects (binding energy ≈ 0.3 eV), respectively.

The origin of the higher bond strength on the defective sites can be inferred from the results of DFT calculations reported in fig. 7.8 [13]. The diagram depicts the bonding of a CO molecule on a step, where two inequivalent Mg atoms are involved. The Mg_5 is the cation laying on a flat terrace whereas Mg_4 is the configuration found on the edge of the step: the double bond with the CO molecule results in a bond strength increase.

A refinement to the above results comes from a more recent work by Freund and coworkers [15]. Their results are summarized in fig. 7.9: the TDS study revals the presence of two peaks, at 52 and 68 K respectively. Also in this case the lower temperature peak is interpreted as arising from the CO molecules desorbing from regular terraces whereas those desorbing from defective sites are indentified as the origin of the 68 K peak. The measurements were performed before and after annealing and the difference between the two spectra confirms this interpretation: the low temperature sites increase after the reordering treatment, whereas the high temperature ones present the opposite trend. The calculated binding energies corresponding to the two desorption peak are 0.15 and 0.25 eV for regular and defective sites respectively. Curiously absent in this data is the 130 K peak previosuly reported [13]. Even if the two works deal with MgO single crystal [13] and with a thin film grown on Mo(001) substrate [15], the thickness of the film

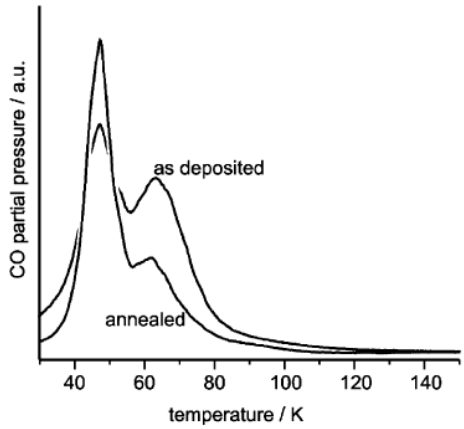

Figure 7.9: TDS spectra for CO on MgO/Mo(001) thin film with a 20 ML thickness. The two courves were acquired immediately after film deposition and after annealing to 1200 K [15].

(20 ML) should exclude substrate influences and strong differences between the two surfaces.

In our experiments the MgO film was exposed to CO at 80 K until saturation. Fig. 7.10 shows the resulting C 1*s* core level high resolution spectrum. It can be well described by using two components, α and β, located at binding energies of 292.9 eV and 290.9 eV, respectively. The two components are very broad, indicating that they include many unresolved contributions. Nonetheless, the interpretation of this result is clarified with the help of the real-time study of the adsorption and desorption processes, illustrated in fig. 7.11.

The spectra reported in the figure were acquired in scanning mode with an overall acquisition time of $\approx$ 25 s/spectrum. An can be seen in the left panel of fig. 7.11, during CO uptake the two peaks α and β grow almost simultaneously, though β may appear first and is significantly larger after the dose. Once the surface was saturated with CO, temperature-programmed photoemission experiments were performed: in the series of C 1*s* spectra reported in the right panel it can be noted that α species desorb well before β ones (the red spectra clearly show this behavior).

Even if this thermal desorption data cannot be compared with those found in literature [13, 14, 15] we can tentatively give an interpretation of

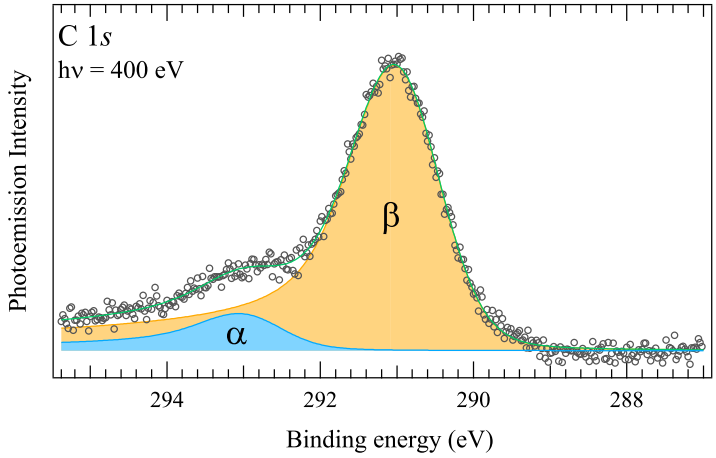

Figure 7.10: High resolution C 1*s* spectrum acquired after CO saturation and corresponding fitting analysis of the spectral components.

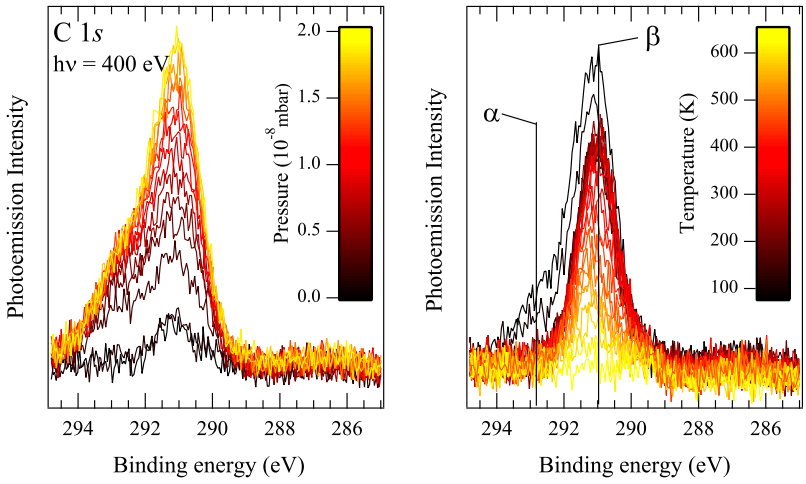

Figure 7.11: Real-time C 1*s* spectra acquired during CO adsorption (left) and desorption (right). The color scale reflects the CO pressure steps during the uptake and the temperature during the thermal desorption experiment, respectively.

this result regarding the thermal stability of this two CO phases on the MgO surfaces. By comparison with previous results we may attribute the α component (the first to disappear in temerature programmed experiments) to CO adsorbed on regular terraces, whereas the β component is attributed to CO adsorbed on defective sites. The large difference in the intensity of the two components with respect to the results reported by Freund and coworkers [15], and their higher thermal stability (note that from the reported TDS results no CO is expected on the MgO surface above 130 K) are of difficult explanation. These effects may arise from the lower thickness of our MgO film, so that the interaction with the Ag substrate may influence the stability of the adsorbed molecules; alternatively, it can be related to different types of defects.

Our next step towards the understanding of the MgO contribution to the chemical reactivity of the model catalyst will be an analysis of the CO oxidation process on the bare surface.

CO oxidation on bare MgO

The main reference for the CO oxidation reaction is a recent DFT study by Hellmann *et al.* on free standing and Ag(100) supported MgO bilayers [16]. The results indicate that the activation barrier on bare MgO/Ag(100) is 0.2 eV lower respect to the Pt(111) surface.

Another appealing feature of MgO as a CO oxidation catalyst is that the CO adsorption energy, as shown in the previous section, is quite low: this assures that CO will not poison the catalyst surface, a typical problem in CO oxidation catalysis at low temperature. On the contrary, the reaction is found to proceed by the Eley-Rideal (ER) mechanism, where oxygen is the adsorbed species reacting with the CO molecule in gas phase. The Langmuir-Hinshelwood (LH) mechanism, which contemplates the adsorption of both reactants as the first reaction step, is here prohibited by the high oxygen coverage at low temperature, preventing CO molecules from sticking on the surface.

After formation, CO_2 desorbs and no trace of carbonate formation results from theoretical calculations. The several absorption bands attributed to carbonate formation observed in InfraRed Absorption Spectroscopy (IRAS) experiments [17] are due to CO-O interaction on defective sites of the MgO layer. In fact, in the simulated system defects haven't been considered.

We investigated CO-O interaction on bare MgO by performing temperature-programmed desorption experiments in an O_2 background pressure

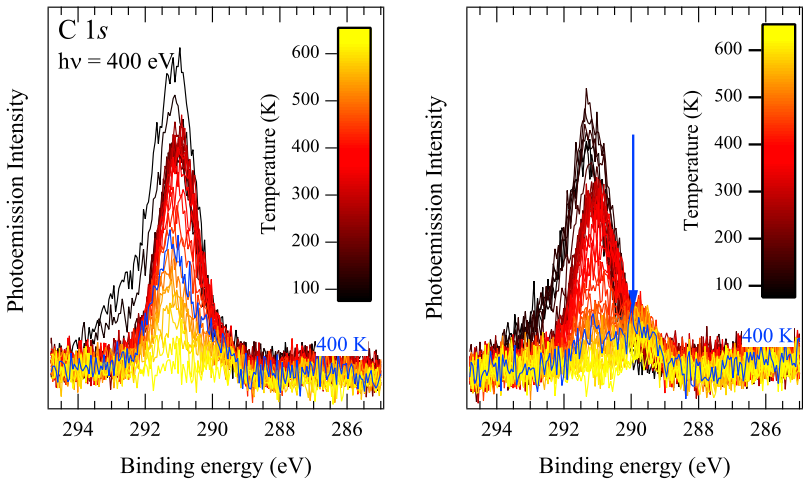

Figure 7.12: Comparison between CO thermal desorption in UHV (left panel) and in oxygen environment (10^{-7} mbar). The blue arrow indicates the new peak, arising from carbonate-like species, the blue spectra are measured at 400 K.

of 1×10^{-7} mbar while monitoring the C 1*s* signal. Fig. 7.12 shows the comparison between thermal desorption experiments in UHV and in O_2 pressure. As we can see, the presence of the oxygen induce the formation of a new peak in C 1*s* spectra, at a binding energy of about 289.7 eV. This new species, indicated by the blue arrow in the right panel, exhibits a higher thermal stability with respect to the α and β phases, (it can be observed also at 400 K, when the other two components have disappeared) and because of its occurrence only with oxygen presence we attribute it to the carbonate formation on MgO defective sites.

A further difference between spectra in the two series is the lower thermal stability of the β phase when annealing in an oxygen atmosphere: at 400 K (indicated by the blue spectrum) the β component is at half of its maximum intensity in the left panel, whereas with oxygen background pressure (right panel) it has almost zero intensity. This is probably due to the fact that in oxygen environment CO has two desorption pathways: regular thermal desorption and the reaction with oxygen that accelerates the desorption rate of the β species.

After this analysis, the comparison between our data on the bare MgO and the results reported in literature [16] is nontrivial. In our experiment we

first saturated MgO with CO and then we reacted this system with oxygen during the thermal desorption. In the experiment reported by Hellmann *et al.*, instead, the opposite mechanism is used: after an initial adsorption of oxygen, it is subsequently made to react with gas phase CO. Nonetheless, we have determined how MgO is involved in the CO oxidation mechanism: this is a good starting point for the analysis of Pt nanoclusters' chemical reactivity.

CO adsorption and desorption on Pt nanoclusers

Platinum is certainly among the most studied transition metal surfaces, and a vast literature exists which is dedicated to its interaction with small molecules such as CO and oxygen.

Upon CO adsorption on Pt(111) surface, the existance of molecules adsorbed on both on-top and bridge sites was reported: this results in two C 1s spectral components separated by 0.7 eV [19, 18]. The binding energies are 286.8 and 286.1 eV for the on-top and bridge states, respectively. Fig. 7.13 reports a sequence of C 1s spectra collected by Kinne *et al.* [18] during CO uptake at 200 K, together with the uptake curves of the total coverage and the separate curves for on-top and bridge sites. One can see that the adsorption starts on the on-top sites, and after an exposure of about 0.5 L (1 Langmuir=1×10^{-6} torr $\cdot 1$ s) bridge-site occupation begins. At saturation

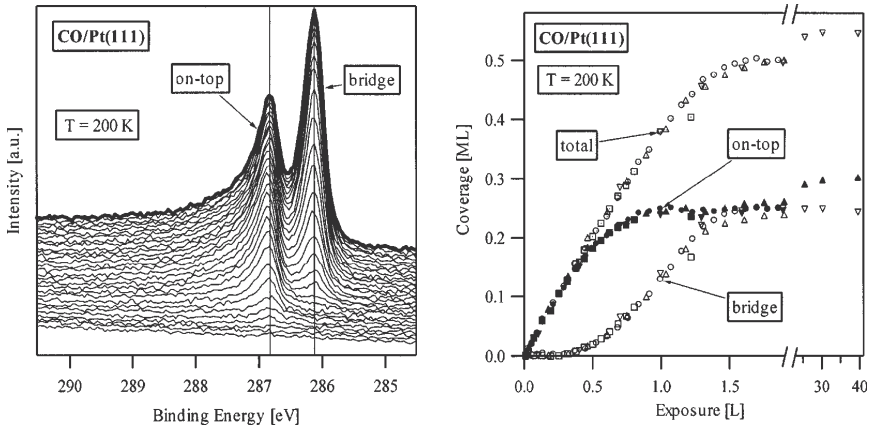

Figure 7.13: CO uptake on a Pt(111) surface: (left panel) sequence of C 1s spectra during CO adsorption at 200 K; (right panel) uptake curves for total, on-top and bridge sites [18].

a c(4 × 2) structure is formed, corresponding to a 0.5 ML coverage, equally divided between on-top and bridge sites. In this case, the higher intensity detected for bridge adsorption arises from photoelectron diffraction effects. From theoretical calculations the on-top configuration results favoured, due to an adsorption energy of 1.36 eV, about 0.2 eV higher than that of bridge sites [20].

CO adsorption on Pt(100) appears to be more complicated. The bare Pt surface reconstructs in a quasi-hexagonal arrangement, even after low temperature annealing. Interaction with CO leads to a removal of the sur-

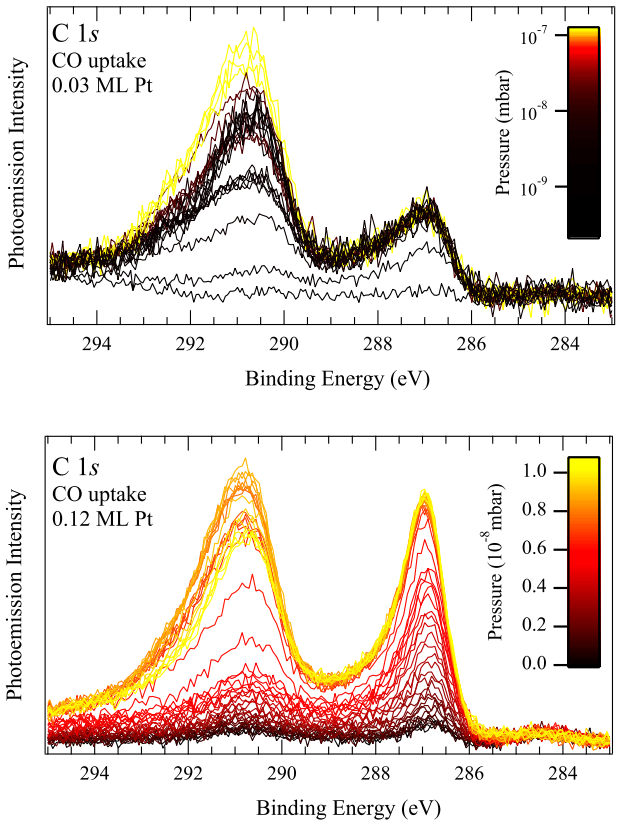

Figure 7.14: C 1*s* spectra measured during CO adsorption on 0.03 ML (upper panel) and 0.12 ML (lower panel) Pt covered sample. The color scale reflects the CO pressure steps during the uptake.

face reconstruction that is converted in a more complex configuration. The adsorption energies are similar to those found for the (111) surface [21], even though the continuous transition from one surface-phase to the other inhibits their precise quantitative determination.

We studied CO adsorption on Pt clusters by measuring both the C 1s and the Pt $4f_{7/2}$ core levels as a function of time during carbon monoxide uptake. Because of the Pt $4f_{7/2}$ spectral components' complexity, we could not retrieve useful information from their analysis. For this reason in the following I will focus only on the C 1s spectra.

In fig. 7.14 two sequences of C 1s spectra are presented, measured during CO exposure on 0.03 and 0.12 ML Pt coverage clusters. From the previous analysis it is known that the two components contributing to the high binding energy peak, at about 291 and 293 eV, arise from CO adsorption on bare MgO. As one might expect, these peaks are not affected by the Pt coverage. However, the other feature at about 287 eV follows the Pt coverage trend, indicating that this new component originates from CO adsorbed on the nanoclusters. The binding energy of this component is very close to that found for on-top adsorption [19, 18], whereas no trace of the bridge-adsorption peak is detected.

Fig. 7.15 reports the evolution of the CO/Pt peak's intensity (blue curve)

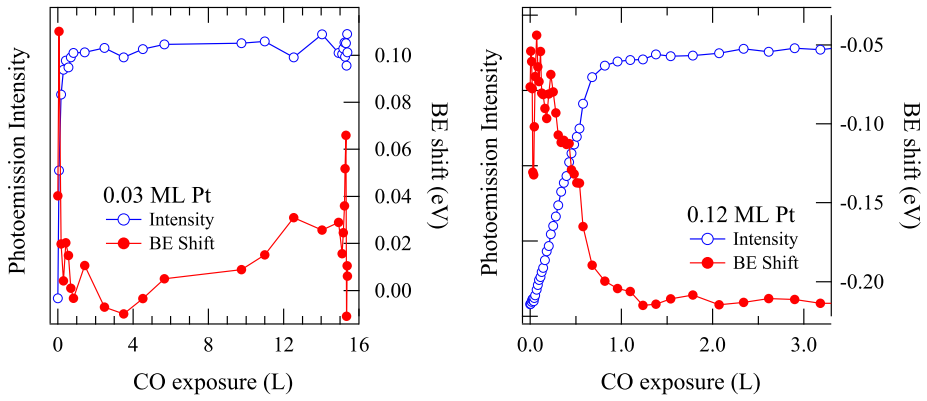

Figure 7.15: Intensity and binding energy shift evolution of the C 1s spectral component related to CO adsobed on Pt clusters for 0.03 (left panel) and 0.12 ML (right panel) Pt coverage.

and binding energy shift (red curve) as a function of the CO exposure for 0.03 and 0.12 ML of Pt coverage. A correlation between these two quantities emerges, that is particularly evident for the high Pt coverage: CO/Pt C 1s component undergoes a 170 meV shift, from the 286.80 eV at the beginning of the exposure to the final 286.97 eV value after CO saturation.

A comparison with previous works on CO adsorbed on Pt stepped surfaces [22, 23] can help in finding a tentative explanation for the binding energy trend. Fig. 7.16 shows C 1s spectra measured during CO adsorption on Pt(322) and Pt(355) surfaces. These surfaces consist of (111) terraces with (100) and (111) oriented steps, respectively. As we can see, several components can be clearly distinguished, even at first glance. On-top and bridge components arise from CO adsorption on (111) terraces, according to previous findings on Pt(111), whereas the other components arise from the CO adsorption on steps. In the left panel of fig. 7.17 two different CO doses on (322) surface are compared: after 0.32 L of CO exposure only the step sites are occupied by adsorbates, whereas larger exposure is needed for

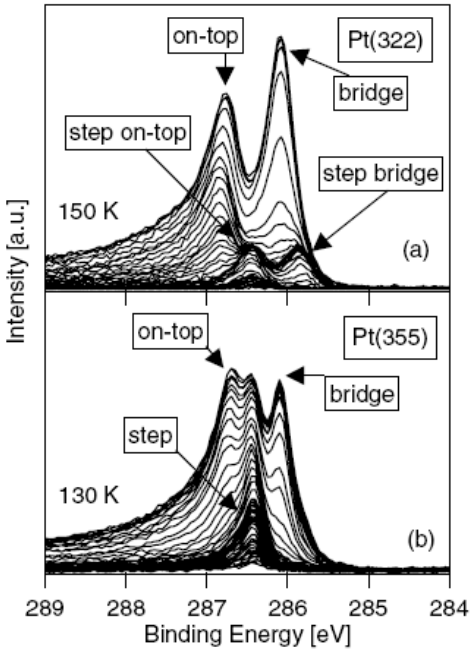

Figure 7.16: Evolution of C 1s spectra during CO adsorption on Pt(322) (upper panel) and Pt(355) (lower panel) surfaces [22].

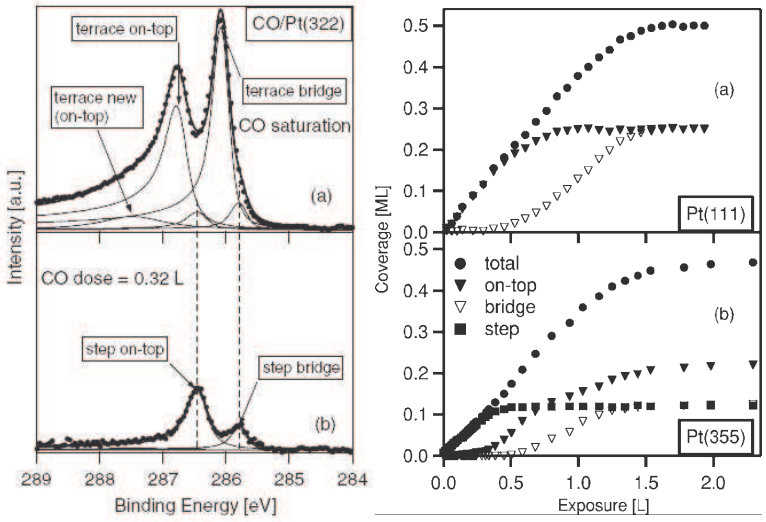

Figure 7.17: (left panel) C 1*s* spectra after exposure of Pt(322) surface to two different doses of CO [22]. (right panel) Uptake curves for the single CO adsorption sites on Pt(355) [23].

the occupation of on-top and bridge sites on the terraces. In the right panel the uptake curves for each adsorption site on (355) surface are plotted and compared with the same quantities measured for the Pt(111) surface: also for this surface the adsorption starts from the step sites (in this case only the on-top adsorption can be detected) and the occupation of terrace sites begins only after saturation of the steps. The binding energy shift between CO molecules adsorbed in on-top sites on terraces and at steps is almost the same for (322) and (355) surfaces and its value is about 0.25 eV.

On the basis of these results we may reexamine our data and formulate a hypothesis regarding the origin of the shift in CO/Pt peak detected in C 1s spectra during the CO uptake: our clusters have certainly stepped surfaces and Pt atoms in under coordinated configurations. At the beginning of CO exposure the adsorption begins on step/undercoordinated sites and the CO/Pt peak is initially found at 286.8 eV. With increasing of the exposure, small terraces are populated and this induces a shift towards higher binding energy. The position we found for the CO/Pt peak at saturation is shifted by 170 meV with respect to the step component: this value, smaller than the 250 meV found for single crystals, arises from the fact that our second signal is the superposition of terrace and step contributions, and not the pure

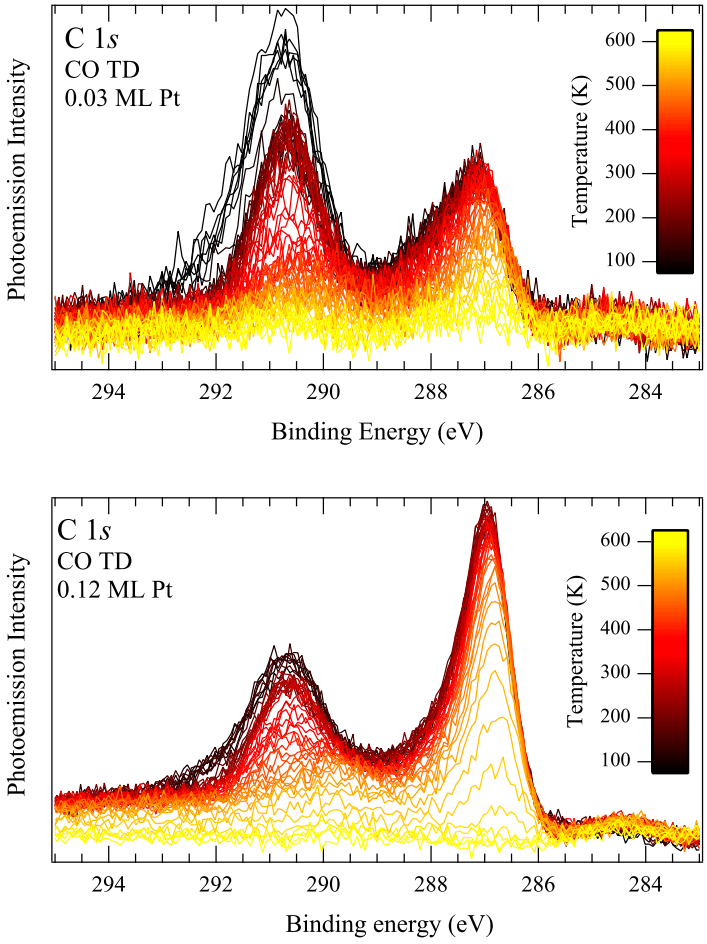

Figure 7.18: C 1*s* spectra measured during CO thermal desorption for 0.03 ML (top) and 0.12 ML (bottom) Pt coverage.

terrace component: the large distribution of inequivalent adsorption sites somehow prevents us from clearly disentangling all the spectral components.

A similar analysis was done for the thermal desorption experiments in UHV reported in fig. 7.18 and 7.19. The binding energy trend is symmetric with respect to the uptake findings, revealing that step sites are not only the first to be covered during CO adsorption, but are also those where CO

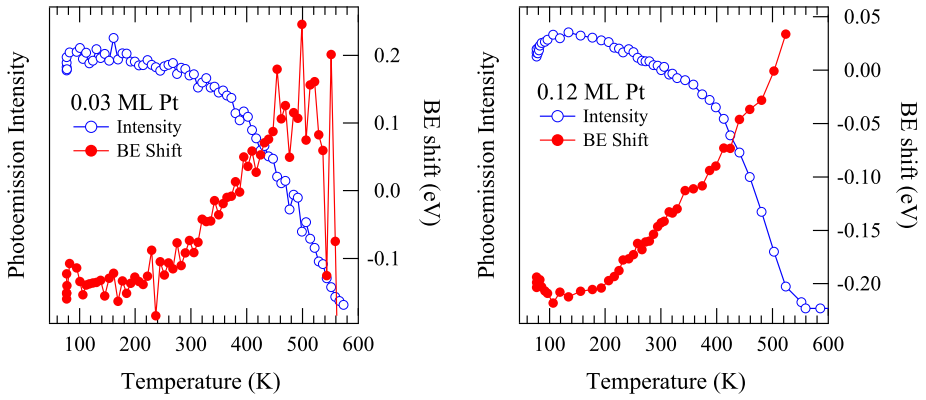

Figure 7.19: Intensity and binding energy shift evolution of the CO/Pt spectral component during thermal desorption experiments for 0.03 (left) and 0.12 ML (right) of Pt coverage.

makes stronger bonds.

In conclusion, these two measurements not only yield information on clusters' interaction with CO molecules, but are also a powerful tool for the investigation of the nanoclusters' morphology. A final experiment on the CO/Pt interaction consisted in a thermal desorption measurement in an oxygen atmosphere. As with the bare MgO, the Pt/MgO system was initially saturated with CO and then the desorption experiment was performed in an oxygen pressure of 1×10^{-7} mbar. Fig. 7.20 shows a comparison between C 1*s* spectra measured during the thermal desorption in UHV and in oxygen background. Two effects are observed in the presence of oxygen. The first, already observed on bare MgO, is the formation of a new component, indicated by the blue arrow in the figure. In the CO/MgO interaction analysis we attributed the growth of this new peak to the formation of carbonate species on defect sites of the MgO surface. The binding energy (290 eV) is very close to the 289.7 eV value found in the previous case, so we assume that this new component has the same origin. Nonetheless, we notice that its intensity is enhanced by the presence of Pt on the MgO surface. By comparing the two series of spectra in fig. 7.20, it is possible to observe that the CO/Pt feature results strongly reduced by the oxygen presence, whereas the CO/MgO peak is largely increased. We can tentatively attribute the enhancement of the carbonate peak to the activation of CO diffusion processes

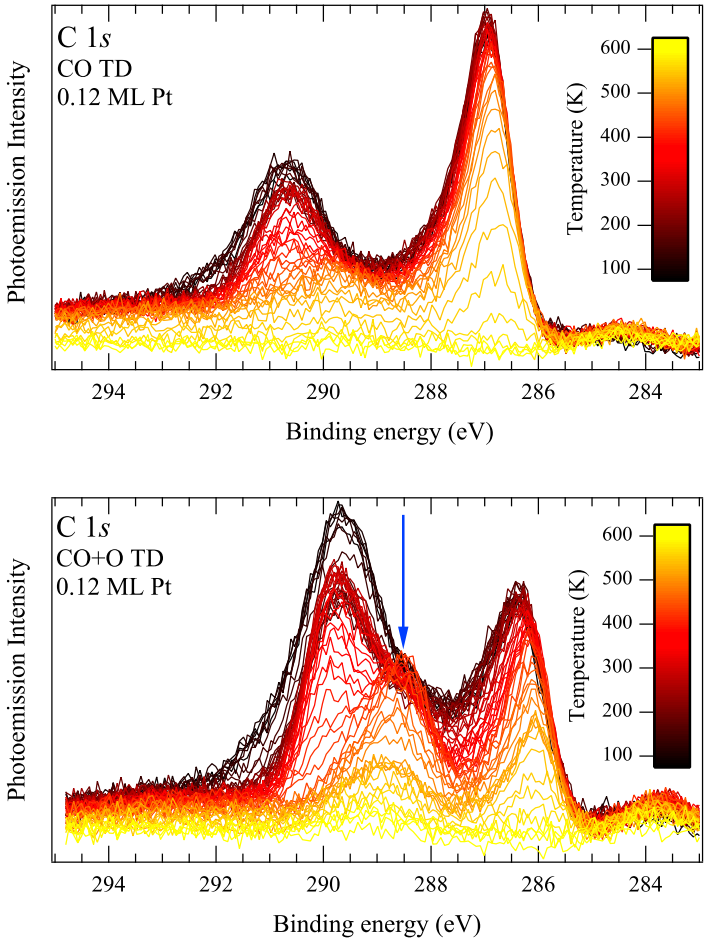

Figure 7.20: C 1*s* spectra measured during CO thermal desorption in UHV (upper panel) and oxygen atmosphere (lower panel). The blue arrow indicates the feature arising from the formation of carbonate-like species.

from Pt clusters to both regular and defective MgO sites. The experimental findings reported in this section represent an important background for the understanding of the final part of the experimental work presented in the next pages.

CO oxidation on Pt nanoclusters

Being CO oxidation one of the most important chemical reaction for industrial processes, its development on Pt based catalysts has been widely studied.

As a first step of the oxidation reaction, oxygen adsorption on Pt single crystals has been studied. The adsorption energies for oxygen on (111) and (100) Pt surfaces are reported by Gu *et al.* [24]. The most stable configurations are the three-fold hollow site on the (111) surface, the bridge site on the (100), with a binding energy of 4.6 eV for both sites.

On the (111) surface oxygen exposure induces the formation of a p(2×2) ordered structure with a 0.25 ML coverage [9], but for Pt(100) the situation is more complicated. As already mentioned, Pt bare surface reconstructs in a quasi-hexagonal arrangement; interaction with oxygen suppresses the reconstruction. Variations in adsorption energies are expected at different coverage, even if the lack of a well defined and stable surface arrangement inhibits a more detailed quantitative analysis.

Kinne *et al.* [25] studied the CO oxidation reaction on Pt(111) single crystal surface by means of high resolution photoemission spectroscopy. The study is conducted by surveying the evolution of C 1s spectra during the exposure to CO of an oxygen precovered surface. As expected, bridge site occupacy is inhibited by the presence of chemisorbed oxygen and CO adsorbs just in on-top sites. As shown in the left panel of fig. 7.21, at a temperature of 120 K a 0.23 ML CO coverage is reached, revealing that also some on-top sites must be forbidden by the oxygen pre-exposure (a higher coverage should be reached if all the on-top sites were available). At this temperature no CO oxidation reaction is observed, as revealed by the constant oxygen coverage.

In the subsequent temperature dependent study, in the range between 275 and 305 K, the activation energy of the reaction was found to be approximately 0.53 eV. In the right panel of the figure, CO oxidation can be inferred from the desorption of the oxygen and the consequent activation of the CO adsorption on the bridge sites.

The role of CO pressure has also been examined revealing that the reaction rate increases with increasing pressure up to approximately 1×10^{-6} mbar, while it is unaffected by further increases above this value.

One of the most important results of this work is the understanding of the roles played by the different oxygen adlayer areas in the kinetics of the reaction. Initially no adsorption of CO is detected, even though a small decrease in oxygen is observed. The small amount of desorbed

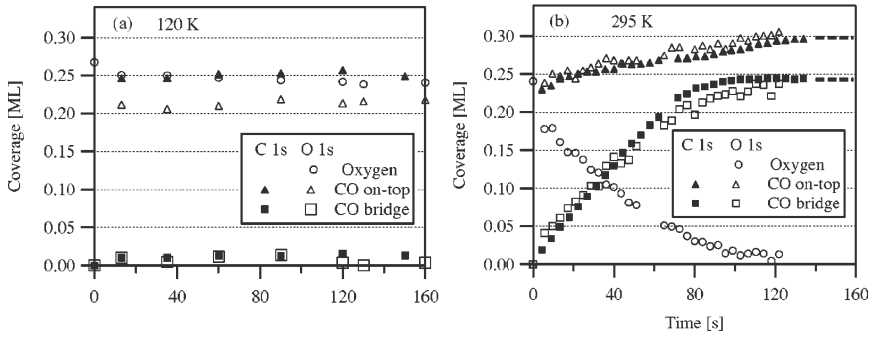

Figure 7.21: (left panel) CO exposure of oxygen pre-covered Pt(111) surface at 120 K. On the bridge sites CO adsorption is inhibited by the presence of the oxygen. (right panel) CO exposure of oxygen pre-covered Pt(111) surface at 295 K. [25].

oxygen (0.03 ML of the initial 0.25 ML coverage) is attributed to the reaction between the CO and the oxygen disorderly adsorbed outside of the p(2×2) ordered layer. The absence of a regular adsorption pattern makes these species more reactive, thus the reaction with CO is favoured.

After this first stage the reaction progresses, but not with the expected first order character: the value resulting from the modelization is about 0.63. This smaller value of the reaction order is explained by assuming that the reaction involve only oxygen atoms at the edges of the p(2×2) areas, with these species presenting a higher reactivity because of the reduced symmetry. The calculations for a kinetic model involving only edge oxygen atoms results in an order of 0.5, suggesting that this explanation is reasonable.

In as previous study on the Pt/MgO system, Heiz and coworkers [26] demonstrated the dependence of the chemical reactivity on the cluster size by using size selected clusters ranging from 8 to 20 atoms. Three different reaction paths result from their analysis, that can be assigned as follows:

- α: CO adsorbed on terrace sites reacts with ionic adsorbed oxygen. This attribution depends on the fact that this phase arises only for larger clusters, where molecular ionic adsorption can be accomplished because of the lower reactivity of fully coordinated Pt atoms.

- β_1: CO and atomic oxygen are both adsorbed on terrace sites.

- β_2: CO and atomic oxygen are both adsorbed on step sites.

Moreover, the analysis of reactivity as a function of cluster size results in

a strong enhancement (4 times) of the chemical reactivity for clusters containing more than 13 atoms: 13-atom clusters represent the phase transition from a 2D to a 3D arrangement [27], leading to a consequent increase of low coordinated atoms that translates into an enhanced chemical reactivity.

Our photoemission spectroscopy study was aimed to understanding of the influence of temperature and cluster size on the CO oxidation reaction. This was achieved by surveying C 1*s* spectra during CO exposure at temperatures ranging from 220 to 400 K, for the three Pt nanocluster nominal

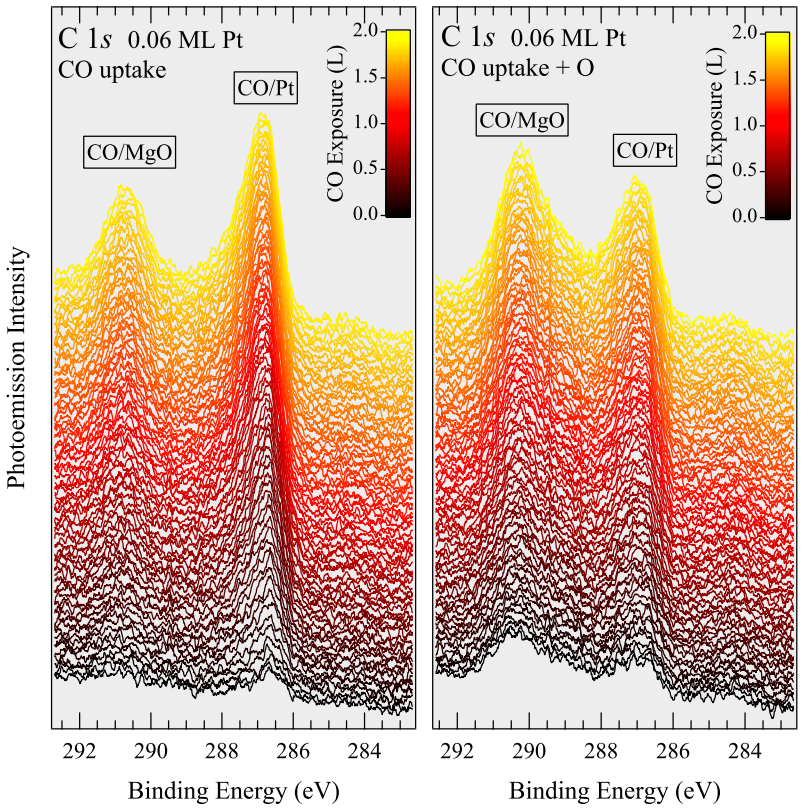

Figure 7.22: Selected snapshot C 1*s* spectra acquired during CO adsorption on clean (left panel) and oxygen pre-saturated (right panel) clusters, for 0.06 ML Pt coverage.

coverages (0.03, 0.06 and 0.12 ML). The measurements during the CO exposure were first performed on clean clusters and subsequently for the same clusters presaturated with oxygen. As an example, fig. 7.22 shows a selection of spectra acquired using the fast snapshot mode during these two types of experiments in the case of 0.06 ML coverage at 220 K. At first glance the main difference between the two measurements is the presence of a new component in the oxygen pre-saturated clusters. This new peak, arising between the CO/MgO and the CO/Pt peaks presents a binding energy similar to the feature induced by carbonate-like species, so we attribute its formation to the same effect detected during thermal desorption experiments in oxygen environment. Identical measurements were performed for each of

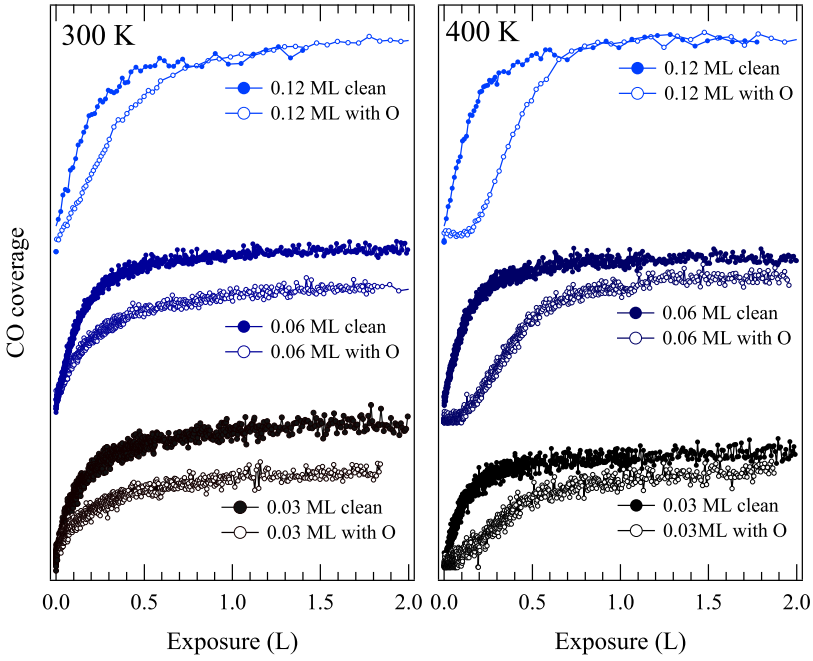

Figure 7.23: CO uptake curves for 0.03, 0.06 and 0.12 Pt coverage. CO coverage has been calculated considering only the low binding energy feature in the C 1*s* spectra, which is realted to CO adsorbed on Pt clusters (CO/Pt). The full circles curves are data from the clean clusters, the open circles are data from the oxygen pre-saturated clusters. Both oxygen and CO exposures were performed at 300 K (left panel) and 400 K (right panel).

the three Pt coverages at several temperatures. CO uptake curves on Pt clusters, reported in fig. 7.23, summarize the differences observed between clean and pre-saturated clusters by varying these two parameters. It is important to note that the chemical sensitivity of photoemission spectroscopy and the previous analysis on CO adsorption on the bare MgO allowed us taking into account only the spectral component due to CO adsorbed on Pt nanoclusters.

The size effect is clear and common to both temperatures: when small clusters (0.03 and 0.06 ML) are pre-saturated with oxygen, the CO coverage does not reach the same saturation point found for clean clusters, whereas for 0.12 ML Pt coverage both the pre-saturated and clean curves reach the same final intensity, even if after different CO exposures.

This effect can probably be attributed to oxygen atoms with a strong bond to Pt which results in a high energy barrier for reaction with CO; as a consequence, oxygen is not removed from the clusters and inhibits CO adsorption. The presence of these oxygen species only on smaller clusters indicates they originate from Pt defective adsorption sites, such as undercoordinated atoms or steps, as suggested by previous theoretical calculations reported in literature [28]. This result is in contrast with previous works, where a higher reactivity was detected for oxygen adsorbed in a disordered manner (as is expected to happen on defective sites) [25].

By comparing the 300 K and the 400 K sequences, this interpretation becomes even more convincing. As the temperature increases the difference between the two uptake curves decreases: this confirms that the lack of CO on oxygen pre-saturated clusters is due to the presence of some residual oxygen atoms. Increasing the temperature facilitates desorption of oxygen and/or catalytic reaction with CO to form CO_2, resulting in an increase of free adsorption sites.

Having considered the clusters' size and coverage effects, we may turn our attention to the effect of temperature on the CO oxidation reaction. In fig. 7.24 the CO uptake curves are shown for CO/Pt adsorption on 0.06 ML clusters, for all the temperatures.

For CO uptakes on the oxygen precovered clusters, the initial adsorption rate clearly decreases as the temperature increases, and in the experiment at 400 K an induction period (a delay in the beginning of CO adsorption) clearly appears. This temperature induced effect may be tentatively explained by one of the two following arguments.

- The first explanation is related to the enhancement of the chemical reactivity induced by the temperature. At high temperature the ini-

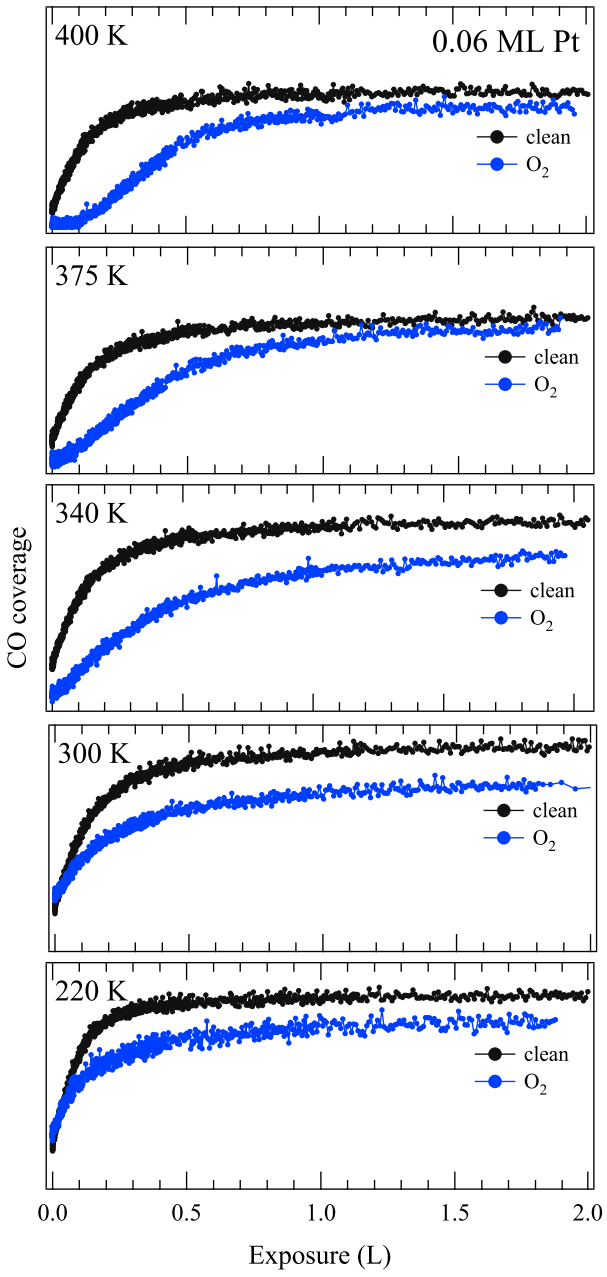

Figure 7.24: CO/Pt uptake curves for 0.06 ML of Pt coverage with temperature ranging from 220 K to 400 K. The black curves arise from the clean clusters, the blue from the oxygen pre-saturated.

tial CO sticking coefficient is low because CO reacts more likely with preadsorbed oxygen than adsorbs on the Pt surface. During this activation period CO_2 formation occurs, so that oxygen atoms leave the surface free for CO adsorption. A confirmation of this interpretation could be obtained from TDS experiments revealing the eventual CO_2 production at the beginning of CO uptake.

At low temperature the trend is opposite: CO rapidly adsorbs even on pre-saturated Pt surface, whereas small CO_2 amounts are formed. However, also for low temperature we notice that the adsorption rate is lower for pre-saturated clusters.

- The second argument is more complicated and relates to the two possible routes for the arrival of CO on the Pt clusters. The total flux of CO onto the cluster surface is the sum of two available channels for uptake of the molecules, namely direct impingement, and arrival from the bare substrate surrounding ($F_{tot} = F_{dir} + F_{diff}$). Assuming that preadsorbed oxygen inhibits the adsorption of CO we may hypothize that in the first part of the exposure the uptake of CO onto the clusters is dominated by arrival from the substrate. This process is called *reverse spillover* and is depicted in fig. 7.25 using the collection zone model [29].

  The model assumes that the clusters are regularly spaced on a rectangular grid with lattice parameter 2L, that every cluster is a perfect sink for CO, and that the system is in a steady state. From the work

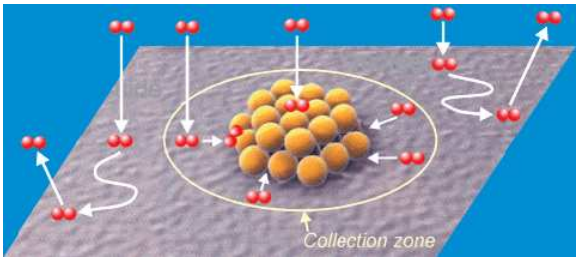

Figure 7.25: The reverse spillover process explained within the collection zone model. This effect depends on the mean diffusion length of the molecule on the support and on the density of clusters [29].

of Henry *et al.* [30], for clusters of mean radius R we can write

$$F_{diff} = 2\pi X_S \alpha J \cdot P\left(\frac{R}{X_S}, \frac{L}{X_S}\right)$$

where P(x,y) is a combination of modified Bessel functions, α is the adsorption probability of CO on MgO, J is the impinging rate of CO on the surface and X_S is the mean free path of the molecule on the MgO surface.

From the pressure p, the molecular mass M, and the temperature T, the arrival rate is simply calculated as

$$J = \frac{p}{\sqrt{2\pi M k_B T}}$$

The mean diffusion length X_S of CO molecules on the MgO substrate can be written analytically as $X_S = \sqrt{D\tau}$, where τ, the mean residence time of the CO molecule, is given by

$$\tau = \nu_a^{-1} e^{\frac{E_{ad}}{k_B T}}$$

and D, the diffusion coefficient of CO on MgO surface, is given by

$$D = a_0^2 \nu_d e^{-\frac{E_{diff}}{k_B T}}.$$

In these last two relations a_0 is the distance between two adsorption sites, E_{diff} and E_{ad} are the diffusion and adsorption energies, ν_d and ν_a are the frequency factors for the diffusion and the adsorption process.

Focusing our attention only on the temperature dependence of F_{diff} we find that

$$F_{diff} \propto \frac{1}{\sqrt{T}} e^{\frac{1}{T}}.$$

This results in a decrease of the CO flux onto the Pt clusters as the temperature increases. Starting from the initial assumption, that reverse spillover is the main source of CO flux onto clusters when clusters are pre-covered with oxygen, this can explain the temperature dependence of the delay in the CO uptake: the CO feed rate to the nanoclusters is not large enough to make the uptake begin.

However, this interpretation suffers from some problems. The strongest initial assumption of the described model is that the system is in a steady state: actually, during the course of the experiment the CO

pressure was changed in four steps (1, 2, 5 and 10×10^{-9} mbar). A second assumption on which the collection model is based is the regular distribution of nanoclusters on the support: chemical vapour deposition does not guarantee this regularity and the use of other deposition techniques would be needed to fulfill this requirement. Nevertheless this model accounts for the temperature effects observed in our experimental data and also this explanation is reliable.

As already mentioned, another factor that complicates the analysis of these experimental results is that oxygen was dosed at the same temperature of the CO exposure; as the temperature changes, oxygen can adsorb on different sites, with different adsorption energes and reactivities, making the temperature effects of difficult interpretation.

7.4 Conclusions

In this chapter it has been evidenced how photoemission spectroscopy allowed the charracterization of Pt nanoclusters' growth on the MgO/Ag(100) support by means of the analysis of the Pt $4f_{5/2}$ core level.

The interaction of Pt nanoclusters with oxygen and CO has been studied by real-time photoemission experiments, giving us information not only on chemical reactivity but also cluster morphology.

We found also that the interaction between adsorbed CO and oxygen on the bare MgO surface results in the formation of carbonate-like species on MgO defect sites. Curiously, this process is enhanced by the presence of Pt clusters: this probably reveals the presence of a CO diffusion process from clusters to MgO that becomes active at high temperatures.

The enhanced temporal resolution of the novel experimental set-up allowed studying the CO oxidation process by monitoring the evolution of the C $1s$ core level during CO exposure on both clean and oxygen pre-saturated Pt clusters. Both size and temperature effects have been detected.

Increasing the temperature results in the decrease of CO adsorption capacity of nanoclusters and in the appearance of an induction period in the uptake curves on the pre-oxidized Pt particles. This can be explained either by an enhancement of CO_2 formation, which may be more favourable than CO adsorption at the beginning of the exposure, or by the reverse spillover mechanism by which CO diffuses on the MgO surface towards the Pt clusters. This last mechanism becomes slower with increasing temperature, resulting in a decrease of CO supply and, as a consequence, a decrease of the CO uptake.

Regarding the clusters' size effects, we observed that for pre-oxidized small clusters the amount of CO detected subsequent to the exposure is less than for clean clusters. This probably occurs because of the presence of some oxygen species with a strong bond to Pt, leading to a low reactivity with CO.

Bibliography

[1] J. Libuda and H.-J. Freund, *Molecular beam experiments on model catalysts*, Surface Science Reports **57** (2005), 157–298.

[2] S. Schintke and W.-D. Schneider, *Insulators at the ultrathin limit: electronic structure studied by scanning tunnelling microscopy and scanning tunnelling spectroscopy*, Journal of Physics: Condensed Matter **16** (2004), R49–R81.

[3] S. Tanuma, C.J. Powell, and D.R. Penn, *Calculations of electron inelastic mean free paths. V. Data for 14 organic compounds over the 50-2000 eV range*, Surface and Interface Analysis **21** (1994), 165–176.

[4] S. Sicolo, L. Giordano, and G. Pacchioni, *Adsorption of Late Transition Metal Atoms on MgO/Mo(100) and MgO/Ag(100) Ultrathin Films: A Comparative DFT Study*, Journal of Physical Chemistry C **113** (2009), 16694–16701.

[5] M. Bäumer and H.-J. Freund, *Metal deposits on well-ordered oxide films*, Progress in Surface Science **61** (1999), 127–198.

[6] L. Giordano, J. Goniakowski, and G. Pacchioni, *Properties of MgO(100) ultrathin layers on Pd(100): Influence of the metal support*, Physical Review B **67** (2003), 045410.

[7] L. Giordano, C. Di Valentin, G. Pacchioni, and J. Goniakowski, *Formation of Pd dimers at regular and defect sites of the MgO(100) surface: cluster model calculations*, Chemical Physics **309** (2005), 41–47.

[8] J. Goniakowski, A. Jelea, C. Mottet, G. Barcaro, A. Fortunelli, Z. Kuntová, F. Nita, A.C. Levi, G. Rossi, and R. Ferrando, *Structures of metal nanoparticles adsorbed on MgO(001). II. Pt and Pd*, The Journal of Chemical Physics **130** (2009), 174703.

[9] N. Seriani and F. Mittendorfer, *Platinum-group and noble metals under oxidizing conditions*, Journal of Physics: Condensed Matter **20** (2008), 184023.

[10] J. Olander, R. Lazzari J. Jupille, B. Mangili, and J. Goniakowski, *Size- and temperature-dependent epitaxy for a strong film-substrate mismatch: The case of Pt/MgO(001)*, Physical Review B **76** (2007), 075409.

[11] A. Baraldi, E. Vesselli, L. Bianchettin, G. Comelli, S. Lizzit, L. Petaccia, S. de Gironcoli, A. Locatelli, T.O. Mentes, L. Aballe, J. Weissenrieder, and J.N. Andersen, *The* (1×1) *→hexagonal structural transition on Pt(100) studied by high-energy resolution core level photoemission*, The Journal of Chemical Physics **127** (2007), 164702.

[12] L. Bianchettin, A. Baraldi, S. de Gironcoli, E. Vesselli, S. Lizzit, L. Petaccia, G. Comelli, and R. Rosei, *Core level shifts of undercoordinated Pt atoms*, The Journal of Chemical Physics **122** (2008), 114706.

[13] J.A. Rodriguez, T. Jirsak, M. Pérez, L. González, and A. Maiti, *Studies on the behavior of mixed-metal oxides: Adsorption of CO and NO on MgO(100),* $Ni_xMg_{1-x}O(100)$*, and* $Cr_xMg_{1-x}O(100)$, The Journal of Chemical Physics **114** (2001), 4186–4195.

[14] H.-J. Freund, *Oxide surfaces*, Faraday Discussions **114** (1999), 1–31.

[15] M. Sterrer, T. Risse, and H.-J. Freund, *CO adsorption on the surface of MgO(001) thin films*, Applied Catalysis A **307** (2006), 58–61.

[16] A. Hellman, S. Klacar, and H. Grönbeck, *Low Temperature CO Oxidation over Supported Ultrathin MgO Films*, Journal of The American Chemical Society **131** (2009), 16636–16637.

[17] E. Guglielminotti, S. Coluccia, E. Garrone, L. Cerruti, and A. Zecchina, *Infrared study of CO adsorption on magnesium oxide*, Journal of the Chemical Society, Faraday Transactions 1 **75** (1979), 96–108.

[18] M. Kinne, T. Fuhrmann, C.M. Whelan, J.F. Zhu, J. Pantförder, M. Probst, G. Held, R. Denecke, and H.-P. Steinrück, *Kinetic parameters of CO adsorbed on Pt(111) studied by* in situ *high resolution x-ray photoelectron spectroscopy*, The Journal of Chemical Physics **117** (2002), 10852–10859.

[19] F. Bondino, G. Comelli, F. Esch, A. Locatelli, A. Baraldi, S. Lizzit, G. Paolucci, and R. Rosei, *Structural determination of molecules adsorbed in different sites by means of chemical shift photoelectron diffraction:* $c(4 \times 2)$*-CO on Pt(111)*, Surface Science **459** (2000), L467–L474.

[20] M. Cacciatore, E. Christoffersen, and M. Rutigliano, *Adsorption Site and Surface Temperature Effects in CO Formation on Pt(111): A New Semiclassical Study*, Journal of Physical Chemistry A **108** (2004), 8810–8818.

[21] M.A. Barteau, E.I. Ko, and R.J. Madix, *The adsorption of CO, O_2, and H_2 on Pt(100)-*(5×20), Surface Science **102** (1981), 99–117.

[22] B. Tränkenschuh, C. Papp, T. Fuhrmann, R. Denecke, and H.-P. Steinrück, *The dissimilar twins—a comparative, site-selective in situ study of CO adsorption and desorption on Pt(322) and Pt(355)*, Surface Science **601** (2007), 1108–1117.

[23] B. Tränkenschuh, N. Fritsche, T. Fuhrmann, C. Papp, J. F. Zhu, R. Denecke, and H.-P. Steinrück, *A site-selective* in situ *study of CO adsorption and desorption on Pt(355)*, The Journal of Chemical Physics **124** (2006), 074712.

[24] Z. Gu and P.B. Balbuena, *Absorption of Atomic Oxygen into Subsurfaces of Pt(100) and Pt(111): Density Functional Theory Study*, Journal of Physical Chemistry C **111** (2007), 9877–9883.

[25] M. Kinne, T. Fuhrmann, J.F. Zhu, C.M. Whelan, R. Denecke, and H.-P. Steinrück, *Kinetics of the CO oxidation reaction on Pt(111) studied by* in situ *high-resolution x-ray photoelectron spectroscopy*, The Journal of Chemical Physics **120** (2004), 7113–7122.

[26] U. Heiz, A. Sanchez, S. Abbet, and W.-D. Schneider, *Catalytic Oxidation of Carbon Monoxide on Monodispersed Platinum Clusters: Each Atom Counts*, Journal of The American Chemical Society **121** (1999), 3214–3217.

[27] S.H. Yang, D.A. Drabold, J.B. Adams, P. Ordejónk, and K. Glassford, *Density functional studies of small platinum clusters*, Journal of Physics: Condensed Matter **9** (1997), L39–L45.

[28] Ž. Šljivančanin and B. Hammer, *Oxygen dissociation at close-packed Pt terraces, Pt steps, and Ag-covered Pt steps studied with density functional theory*, Surface Science **515** (2002), 235–244.

[29] M.A. Röttgen, S. Abbet, K. Judai, J.-M. Antonietti, A.S. Wörz, M. Arenz, C.R. Henry, and U. Heiz, *Cluster Chemistry: Size-Dependent Reactivity Induced by Reverse Spill-Over*, Journal of The American Chemical Society **129** (2007), 9635–9639.

[30] C.R. Henry, C. Chapon, and C. Duriez, *Precursor state in the chemisorption of CO on supported palladium clusters*, The Journal of Chemical Physics **95** (1991), 700–705.

Chapter 8

Graphene on Ir(111): growth, properties and supported systems

8.1 Introduction

Graphene is the name given to a single layer of carbon atoms tightly packed into a two-dimensional honeycomb lattice. It is the building block for all the other graphitic materials: it can be wrapped up into a zero-dimensional fullerenes, rolled into one-dimensional nanotubes or stacked into three-dimensional graphite (Fig. 8.1).

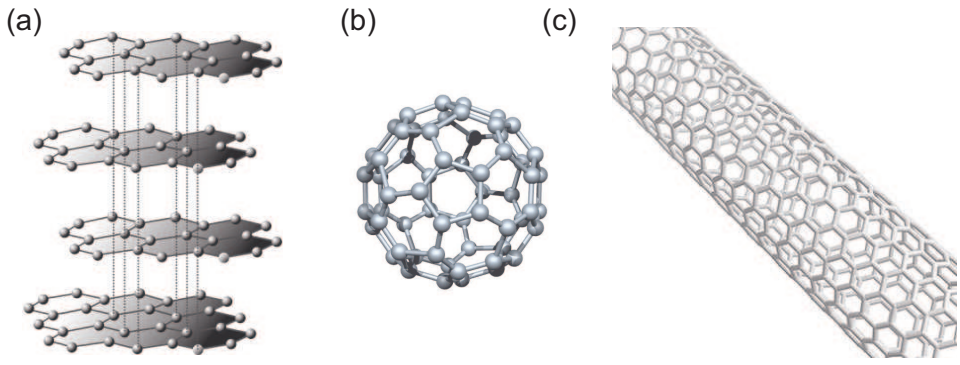

Figure 8.1: Graphene is the constituent of the graphitic materials: graphite (a), fullerenes (b) and carbon nanotubes (c).

Theoretically, graphene has been studied for more than fifty years and is widely used for describing properties of carbon-based materials. On the other hand, graphene was considered a sort of "academic toy" since, altough known as the building block of 3D materials, it was presumed not to exist in the free state being unstable with rescpect to the formation of curved structures such as fullerenes and nanotubes. In 2004 this common idea was refuted with the discovery of free-standing graphene carried out by the Novoselov and Geim group in Manchester [1].

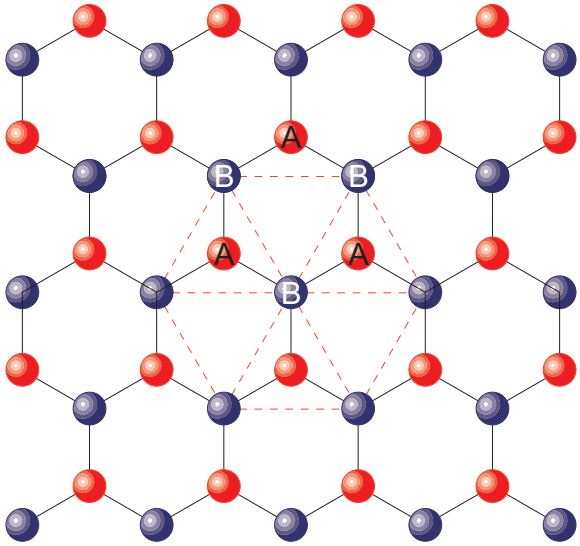

Figure 8.2: Representation of the graphene lattice. The two inequivalent triangular lattices A and B are highlighted.

The honeycomb lattice of graphene, pictured in fig. 8.2, consist of two interpenetrating triangular sublattices: the sites of one sublattice are at the centers of triangles defined by the other. The lattice has thus two atoms per unit cell, designated as A and B in the figure, and is invariant under 120° rotations around each lattice site. A carbon atom has one s and three p valence orbitals. The s orbital and the two in-plane p orbitals are hybridized in graphene's strong covalent bonding (sp^2) and do not contribute to its conductivity. The remaining p orbital, oriented perpendicular to the molecular plane, is odd under inversion in the plane and hybridizes to form π (valence) and π^* (conduction) bands.

In the Bloch description of the electronic structure of solids, orbital energies depend on the momentum of charge carriers in the crystal Brillouin

zone. In the case of graphene, the π and π^* bands are decoupled from the σ and σ^* bands because of inversion symmetry and are closer to the Fermi energy because they partecipate to a lesser extent in the bonding. In a neutral graphene sheet, valence and conduction band meet at the Fermi energy, forming conical valleys that touch at two of the high-symmetry points in the Brillouin zone.

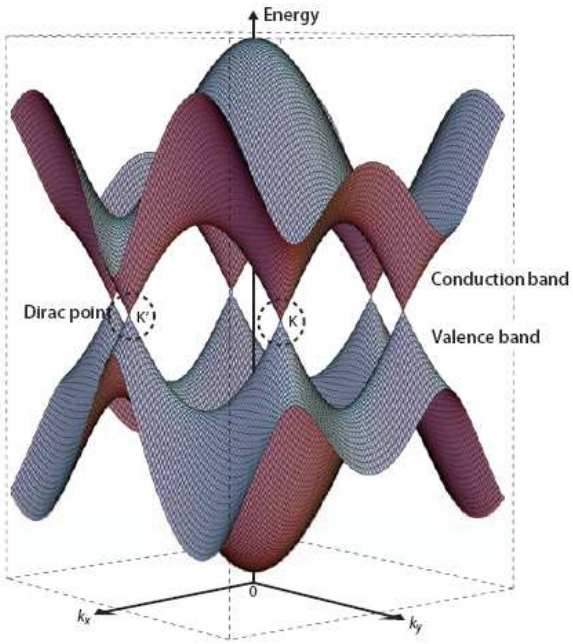

Figure 8.3: Energy bands near the Fermi level in graphene. The conduction and valence bands cross at points K and K′. From [2].

From all the the above considerations follows that graphene can be considered a zero-gap semiconductor where the valence and the conduction band energies are linear functions of momentum (at least close to high-symmetry points). This last property implies that the velocity of electrons in graphene is constant, independent of momentum, much like the velocity of photons, and leads to the conclusion that in graphene the charge carriers (both electrons and holes) mimic relativistc particles and are naturally described starting with the Dirac equation for massless particles (massless Dirac fermions) with an effective speed of light $v_F \approx 10^6$ m/s [1].

[1]It is worth noting that graphene's relativistic behaviour does not arise from required

The graphene's relativistic character produces some intriguing phenomena such as the *ambipolar electric field effect* (due to the possibility to tune continuously charge carriers between electrons and holes) [3] or an anomlous behaviour of the quantum Hall effect [4]. From the point of view of possible applications, on the other hand, other properties of this material may be more important:

- the high mobility of charge carriers at room temperature appears almost independent from dopant concentration, which translates into ballistic transport on the submicrometer scale (0.3 μm at 300 K) and into a resistivity (1×10^{-6} Ω/cm) that at room temperature is lower than that of silver(1.7×10^{-6} Ω/cm) [5];

- altough the gap between valence and conduction band is zero for ideally boundless graphene, thanks to quantum confinement effects its value can be tailored up to fractions of electronvolts by carving graphene nanoribbons of proper size [6, 7];

- graphene appears to be the strongest material ever tested, since measurements have shown that its breaking strength is about 100 times higher than that of steel [8].

The above described characteristics open a wide range of possibilities for graphene-based devices.

- *Gas sensors.* Due to graphene's bi-dimensional structure, its whole volume is exposed to the surrounding environment, making this material very efficient in detecting adsorbed molecules: adsorbed molecule cause changes in electrical resistance and graphene's extremely low resistance allows detecting these changes with incredibly good signal-to-noise ratios [9].

- *Field-emission electronic devices.* Graphene exhibits a pronounced response to perpendicular external electric fields [1] giving the possibility to design all-graphene planar Field-Effect Transistors (FET): in such devices source, drain and gate terminals as well as the conducting channel would be entirely realized in graphene allowing a much higher integration scale than that achievable with silicon [10, 11].

consistency with Lorentz invariance, but simply from the symmetry of the honeycomb lattice.

- *Transparent conducting electrodes.* From the optical point of view, graphene absorbs only about 2.3% of the incident white light [12]. The combination of transparency, extraordinary high electrical conductivity, mechanical strength and flexibility, together with the possibility to deposit a single layer of material from a solution, makes graphene an ideal candidate for transparent conducting electrodes required for applications such as touch-screens, liquid crystal displays, organic photovoltaic cells and organic light-emitting diodes [13, 14].

The above mentioned applications are only the most explored possibilities. The basic difficulty, however, common to all the possible projects, is the large-scale graphene production. Up to now, in absence of graphene wafers, many experimental groups are using samples obtained by micromechanical cleavage of bulk graphite, the same technique that allowed isolation of the first graphene flakes [1]. After fine-tuning, the application of this technique provides high-quality graphene crystallites up to 100 μm in size, large enough for most research purposes. The most important drawback of this technique, on the other hand, is the large amount of time needed for individuating the rare graphene crystallites hidden among the thousands of thick graphite flakes produced during exfoliation process.

Another method for graphene preparation consists in dispersing graphite oxide paper in pure hydrazine, so that oxygen can be removed and single graphene sheets with restored planar geometry can be deposited on a silicon or silicon oxide wafer [15].

The preparation of single-layer graphene by thermal decomposition of silicon carbide (SiC) has been proposed as a viable route for the synthesis of uniform, wafer-size graphene layers for technological applications. If field-effect devices are the objective, this procedure presents the advantage that the graphene layer is already deposited on an insulating support, strongly resembling the typical structure of an actual electronic device. However, at present the large-scale structural quality is limited by the lack of continuity and uniformity of the film: the average domain size is 30-100 nm on the Si-terminated SiC(0001), whereas on the C-terminated surface larger domains up to 200 nm can be obtained. Moreover, decomposition of SiC is not a self-limiting process and, as a result, regions of different film thicknesses coexist, as shown by low energy electron microscopy imaging [16, 17].

Our interest, actually, was attracted by a fourth method of graphene preparation based on hydrocarbon dissociation on transition metal (TM) surfaces. Graphene on metal surfaces has been known for almost forty years

from industrial heterogeneous catalysis, where, for reactions involving hydrocarbons, the deposition of graphitic carbon on the catalyst surface is a major reason for deactivation. Recent investigations have shown that these graphitic layers consist of few graphene layers only, or even of monolayers [18].

For the decomposition method mostly ethylene is used, but the decomposition of propane, methane and acetylene works as well. The molecules are either adsorbed at room temperature, after which the samples are annealed to decompose the molecules and induce the hydrogen desorption, or the molecules are directly deposited at high temperature. It appears that with this method the film growth can easily be restricted to single layers. The decomposition of the hydrocarbon molecules, in fact, is catalyzed by the transition metal surface, therefore once the surface is fully covered with the first graphene layer the process is suppressed. Proofs that actually single layers can be obtained by the described preparation method are provided by scanning tunneling microscopy (STM) [19, 20, 21, 22].

Graphene layers grown on transition metal surfaces usually present periodically corrugated structures that result from the small lattice mismatch between graphene (lattice constant of bulk graphite is 2.46 Å) and the hexagonally close-packed metal surfaces [lattice constants are 2.49 Å for Ni(111), 2.69 Å for Rh(111), 2.71 Å for Ru(0001), 2.72 Å for Ir(111) and 2.77 Å for Pt(111)]. Superimposing the graphene and the substrate lattices therefore leads to coincidence structures with large lattice constants or to incommensurate structures with similarly large quasi-periodicities. These are also known as Moiré structures. In all the mentioned cases, the lattice constant of the graphene layer does not change more than approximately 1% with respect to bulk graphite, consistent with the high in-plane stiffness of the graphene sheets. The extreme uniformity of some of the Moiré structures makes these systems perfect templates for the growth of nanostructures. This idea was successfully pursued for the graphene Moiré structure on Ir(111) on which iridium clusters were first grown [20], followed by platinum, tungsten and rhenium [23].

Another critical aspect of graphene-TM systems is the strength of the interaction with the different metal substrates. Recent studies which combine near-edge x-ray absorption fine structure (NEXAFS) and photoemission spectroscopy measurements on Pt, Ir, Rh and Ru substrates have shown that going from $5d$ to $4d$ transition metals the interaction of graphene changes from very weak to strong chemical bond with the substrate [24]. More in detail, Pt(111) results the less interacting surface, while graphene-metal interaction increases going from Ir to Rh and Ru.

Graphene on Ir(111)

Among the transition metal crystals that can be used as substrates for graphene growth, the Ir(111) surface raised our interest for mainly two reasons: the high quality of the graphene layer that can be grown on this surface [21, 22] and the weakness of the C-Ir interaction [24, 25]. A brief review of the system characteristics, however, may help in understanding the properties that make Ir(111) such an interesting substrate for graphene preparation.

Upon ethylene decomposition on the bare Ir surface above 800 K, and reordering during annealing at temperatures as high as 1470 K, the resulting C atoms form a graphene layer. As already mentioned for transition metal substrates in general, ethylene dissociation can only take place on the uncovered Ir(111) surface; this makes it a self-limiting process and multiple layer regions are avoided.

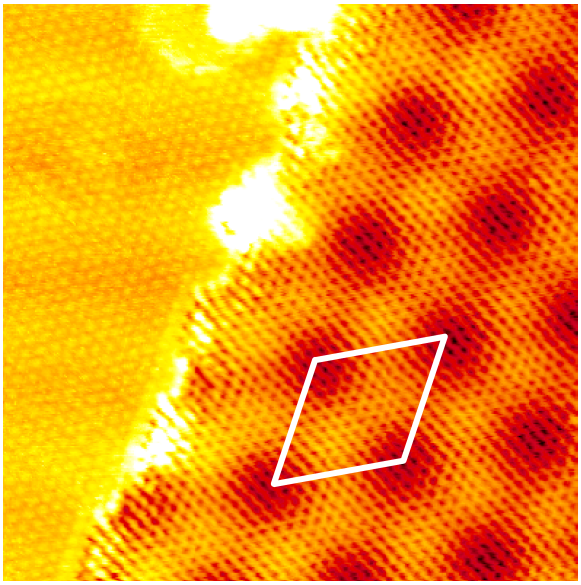

Figure 8.4: STM image of a graphene flake attached to an iridium step edge. In the left side of the picture the bare Ir(111) surface is imaged; on the right side the graphene moiré pattern is visible and the superstructure unit cell is marked as a white rhombus (100 Å×100 Å, $U_T = 0.17$ V and $I_T = 21$ nA; from [21]).

Besides the expected honeycomb structure of graphene, a superstructure can be clearly identified in scanning tunneling microscopy (STM) images

(fig. 8.4) and is also confirmed by the analysis of the LEED pattern. This graphene superstructure can be viewed as a moiré. A moiré pattern results from the superposition of two regular lattices and has a reciprocal lattice vector that is the difference of the constituting reciprocal lattice vectors. It is a phenomenon very similar to the one that originates the well known beats from the superposition of two sound waves. The superposition of the graphene lattice with a periodicity of 2.45 Å (as measured in STM and low-energy electron diffraction (LEED) experiments), and the Ir lattice with atomic nearest-neighbor distance of 2.715 Å, yields a superstructure with periodicity of 25.3 Å that corresponds to 9.32 Ir unit cells and to 10.32 unit cells of graphene [21].

Within a single moiré cell, the base of the surface structure, three different regions can be distinguished, which differ by the arrangement of carbon atoms with respect to the underlying iridium surface sites. The labeling given in the following corresponds to the type of iridium surface site located below the center of the carbon rings in the region:

- **hcp region:** in this region the graphene honeycomb rings are centered on an iridium hcp site, i.e. over an iridium atom in the *second* layer of the crystal. In this configuration, every second carbon atom is positioned on the other three-fold coordinated site, namely the fcc site, and every second atom is on top of an iridium substrate atom.

- **fcc region:** in this region the graphene honeycomb rings are centered on an iridium fcc site, i.e. over an iridium atom in the *third* layer of the crystal. In this configuration, every second carbon atom is positioned on a fcc site, and every second atom is on top of an iridium substrate atom.

- **atop region:** in this region the graphene honeycomb rings are centered on an iridium atom of the first layer. In this configuration, all the carbon atoms sit in a three-fold coordinated site, being alternatively in a hcp and in a fcc site.

Actually, the above descriptions define single points within the moiré cell, rather than real regions; due the small mismatch between iridium and carbon lattice parameters, however, the relative positions of the atoms change only slightly in the neighbourhood of this points, so that small regions with similar atomic configurations can be identified, as clearly represented in fig. 8.5.

The geometrical structure of these regions strongly influences the bondings between carbon and iridium atoms and, as a consequence, their elec-

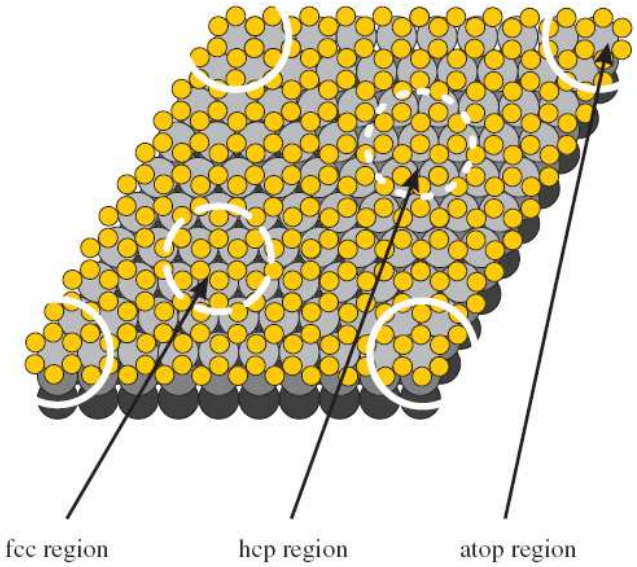

Figure 8.5: Schematic representation of the three regions individuated within the moiré unit cell. The superstructure is constructed by superposition of the graphene lattice (yellow balls) onto the Ir(111) surface (gray balls). The darker shades of gray represent the second and third layers of the iridium substrate. White arcs in the corners of the cell indicate the *atop* regions, where an iridium atom of the topmost layer is centered in the graphene honeycomb and the carbon atoms cover the threefold coordinated hollow sites. In the fcc region indicated with the dashed circle and the hcp region (dotted circle) there are threefold coordinated hollow sites centered under the carbon ring: either an fcc site (in the fcc region) or an hcp site (in the hcp region). Every second carbon atom is located at the other hollow site and every second above an iridium surface atom. From [21].

tronic structure and chemical properties. The different properties of the three regions play a fundamental role, e.g., in the case of cluster adsorption: STM investigations, in fact, evidenced how Ir cluster adsorb preferentially on *hcp* regions, while *fcc* regions may be occupied only below 160 K and no clusters have been observed in the *atop* regions. This behaviour is strongly related with the hybridization of carbon bondings with the substrate and the metallic clusters and will be more extensively discussed in the section dedicated to the study of transition metal clusters deposited on graphene (sec. 8.4).

One of the most remarkable properties of the graphene layer grown on the Ir(111) substrate is its high structurale coherency. STM studies,

in fact, showed that the graphene layer contains only a very low density of zero-dimensional defects, such as edge dislocation cores consisiting of heptagon-pentagon pairs of carbon atom rings found at the domain boundaries between adjacent graphene crystallites with small-angle misorientations. Moreover, carbon rows present large-scale continuity over terraces and step edges: graphene appears to lie like a blanket over step edges across surface regions which size is in the micrometer range [22]. The resulting uniformity of the moiré structure makes this system a perfect template for ordered nanostructures.

As the graphene-substrate interaction is concerned, the narrowness of the C 1s signal in photoemission studies [24], compared to the same measurements peformed on graphene grown over other transition metal surfaces, indicates that carbon atoms interact very weakly with iridium surface atoms. A confirmation of the weakness of the C-Ir interaction comes from angle-resolved photoemission spectroscopy (ARPES) investigations on the band structure of the graphene/Ir(111) system. As explained above, graphene valence and conduction bands are expected to degenerate at high symmetry points of the reciprocal lattice (K points) forming the so-called Dirac cones and the Dirac points at the Fermi level of the system. The interaction with transition metal substrates influences the band structure and opens gaps between Dirac points and the Fermi level, but in the case of the Ir(111) substrate ARPES measurements display the expected Dirac cones with the Dirac points shifted only slightly above the Fermi level (≤ 0.2 eV), in a situation very similar to that expected for the ideal free-standing graphene [25].

The weak C-Ir interaction has been the subject of our photoemission spectroscopy investigastions on the first stages of graphene growth on iridium and will be treated in detail in the next section. In sec. 8.3 the unexpected angular dispersion of the C 1s core level binding energy will be reported. An example of how photoemission experiments can give information on the electronic properties and the morphology of transition metal clusters deposited on this peculiar nanostructured template will be finally presented in sec. (8.4): in particular results on gold, platinum and rhodium clusters will be outlined.

8.2 First stages of graphene growth on Ir(111)

The majority of the works that can be found in literature about graphene grown on transition metal surfaces focuses on the physical and electronic

structure of the films, while the nucleation and growth mechanisms, that can greatly influence the final quality of the graphene layer, remain largely unexplored experimentally. At the same time, peculiar mechanisms for the growth of the graphene layer, strikingly different from those observed for bidimensional metal islands on metals, have been proposed, making this investigation topic even more attractive. One example of these mechanisms can be found in the growth process of graphene on the Ru(0001) surface: this process appears to proceed by means of the addition of small clusters of 5 carbon atoms rather than monomers [26]. In the case of iridium substrate, on the other hand, a Smoluchowski ripening process has been proposed for the graphene island coalescence, with the entire carbon islands moving on the iridium surface at high temperature [27].

A fundamental issue, not yet addressed in the onset of graphene formation on the Ir(111) surface, relates to the process that from carbidic clusters leads to the development of graphene islands. Although it is evident that lattice mismatch and island size play a crucial role, very little is known about the atomic-scale mechanism of the transition from strong- to weak-interacting carbon layers. Understanding and controlling such mechanism are fundamental targets for tailoring the morphology and the electronic properties of the graphene layer on iridium, an indispensable starting point for the development of graphene-based nano-scale devices.

The fast data acquisition mode and the high energy resolution of the novel experimental set-up developed for the SuperESCA beamline (described in chapter 4) together with the high sensitivity to the local environment of C $1s$ and Ir $4f_{7/2}$ core levels, allowed us probing *in situ* the carbon cluster-substrate interaction during graphene growth. The combination of experimental results and density functional theory (DFT) calculations resulted in the possibility of building a consistent *scenario* for the investigated mechanism.

8.2.1 Experimental details

The Ir(111) surface was cleaned by repeated cycles of Ar^+ sputtering and annealing at 1470 K, followed by oxygen treatment at 1000 K to remove carbon atoms eventually segregated from the bulk crystal, and by hydrogen exposure at 800 K in order to remove oxygen atoms adsorbed on the crystal surface during the previous procedure.

As for the graphene layer, carbon atoms were obtained by dosing ethylene (C_2H_4) at pressures ranging from 1×10^{-9} to 5×10^{-7} mbar in a temperature range between 300 and 1270 K. Two methods for the prepara-

tion of the graphene layer were used: in the following they will be indicated as *chemical vapor deposition* (CVD) and *temperature programmed growth* (TPG), accordingly to Coraux *et al.* [27]. In the case of CVD procedure, ethylene was dosed either by means of the molecuar beam apparatus (estimated pressure $\approx 1 \times 10^{-7}$ mbar) or by ambient pressure (when lower pressures, and consequently slower growth process, were of interest); in our experiments the iridium surface was mantained at a fixed high temperature, ranging from 820 to 1270 K. The second growth method, TPG, consisted in the adsorption of ethylene molecules at room temperature, followed by their dissociation during an annealing at temperatures higher than 900 K. As will be explained more in detail in sec. 8.2.3, the use of both preparation procedures allowed investigating the different island morphologies that occur during the formation of the graphene sheet on the Ir(111) surface.

8.2.2 *Ab-initio* calculation details

Theoretical calculations have gained great importance in the last years both for the interpretation of the photoemission results and as a fundamental tool to build a more complete picture of the system under investigation. Our studies on the first steps of graphene growth appear to be a good example of how the synergy between theory and experiments can lead to valuable results.

All the calculations reported in this chapter have been performed in collaboration with D. Alfé and M. Pozzo from University College London, using the VASP code [28].

Theoretical simulations are based on the determination of the total energy of the system, through a self-consistent solution of the Schrödinger equation

$$\hat{H}_{tot}|\Psi_{tot}>= E_{tot}|\Psi_{tot}> . \tag{8.1}$$

The Hamiltonian operator is given by

$$\hat{H} = \hat{T} + \hat{U} + \hat{W}. \tag{8.2}$$

where $\hat{T}$ is the kinetic energy operator, $\hat{U}$ represents the interaction of the electrons with the coulombic field due to the nuclei and $\hat{W}$ is the electron-electron interaction energy. The theoretical results reported in the following section were obtained solving eq. 8.1 within the density functiona theory (DFT) framework, using the pseudo-potentials obtained with the projector augmented-wave method (PAW potentials) [29, 30] and the exchange-correlation functional developed by Perdew, Burke and Ernzerhof (PBE) [31] to approximate the $\hat{W}$ term in eq. 8.2.

The Ir(111) surface was modeled by a 9-layer slab; this means that contribution due to iridium atoms in the first nine layers of the crystal were considered for the calculation of the system total energy. In order to determine the geometry adopted by the graphene layer, a (10×10) graphene sheet was overlaid over a (9×9) Ir(111) super-cell at 3 Å from the iridium surface, then the first two iridium layers, together with graphene, were allowed for relaxation until the energy minimum of the system was reached. The relaxation was stopped when the total energy converged to less than 10^{-5} eV and the forces on all the atoms to less than 0.005 eV/Å. Such a tight convergence requirement is needed because during the relaxation the graphene layer tends to move away from the surface, and eventually it ends up at a distance of $\approx$ 4 Å. The resulting geometry is reported in fig. 8.6, which shows the graphene layer 3.8 Å above the iridium surface and the typical moiré pattern with a corrugation of 0.3 Å, in agreement with previous results [20, 21].

To obtain the structural model for the carbon clusters described in sec. 8.2.3, the geometry of the clusters was allowed for full relaxation after a short simulated annealing.

The relation between the thoretical results and the experimental findings about the carbon-Ir(111) system was given by the determination of Ir $4f_{7/2}$ and C $1s$ core level shifts due to the interaction of iridium surface atoms with carbon clusters. The origin of core level shifts (CLS) and surface core level shifts (SCLS) has already been treated in detail in sec. 2.4.1 and 2.4.2. However, it is worth describing briefly how these quantities can be calculated with high accuracy using DFT, considering as an example the case of Ir $4f_{7/2}$ surface core level shift. The Surface core level shift is defined as the difference between the binding energy (BE) of a core electron in a bulk atom, $\mathrm{BE_{bulk}}$, and the one in a surface atom, $\mathrm{BE_{surf}}$:

$$\mathrm{SCLS} = \mathrm{BE_{buk}} - \mathrm{BE_{surface}} \tag{8.3}$$

where BE is the all-electron total energy $\mathrm{E^{AE}}$ difference between the final state (i.e., the system with (N-1) atoms in the ground state and one excited atom) and the initial state (i.e., the system with N atoms in the ground state):

$$\mathrm{BE} = \mathrm{E^{AE}}((\mathrm{N}-1)\mathrm{Ir}, 1\mathrm{Ir}^*) - \mathrm{E^{AE}}(\mathrm{NIr}, 0\mathrm{Ir}^*). \tag{8.4}$$

Final state core level binding energies can be accurately computed by describing the excited atom by a pseudopotential generated in the core-excited

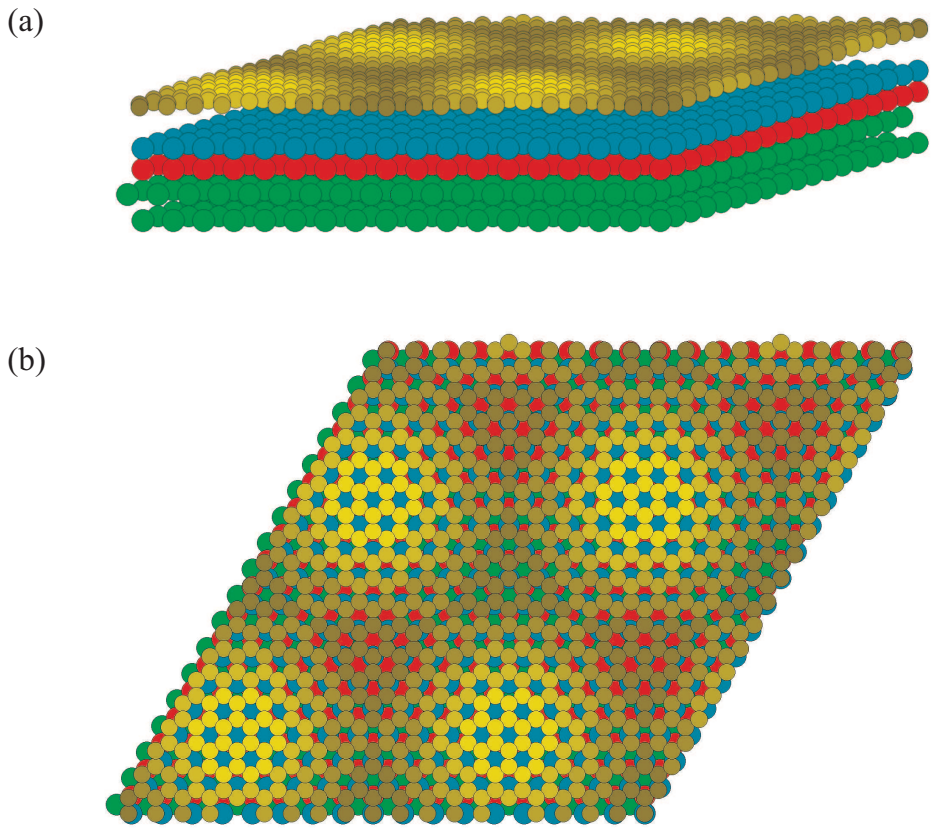

Figure 8.6: Side view (a) and top view (b) of the calculated graphene structure. The shading of carbon atoms (yellow) reflects the graphene layer corrugation: lighter colour indicates larger height with respect to the iridium surface, as computed by DFT simulation. Four Ir layers are also represented: the first (blue), the second (red) and the third (green) layers are clearly visible also in the top view, where allow easy identification of the three regions within the moiré unit cell, in agreement with the schematic representation reported in fig. 8.5.

configuration. In this formulation the core-level BE is given by the pseudopotential total energy difference supplemented by an additive constant that can be determined for the isolated atom

$$\begin{aligned} \mathrm{BE} &= \mathrm{E}^{\mathrm{PS}}((\mathrm{N}-1)\mathrm{Ir}, 1\mathrm{Ir}^*) - \mathrm{E}^{\mathrm{PS}}(\mathrm{NIr}, 0\mathrm{Ir}^*) + \\ &+ [\mathrm{E}^{\mathrm{AE}}_{\mathrm{at}}(\mathrm{Ir}^*) - \mathrm{E}^{\mathrm{PS}}_{\mathrm{at}}(\mathrm{Ir}^*) - \mathrm{E}^{\mathrm{AE}}_{\mathrm{at}}(\mathrm{Ir}) + \mathrm{E}^{\mathrm{PS}}_{\mathrm{at}}(\mathrm{Ir})]. \end{aligned} \tag{8.5}$$

When comparing different geometries the additive term cancels out leaving:

$$\mathrm{SCLS} = \mathrm{E}^{\mathrm{PS}}_{\mathrm{bulk}}((\mathrm{N}-1)\mathrm{Ir}, 1\mathrm{Ir}^{*}_{\mathrm{bulk}}) - \mathrm{E}^{\mathrm{PS}}_{\mathrm{surf}}((\mathrm{N}-1)\mathrm{Ir}, 1\mathrm{Ir}^{*}_{\mathrm{surf}}). \tag{8.6}$$

This latter quantity is compared with the experimental shifts. The same procedure can be adopted to determine the shifts of C 1s binding energy for carbon atoms in different configurations inside the clusters, as will be described below.

8.2.3 Results and discussion

Graphene-iridium interaction

In the first set of experiments ethylene was dosed on the Ir(111) surface using the molecular beam apparatus (described briefly in sec. 3.1.1), obtaining a local pressure on the sample of 1×10^{-7} mbar. Ethylene is known to completely dissociate at about 800 K; for this reason the lowest temperature chosen for our experiments was 820 K. Fig. 8.7 shows the C 1s and Ir $4f_{7/2}$ spectra of the clean iridium surface and those obtained upon dosing ethylene at 820 and 1270 K. In the Ir $4f_{7/2}$ spectrum of the clean surface (panel (a)), the bulk component at 60.86 eV and the surface component can be distinguished; because of the reduced coordination of first-layer Ir atoms respect to the bulk, the surface component moves to lower binding energy. The measured SCLS is of -545 meV, in good agreement with previous determinations [32] and with our theoretical result of -550 meV.

After exposure to ethylene at 820 K (panel(b)), the C 1s spectrum presents a dominant component at about 284.1 eV, but the tails at higher and lower binding energies indicate the presence of inequivalent carbon species on the surface that interact differently with the underlying iridium substrate. The Ir $4f_{7/2}$ spectrum, on the other hand, shows a reduced surface component and a new feature at about -240 meV respect to the bulk component appears, due to the first-layer Ir atoms interacting with C atoms.

At the highest temperature (1270 K, panel (c)), the C 1s spectrum consist of a single, narrow peak ($\approx$ 250 meV, full width at half maximum) indicating that a well ordered graphene layer was obtained. This result is confirmed by the LEED pattern that, together with the spots of the clean Ir(111) surface, shows those due to the graphene lattice and the extra spots of the moiré superstructure (fig. 8.8), in agreement with the results reported in the literature [21, 24].

The Ir $4f_{7/2}$ spectrum corresponding to the surface covered by the graphene layer, reported in the upper part of panel (c), is very similar to that of

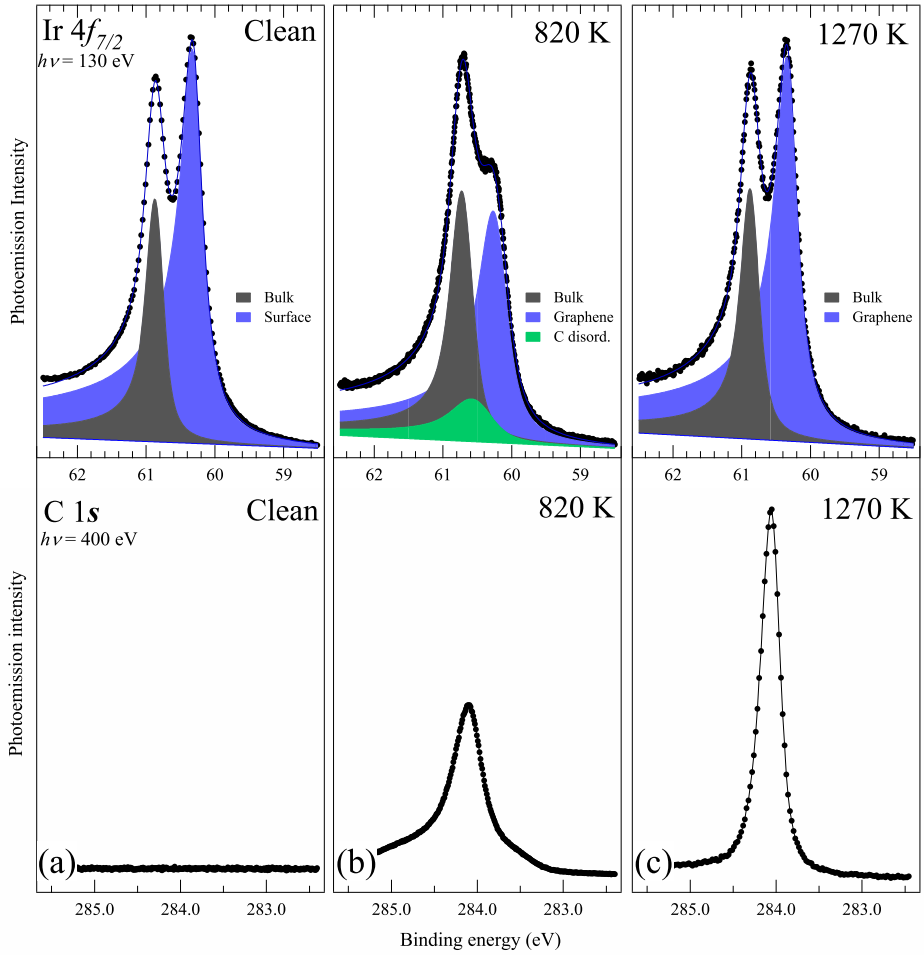

Figure 8.7: High resolution Ir $4f_{7/2}$ and C $1s$ spectra of the clean Ir(111) surface (a), after saturation with ethylene at 820 K (b) and 1270 K (c). All the spectra were acquired at room temperature.

the clean iridium surface, with a measured SCLS of -535 meV. This result is quite surprising, since it is well known that a small amount of impurities on the sample surface induces substantial variations in the spectral position and the line-shape of the surface component in a transition metal core level. In this case, at the contrary, we found that the presence of the large amount of carbon, revealed by the C $1s$ spectrum, leaves the iridium spectrum substan-

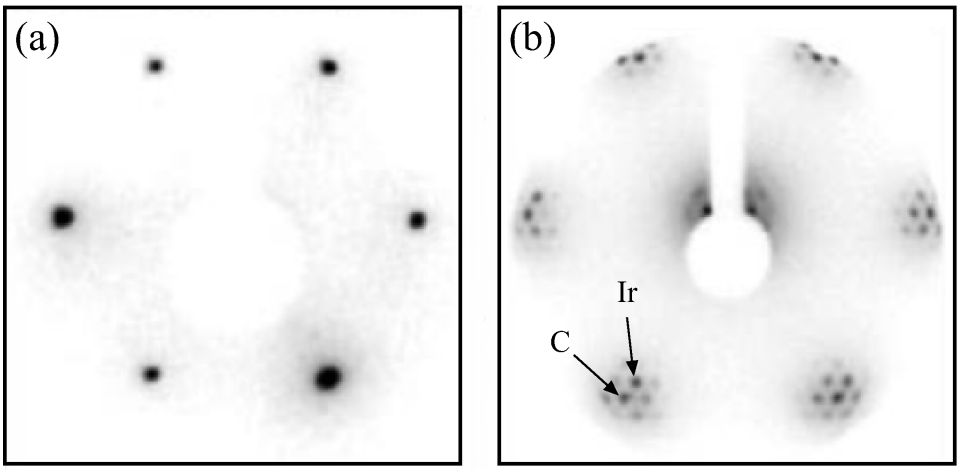

Figure 8.8: LEED pattern of the clean Ir(111) surface (a) and of the graphene/Ir(111) system (b). In panel (b) the spots due to the Ir atoms and those due to the honeycomb lattice of carbon atoms are outlined. The other diffraction spots surrounding these two are related to the presence of the incommensurate moiré superstructure.

tially unchanged. We can see how, in this way, photoemission spectroscopy provides a direct indication that the interaction between graphene and the Ir(111) surface is very small: any modification of the electronic properties due to charge transfer between graphene overlayer and iridium substrate, to surface hybridization or core-hole screening, in fact, are expected to produce significant and measurable SCLSs.

This result is further corroborated by the DFT calculations of the Ir $4f_{7/2}$ binding energy in presence of the graphene layer. Because of the corrugation of graphene, first-layer Ir atoms are in principle not all equivalent. To compare experimental and theoretical SCLS, we therefore computed this quantity for two different Ir atoms, one right below a carbon atom (in the *hcp* region of the moiré unit cell) and one below the centre of an hexagon of carbon atoms (*atop* region; refer to sec. 8.1 for a detailed description of the regions within the moiré unit cell). The calculated values for the SCLSs are of -551 and -549 meV, respectively, in very good agreement with the experimental findings. This result definitly confirms that the graphene overlayer does not affect the iridium surface appreciably.

Still, the surface morphology and the electronic properties of the incom-

plete graphene layer are not clear. The evolution of the C cluster-substrate interaction that, from a situation with inequivalent carbon adspecies differently interacting with the substrate (as depicted in fig. 8.7, panel (b)), leads to the formation of a complete graphene layer, almost not interacting with iridium (panel (c)), is the subject of another series of investigations described below.

From carbon clusters to graphene

To understand the interaction of C clusters with the Ir substrate prior to the formation of a perfect graphene layer, we monitored in situ the evolution of C 1s and Ir $4f_{7/2}$ spectra during preparation with the two methods denoted above as TPG and CVD. These two procedures are known to produce carbon islands with different morphologies, as seen in STM images [27]: while using CVD method the clusters grow exclusively at step edges because of rapid carbon diffusion and occupation of preferred configurations, in the case of the TPG procedure flat carbon islands formation takes place also on terraces.

In the first set of experiments (TPG method) the iridium surface was first saturated with ethylene at 300 K, then an annealing series at increasing temperatures was performed in the range 770–1270 K. Photoemission spectra were acquired at room temperature after each annealing step. The C 1s and Ir $4f_{7/2}$ spectra obtained for this first procedure are reported in fig. 8.9.

The presence of three different components at 284.12 eV (C_A), 283.94 eV ((C_B)) and 283.61 eV ((C_C)) in the C 1s spectra reflects the presence of inequivalent carbon species that behave differently upon increasing temperature. While C_A and C_C remain always at the same binding energy and their intensity is just reduced, C_B increases in intensity, becomes narrower (indicating that the surface is becoming more ordered) and moves progressively towards higher binding energy to end up at 284.10 eV, the same value measured for the graphene layer (see panel (a) of fig. 8.10). The analysis of the peak intensities reveals that the decrease of C_C corresponds to the increase of $(C_A + C_B)$ (fig. 8.10 (b)). In the following discussion this behaviour will be explained as due to changes in the morphology of carbon clusters.

The Ir $4f_{7/2}$ core level spectra reported in the right panel of fig. 8.9 present the bulk component together with that of the clean (or, better, graphene covered) surface and a third, broad peak in between due to a new first-layer population of iridium atoms which strongly interact with carbon clusters. Upon increasing the annealing temperature, this extra peak dimin-

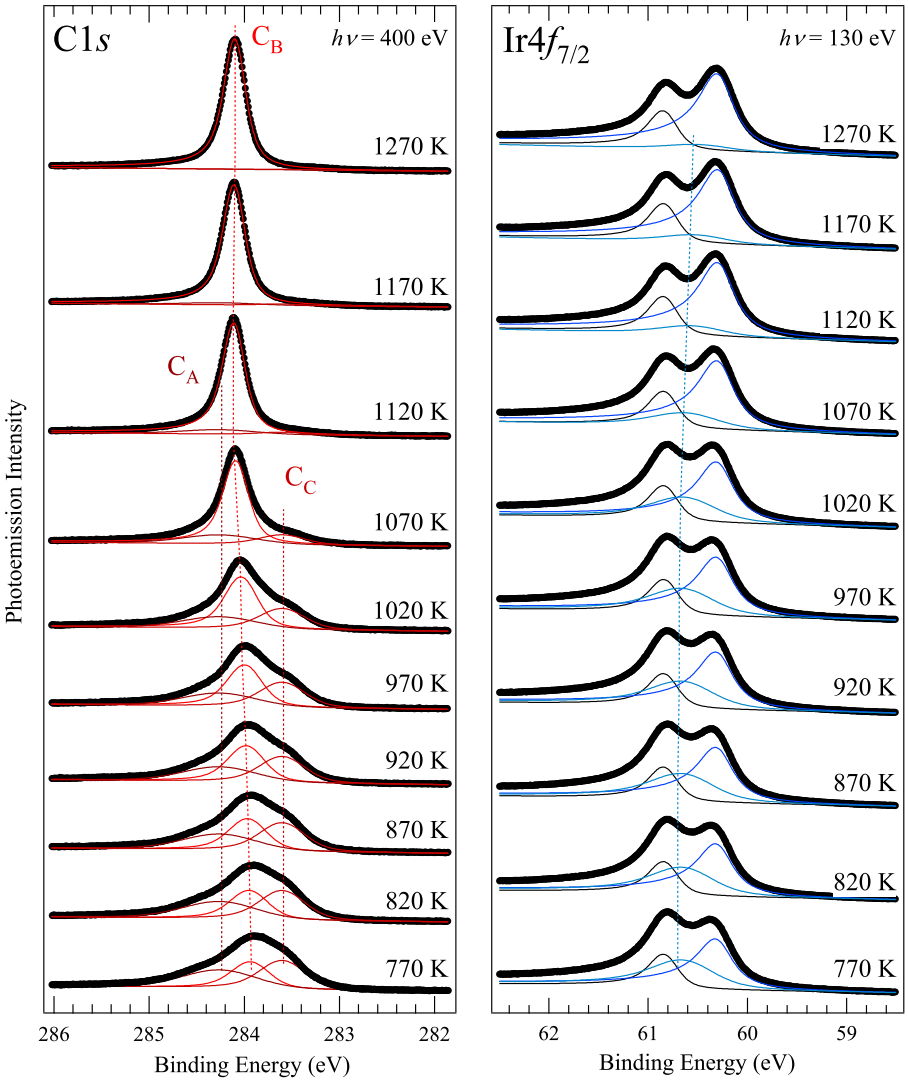

Figure 8.9: C 1s (left panel) and Ir 4$f_{7/2}$ (right panel) spectra acquired after annealing at different temperatures the Ir(111) surface satureated with ethylene at 300 K. The spectra were measured at 300 K. The different spectral componenets, as explained in the text, represent inequivalent carbon and iridium atoms. The vertical lines are intended only as a guide for the eye to follow the evolution of the photoemission features.

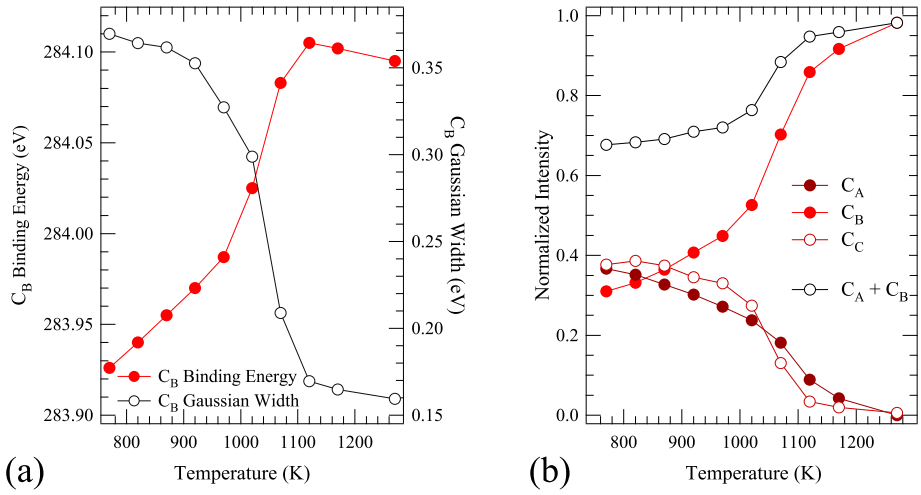

Figure 8.10: (a) Evolution of binding energy and gaussian width of the C_B spectral component individuated in the C 1*s* core level spectra. (b) Evolution of the intensity of the three spectral components as a function of the annealing temperature. Note how the decrease of C_B intensity (dark red open circles in the graph) is paralleled by the increase of $(C_A + C_B)$ (black open circles).

ishes in intensity and undergoes a progressive shift: the corresponding value of the SCLS changes from -225 meV at 770 K to -390 meV at 1270 K.

For the second series of experiments we used the CVD procedure: we dosed ethylene with the molecular beam on the iridium surface at three different temperatures: 820, 970 and 1270 K. During the exposure, C 1*s* core level spectra were measured using the fast snapshot acquisition mode described in detail in sec. 4.1.6; the acquisition time was set to 400 ms/spectrum. Panels (a), (b) and (c) in fig. 8.11 report a selection of real-time photoemission spectra of the C 1*s* core level during exposure of Ir(111) to ethylene at 820, 970 and 1270 K, respectively. Panels (d), (e) and (f) display the evolution of the intensities of the spectral components; the intensity of the single component is normalized to the value of the total intensity of the C 1*s* peak at saturation.

As for this second procedure is concerned, the most significant results arise from the real-time data of the C 1*s* spectra measured during ethylene uptake at 820 K shown in panel (a) of fig. 8.11: the sequence of spectra

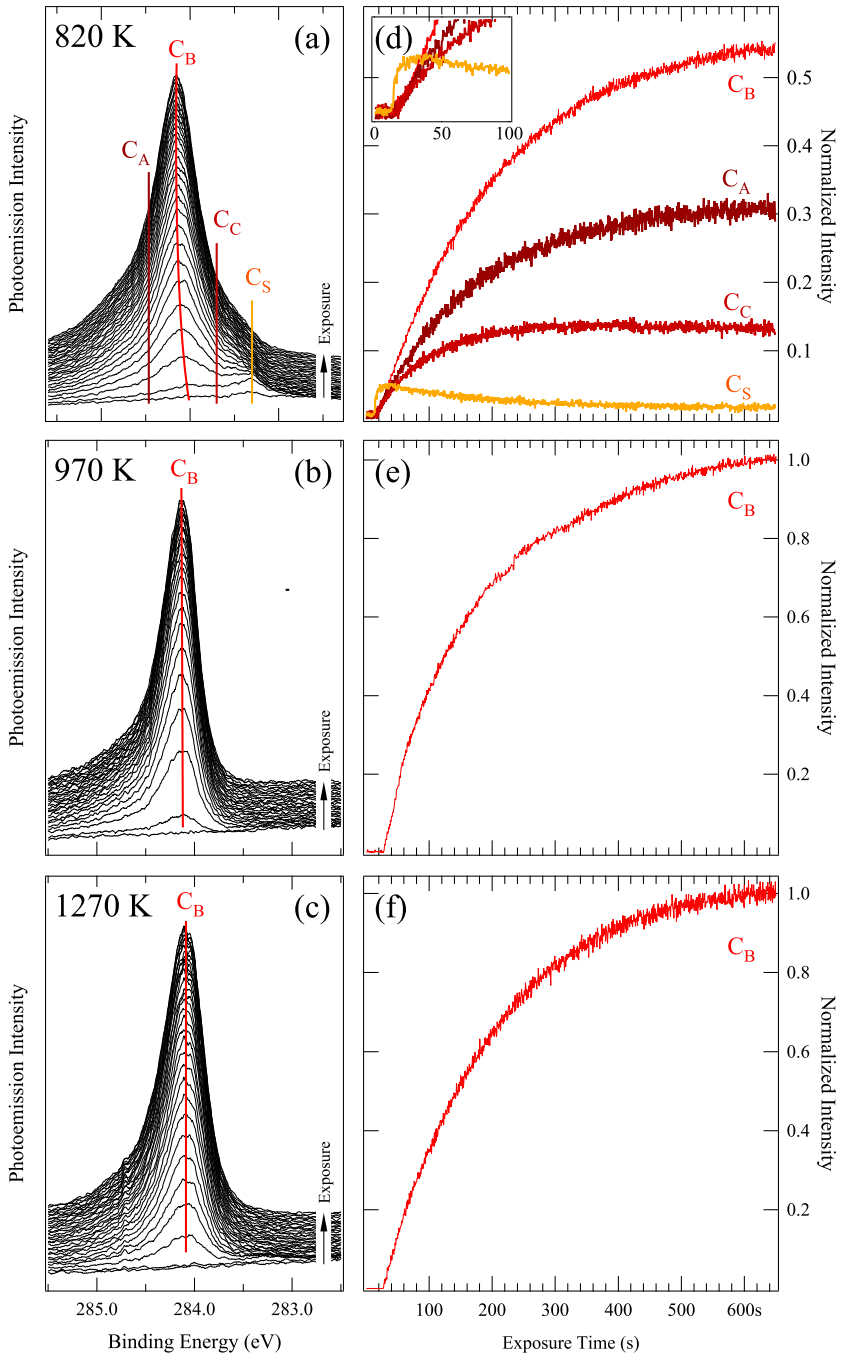

Figure 8.11: (a)(b)(c) Selection of real-time C 1*s* spectra acquired during ethylene exposure at 820, 970 and 1270 K, respectively. The spectra were acquired in snapshot mode; the counting time was set to 400 ms. (d)(e)(f) Corresponding trends of the C 1*s* spectral components. The inset in panel (d) is a zoom showing the trend of C_S intensity during the first 100 s of ethylene exposure.

can be fitted with the same three components used for the analysis of the annealing experiment, plus a fourth component at 283.35 eV, denoted as C_S, which is compatible with the existence of carbon atoms at the step edges of the iridium crystal. The inset in panel (d) of fig. 8.11 shows a zoom of the behaviour of C_S in the first 100 s of ethylene uptake. The C_S component grows immediately at the beginning of the exposure, which is compatible with a mechanism where carbon atoms, highly mobile at 820 K, occupy first the most preferred sites at the step edges. With further ethylene dose, the C_S intensity decreases, most probably because carbon atoms at the steps are included in the graphene layer, that is known to grow on top of the steps, as observed in STM measurements [27].

In order to eventually exclude the role of the ethylene pressure on the results obtained from the molecular beam experiments, the uptake at 820 K was performed also dosing ethylene from ambient pressure, ranging from 1×10^{-9} to 5×10^{-7} mbar. In this case the evolution of the C $1s$ and the Ir $4f_{7/2}$ spectra was followed using the "Time Resolved" acquisition in the standard sweep mode (refer to chapter 4 for an explanation of the different acquisition procedures included in the software).

As can be seen in panels (a) and (b) of fig. 8.12, no substantial differences in the evolution of C $1s$ spectra can be appreciated with respect to the series reported in fig. 8.11.

The results of the Ir $4f_{7/2}$ series are reported in panels (c) and (d) of fig. 8.12. Here the vertical lines denote the vertical position of the three components used to fit the spectra: besides the Ir_{bulk} and the $Ir_{surface}$ components (black and blue line, respectively), a third peak between the two, Ir_C (green line), is present. The binding energy of Ir_C moves towards lower values with increasing coverage, to end up close to $Ir_{surface}$ at saturation. The evolution of this iridium component is analogous to that found for the Ir $4f_{7/2}$ extra peak in the case of the annealing experiment (see fig. 8.9). In panel (d) of fig. 8.12 the evolution of the intensities of these three spectral component is reported as a function of ethylene exposure. The intensity of the single components is normalized to the value of $Ir_{surface}$ of the clean surface. Upon increase of the exposure, the $Ir_{surface}$ decrease is accompanied by the Ir_C increase, while Ir_{bulk} decreases because of C adsorption and graphene formation on the surface.

As far as dosing ethylene at higher temperatures is concerned, it can be observed that throughout the series displayed in panels (b) and (c) of fig. 8.11 the C $1s$ line-shape consist of a single component from the beginning of the uptake process. This important result suggests that when ethylene is dosed above 970 K the graphene layer begins to form even at low

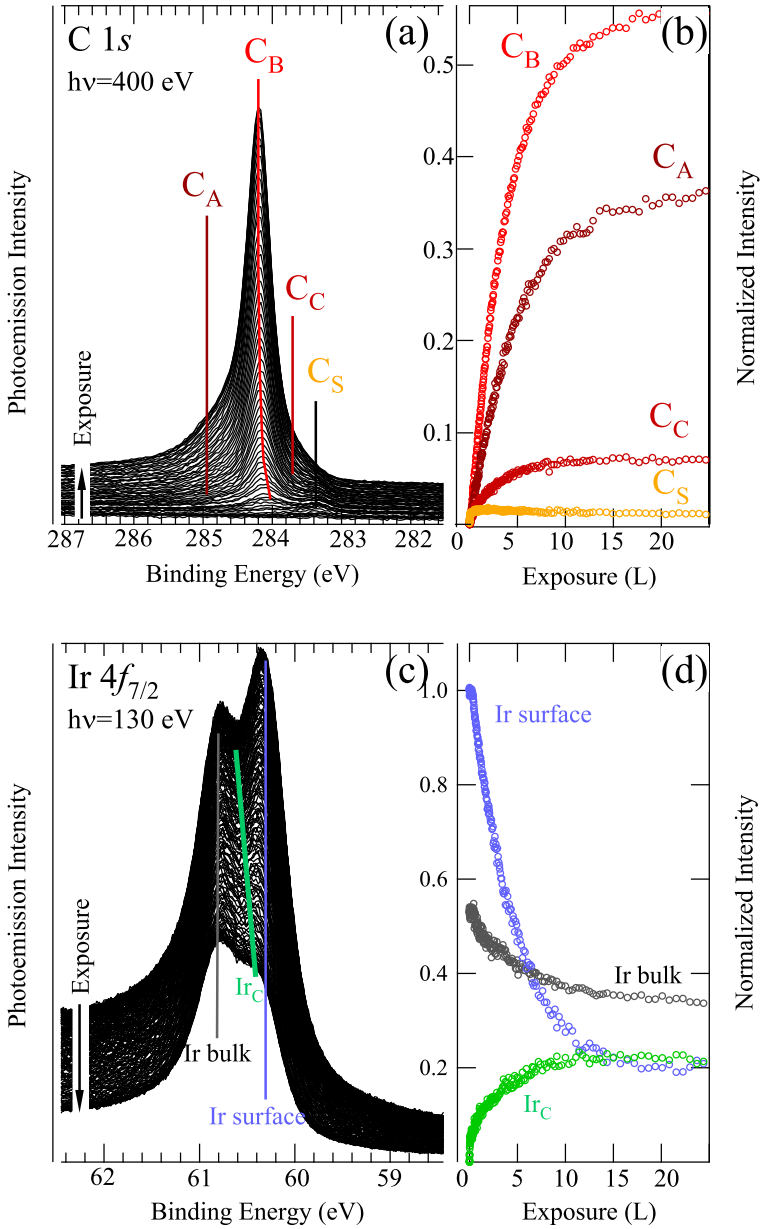

Figure 8.12: (a) Selection of real-time photoemission spectra of the C 1s core level during ethylene exposure on Ir(111) at 820 K. Acquisition time is 9 s/spectrum. (b) Evolution of the intensity of C 1s spectral components as a function of ethylene exposure measured in Langmuir. (c) Selection of real-time photoemission spectra of the Ir $4f_{7/2}$ core level during ethylene exposure at 820 K. Acquisition time is 10 s/spectrum. (d) Evolution of the intensity of Ir $4f_{7/2}$ spectral components as a function of ethylene exposure.

coverage. At the contrary, the results obtained at 820 K indicate that at this temperature, in the whole coverage range till saturation the interaction between Ir substrate and C islands remains rather large if compared with the ordered graphene layer.

The photoemission spectroscopy results outlined so far evidence that the C-Ir system presents remarkable differences in cluster-substrate interaction arising at different growth temperature and carbon coverage. In order to shed light on the origin of these behaviours, we performed DFT calculations that follow the evolution of carbon cluster morphology with cluster size. Since honeycomb rings (HR) can be considered the graphene buiding blocks, we identified the size of the clusters by means of the number of HR they are formed of. Clusters constituted of 1, 3, 7 and 19 HR have been mapped, containing an overall number of 6, 13, 24 and 54 carbon atoms, respectively. Fig 8.13 shows the structural models obtained for the four clusters simulated. In fig. 8.13 (a) the structure of a single honeycomb ring is depicted. Its geometry is quite simple: the C atoms sit in bridge sites between two adjacent Ir atoms, forming a planar cluster with C-Ir distance of 1.62 Å and the symmetry axes oriented along the $[10\overline{1}]$ direction of the underlying iridium surface.

The increase of the number of honeycomb rings has drastic effects on cluster morphology. The cluster with 3 HR (fig. 8.13 (b)) abandons the flat configuration and bends upwards, assuming a dome-like shape. In this configuration the central C atom is at distance of 2.53 Å from the iridium surface and only the C atoms at the periphery of the island remain close to the Ir substrate. This bending process is accompanied by a rotation of the symmetry axes by 11°. For larger cluster sizes the unsticking process goes further on: the top C atoms for clusters containing 7 and 19 HR move apart by 2.63 and 3.13 Å, respectively. At the same time the cluster undergoes further rotation, approaching the value of 30° of the final graphene layer.

To relate theory and experiments we computed Ir $4f_{7/2}$ and C $1s$ core level shifts for some of the clusters represented in fig. 8.13 and compared them with experimental results. For clusters consisting of 1 and 7 honeycomb rings we calculated the CLS for representative iridium and carbon local configurations, labeled $\mathrm{Ir_i}$ ($\mathrm{i} = 1, \ldots, 5$) and $\mathrm{C_j}$ ($\mathrm{j} = 1, \ldots, 4$) in fig. 8.13.

In the case of a single carbon ring (panel (a)), $\mathrm{Ir_1}$ and $\mathrm{Ir_2}$ present a SCLS of -325 and +498 meV, respectively. The absence in the experimental spectra of Ir $4f_{7/2}$ components with binding energy larger than the bulk value, suggests that this local configuration is not present. In the case of a cluster consisting of 7 HR (panel (c)), SCLSs for $\mathrm{Ir_3}$, $\mathrm{Ir_4}$ and $\mathrm{Ir_5}$, result to be

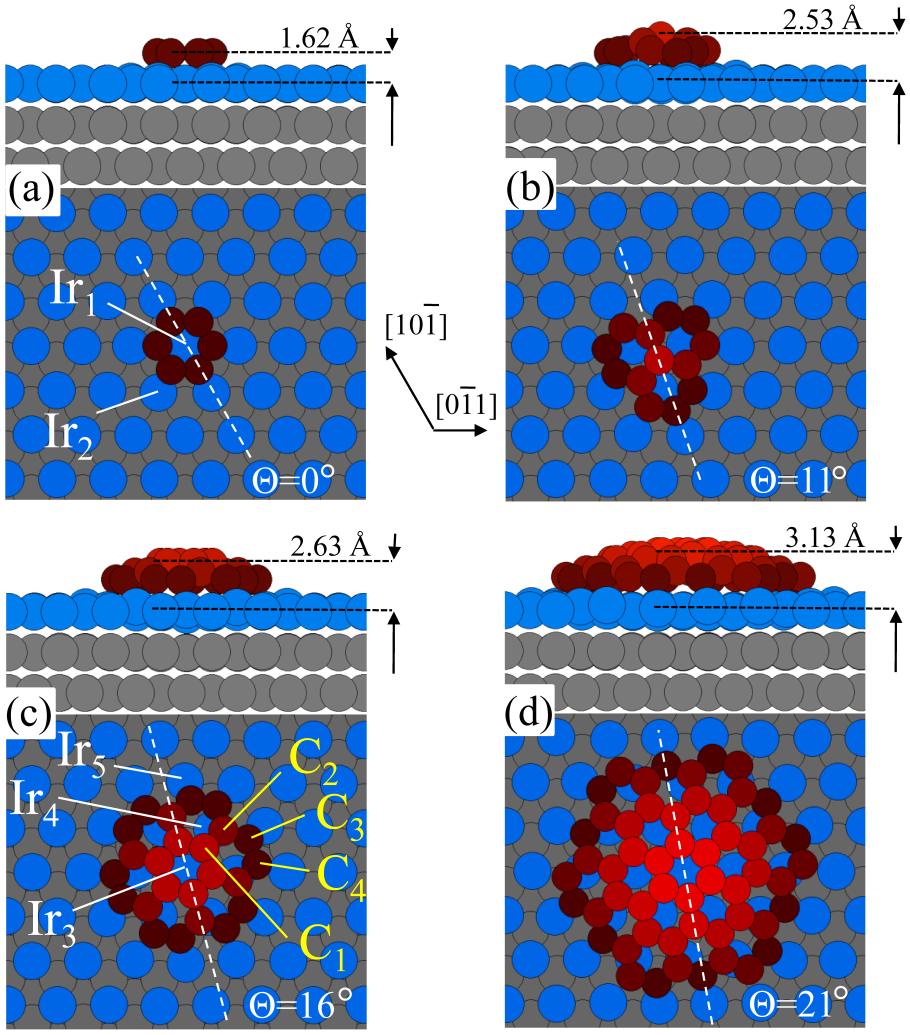

Figure 8.13: Calculated structural models of the carbon clusters formed by 1 (a), 3 (b), 7 (c) and 19 (d) honeycomb rings. The different Ir and C local configurations for which CLSs have been computed are indicated (see text). The distance of the central C atoms from the iridium substrate as well as the orientation of the cluster with respect to the [10$\bar{1}$] direction of Ir(111) are also shown.

-551, -132 and -270 meV, respectively. This finding indicates that even for a very small carbon island the interaction of the Ir atoms placed just below the centre of the dome (Ir_3) is very small, being the SCLS the same found for the clean Ir(111) surface and the graphene/Ir(111) system. Only the iridium atoms directly bonded with the carbon atoms at the cluster edge strongly interact with carbons, and present SCLSs that fall in the binding energy region of the broad extra component resulting from the fitting procedure of the Ir $4f_{7/2}$ spectra showed in fig. 8.12 (c).

For the 7 HR cluster, the core level shifts of C_2, C_3 and C_4 atoms have been calculated with respect to the C_1 configuration. This last carbon species, in fact, as demonstrated by the Ir_3 SCLS value mentioned above, appears to be in a configuration very close to that of the final graphene layer, so that it represents a good reference for the estimation of binding energy shifts. The values obtained for the CLSs of the three carbon configurations within the cluster are +268, -348 and -439 respectively. The comparison with experimental results allowed us to distinguish three types of carbon atoms:

- carbon atoms sitting at the periphery of the clusters, bonded to other two carbon atoms (C_3 and C_4), show a negative CLS, as for C_C (see fig. 8.9;

- carbon atoms bonded with three carbon atoms and directly bonded to the periphery atoms (C_2) show a positive CLS, as for C_A;

- the atoms at the centre of the clusters, in configurations very similar to that of the final graphene layer, originate the C_B component in the C 1*s* spectra.

The close correspondence of experimental and theoretical core level shifts suggests that while growing, the carbon clusters remain strongly bonded to the substrate only at the periphery (C_C atoms) as a result of the C $2p$ hybridization with the first layer Ir *d* band. When the annealing temperature increases, the carbon islands diffuse on the iridium surface and coalesce via Smoluchowski ripening [27]: this process leads to the formation of larger clusters and to the consequent decrease of the N_P/N_T ratio (where N_P is the number of atoms at the periphery and N_T is the total number of atoms in the cluster). This interpretation is in good agreement with the behaviour reported in the series of C 1*s* of fig. 8.9: small compact islands with a large number of atoms at the edge (C_C) and near-edge (C_A) nucleate to form large islands at 1270 K. After the annealing at this temperature, the

relative population of C_A and C_C species is in the order of 0.1%, i.e. below our sensitivity limit. The parallel narrowing of the C_B component (see fig. 8.10 (a)) directly correlates with the distribution of C-C distances that gets narrower and moves towards the 1.421 Å value found for graphene.

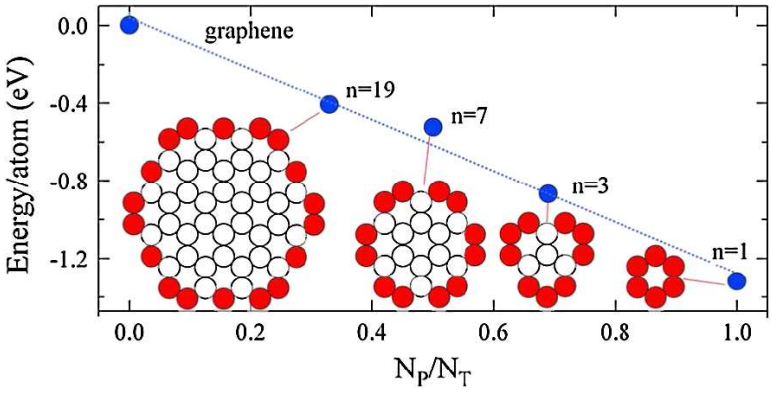

Figure 8.14: Evolution of the binding energy/atom as a function of the ratio of carbon atoms at the periphery N_P and the total number N_T in each carbon cluster.

A further support to our interpretation about the role of atoms at the cluster edge is given by the graph in fig. 8.14. Here the evolution of the calculated binding energy/atom in the cluster is reported as a function of N_P/N_T for different cluster sizes. The graph displays a remarkable linear behaviour and indicates once more that the islands are bonded to the substrate mainly with the carbon atoms at the edges. This gives further support to the importance of the correlation between the bonding interaction of the cluster and the number of atoms at the periphery.

Conclusions

In the experiments described above, high-resolution photoelectron spectroscopy proved to be a powerful tool for a detailed analysis of the electronic properties and the morphology of the graphene layer grown on the Ir(111) surface. The energy- and temporal-resolution gained with our new experimental set-up, then, allowed monitoring the initial steps of the graphene growth on this substrate.

In the first part of the investigation, the weakness of the graphene-Ir(111) interaction has been definitely confirmed by the analysis of the Ir $4f_{7/2}$ spectra for the clean iridium surface and for the graphene/Ir(111) system.

The second series of real-time experiments, in combination with theoretical calculations, showed that the transition from carbidic carbon clusters to a low interacting graphene layer proceeds via formation of dome-shaped carbon nano-islands which interaction with the iridium substrate takes place only at the cluster edge.

The understanding of the new mechanism of cluster formation outlined in this section, which results in nanosized non-interacting carbon regions, can be considered the starting point for rationally designing and preparing graphene-based nanoscale devices.

8.3 Band dispersion in the C 1s core level of graphene

The assumption that only the external valence electrons partecipate in the bonding of atoms is at the base of our understandig of the solid state. When several atoms are brought together into a molecule, the external electrons are involved in the chemical bondings through the formation of molecular orbitals with a discrete set of allowed energy levels. In the case of solids, the Schrödinger equation is solved by means of Bloch waves, leading to the following electronic wave function:

$$\Psi_{n\mathbf{k}}(\mathbf{r}) = e^{i\mathbf{k}\cdot\mathbf{r}} u_{n\mathbf{k}}(\mathbf{r}) \tag{8.7}$$

where $u_{n\mathbf{k}}(\mathbf{r})$ is a function with the same periodicity of the crystal lattice and $\mathbf{k}$ is the wave vector, related to the momentum of the electron. In this case the available energies depend on $\mathbf{k}$ that, in turn, can assume values within the First Brillouin Zone of the corresponding reciprocal lattice. This leads to the well-known energy band dispersion E($\mathbf{k}$) in solids. Angular resolved photoemission spectroscopy (ARPES) can be effectively used to map band dispersion.

Electrons in the deep core states, on the other hand, are expected not to partecipate in the bonding of solids, and thus not to show any band-like dispersion. This assumption is of fundamental practical importance for the interpretation of photoemission results: as already discussed in sec. 2.4 and exploited in all the experimental results presented in this thesis, large part of the information that can be obtained with this technique is related to the fact that the precise value of the core level binding energy depends on the chemical environment of the emitting atom, but is tacitly assumed that it has a single, well-defined energy, i.e. it does not show any dispersion.

Partially contradicting the well-established model of interatomic bonding in solids, in this section I will report the observation of a sizeable band-like dispersion of the C 1s core level in graphene. The dispersion is observed as an emission-angle dependent binding energy modulation. In the following discussion it is shown that under appropriate conditions only the bonding or anti-bonding states can be observed. Finally, it will be outlined how a very similar dipersion is obtained by theoretical calculations performed within the *tight-binding* framework, further supporting our experimental findings.

8.3.1 Experimental and computational details

The graphene film on Ir(111) was prepared *in situ* by repeated cycles of ethylene dosing at 300 K and subsequent annealing to 1470 K, which ensures the formation of a long-range ordered layer [25]. In section 4.2 I have pointed out that the novel experimental set-up supports angular-resolved acquisition in "Sweep Mode" and in "Fixed (or Snapshot) Mode". Both of these two acquisition methods were used in the experiments described below in order to obtain the photoemission angular distribution for different photoelectron kinetic energies. Fast angular scans ("Fixed Mode") were measured at $h\nu =$ 500 eV and $h\nu = 600$ eV: the acquisition of 420 C 1s spectra that fill 1/3 of the emission hemisphere took less than 30 minutes. At the other photon energies larger number of spectra were acquired in "Sweep Mode": 1300 spectra at $h\nu = 350$ eV, 820 at $h\nu = 400$ eV and 2270 at $h\nu = 700$ eV. Such scans took several hours to be completed.

For the analysis of the data all the spectra taken at one photon energy were first aligned to the Fermi level of the Ir substrate, then they were fitted with the same line shape parameters, but the binding energy was left free in the fit. The actual peak fits were made using the Doniach-Ŝunjić line profile (refer to sec. 2.3.2) with a Lorentzian width of 130 meV, an asymmetry parameter of 0.093, a Gaussian width depending on the photon energy and a linear background. Actually, we observed a small variation of the lineshape over the entire data set taken at any given photon energy. However, a good fit to all the spectra can be obtained with a single set of parameters describing the line shape. Arbitrariness in the exact values of these parameters induces a small uncertainty in the absolute degree of binding energy modulation of about 5 meV.

As already pointed out in sec. 2.5, in order to analyze angular dependent measurements the results need to be compared with theoretical calculations that take into account also multiple scattering processes. The photoemission intensity calculations reported in the following section were

performed with the program package for Electron Diffraction in Atomic Clusters (EDAC) [33]. The photoemission intensity at each emission angle was calculated as the incoherent sum of the intensities for the two atoms in the graphene unit cell. The simulations were performed on a flat, free-standing graphene layer. The lattice parameter was set to 2.466 Å. The influence of the underlying Ir(111) substrate, that of small changes of the lattice parameter, as well as that of a relatively small corrugation of the graphene layer with moiré periodicity was tested and no significant changes were found in the diffraction patterns.

The experimental results on the band-like dispersion of the C 1*s* core level have been supported with thoretical calculations performed within a *tight-binding* model. Numerical simulations were performed in collaboration with the group of Prof. Ph. Hofmann of Interdisciplinary Nanoscience Center (iNANO) of the University of Aarhus (Denmark). In the tight-binding approach the electronic wave functions in a solid are approximated as a superposition of wave functions for isolated atoms located at each atomic site. When atoms are placed in a crystal, however, the atomic wave functions overlap adjacents atomic sites; as long as electrons are assumed to be tightly bound, the overlap is small and the interactions between different atomic sites can be treated as perturbations.

8.3.2 Results and discussion

Fig. 8.15 illustrates significative examples of the binding energy modulations we found for the C 1*s* core level. Each panel shows a group of spectra taken at a fixed polar emission angle θ as a function of the azimuthal emission angle ϕ. Clear shifts of the peak position can be observed. In panel (f) a comparison between the spectrum taken at normal emission and one taken at $\theta = 25°$ makes the binding energy variation even more evident.

From the fitting procedure, binding energy values of the C 1*s* core level were obtained for all the spectra in each azimuthal scan: fig. 8.15 (g) shows the binding energy modulation as a function of the azimuthal angle for the polar scans reported in panels (a)–(e); the markers in the plots correspond to the spectra displayed in those panels. Strong changes are evident: the largest binding energy difference spans a range of ≈ 60 meV. The periodicity of the modulations is of $\approx 60°$, compatible with the six-fold symmetry of the graphene lattice.

In order to analyze the intensity variations of the photoemission peak, we calculated the modulation function for each polar emission angle. The modulation function is defined as $(I(\theta, \phi) - I_0(\theta))/I_0(\theta)$, where $(I(\theta, \phi)$ is

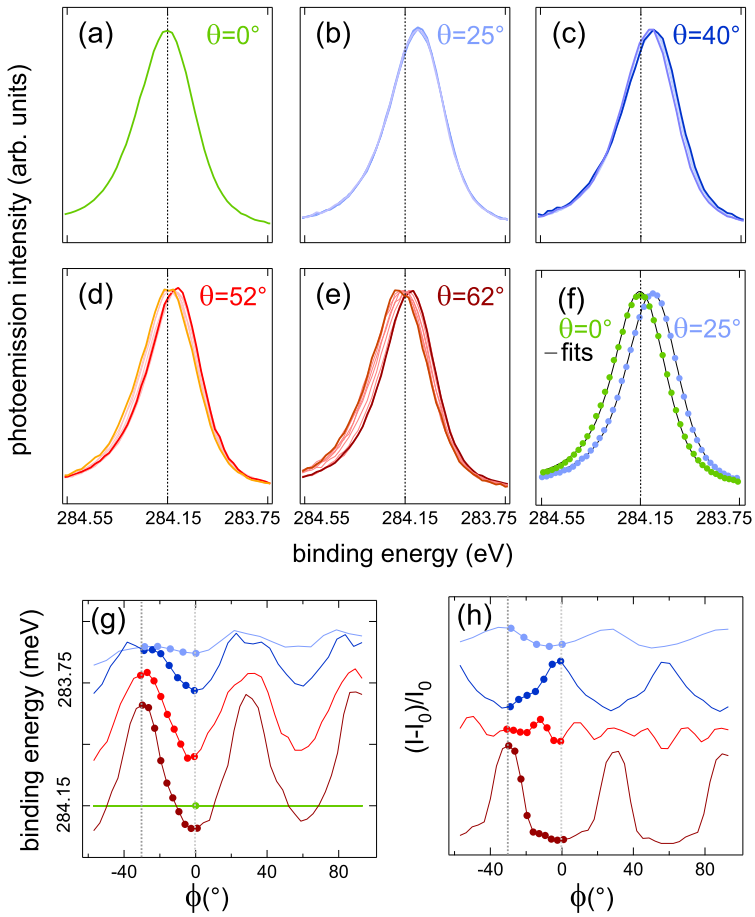

Figure 8.15: (a)–(e) C 1*s* photoemission spectra taken at a photon energy of 400 eV, for fixed polar emission angles θ in each panel but at different azimuthal emission angles ϕ. All the spectra are normalized to the same height and shown as a group plot, such that binding energy variations become evident. (f) Comparison of the spectrum taken at $\theta = 0°$ and one taken at 25°. The lines are the fits through the data points. (g) C 1*s* binding energy modulation displayed as a function of the azimuthal angle. The markers correspond to the spectra reported in the previous panels. The green horizontal line marks the binding energy at normal emission. The binding energy uncertainty is smaller than 10 meV. (h) Intensity variation of the C 1*s* peak as a function of azimuthal angle. The curves are shifted vertically for clarity.

the peak intensity of the C 1s spectrum acquired at the corresponding azimuthal and polar angles, and $I_0(\theta)$ is the average value of the intensity computed for each azimuthal scan. In fig. 8.15 (h) strong modulations can be observed, caused by photoelectron diffraction effects in the final state (see sec. 2.5). Although the intensity variations follow the point symmetry of the graphene lattice, they are not correlated with the binding energy modulations reported in panel (g): the main structures, in fact, are in phase for some polar emission angles and out of phase for others.

Fig. 8.16 shows the complete data set acquired over many polar and azimuthal angles and at different photon energies. It is important to note that since a good fit to all the spectra is obtained with a single spectral component using always the same parameters, we can exclude the existence of unresolved components: in this case, in fact, their intensities would modulate differently, changing the shape of the peak.

The left panel of the figure shows the resulting intensity modulation function (color) compared to the simulation for a flat, free-standing layer of graphene (grayscale). Note that no artificial symmetry was imposed on the data: the experimental modulations are as symmetric as they appear and the excellent agreement with the calculated values greatly enhances our confidence in the data analysis.

The right panel of the figure displays the binding energy modulations as a function of $\mathbf{k}_{\parallel}$, the wave vector component parallel to the surface, which is the only relevant wave vector for a two-dimensional system like graphene. As the portion of the reciprocal space covered by the experiment increases at higher photon energies, a periodic pattern becomes clearly visible which, however, does not coincide with the reciprocal lattice mesh. Firstly, we can note that at the origin ($\mathbf{k}_{\parallel} = (0, 0)$) the binding energy is at its global maximum value for all the photon energies. Other local maxima can be found at the next-nearest neighbor reciprocal lattice points, and experiments at 600 and 700 eV show that this occurs again at the next-nearest neighbors of these latter points. Interestingly, at all the other reciprocal lattice points the binding energy takes its minimum value. We can summarize these results describing the periodic pattern with two complementary sublattices: the binding energy is at its maximum value at all the points connected by vectors that are $\sqrt{3}$ times longer than the primitive vectors and rotated by 30°, and it is at its minimum value at all the other reciprocal lattice points.

The observed binding energy variations can be explained by several different mechanisms. A first explanation contemplates the presence of several unresolved components from carbon atoms in chemically inequivalent envi-

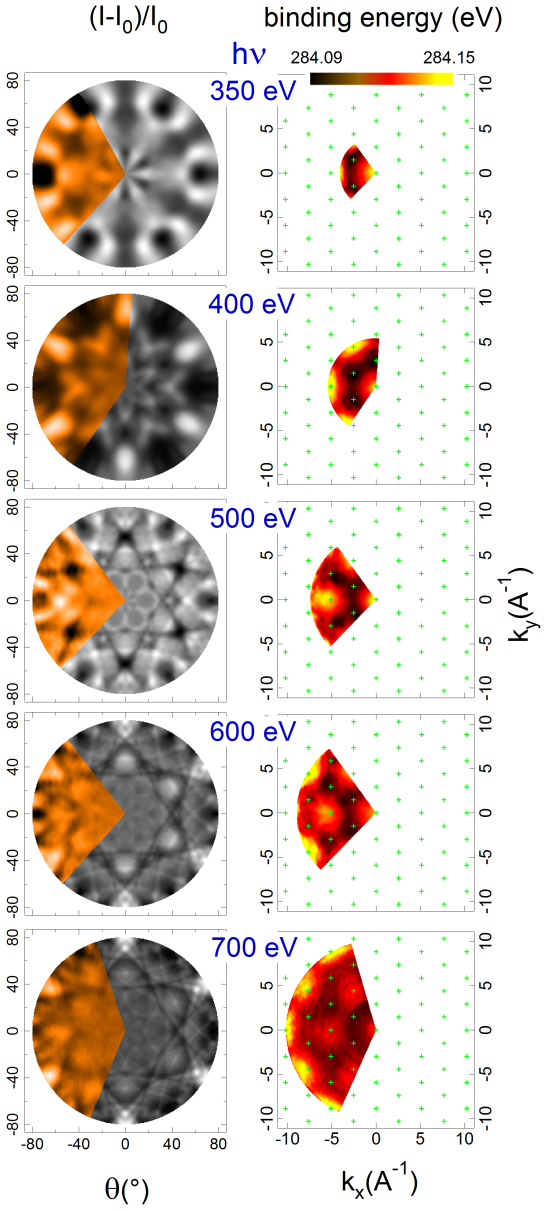

Figure 8.16: Left panel: stereographic projection of the photoemission intensity modulation as a function of emission angle for scans taken at different photon energies. The colored fraction of the disk are the data, the greyscale part is a calculation of the expected intensity. Right panel: The corresponding binding energy variations obtained from the peak fitting. Note that these variations are shown as a function of the wave vector parallel to the surface rather than emission angle. The green crosses correspond to the reciprocal lattice points of graphene, i.e. to the $\overline{\Gamma}$ points.

ronments: the relative intensity between these features could change due to photoelectron diffraction effects and thereby mimic a peak shift. This appears highly unlikely in the present case, not only because of the excellent agreement with the intensity calculation for a single component (evident in the left panel of fig. 8.16), but also because a peak shift of the observed magnitude would essentially require a complete supression of peak intensities in certain directions: this is actually quite unrealistic in the case of intensity modulations due to photoelectron diffraction effects. It would also be very unlikely for such a mechanism to lead to a binding energy modulation which is periodic in reciprocal space.

The second possible explanation is the recoil effect that follows directly from the momentum conservation principle. For photoelectrons with kinetic energy up to some keV, the momentum of the electron is much larger than that of a photon with the same energy, so that the final momentum of the emitting atom is mostly due to momentum transfer from the photoemitted electron. In this way part of the photoelectron's energy is used to excite lattice vibrations, resulting in an overestimation of the binding energy. This effect has been reported for the C 1s level of graphite [34] in hard X-ray photoemission experiments (HAXPES), with photon energy in the 6–8 keV range. In this case, in fact, the recoil effect is of considerable size, several hundred meV, but its magnitude should be insignificant for the low energies used here. Another argument against this explanation is that recoil effects are not expected to lead to any periodic modulation.

The third possibility is an initial state effect: a band-like dispersion of the C 1s core level. The simplest picture that we can imagine for this situation consist in the formation of a σ-type band between the 1s states of the two atoms in the unit cell of graphene (see fig. 8.2). Fig. 8.17 (a) shows a tight-binding calculation of such a band. The absolute binding energy and the band width are arbitrarily chosen to mimic those observed experimentally; this does not invalidate the results, since it is well known that with this kind of calculations the *absolute* values for the energy levels are not reliable results. The dispersion shown in the figure presents two bands with the highest energy separation at $\overline{\Gamma}$ and degeneracy at the $\overline{\mathrm{K}}$ point of the two-dimensional Brillouin zone. In the following these two bands will be referred, somewhat loosely, as the bonding and the anti-bonding band.

At a first sight, also this hypothesis appears not to be compatible with the experimental data we collected. The dispersion of fig. 8.17 (a) would imply the presence of two components in the C 1s peak at $\overline{\Gamma}$ but only one at $\overline{\mathrm{K}}$; this would result in a single, narrow C 1s peak at $\overline{\mathrm{K}}$ and a broad,

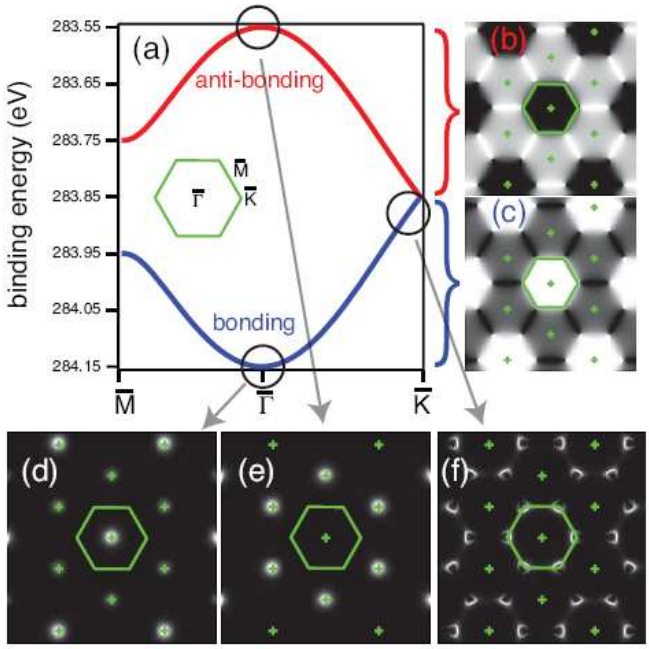

Figure 8.17: (a) Result of a tight-binding calculation for a σ-type band formed from the C 1s core states in graphene. The bonding (blue) and anti-bonding (red) bands are degenerate at $\overline{\mathrm{K}}$ and show the highest splitting at $\overline{\Gamma}$. The inset shows the Brillouin zone of graphene. (b) and (c) Calculated photoemission intensity from all the anti-bonding and bonding states, respectively. The grey-scale is chosen such that bright corresponds to high intensity. The green crosses mark the reciprocal lattice of graphene and the green hexagon the first Brillouin zone. (d)–(f) Calculated photoemission intensity from the states in the binding energy windows indicated by the small circles in (a). Note the similarity of the emission pattern from the bonding states in (d) with the positions of maximum binding energy in the right panel of fig. 8.16.

or even split, peak at $\overline{\Gamma}$. As pointed out above, on the other hand, the almost identical peak shape for all emission directions appears to rule out this scenario. Another discrepancy with experimental data arises from the fact that the σ-band should be periodic in reciprocal space, e.g. the peak position and width should be the same at all $\overline{\Gamma}$ points. According to the right panel of Fig. 8.16, this is not the case either. Most of the $\overline{\Gamma}$ points marked in the figure appear close to either a maximum or a minimum in the binding energy but clearly the observed periodicity is not the same as that

of the reciprocal lattice.

The hypothesis of band dispersion can, however, be reconciled with the experimental data by taking into account a peculiar interference effect already studied in detail for the valence band of graphite and graphene [35, 36]. This effect is caused by the presence of two atoms in the unit cell of graphene: in the most simple picture this interference can be interpreted as a type of Young's double slit phenomenon in which the two atoms in the unit cell act as electron sources.

Figures 8.17 (b) and (c) represent the results of the calculated photoemission intensities for all the anti-bonding and all the bonding states. These calculations clearly illustrate the strength of the interference effect: in the first Brillouin zone, for instance, emission from the anti-bonding states is entirely suppressed, while it is intense from the bonding states. In the neighboring zones it is the other way round. The emission intensities for smaller energy windows at the top of the anti-bonding band, at the bottom of the bonding band, and just below the Dirac point at $\overline{\mathrm{K}}$ are displayed in fig. 8.17 (d), (e) and (f), respectively. In the case of states below the Dirac point (panel (f)), the constant energy contour shows a triangular shape, as expected for the non-linear dispersion away from $\overline{\mathrm{K}}$. The photoemission intensity around this triangular contour shows strong variations which are caused by the interference effect and very similar to the results obtained for the valence π-band of graphite and graphene [35, 36].

The intensity variations reported in fig. 8.17 (b) and (c) suggest that the interference effect should be even more stronger for emission from the bottom of the bonding band and the top of the anti-bonding one at the $\overline{\Gamma}$ point: from fig. 8.17 (d) and (e) it is evident clearly seen that the intensity variations of the two bands are opposite to each other: for some $\overline{\Gamma}$ points only the bonding band is observed, for others only the anti-bonding band. In particular we note that at normal emission only the bonding band is visible. This phenomenon can be easily explained: for the bonding band the wave functions centered on the two atoms in the unit cell emit in phase and this band is observed. For the anti-bonding wave function, the two atomic wave functions emit out of phase, thus suppressing the photoemission.

The presence of this interference effect reconciles the hypothesis of a σ-band formation with the data. First of all, it explains the fact that the peak shape is very similar for all emission directions. For emission near $\overline{\mathrm{K}}$, in fact, the peak is narrow because of the degeneracy of the bands at $\overline{\mathrm{K}}$; at the $\overline{\Gamma}$ points the peak is also narrow, in contrast to naive expectation, because it does not show both the bonding and the anti-bonding bands but

rather only one of them at every given $\overline{\Gamma}$ point. The interference explains also the apparently incorrect periodicity of the band dispersion in reciprocal space. Due to this effect, in fact, not all $\overline{\Gamma}$ points are equivalent, because one either observes emission from the bonding or from the anti-bonding band. The binding energy modulation patterns reported in fig. 8.16 are in perfect agreement with the calculated photoemission intensity for the bonding band displayed in fig. 8.17: the highest binding energy value, in fact, corresponds to emission from the lower part of the bonding band.

The fact that only the bonding or the anti-bonding state is ever observable for a given emission direction permits a simple estimate of the maximum bonding/anti-bonding energy difference in graphene: its size corresponds directly to the difference of observed binding energies at inequivalent $\overline{\Gamma}$ points. Combining all the available data from $\overline{\Gamma}$ points showing either the bonding or the anti-bonding band, we evaluate the size of the splitting to be 60 ± 10 meV. In the case of an incomplete extinction of one of the peak components, we would underestimate the true degree of dispersion. Such an incomplete extinction should, however, also be observable as a change of the peak shape.

A final consideration can be made by comparing the measured binding energy difference to the size of the bonding/anti-bonding splitting of the molecular orbitals in small carbon-containing molecules such as ethine (C_2H_2, C-C distance of 1.2 Å, splitting of 105 meV [37]) and ethylene (C_2H_4, C-C distance of 1.34 Å, expected splitting of 20–30 meV [38]). Assuming that the matrix element for hopping between the core electrons on the two carbon atoms depends exponentially on the C-C distance and that the size of the splitting scales linearly with the number of nearest neighbors, from the splitting values of C_2H_2 and C_2H_4 we would extrapolate a total bandwidth of ≈ 30 meV for graphene, somewhat smaller than found experimentally.

8.3.3 Conclusions

In conclusion, we have shown that the interaction between neighboring atoms in graphene is sufficiently strong to induce the formation of a σ-band derived from the carbon $1s$ state.

Apart from the fundamental importance of these results for the localization of deep core levels in solids, a dependence of the core level binding energy on the emission angle can have implications for the interpretation of high-resolution core level data from graphene, graphite and related materials. The absolute magnitude of the binding energy variation observed here, in fact, is appreciable compared with usual chemical shifts and could

easily be interpreted incorrectly. For instance, an apparent shift of the C 1s peak as a function of polar emission angle might be mistaken for signs of a surface core level shift in graphite because of the higher surface sensitivity achievable with off-normal emission. From the complete data set, however, we concluded that the reported binding energy dispersion is inconsistent with the observation of multiple C 1s components.

Additionally, the existence of two atoms in the unit cell gives rise to interference effects in the photoemission process. These lead to a strong suppression of either the bonding or the anti-bonding band for different emission directions, such that the absolute size of the splitting could be determined from the binding energy modulation throughout the entire data set.

Finally, the fact that we can choose to observe only the bonding or only the anti-bonding state under certain conditions opens a unique opportunity for detailed as well as time-resolved studies of bonding in solids.

8.4 Transition metal clusters on graphene

Clusters have peculiar properties respect to the corresponding bulk materials. Their structural, electronic, magnetic and optical properties change with size, and also *new* properties can be revealed due to quantization effects that are not present neither in the isolated atoms nor in the bulk phase. All possible applications related to the nanometric-size-dependent properties of the clusters contemplate the use of supported nanoclusters, i.e. cluster deposited on a solid surface which can influence their properties.

From this point of view, a good choice of the support appears of fundamental importance, and studies focused on the cluster-support interaction gain much attention. The exceptional properties of graphene (as described in sec. 8.1) make this material an intriguing support for nano-clusters: its mechanical strength and the well known chemical inertness of graphite should prevent graphene from deteriorating under conditions of use, while, on the other hand, the characteristic electronic structure and charge transport mechanism could make this support an active element in adding new functionalities to the supported cluster system.

Let's consider how an ideal nano-cluster system should be: since the cluster response depends upon the cluster size, monodispersed cluster arrays would be the optimal choice (studies on magnetic properties of Co clusters [39] and on catalytic properties of Au clusters [40] are just two exemples of this approach); moreover, a regular array of clusters would be

desirable, so that the identical environment of each cluster would produce a uniform response to an external stimulus. Such systems can be useful, e.g., for data storage (giving the possibility to address a single magnetic cluster) or for applications in catalysis (the response of the system would be the additive superposition af all single cluster effect, being, at the same time, characteristic of a cluster of a well defined size and environment).

The moiré pattern formed by a graphene layer grown on the Ir surface (described previously in sec. 8.2) provides a unique template for the formation of ordered cluster superlattices. First STM studies on Ir clusters deposited on the graphene/Ir(111) surface, showed that the presence of the moiré cells allows the nucleation of the metal ad-particles in a regular array with a cluster size distribution, much narrower than that obtained on *flat* supports [20].

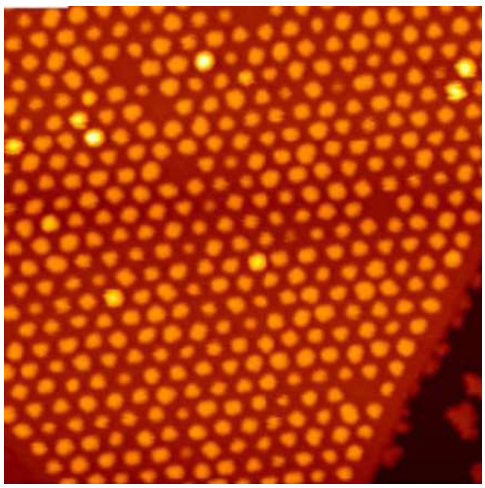

Figure 8.18: STM image (500×500 Å^2) of a cluster superlattice obtained after deposition of 0.10 ML od Ir on a graphene flake grown on the Ir(111) surface [20].

Experimental and theoretical works [20, 41] pointed out that, in presence of metal deposits, C-C bonds rehybridize from sp^2 to sp^3 at specific locations within the moiré unit cell, and in between the Ir substrate and the deposited clusters. Rehybridization is possible where locally the carbon rings are centered around a three-fold coordinated hcp or fcc site (the hcp and fcc regions introduced in sec. 8.2). Here three of the six C atoms sit directly over an Ir surface atom and rehybridization results in a tetrahedral geometry with strong dimond-like carbon-metal bonds, so that every other C atom binds

either to an Ir surface atom below it or to a metal adatom above. Recent STM investigations reported the possibility to prepare highly ordered superlattices with rhenium, gold and iron clusters deposited at 90 K, and with iridium, tungsten and platium also at room temperature (300 K) [23].

Within this scenario we decided to use photoemission spectroscopy to investigate the morphology and the electronic structure of gold, platinum and rhodium clusters deposited on the graphene/Ir(111) surface.

8.4.1 Gold clusters on graphene/Ir(111)

Experimental details

The deposition of gold clusters was obtained by evaporating Au atoms in front of the sample. The evaporator consisted in a gold coated tungsten filament that was resistively heated up to gold evaporation temperature. During the experiments, three different amounts of gold were evaporated on the graphene surface held at 30 K: keeping the evaporation conditions constant (i.e. using the same filament current and setting the same filament-sample distance) gold was evaporated for 120, 210 and 480 s. An estimation of the amount of gold deposited during each avaporation can be obtained by comparing the photoemission intensity of Au $4f_{7/2}$ and Ir $4f_{7/2}$ levels. By taking into account the inelastic scattering events experienced by the electrons in passing from the deeper layers to the surface before leaving the sample, it is possible to calculate the attenuation of the signal using a mean-free-path model. The characteristic attenuation length depends on the material that has to be passed through and on the electron kinetic energy and is well approximated by the model developed by Tanuma, Powell and Penn [42]. Assuming that each single moiré cell is occupied by a Au cluster, a rough estimation of the average number of atoms per cluster can be deduced.

t(s)	coverage (ML)	atoms/cluster
120	0.055 ± 0.015	4 ± 1
210	0.12 ± 0.03	9 ± 2
480	0.24 ± 0.04	19 ± 3

Table 8.1: Estimation of the Au coverage on the graphene surface after evaporation. The evaluation of the average number of atoms per cluster is based on the assumption that every moiré cell of the graphene layer hosts a Au cluster.

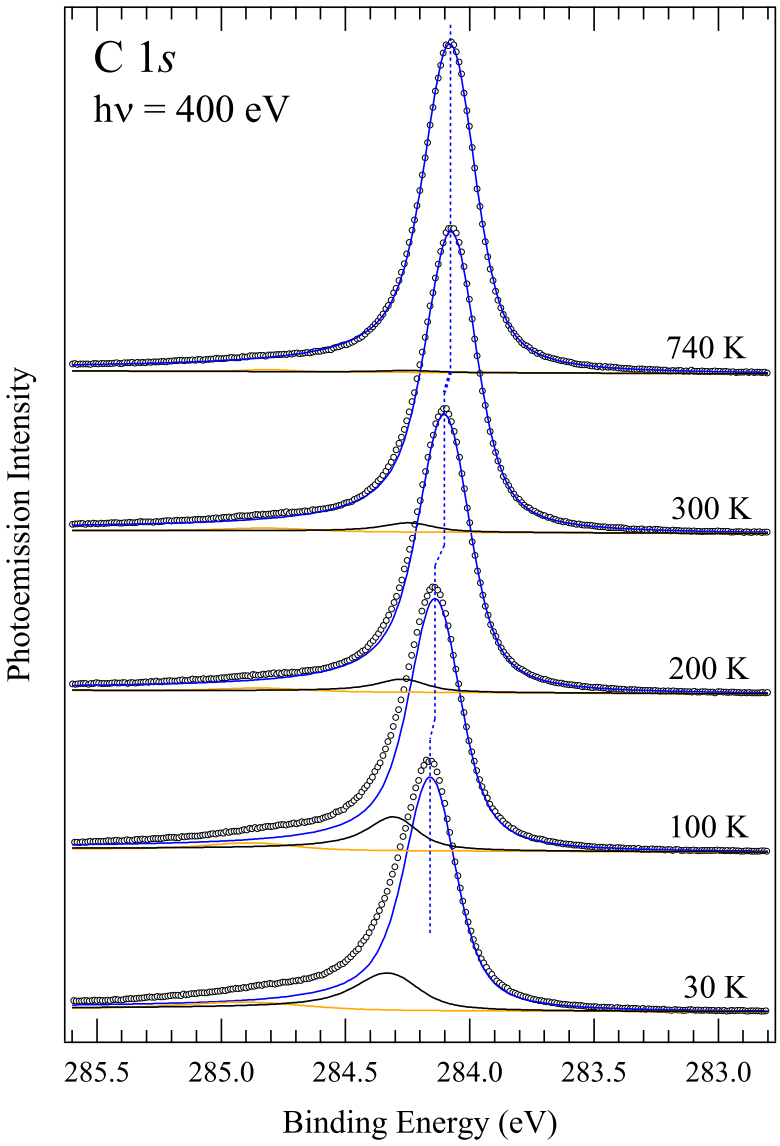

Figure 8.19: Series of C 1*s* spectra acquired after annealings at increasing temperatures. Au coverage is 0.24 ML. The spectral componenets obtained from the fitting procedure are also indicated.

The resulting values are summarized in table 8.1.

After Au deposition at 30 K, the sample underwent several flash annealings at increasing temperatures up to 1440 K in order to investigate the cluster evolution with temperature and test their thermal stability. After deposition and after each annealing, spectra of the Au $4f_{7/2}$, C $1s$ and Ir $4f_{7/2}$ core levels were acquired, as well as valence band.

Results and discussion

Fig. 8.19 shows the series of C $1s$ spectra acquired at the highest Au coverage. Two small components at high binding energy can be distinguished only up to 300 K and their shifts relative to the main component are of 160 meV and 720 meV: these values are compatible with those found, with *ab initio* simulations and photoemission measurements, for amorphous carbon samples that present an intermediate sp^2/sp^3 hybridization [43]. The two components are probably due to C atoms bound to a Au cluster that are also more strongly bonded to the Ir substrate. This interpretation appears reasonable, if we consider that first-principles calculations indicate that the adsorption of a cluster on a moiré cell substantially deforms the graphene geometry and influences the electronic structure as far as several cells from the cluster boundary.

The intensity of the two extra components decreases with temperature; at the same time the intensity of the main component increases. This behaviour suggests that the clusters are undergoing a morphological transformation which results in a conversion of initially perturbed C atoms in atoms with an electronic configuration absolutely similar to that of the clean graphene surface. This is compatible with a cluster aggregation picture where the average cluster size is increasing and their interaction with the underlying graphene layer is becoming weaker because of the formation of strong metal-metal bonds. From the reported spectra it is also possible to appreciate a progressive shift of the main component towards lower binding energy with increasing temperature, resulting in an overall shift of 80 meV at 740 K. This effect could be related to a long-range perturbation due to the increased dimension of the clusters: small clusters strongly interact with the substrate giving raise to strong local perturbation, while the effect of larger clusters is less pronounced but is extended to a larger region of the support.

The analysis of Au $4f_{7/2}$ core-level spectra reported in fig. 8.20 evidences two unambiguous trends: the decrease of the spectral lineshape width is paralleled by a reduction of the overall photoemission intensity. These trends

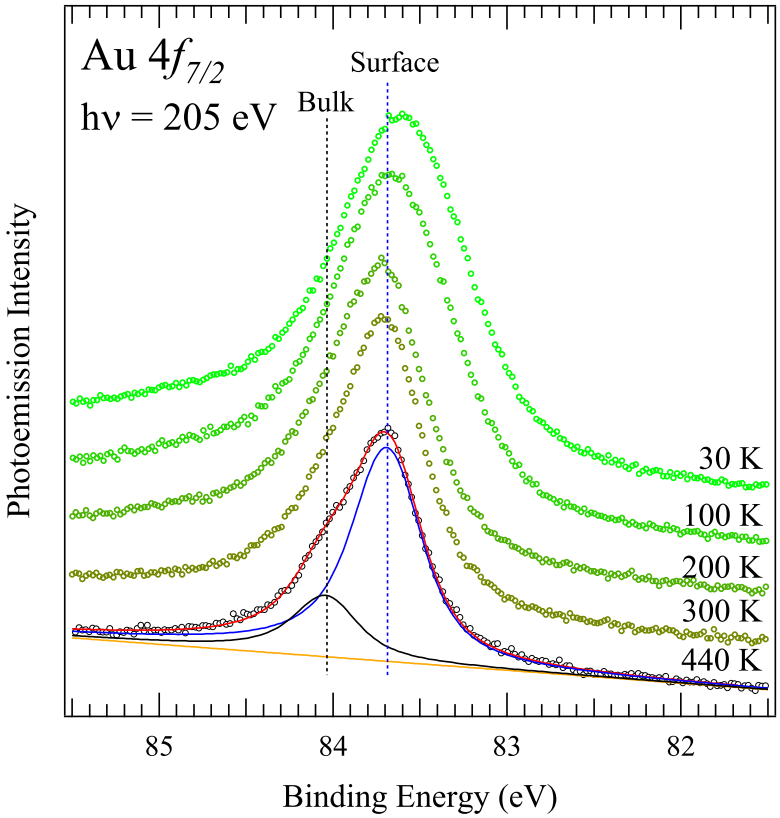

Figure 8.20: Series of Au $4f_{7/2}$ photoemission spectra obtained after annealings at increasing temperatures

are compatible with a situation where the large number of small clusters obtained after Au deposition at low temperature (presenting Au atoms in a broad distribution of inequivalent configurations) evolves in the formation of larger 3D aggregates with a consequent decrease of the photoemission intensity due to the screening effect on the signal arising from inner atoms.

After the annealing to 400 K two spectral components separated by 350 meV can be distinguished. In order to explain this behaviour we need to consider that for relatively large clusters the highly packed facets (such as (111) and (100)) are expected to form because of their lower internal energy and entropy respect to disordered or stepped micro-facets. This argument points towards assigning the higher binding energy component as due to

bulk-like Au atoms, meanwhile the lower one is related to the presence of ordered surfaces. This interpretation is strongly corroborated by the work of Heinmann *et al.* on Au single crystals, where a surface core level shift of -350 meV is found for the (111) surface respect to the bulk [44], in perfect agreement with our findings. Above 400 K, thus, the presence of the surface component in the Au $4f_{7/2}$ spectra suggests the formation of well ordered Au clusters, with a morphology very similar to that observed in STM images after annealing at temperature higher than 300 K, when the average cluster size increases to more than one hundred atoms [23]. STM images of gold clusters grown on graphite also show large and flat facets corresponding to (111) and (100) surfaces [45].

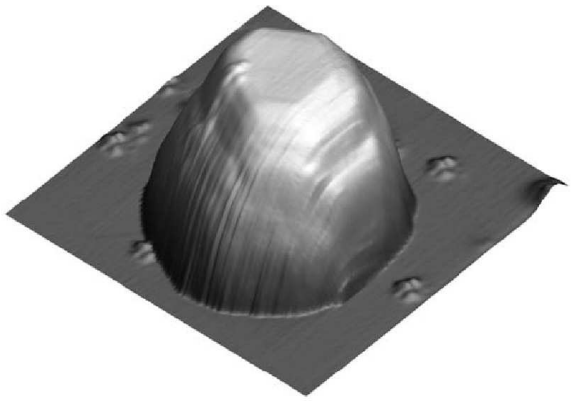

Figure 8.21: STM image of a Au cluster on graphite (10×10 nm^2). Cluster height is 2.5 nm. Facet area is 47 nm^2. From [45].

By analysing the Ir $4f_{7/2}$ core level after the avaporation of 0.24 ML of gold at 30 K, it becomes evident that the bulk and surface components are not sufficient to describe accurately the spectra: the strong modulation of the fit residual can be adjusted only with the introduction of a third spectral component. The line-shape of this additional feature has been fixed to be the same of the surface one: in fact, since at low temperatures we can confidently exclude intercalation processes, the assignement of the extra component as due to Ir surface atoms interacting with above C atoms appears reasonable. The modified environment due to C atoms that, in turn, interact with the above Au clusters, induces a binding energy shift of +160 meV for Ir atoms in correspondence of the adparticles respect to those below an unperturbed

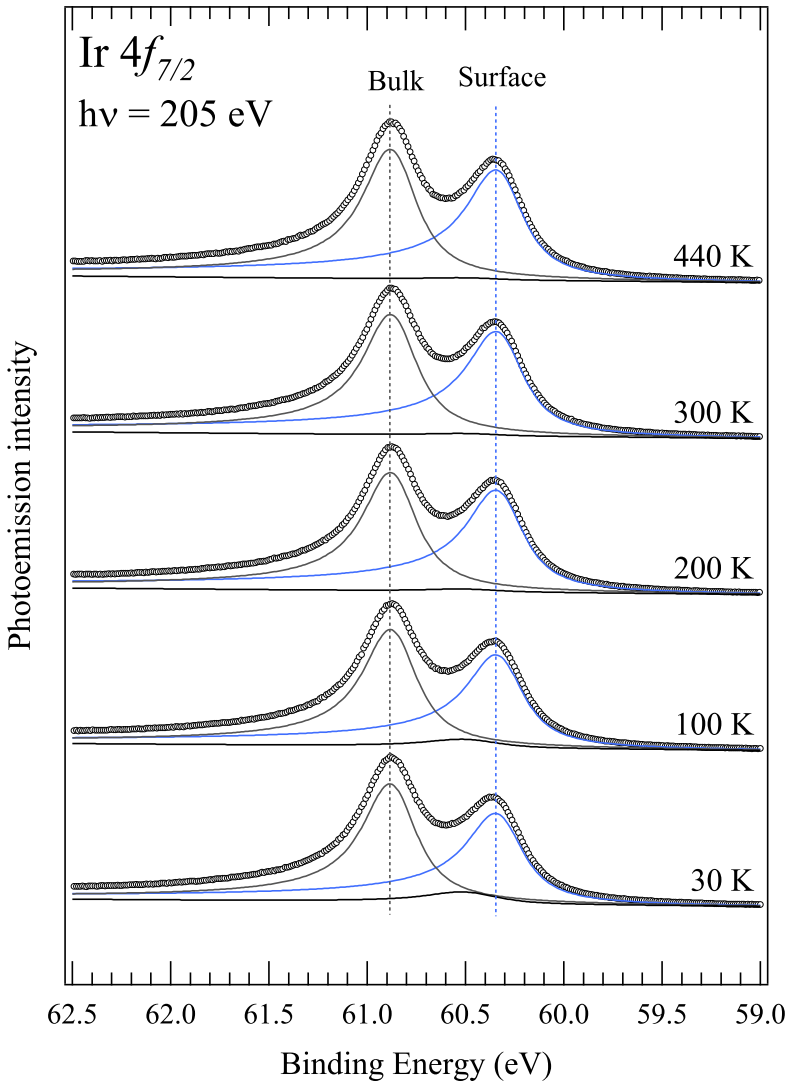

Figure 8.22: Series of Ir $4f_{7/2}$ photoemission spectra obtained after deposition of 0.24 ML of Au and annealing at the indicated temperatures.The spectral components obtained from the fitting procedure are also represented.

graphene region (surface component).

In fig. 8.22 the evolution of the three spectral components of the Ir $4f_{7/2}$ core level is summarized for the 0.24 ML deposition: upon annealing, an increase of the surface component is observed, parallelled by a decreased intensity of the extra component that definitly disappears at the threshold temperature (440 K). This behaviour confirms the interpretation of the C $1s$ spectra: large gold clusters formed after annealings above the threshold temperature interact very weakly with the graphene/Ir(111) surface and show a morphology trend comparable to that observed in the case of a graphite support (see fig. 8.21).

A further confirmation of the weak interaction between large Au clusters and graphene comes from the valence band spectra (see fig. 8.23). The σ and π bands of unperturbed graphene, found at binding energy of 21.2 eV and 7.6 eV respectively, gain intensity with increasing annealing temperature, corresponding to increasing cluster size.

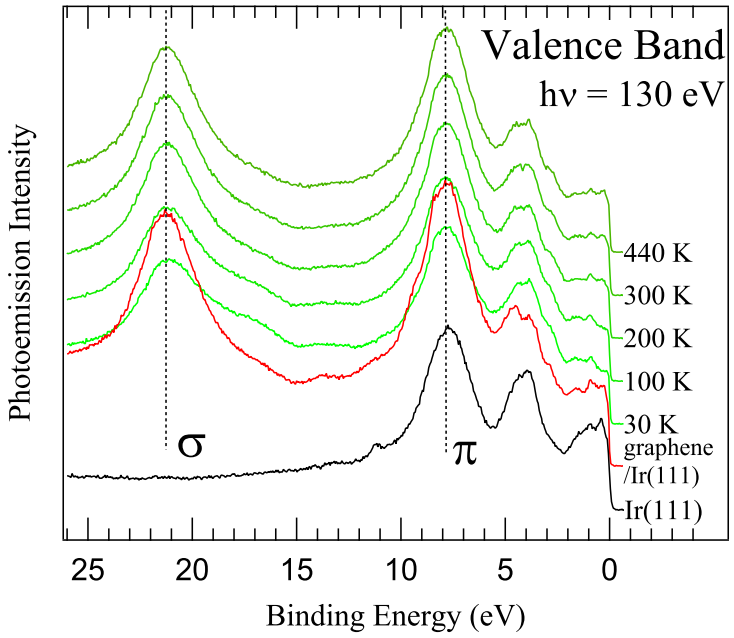

Figure 8.23: Valence band of clean Ir(111), of clean graphene deposited on Ir(111) and after deposition of 0.24 ML of Au and annealings at the indicated temperatures.

A final set of annealings was devoted to the investigation on the *thermal stability* of the gold clusters. In the temperature range between 440 K and 1040 K, the Au $4f_{7/2}$ spectra present an approximately constant bulk component, limited by the attenuation due to the mean-free-path effect, while the surface intensity decreases monotonically to about the 60% of the initial value. This variation suggests that gold clusters are undergoing aggregation processes leading to important changes in their morphology: small flat clusters tend to coalesce forming larger 3D particles so that the surface-to-volume ratio decreases.

The spectra reported in fig. 8.24 illustrate the behaviour of the clusters

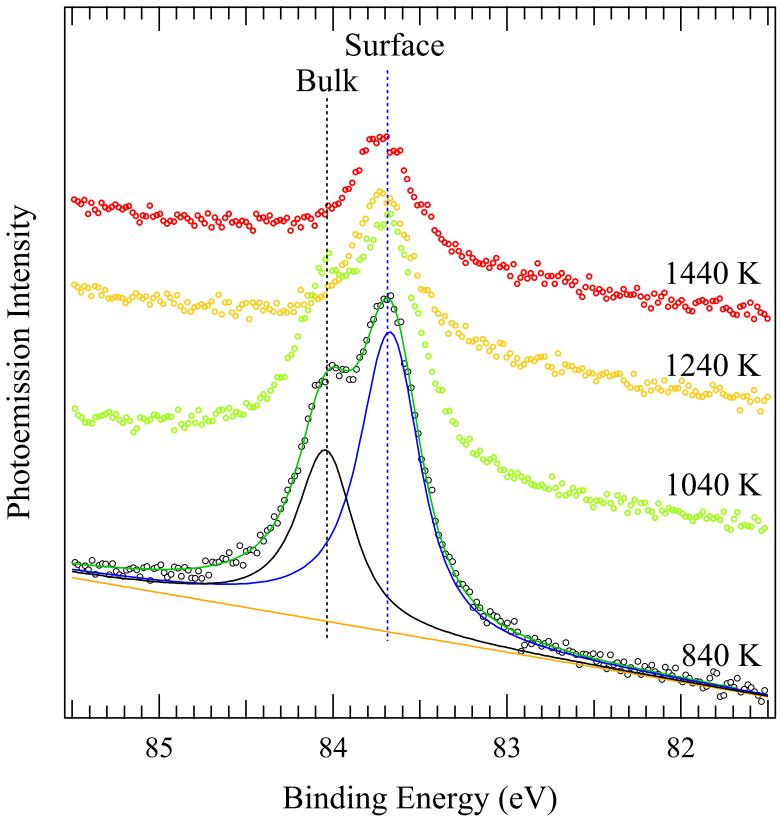

Figure 8.24: Au $4f_{7/2}$ spectra after high-temperature annealings. The overall decrease of intensity and the disappearance of the bulk component can be appreciated.

at temperatures above 1040 K. Going from 1040 K to 1440 K the Au bulk component almost disappers and the surface intensity is halved. The reduction of the cluster bulk can be explained either by the desorption of Au atoms or by their intercalation below the graphene layer followed, eventually, by the diffusion in the Ir bulk. The absence of extra spectral components related to the formation of an Ir-Au alloy, and the very low value (-1.2 eV) of the segregation energy for the Au solute in the Ir host [46] tend to exclude the latter hypothesis.

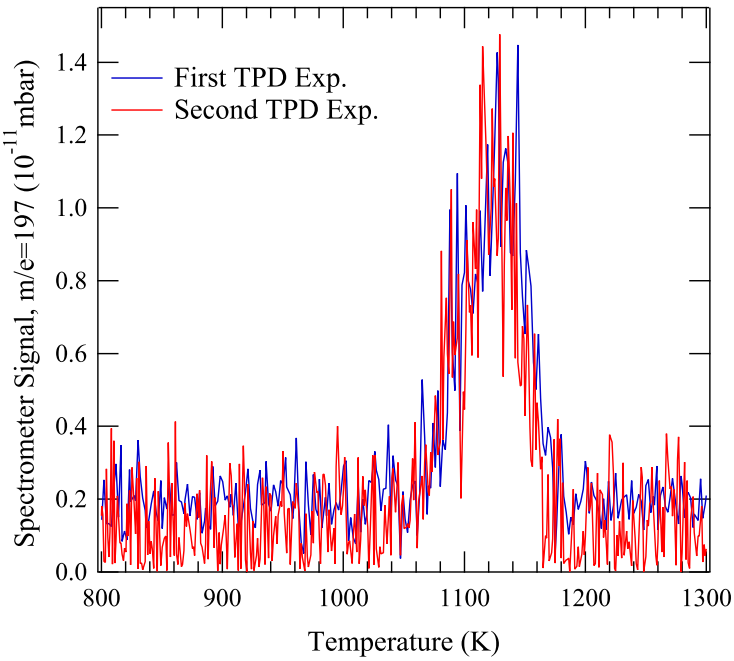

Figure 8.25: Desorption spectra for mass 197 a.m.u. as a function of temperature during the heating ramp. The TPD experiment was repeted twice and both curves are reported on the graph in order to underline the repeatibility of the result.

In order to obtain a final confirmation of the desorption of Au atoms from the surface, a temperature programmed desorption (TPD) experiment was performed. After deposition of 0.22 ML of Au on the graphene at 240 K (the coverage was evaluated by comparison of the Ir and Au core level intensities as described at the beginning of this section), a programmed temperature ramp was started and the mass spectrometer signal for mass

197 a.m.u. (the Au atomic mass) was recorded as a function of temperature. As can be inferred from fig. 8.25, Au desorption begins at 1070 K and, after the maximum of the intensity at 1130 K, at 1180 K all the Au atoms have desorbed from graphene. This measurement is a direct proof of the desorption of single Au atoms from the graphene surface and explains the reduced intensities of bulk and surface spectral components after annealings above 1040 K.

8.4.2 Platinum clusters on graphene/Ir(111)

Experimental details

Platinum atoms were evaporated by heating a Pt filament in front of the sample. The sample was cooled at 30 K by means of a cryostat filled with liquid He. In order to explore the behaviour of the system as a function of the cluster size, three different evaporation times were used (30, 60 and 120 s) which correspond to three different amounts of Pt on the surface. The corresponding coverage and extimated cluster size are summarized in table 8.2. The evaluation of the coverage, as described for the Au clusters, is based on intensity ratio between the Ir $4f_{7/2}$ and the Pt $4f_{7/2}$ peaks.

t(s)	coverage (ML)	atoms/cluster
30	0.04 ± 0.01	3 ± 1
60	0.07 ± 0.01	6 ± 1
120	0.14 ± 0.03	11 ± 2

Table 8.2: Estimation of the Pt coverage on the graphene surface after evaporation. The evaluation of the average number of atoms per cluster is based on the assumption that every moiré cell of the graphene layer hosts a Pt cluster.

The experiment focused on the temporal evolution of the clusters at 30 K, i.e. on the diffusion and nucleation processes that lead from single Pt adatoms to the formation of dimers and, subsequently, larger aggregates. The high flux of SuperESCA beamline and the detection efficiency of the new analyser/detector system allowed the acquisition of real-time series of well resolved Pt $4f_{7/2}$ spectra with a time interval of 30 seconds between each spectrum: measurements were performed at liquid He temperature immediately after Pt deposition. When the investigated system was finally

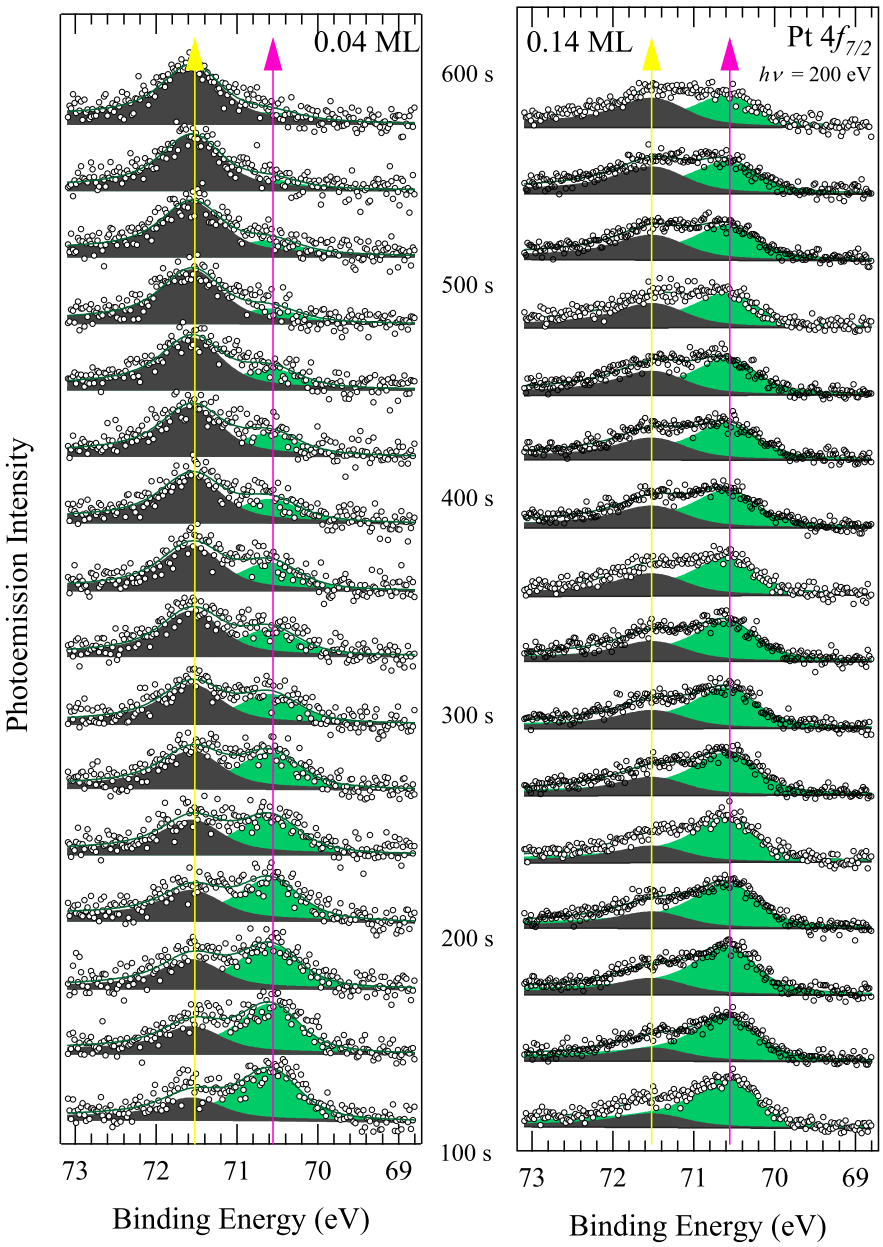

Figure 8.26: Temporal evolution of Pt $4f_{7/2}$ spectra acquired at 30 K, corresponding to 0.04 ML (left panel) and 0.14 ML (right panel) of Pt coverage. The time-ticks indicate the temporal scale of the observed cluster evolution; the delay between platinum evaporation and spectra acquisition, necessary for placing the sample in the correct position, has been taken into account.

stabilized, as judged from the Pt spectra, C 1s and Pt $4f_{7/2}$ spectra were also measured with better statistics.

Results and discussion

Fig. 8.26 reports the evolution of the Pt $4f_{7/2}$ spectra for coverages corresponding to 0.04 and 0.14 ML, i.e. the smaller and the larger amount of Pt deposited on graphene during the experimental session. During data analysis, we decided that the most reasonable approach to obtain quite good fits without introducing a large number of degrees of freedom was describing the spectra by means of only two components at 71.52 and 70.56 eV respectively. It is worth noting that the line-shape of the two spectral components is quite different if compared with that obtained for Pt(111) and Pt(100) surfaces [47, 48], the main diffrence being the widths of the two peaks that, in this case, are larger than those found for the single crystal surfaces. The origin of this difference can be ascribed to: (i) an increase of the Gaussian width due to distinct vibrational properties of the clusters respect to the single crystals; (ii) an increase of the lorentzian width due to a shorter lifetime of the hole in the ionized state in the clusters; (iii) an inhomogeneous broadening due to the presence of unresolved structural components due, e.g., to clusters nucleated in different positions of the moiré lattice. This latter consideration, actually, warns that the subdivision of the Pt atom population in only two categories may be really a strong approximation. However, the trend in the two series reported in fig. 8.26 is pretty clear: the spectral weight moves from the low-binding energy component to the high-binding energy one. Considering that, due to their lower coordination number, single atoms are expected to present lower binding energy, and taking into account the published results for the Ir clusters [41], the low binding energy component of the Pt spectra can be assigned to single adatoms that easily diffuse on the graphene surface (even at 30 K) forming larger clusters. This interpretation is in agreement with bond strength considerations: the binding energy for the Pt-Pt bond is larger than that for Pt-C one, while, at the same time, the diffusion barriers for transition metals on graphite are known to be quite small, allowing single adatoms reaching the most favorable configuration that maximize the number of Pt-Pt bondings.

Let's consider the temporal trends for the two populations in the case of the two Pt coverages shown in fig. 8.26. By reporting the intensities of the two spectral components in a graph as a function of time (fig.8.27), and fitting the trends with an exponential function ($f(t) \propto e^{-\frac{t}{\tau}}$) it becomes evident that the transition form low to high binding energy species is faster

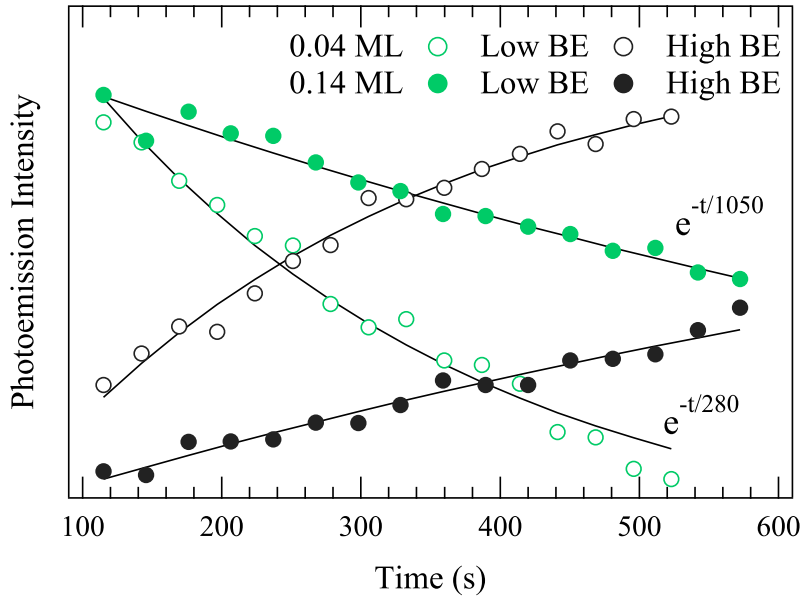

Figure 8.27: Normalized intensity of the low and the high binding energy components of the Pt $4f_{7/2}$ spectra, for 0.04 ML (open circles) and 0.14 ML (filled circles) Pt coverage. Black lines are the corresponding fitting functions.

at lower coverage: the resulting time constants, in fact, are $\tau = 280$ s and $\tau = 1050$ s for the case of 0.04 ML and 0.14 ML coverage, respectively.

This result underlines an unexpected behaviour of Pt adatoms diffusion on the graphene surface. A possible picture for the investigated system that could explain this peculiar effect is the following. At low coverage, the Pt adatoms diffuse rapidly on graphene and form larger aggregates that, above a certain threshold dimension, present a reduced mobility, at least at the temperature of our experiments; due to the small amount of Pt deposited on the surface, the number of such large clusters is limited. At higher coverage, the number of large clusters that can be formed is substantially larger, even if several single Pt adatoms can be found on the surface: the presence of the larger Pt aggregates that deform the graphene lattice could strongly change the diffusion barrier for the adatoms slowing down, in this way, the diffusion and aggregation process.

In order to obtain a more correct evaluation of the number of atoms per cluster, it is worth building a simple model for cluster nucleation, assuming

that all the atoms in a moiré cell aggregate in a single cluster. This model can be applied when the probability for a Pt atom to diffuse in a moiré cell different from the one it has been deposited is negligible, and results in a Poisson distribution of the number of atoms per cluster, $P(n) = \frac{\overline{n}}{n!}e^{-\overline{n}}$ [20], where $\overline{n}$ is the average value of the distribution. Because of the high mobility of single atoms and dimers on graphene, the Poisson distribution with $\overline{n} = 1$ does not describe correctly the average number of atoms per cluster at equilibrium in the case of 0.01 ML coverage. Actually, this coverage has been studied by N'Diaye *et al.* by means of scanning tunneling microscopy [23] for Ir clusters on graphene at 390 K: these measurements reveal that clusters nucleate only in one moiré cell every 4.3 and are constituted by an average value of 4.5 atoms. A similar situation could happen for the 0.04 ML Pt coverage described in this section: if cluster nucleation takes place only in a fraction of the moiré cells, the average Pt atoms/cluster could be higher than 3.

C 1s and Ir $4f_{7/2}$ spectra were also acquired after the real-time measurements described above, when equilibrium was reached. As can be seen in fig. 8.28, the C 1s main spectral line moves towards higher binding energy with increasing coverage. Two components at +750 and +160 meV also appear, while the intensity of the main peak decreases. The line-shape and the binding energy values of the two extra components are very similar to those found in the case of Au clusters (sec. 8.4.1). The shift towards higher binding energy of the main line may be explained as due to a charge transfer from the metal clusters to the graphene lattice.

The surface models in fig. 8.28 represent the inequivalent configurations of the carbon atoms that occur upon cluster adsorption; these differences account for the C 1s spectral components obtained from the fitting procedure:

- (A) carbon atoms of the unperturbed graphene;
- (B) average perturbation of the carbon atoms due to the delocalized charge transfer from the Pt clusters; this effect influences the whole graphene layer;
- (C) carbon atoms near a Pt cluster feel only a weak perturbation resulting in a shift of +160 meV;
- (D) carbon atoms directly coordinated with Pt clusters present a more significant shift of +750 meV.

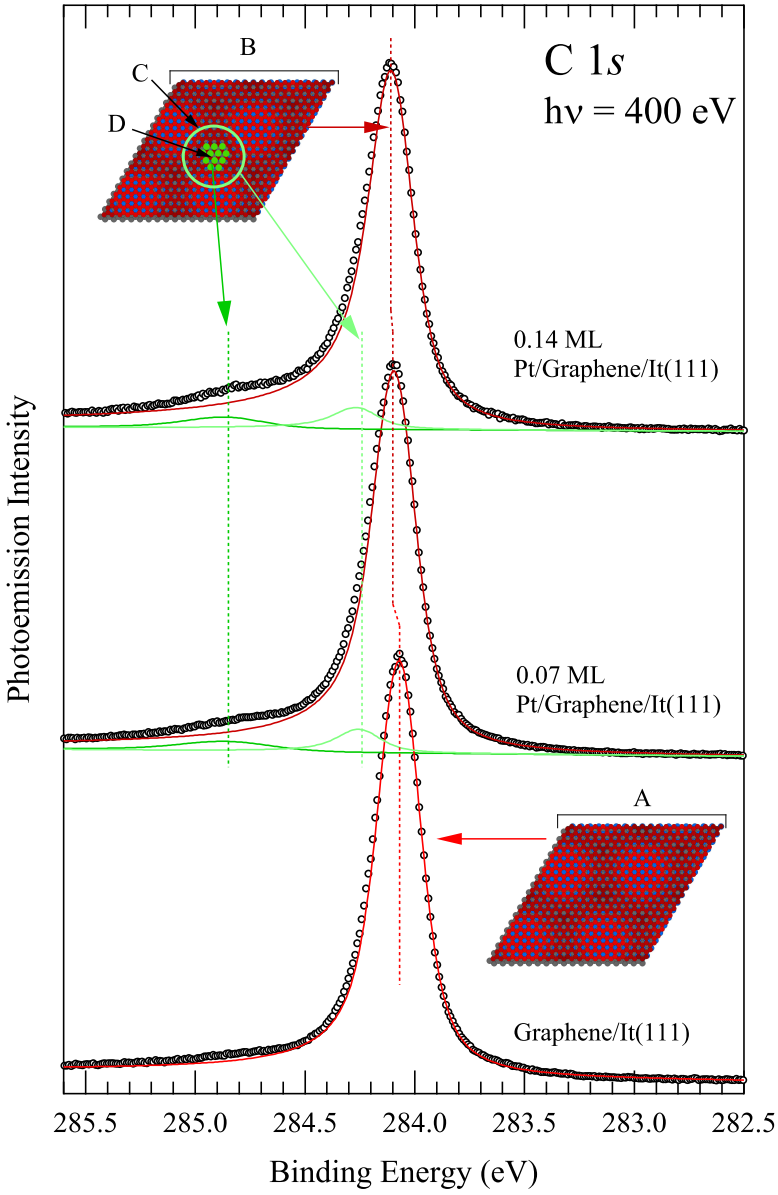

Figure 8.28: C 1*s* core level spectra for different platinum coverage. The spectra were acquired immediately after platinum evaporation at 30 K. The models reported in the insets illustrate the different configurations of carbon atoms that originates the observed spectral components (See text).

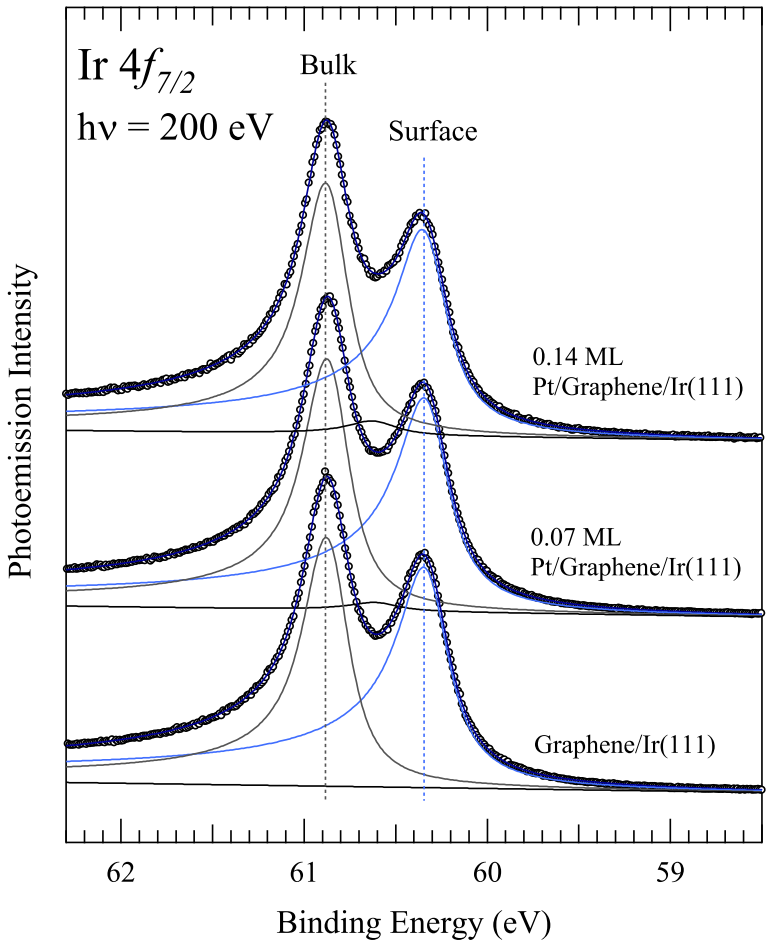

Figure 8.29: Ir $4f_{7/2}$ core level spectra for different platinum coverage. The spectra were acquired immediately after platinum evaporation at 30 K.

Ir $4f_{7/2}$ spectra shown in fig. 8.29 present a behaviour very similar to that observed in the case of Au clusters. The surface component shows a reduction that goes from 2.9% to the 6.3% for the highest Pt coverage. These values are related to the fraction of Ir surface atoms perturbed by the presence of Pt clusters.

A simple model which contemplates only planar Pt islands, so that the surface density of perturbed Ir atoms should be directly proportional to

the density of deposited Pt atoms, does not fit the experimental data: in fact, while at 0.04 ML the 2.9% of the Ir atoms is perturbed, at 0.14 ML the perturbed fraction of Ir atoms is only 6.3%, indicating that clusters reorganize in two or more layers even at this low Pt coverage. However, recent experimental [20] and theoretical [49] works show that Ir clusters should be planar if made by less than 25 atoms at 30 K; moreover, another experimental paper [23] states that Pt tends to form wider islands with less atomic layers than Ir. The indications on the morphology of Pt islands are, thus, controversial and additional investigations are needed.

8.4.3 Rhodium clusters on graphene

Experimental details

Rhodium atoms were obtained from a Rh filament resistively heated effect. The amount of deposited rhodium investigated in these photoemission experiemnts ranges from low- to medium-coverage, obtained by evaporating the metal during periods of 60, 120 and 240 s. The corresponding coverages and the average number of Rh atoms per cluster have been extimated from the intensity ratio between the C $1s$ and the Rh $3d_{5/2}$ core levels and are reported in table 8.3. Rh $3d_{5/2}$, C $1s$ and Ir $4f_{7/2}$ spectra were acquired immediately after deposition at 30 K and after each annealing up to 1140 K.

t(s)	coverage (ML)	atoms/cluster
60	0.09 ± 0.02	8 ± 2
120	0.17 ± 0.03	15 ± 3
240	0.37 ± 0.06	33 ± 6

Table 8.3: Estimation of the Rh coverage on the graphene surface after evaporation. The evaluation of the average number of atoms per cluster is based on the assumption that every moiré cell of the graphene layer hosts a Pt cluster.

Results and discussion

The C $1s$ series of spectra acquired for the highest coverage shows well defined trends. The fitting procedure results satisfactory with three components at 284.10, 284.29 and 284.59 eV respectively. As already seen for gold

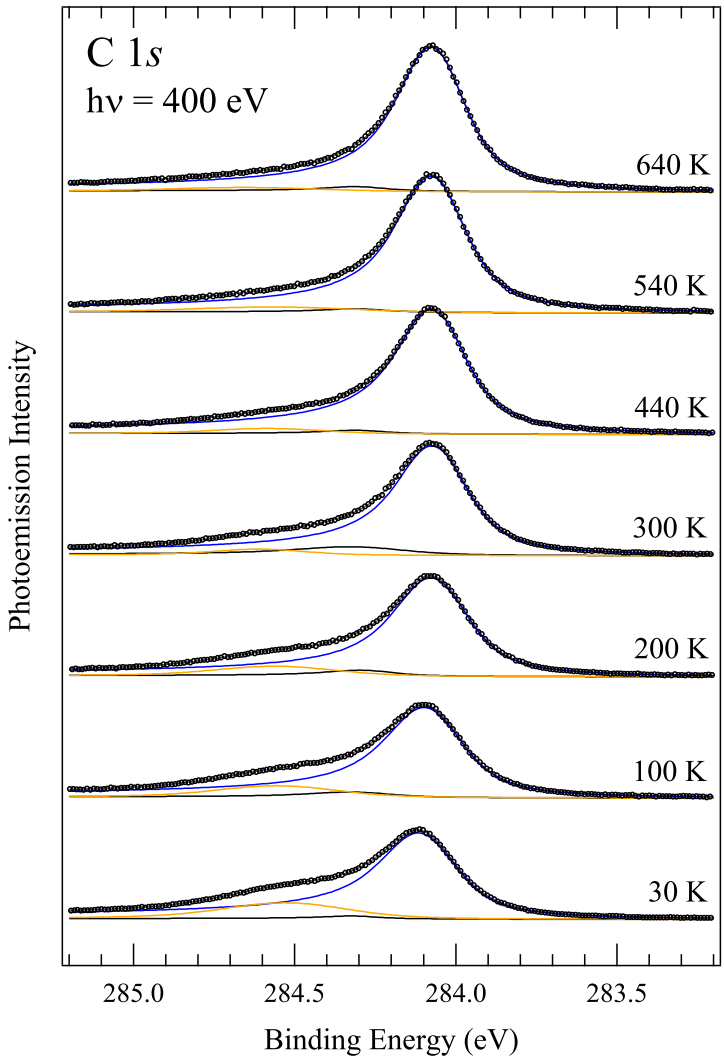

Figure 8.30: Series of C 1*s* spectra acquired after annealings at increasing temperatures. Rh coverage is 0.37 ML. The spectral components obtained from the fitting procedure are also indicated.

and platinum, the feature at the highest binding energy can be assigned to C atoms that re-hybridize when bondings are formed with Rh atoms in the clusers or with Ir atoms in the substrate. As can be noted in fig. 8.30, this component is indeed evident just after deposition at 30 K. After the first annealings at 100 and 200 K, the spectral weight already moves from the highest binding energy component to the main line at 284.10 eV. A third component at 284.29 eV also appears. The evolution described above indicates that the higher the annealing temperature is, the larger is the number of graphene atoms recovering the unperturbed configuration, while the signal of the C atoms directly interacting with the clusters diminishes. This behaviour can be due to an aggregation process of the Rh atoms: at high temperature larger clusters are formed which interact more weakly with the underlying graphene layer.

Rh $3d_{5/2}$ spectra, reported in fig. 8.31, show an overall decrease of the signal intensity at higher temperatures. This is probably due to the increased screening effect and is compatible with the cluster aggregation hypothesis. More in detail, spectra measured immediately after the deposition process and after the annelings at 100 and 200 K are characterized by a single, broad component that suggests the presence of a broad distribution of inequivalent Rh atoms, i.e. with different electronic configurations. This can be due to (i) inequivalent adsorption sites; (ii) differences for Rh atoms settled in the same adsorption sites, but in different regions of the moiré cell; (iii) a broad distribution of Rh interatomic distances, which is expected when small clusters with various morphologies are present on the surface. It is not possible to exclude, however, an effect due to different vibrational properties and final-state effects for Rh atoms in different configurations.

After the annealing at 300 K, three distinct components begin to be distinguished: the most intense signal at 306.67 eV and the two minor features at 307.09 and 306.36 eV respectively. Taking into account the typical morphology of supported clusters, which usually present close-packed surfaces [(111) and (100)] and a bulk structure very similar to that of a single crystal, the spectral component at highest binding energy can be assigned to the bulk Rh atoms ($n_{coord} = 12$), the intermediate component at -420 meV to the cluster surfaces ($n_{coord} = 9$) and, finally, the feature at the lowest binding energy (-730 meV) to atoms positioned at cluster edges, which present an even lower coordination number ($n_{coord} \leq 7$). In the inset in fig. 8.31 an ideal Rh cluster is schematized where surface and edge atoms are highlighted.

The above interpretation is based on a previous analysis of the Rh $3d_{5/2}$ core level measured for single adatoms and dimers deposited on Rh(111) and Rh(100) surfaces and verified with *ab-initio* simulations [47]. That work is

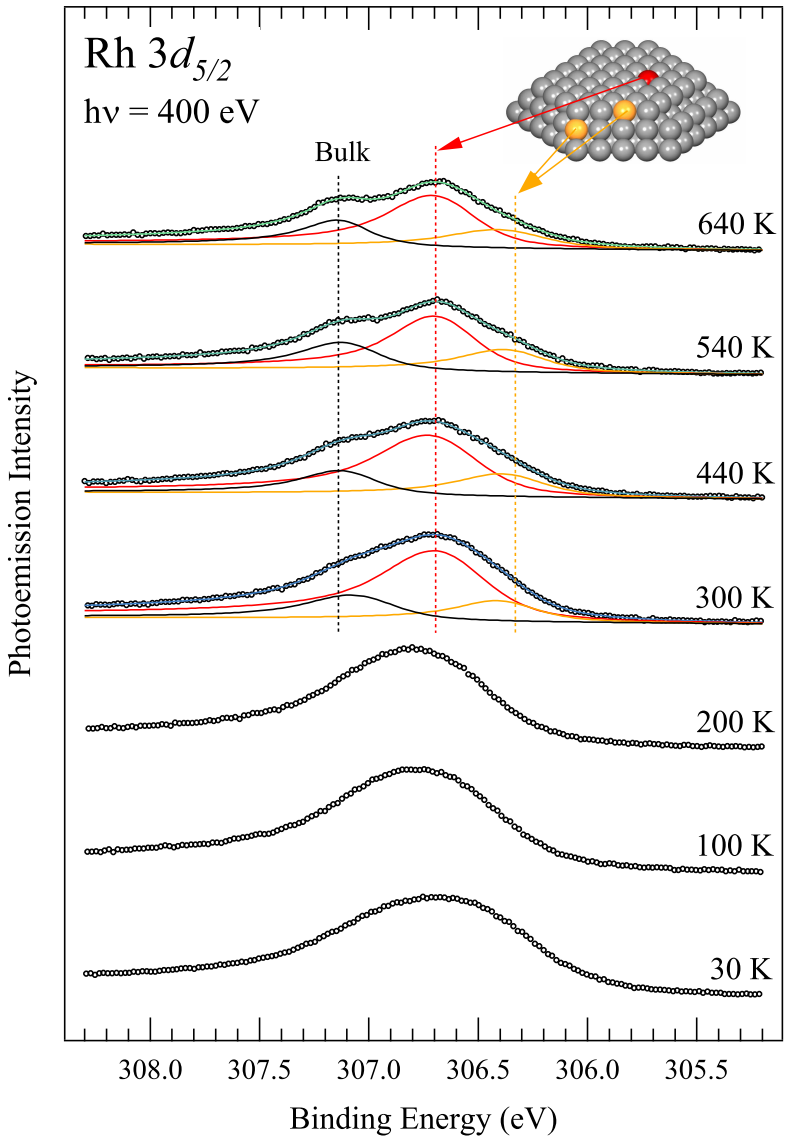

Figure 8.31: Series of Rh $3d_{5/2}$ spectra acquired after annealings at increasing temperatures. Rh coverage is 0.37 ML. Above 300 K, the spectral components obtained from the fitting procedure are also indicated. The model of rhodium cluster represented in the inset summarizes the assignement of the spectral components.

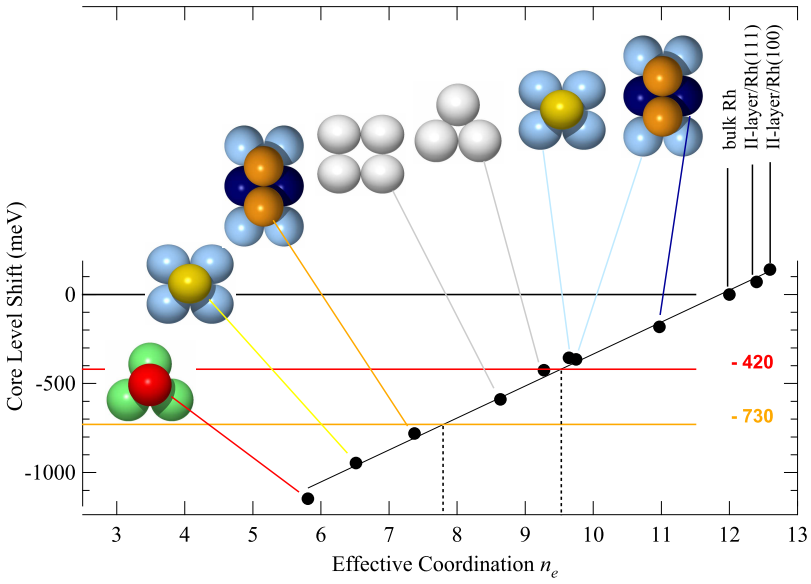

Figure 8.32: Rh $3d_{5/2}$ core level shifts as a function of the effective coordination number of the emitting atom [47]. The red and yellow lines indicate the shift measured for rhodium clusters deposited on graphene/Ir(111).

summarized in fig. 8.32, where the core-level shifts are plotted as a function of the *effective* coordination number. In the graph, the shifts found in the present work for the Rh clusters are also reported, in order to compare them with the previous results. It is important noting that the *effective* coordination number takes into account also structural relaxation effects in the neighbourhood of the emitting atom: since in nanometer-sized clusters the interatomic distances are generally shorter than those measured in bulk crystals, cluster atoms show larger *effective* coordination number than single crystal atoms with a corresponding *real* coordination number.

As for the temperature dependence, the bulk and edge components do not change significantly going from 300 to 640 K, while the surface intensity decreases in a way compatible with a picture where small clusters aggregate forming larger ones. In fact, when large clusters are formed, the increased number of *bulk* atoms is balanced by the enhanced screening effect, due to the increased average height of the clusters, leaving the bulk intensity substantially unaltered. On the other hand, the diminished number of surface atoms is merely a geometric effect when the dimension of the clusters in-

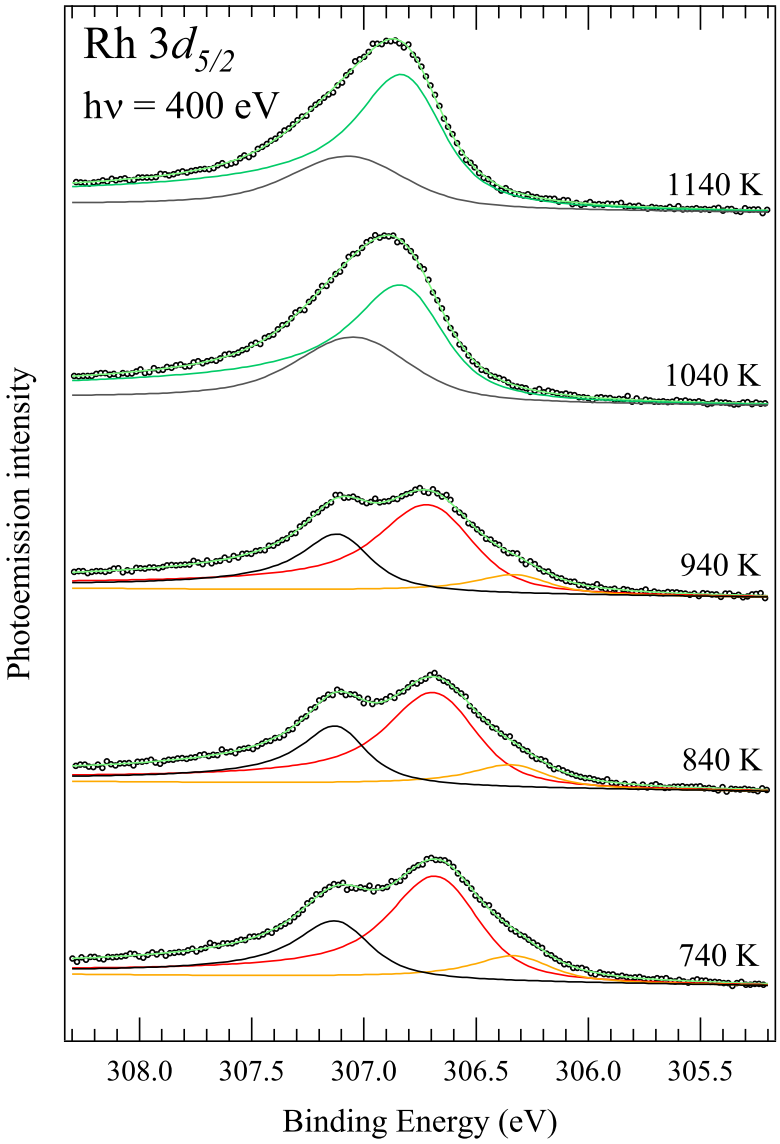

Figure 8.33: Series of Rh $3d_{5/2}$ spectra acquired after annealings in the temperature range 740–1140 K. Rh coverage is 0.37 ML. The spectral components obtained from the fitting procedure are also indicated.

creases.

The annelings at temperatures above 940 K resulted in very interesting effects, evidence that a substantial transformation is taking place. The three distinct spectral components previously identified in Rh $3d_{5/2}$ spectra are not observed after annealing at 1040 K (fig. 8.33). The main photoemission line of the C 1*s* core level (fig. 8.34) at 284.10 eV is replaced by a feature at 284.29 eV; at the same time a broad and intense component appears at 284.93 eV. In the Ir $4f_{7/2}$ spectra, on the other hand, the surface component, only slightly affected by the presence of rhodium clusters on the graphene layer up to 940 K, loses about 60% of its intensity and shifts towards lower binding energy by an amount of about 100 meV.

All these elements can satisfactory fitted in a picture where the Rh clusters intercalate below the graphene layer:

- After intercalation, Rh atoms come in direct contact with the Ir surface atoms; the Rh-Ir interaction, that appears to be much stronger than the graphene-Ir one studied in sec. 8.2, strongly modifies the iridium surface , leading to the reduction of the corresponding spectral component. On the other hand, the bulk component does not change significantly, so that an explanation based only on the screening effect would not be satisfactory.

- The significant modification in the line shape of the C 1*s* core level can be explained as due to graphene strongly interacting with the underlying rhodium islands; after intercalation, in fact, at least part of the graphene layer sits on Rh atoms. The strict correspondence with C 1*s* line shape measured in the case of a graphene layer grown on the Rh(111) substrate (fig. 8.36, panel (a)) supports our interpretation. The high binding energy feature has been assigned by Preobrajenski *et al.* to C atoms at the top of the moiré corrugation, while the low binding energy component is due to the lower parts of the graphene layer strongly bonded to the rhodium substrate [24]. Slight differences among the two reported spectra are probably related to the fact that the intercalated Rh layer is not complete, since the maximum Rh coverage we dealt with, and for which spectra have been reported in fig. 8.36, is only 0.37 ML. It is also possible to note an overall intensity increase of the C 1*s* core level after annealing at 1040 K: this is due to the fact that after intercalation the electrons photoemitted by C atoms do not undergo any screening effect.

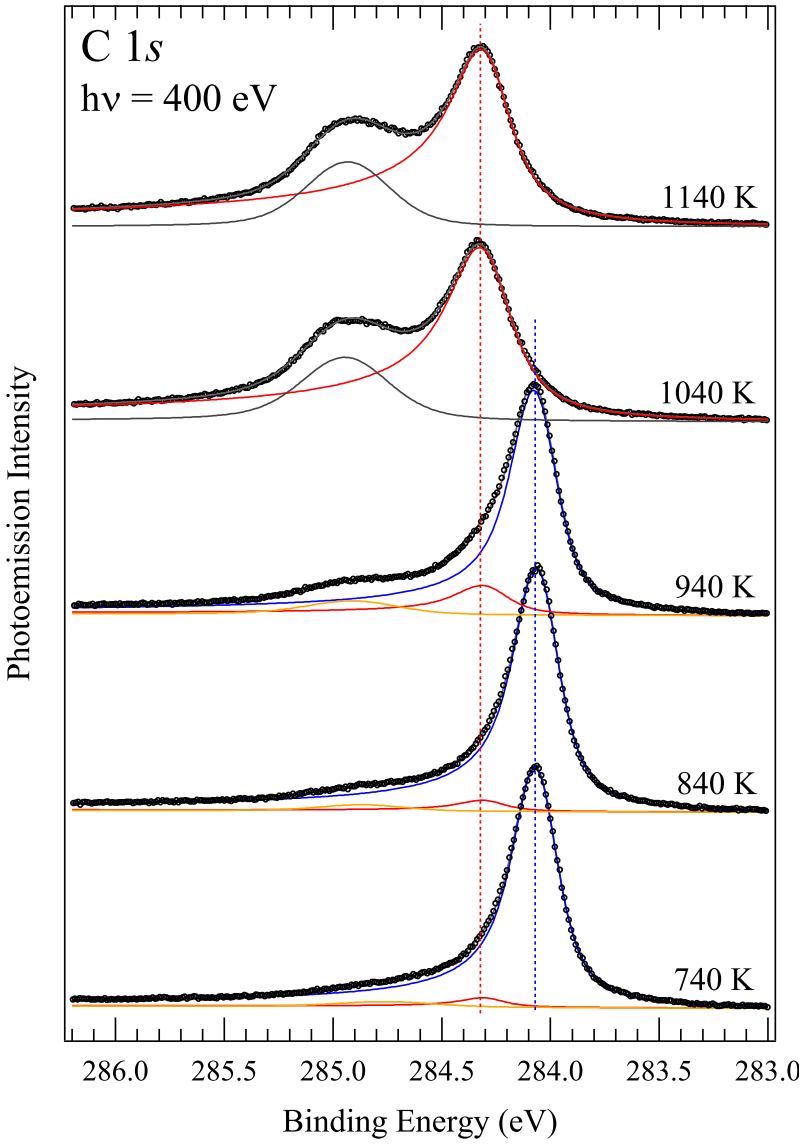

Figure 8.34: Series of C 1*s* spectra acquired after annealings in the temperature range 740–1140 K. Rh coverage is 0.37 ML. The spectral components obtained from the fitting procedure are also indicated.

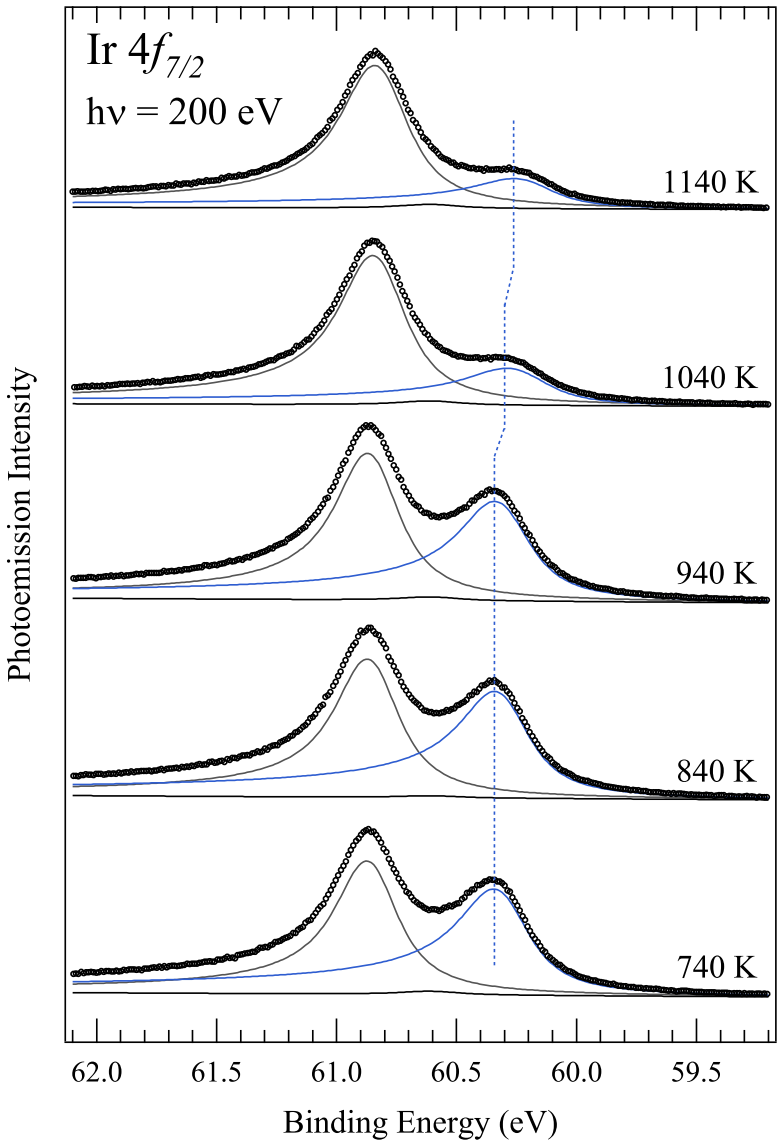

Figure 8.35: Series of Ir $4f_{7/2}$ spectra acquired after annealings in the temperature range 740–1140 K. Rh coverage is 0.37 ML. The spectral components obtained from the fitting procedure are also indicated. The vertical lines are intended only as a guide for the eyes.

- By observing that the Rh $3d_{5/2}$ does not decrease and by taking into account the low segregation energy for Rh atoms in an Ir host, we can exclude the formation of a Rh-Ir alloy. The disappearance of the surface component in the Rh $3d_{5/2}$ line shape can be explained by considering that when rhodium intercalates below graphene, the surfaces of Rh islands interact with the graphene overlayer. If we compare Rh $3d_{5/2}$ spectrum with that obtained in the case of graphene grown on Rh(111) (fig. 8.36, panel (b)) we can appreciate the good agreement between the positions of the Rh $3d_{5/2}$ components that can be identified in the two systems, except for the bulk component that is completely lacking in the case of intercalated rhodium. This last observation suggests that the intercalated Rh atoms form thin two-dimensional islands, which prevents Rh atoms from reaching bulk-like coordination.

8.4.4 Conclusions

The experiments described above are good examples of how photoemission spectroscopy can be successfully applied to the detailed analysis of morphology and electronic properties of supported transition metal clusters. These properties, in turn, play a fundamental role in determining the chemical behaviour of the system under investigation.

In the case of gold clusters deposited on graphene, we found that ordered three-dimensional clusters with well defined facets are formed. Moreover, we discovered that above 1040 K Au atoms begin to evaporate from the sample surface, establishing a thermal limit for the system stability.

In the experiments focused on platinum clusters, we observed a high mobility of single Pt adatoms on the graphene surface even at 30 K. The diffusion process leads to the aggregation of Pt atoms: the resulting clusters induce a long range perturbation of the graphene layer that reduces the adatom mobility.

In the case of graphene supported rhodium clusters, the line shape of Rh $3d_{5/2}$ core level spectra suggests the formation of three-dimensional clusters: the high energy resolution measurements allowed the identification of the spectral components due to ordered facets and edges in the clusters. Annealings at temperatures above 1040 K induces the intercalation of Rh atoms between the graphene layer and the iridium substrate.

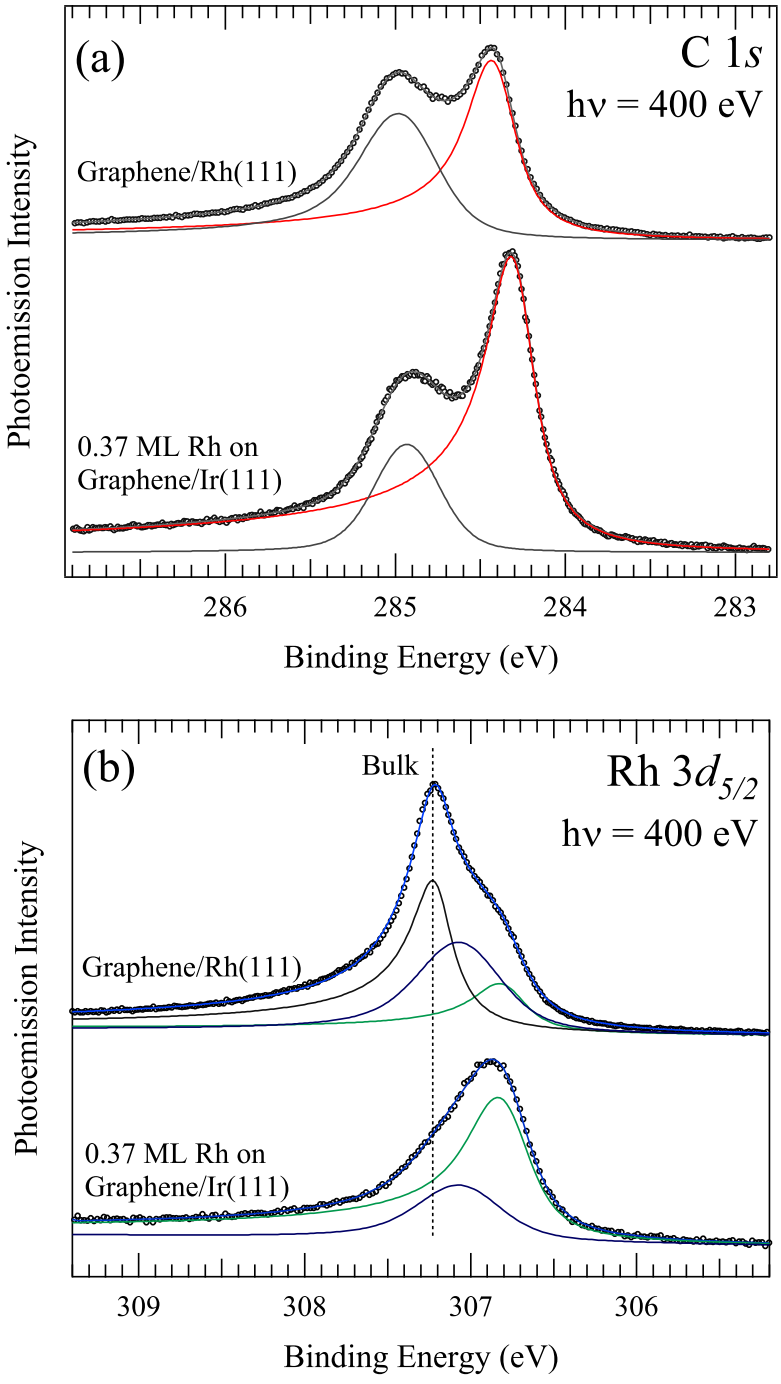

Figure 8.36: Comparison of C 1*s* (a) and Rh $3d_{5/2}$ (b) core level spectra measured for rhodium clusters on graphene/Ir(111) after annealing at 1140 K with those obtained in the case of a graphene layer grown on the Rh(111) surface.

Bibliography

[1] K.S. Novoselov, A.K. Geim, S.V. Morozov, D. Jiang, Y. Zhang, S.V. Dubonos, I.V. Grigorieva, and A.A. Firsov, *Electric Field Effect in Atomically Thin Carbon Films*, Science **306** (2004), 666–669.

[2] T. Ando, *The electronic properties of graphene and carbon nanotubes*, NPG Asia Materials **1** (2009), 17–21.

[3] A.K. Geim and K.S. Novoselov, *The rise of graphene*, Nature Materials **6** (2007), 183–191.

[4] K.S. Novoselov, D. Jiang, F. Schedin, T.J. Booth, V.V. Khotkevich, S.V. Morozov, and A.K. Geim, *Two-dimensional atomic crystals*, Proceedings of the National Academy of Science **102** (2005), 10451–10453.

[5] S.V. Morozov, K.S. Novoselov, M.I. Katsnelson, F. Schedin, D.C. Elias, J.A. Jaszczak, and A.K. Geim, *Giant Intrinsic Carrier Mobilities in Graphene and Its Bilayer*, Physical Review Letters **100** (2008), 016602.

[6] V. Barone, O. Hod, and G.E. Scuseria, *Electronic Structure and Stability of Semiconducting Graphene Nanoribbons*, Nano Letters **6** (2006), 2748–2754.

[7] M.Y. Han, B. Özyilmaz, Y. Zhang, and P. Kim, *Energy Band-Gap Engineering of Graphene Nanoribbons*, Physical Review Letters **98** (2007), 206805.

[8] C. Lee, X. Wei, J.W. Kysar, and J. Hone, *Measurement of the Elastic Properties and Intrinsic Strength of Monolayer Graphene*, Science **321** (2008), 385–388.

[9] F. Schedin, A.K. Geim, S.V. Morozov, E.W. Hill, P. Blake, M.I. Katsnelson, and K.S. Novoselov, *Detection of individual gas molecules adsorbed on graphene*, Nature Materials **6** (2007), 652–655.

[10] M.C. Lemme, T.J. Echtermeyer, M. Baus, and H. Kurz, *A Graphene Field-Effect Device*, IEEE Electron Device Letters **28** (2007), 282–284.

[11] T.J. Echtermeyer, M.C. Lemme, M. Baus, B.N. Szafranek, A.K. Geim, and H. Kurz, *Nonvolatile Switching in Graphene Field-Effect Devices*, IEEE Electron Device Letters **29** (2008), 952–954.

[12] R.R. Nair, P. Blake, A.N. Grigorenko, K.S. Novoselov, T.J. Booth, T. Stauber, N.M.R. Peres, and A. K. Geim, *Fine Structure Constant Defines Visual Transparency of Graphene*, Science **320** (2008), 1308.

[13] G. Eda, G. Fanchini, and M. Chhowalla, *Large-area ultrathin films of reduced graphene oxide as a transparent and flexible electronic material*, Nature Nanotechnology **3** (2008), 270–274.

[14] X. Wang, L. Zhi, and K. Müllen, *Transparent, Conductive Graphene Electrodes for Dye-Sensitized Solar Cells*, Nano Letters **8** (2008), 323–327.

[15] V.C. Tung, M.J. Allen, Y. Yang, and R.B. Kaner, *High-throughput solution processing of large-scale graphene*, Nature Nanotechnology **4** (2009), 25–29.

[16] H. Hibino, H. Kageshima, F. Maeda, M. Nagase, Y. Kobayashi, , and H. Yamaguchi, *Microscopic thickness determination of thin graphite films formed on SiC from quantized oscillation in reflectivity of low-energy electrons*, Physical Review B **77** (2008), 075413.

[17] T. Ohta, F. El Gabaly, A. Bostwick, J. L. McChesney, K. V. Emtsev, A.K. Schmid, T. Seyller, K. Horn, and E. Rotenberg, *Morphology of graphene thin film growth on SiC(0001)*, New Journal of Physics **10** (2008), 023034.

[18] S. Helveg, C. López-Cartes, J. Sehested, P.L. Hansen, B.S. Clausen, J.R. Rostrup-Nielsen, F. Abild-Pedersen, and J.K. Nørskov, *Atomic-scale imaging of carbon nanofibre growth*, Nature **427** (2004), 426–429.

[19] S. Marchini, S. Günther, and J. Wintterlin, *Scanning tunneling microscopy of graphene on Ru(0001)*, Physical Review B **76** (2007), 075429.

[20] A.T. N'Diaye, S. Bleikamp, P.J. Feibelman, and T. Michely, *Two-Dimensional Ir Cluster Lattice on a Graphene Moiré on Ir(111)*, Physical Review Letters **97** (2006), 215501.

[21] A.T. N'Diaye, J. Coraux, T.N. Plasa, and T. Michely, *Structure of epitaxial graphene on Ir(111)*, New Journal of Physics **10** (2008), 043033.

[22] J. Coraux, A.T. N'Diaye, C. Busse, and T. Michely, *Structural Coherency of Graphene on Ir(111)*, Nano Letters **8** (2008), 565–570.

[23] A.T. N'Diaye, T. Gerber, C. Busse, J. Mysliveček, J. Coraux, and T. Michely, *A versatile fabrication method for cluster superlattices*, arXiv:0908.3800v1 (2009).

[24] A.B. Preobrajenski, M.L. Ng, A.S. Vinogradov, and N. Mårtensson, *Controlling graphene corrugation on lattice-mismatched substrates*, Physical Review B **78** (2008), 073401.

[25] I. Pletikosič, M. Kralj, R. Brako, J. Coraux, A.T. N'Diaye, C. Busse, and T. Michely, *Dirac Cones and Minigaps for Graphene on Ir(111)*, Physical Review Letters **102** (2009), 056808.

[26] E. Loginova, N.C. Bartelt, P.J. Feibelman, and K.F. McCarty, *Evidence for graphene growth by C cluster attachment*, New Journal of Physics **10** (2008), 093026.

[27] J. Coraux, A.T. N'Diaye, M. Engler, C. Busse, D. Wall, N. Buckanie, F.-J. Meyer zu Heringdorf, R. van Gastel, B. Poelsema, and T. Michely, *Growth of graphene on Ir(111)*, New Journal of Physics **11** (2009), 023006.

[28] G. Kresse and J. Furthmüller, *Efficient iterative schemes for* ab initio *total-energy calculations using a plane-wave basis set*, Physical Review B **54** (1996), 11169–11186.

[29] P.E. Blöchl, *Projector augmented-wave method*, Physical Review B **50** (1994), 17953–17979.

[30] G. Kresse and D. Joubert, *From ultrasoft pseudopotentials to the projector augmented-wave method*, Physical Review B **59** (1999), 1758–1775.

[31] J.P. Perdew, K. Burke, and M. Ernzerhof, *Generalized Gradient Approximation Made Simple*, Physical Review Letters **77** (1996), 3865–3868.

[32] M. Bianchi, D. Cassese, A. Cavallin, R. Comin, F. Orlando, L. Postregna, E. Golfetto, S. Lizzit, and A. Baraldi, *Surface core level shifts of clean and oxygen covered Ir(111)*, New Journal of Physics **11** (2009), 063002.

[33] F.J. García de Abajo, M.A. Van Hove, and C.S. Fadley, *Multiple scattering of electrons in solids and molecules: A cluster-model approach*, Physical Review B **63** (2001), 075404.

[34] Y. Takata, Y. Kayanuma, M. Yabashi, K. Tamasaku, Y. Nishino, D. Miwa, Y. Harada, K. Horiba, S. Shin, S. Tanaka, E. Ikenaga, K. Kobayashi, Y. Senba, H. Ohashi, and T. Ishikawa, *Recoil effects of photoelectrons in a solid*, Physical Review B **75** (2007), 233404.

[35] E.L. Shirley, L.J. Terminello, A. Santoni, and F.J. Himpsel, *Brillouin-zone-selection effects in graphite photoelectron angular distributions*, Physical Review B **51** (1995), 13614–13622.

[36] M. Mucha-Kruczyński, O. Tsyplyatyev, A. Grishin, E. McCann, V.I. Falko, A. Bostwick, and E. Rotenberg, *Characterization of graphene through anisotropy of constant-energy maps in angle-resolved photoemission*, Physical Review B **77** (2008), 195403.

[37] B. Kempgens, H. Köppel, A. Kivimäki, M. Neeb, L.S. Cederbaum, and A.M. Bradshaw, *Core Level Energy Splitting in the C* 1*s Photoelectron Spectrum of* C_2H_2, Physical Review Letters **79** (1997), 3617–3620.

[38] H. Köppel, F.X. Gadea, G. Klatt, J. Schirmer, and L.S. Cederbaum, *Multistate vibronic coupling effects in the K-shell excitation spectrum of ethylene: Symmetry breaking and core-hole localization*, Journal of Chemical Physics **106** (1997), 4415–4429.

[39] N. Weiss, T. Crena, M. Epple, S. Rusponi, G. Baudot, S. Rohart, A. Tejeda, V. Repain, S. Rousset, P. Ohresser, F. Scheurer, P. Bencok, and H. Brune, *Uniform Magnetic Properties for an Ultrahigh-Density Lattice of Noninteracting Co Nanostructures*, Physical Review Letters **95** (2005), 157204.

[40] H.-G. Boyen, G. Kästle, F. Weigl, B. Koslowski, C. Dietrich, P. Ziemann, J.P. Spatz, S. Riethmüller, C. Hartmann, M. Möller, G. Schmid, M.G. Garnier, and P. Oelhafen, *Oxidation-Resistant Gold-55 Clusters*, Science **297** (2002), 1533–1536.

[41] P.J. Feibelman, *Pinning of graphene to Ir(111) by flat Ir dots*, Physical Review B **77** (2008), 165419.

[42] S. Tanuma, C.J. Powell, and D.R. Penn, *Calculations of electron inelastic mean free paths. V. Data for 14 organic compounds over the 50-2000 eV range*, Surface and Interface Analysis **21** (1994), 165–176.

[43] R. Haerle, E. Riedo, A. Pasquarello, and A. Baldereschi, sp^2/sp^3 *hybridization ratio in amorphous carbon from C 1s core-level shifts: X-ray*

photoelectron spectroscopy and first-principles calculation, Physical Review B **65** (2001), 045101.

[44] P. Heinmann, J.F. van der Veen, and D.E. Eastman, *Structure-dependent surface core level shifts for the Au(111), (100) and (110) surfaces*, Solid State Communications **38** (1981), 595–598.

[45] H. Hövel and I. Barke, *Morphology and electronic structure of gold clusters on graphite: Scanning-tunneling techniques and photoemission*, Progress in Surface Science **81** (2006), 53–111.

[46] A.V. Ruban, H.L. Skriver, and J.K. Nørskov, *Surface segregation energies in transition-metal alloys*, Physical Review B **59** (1999), 15990–16000.

[47] A. Baraldi, L. Bianchettin, E. Vesselli, S. de Gironcoli, S. Lizzit, L. Petaccia, G. Zampieri, G. Comelli, and R. Rosei, *Highly undercoordinated atoms at Rh surfaces: interplay of strain and coordination effects on core level shift*, New Journal of Physics **9** (2007), 143.

[48] L. Bianchettin, A. Baraldi, S. de Gironcoli, E. Vesselli, S. Lizzit, L. Petaccia, G. Comelli, and R. Rosei, *Core level shifts of undercoordinated Pt atoms*, The Journal of Chemical Physics **128** (2008), 114706.

[49] P.J. Feibelman, *Onset of three-dimensional Ir islands on a graphene/Ir(111) template*, Physical Review B **80** (2009), 085412.

Appendix A

Publications

The characteristics of the newly developed delay-line detectors are described in:

G. Cautero, R. Sergo, L. Stebel, P. Lacovig, P. Pittana, M. Predonzani, S. Carrato, *A two-dimensional detector for pump-and-probe and time resolved experiments*, Nuclear Instruments and Methods A **595** (2008), 447–459.

The study on the Pd/Ru(0001) bimetallic interface can be found in:

E. Golfetto, A. Baraldi, M. Pozzo, D. Alfé, A. Sala, P. Lacovig, E. Vesselli, S. Lizzit, G. Comelli, and R. Rosei, *Determining the Chemical Reactivity Trends of Pd/Ru(0001) Pseudomorphic Overlayers: Core-Level Shift Measurements and DFT Calculations*, Journal of Physical Chemistry C **114** (2010), 436–441

Part of the work related to the graphene/Ir(111) system can be found in:

P. Lacovig, M. Pozzo, D. Alfé, P. Vilmercati, A. Baraldi, and S. Lizzit, *Growth of Dome-Shaped Carbon Nanoislands on Ir(111): The Intermediate between Carbidic Clusters and Quasi-Free-Standing Graphene*, Physical Review Letters **103** (2009), 166101.

- Commented in: J.O. Sofo, and R.D. Diehl, *Viewpoint: Geodesic carbon nanodomes*, Physics **2** (2009), 84.

- Commented in: L. Donaldson, *Graphene speeds up computers*, Materials Today **12**, issue 12 (2009), 12.

S. Lizzit, G. Zampieri, L. Petaccia, R. Larciprete, P. Lacovig, E.D.L. Rienks, G. Bihlmayer, A. Baraldi, and Ph. Hofmann, *Band dispersion in the deep* 1*s core level of graphene*, Nature Physics, accepted for publication **doi:** 10.1038/nphys1615

Further works on

- the Pd nucleation on graphite and carbon nanotubes,

- the nucleation of Rh clusters on graphene,

- and the CO oxidation process on Pt nanoclusters deposited on MgO/Ag(100)

are currently in preparation.

Appendix B

Abbreviations

AFM	Atomic Force Microscopy
ARPES	Angular Resolved PhotoElectron Spectroscopy
BE	Binding Energy
CVD	Chemical Vapour Deposition
CL	Core Level
DFT	Density Functional Theory
ER	Eley-Rideal reaction mechanism
ESCA	Electron Spectroscopy for Chemical Analysis
FWHM	Full Width at Half Maximum
GIXS	Grazing Incidence X-ray Scattering
HAXPES	Hard X-ray PhotoElectron Spectroscopy
IMFP	Inelastic Mean Free Path
LEED	Low Energy Electron Diffraction
LH	Langmuir-Hinshelwood reaction mechanism
PES	PhotoElectron Spectroscopy
SCLS	Surface Core Level Shift
SEM	Scanning Electron Microscopy
SPA-LEED	Spot Profile Analysis - Low Energy Electron Diffraction
STM	Scanning Tunneling Microscopy
TEM	Transmission Electron Microscopy
TM	Transition Metal
XPD	X-ray Photoelectron Diffraction
XPS	X-ray Photoelectron Spectroscopy
UHV	Ultra-High Vacuum

Acknowledgements

First of all I would like to thank my tutors, Alessandro and Silvano, for showing me how to carry forward a scientific project with accuracy, enthusiasm, efficiency and honesty.
... for their continuous help during these three years: without their support I probably wouldn't have even begun this PhD project.
... and, mostly important, for their friendship.
Thank you very much!

I wish to thank Giuseppe for giving me the possibility to follow the activities related to my PhD project during these years.

Many thanks also
... to my colleagues of the "Instrumentation & Detector Lab": Dario, Rudi, Marco, "Harry" (aka Luigi), Alessandro (Gub), Enrico and Marco (Ricky Boba), for their help in the instrumental part of the project and for sharing with me this experience.
... to Rosanna, Erik, "Guf", Alessandro, Alberto, Marco, Philip, Sandra and Michele with whom I nicely spent many hours (during days and nights) for setting-up experiments and during measurements at SuperESCA.
... to "Pitt" for his curiosity about *everything* that led to *philosophical* conversastions at improbable night hours after my measurement shifts at the beamline.
... to Christian and Luca, they know why...
... and to Giancarlo, Francesco, Andrea and Piero: those long and slow *VOLPE* experiments on ID16 at Grenoble can be considered the starting point of this adventure.

I want to thank my parents and my syster, who, as always, helped me also in this project of mine.

Sincere thanks to Cristina, who never stopped believing in me as a person and in my possibilities for successfully concluding this project. Thank you for all!

And to Nicola. Each time, sitting on my knees in front of the laptop, your "Dad, tell me again about your... graphite... pencils... iridium... You know, I like those *technological things*!" pushed me forward to the completion of this work.